Weilin Xu



Mesoscale Analysis of Hydraulics

Springer

Mesoscale Analysis of Hydraulics

Weilin Xu

Mesoscale Analysis of Hydraulics

Springer

Weilin Xu
Sichuan University
Chengdu, China

ISBN 978-981-15-9784-8 ISBN 978-981-15-9785-5 (eBook)
https://doi.org/10.1007/978-981-15-9785-5

This Springer imprint is published by the registered company Springer Nature Singapore Pte Ltd.
The registered company address is: 152 Beach Road, #21-01/04 Gateway East, Singapore 189721, Singapore

Foreword I

In the world today, the height of large dams has exceeded 300 m resulting in flow velocity faster than 50 m/s at its appurtenant water release structures. Thus the safe flood passage at such very high dams is becoming more and more challenging. In fact, high-velocity flows have been at the origin of the most severe damages encountered at hydraulic structures of large dam projects.

Cavitation is most often the greatest threat to spillways and water release structures as low-level outlets. Whether cavitation is likely to occur is normally analyzed in practice by the help of the cavitation number. However, the cavitation number characterizing the flow as a whole does not allow to determine precisely if cavitation occurs locally near wall surfaces and thus causes cavitation erosion. Currently, actively forced flow aeration is one of the main mitigation measures against cavitation damage. Nevertheless, cavitation can be only avoided if the physical aeration process is well understood and governed by an appropriate determination of the control conditions of aeration. Two phase water-air flows occur when air enters into the water flow and water drops are separated from the water body. Hence, the mechanisms of forming air bubbles and water drops near the free surface is a key for studying water-air phase flows. Furthermore, it is important to know whether small-scale penetrating eddy motions occur in high-velocity flows and if separated water drops result in severe atomized precipitation onto the water surface. Finally, the knowledge on coupled water-sediment-air flows is essential.

All these described multiphase flow features have in common that air bubbles, cavitation bubbles, water drops, sand particles and small eddies are involved which all occur on a mesoscale. Thus, a new approach has been chosen in the book by using mesoscale analysis. In a physical sense, all the above described flow phenomena are the result of the interactions between discontinuous multiphase medium, which are difficult to study in detail with traditional continuous medium approaches. By analyzing water flow movements from a mesoscopic perspective, the author gives new insights in mesoscopic mechanisms which are essential for differentiation criterion of cavitation, aeration reduction, water-air phase flows, energy dissipation of plunging jets, spray and water foam formation, as well as debris flows. With his analytical findings the author gives promising input for new engineering technologies. With its systematic hydraulic approach from the macroscale to the mesoscale, the book may

inspire new research fields and may become a reference in hydraulics with focus on high-velocity flows occurring at very large dams.

Dr. Anton J. Schleiss
Professor emeritus
Honorary President ICOLD and Chairman of
Technical Committee on Hydraulics for Dams,
Ecole polytechnique fédérale de Lausanne
(EPFL), Lausanne, Switzerland

Foreword II

Hydraulic engineering is one of the foundational elements of civil engineering that helps sustain the natural environment and enables a built environment that enhances the well-being of society. The fundamental physics of hydraulics has not changed over the past few decades but the application of hydraulic engineering principles to address issues facing society has changed significantly as unexpected consequences have been experienced. Problems are necessarily more complex, more inter-connected and dynamic—often requiring inter-disciplinary solutions. This trend is compounded by implementation of larger and more complex hydraulic infrastructure that is partly mitigated by the increasing ability to detect and predict environmental consequences. One example is the increasing size of dams, some of which exceed 300 m in height, and require management of spillway flow velocities that may exceed 50 m/s and operate under very different conditions than the large dams of previous decades. In this monograph, Professor Xu sets the foundation for developing greater insights for the flow structure that bridges the gap between the micro-scale that can be studied in the laboratory such as the dynamics of air bubbles and macroscale processes that can be captured adequately by depth-averaged or sectionally averaged flow metrics—usually described by the integral form of the governing equations. It is this intermediate (or meso-) scale where many processes originate and solutions can be found.

Professor Xu connects laboratory-scale research that captures the finer scales on the mesoscale spectrum with his extensive experience addressing applied problems in prototype and field studies. This text is timely as emerging sensor technologies have allowed much greater temporal and spatial resolution of both laboratory and field measurements which when coupled with visualization enables greater insights to the phenomenon and how undesirable ramifications can be addressed. These processes are illustrated throughout the text to create an excellent teaching tool as well as providing a reference for researchers and practitioners. Professor Xu provides a detailed elicitation of the processes through detailed reference to the relevant literature and enriched by his personal experiences on resolving large-scale applied problems. Problems addressed span air entrainment, 2-phase air-water flows, high velocity flows and energy dissipation. The applications are numerous and diverse, including cavitation effects in hydraulic infrastructure, ecological application such as

the initiation and persistence of total dissolved gas downstream of large dams and the consequences and remedies for flood discharge atomization. Maintaining the theme of high velocity flows, there are detailed insights into forced sediment deposition patterns around hydraulic jumps in open channels under flood flow conditions that can result in catastrophic failure, potential loss of life and severe property damage. Design measures are developed that mitigate for this potential occurrence.

This text provides insights to the complexity of flow characteristics associated with hydraulic infrastructure and design concepts for the avoidance of adverse consequences under extreme flow conditions.

October 2020

Dr. Peter Goodwin
Professor
Former President of IAHR, President of the
University of Maryland Center for Environmental
Science, Cambridge, MD, US

Acknowledgments

I have been grateful to those who have assisted me during the writing of this academic work.

My gratitude goes to my students. They are Bai Lixin, Wei Wangru, Luo Jing, Li Yao, Zhang Yalei, Zhai Yan Wei, Yuan Hao, Li Jianbo, Mao Dongping, Zhong Xiaofeng, Li Yilan, A Rong, Chen Siyu, Ye Fangzhou and so on. Without years of their joint efforts in exploration, the publication of this book would not have been possible. I sincerely hope all my students can have a better and brighter future.

I would like to give my thanks to my team members: Liu Shanjun, Wang Wei, Zhang Jianmin, Deng Jun, Tian Zhong, Zhang Faxing, Qu Jingxue, Yu Ting and Zhou Maolin. From long-term collaboration with them, I have benefited a lot, which helped to enrich the content of this book, and also made it possible to apply it in many world-class large-scale water conservancy and hydropower projects. I feel deeply honored to be part of such an outstanding team.

I would like to give my thanks to my colleagues: Liu Xingnian, Wang Xiekang, Yang Xingguo, Zhou Jiawen, Nie Ruihua, Li Naiwen, Chen Ridong and Huang Er. Thanks to their academic contribution, this book not only contained the contents of high dam hydraulics, but also that of mountain torrents and sediment disasters, which opened up a new field for the mesoscopic analysis of hydraulics.

I also owe my sincere gratitude to many experts who have consistently provided me with valuable suggestions and supports in relevant research and work through all these years of writing this book. Most of them are my learning models.

Last but not least, I would like to give my thanks to Wang Wei, Yu Ting, Wei Wangru, Luo Jing and Zhang Jianmin, who have given strong supports and generous helps to me during the writing and publication of this book.

Contents

About the Author

Weilin Xu is Professor at Sichuan University (SCU) in Chengdu, China. He received the National Science Fund for Distinguished Youth Scholars, the Changjiang Chair-professor. He is Director of the State Key Laboratory of Hydraulics and Mountain River Engineering. He is the executive member of the council of Chinese Society of Hydroelectric Engineering, the executive member of the council of Chinese Society of Large Dam Engineering and member of the Hydraulics for Dams Technical Committee of the International Commission on Large Dams. He has mainly worked on the high dam hydraulics. He has undertaken many basic research projects, including key research projects supported by the National Natural Science Foundation and the National Key Basic Research Plan. Besides, he has taken charge of many high dam engineering research projects. He has published over 100 papers, and he has published four monographs. His achievements have been applied in high dam projects such as Jinping-I Hydropower Station, Xiangjiaba Hydropower Station, Xiluodu Power Station and Pubugou Hydropower Station. Additionally, lots of prizes have been awarded to Professor Xu, which included "National Award for Technological Invention" and "National Award for Science and Technology Progress".

List of Main Symbols

C_a	Air concentration
C_w	Water concentration
C_{mean}	Mean cross-sectional concentration
D_w	Water-phase turbulent diffusion coefficient
C_p	Particle concentration
D_a	Air-phase turbulent diffusion coefficient
D_v	The distance between the bottom boundary and the center of the CB
d_{mean}	Mean air bubble diameter
d_{50}	Quartz sand particles of mean diameters
E	Modulus of elasticity
Et'	Dimensionless tensile modulus of elasticity
F	Bubble frequency
f	Flow-rate ratio
H	Compressive deformation height of flexible materials
h	Height of the convex body
I_{max}	Maximum rainfall intensity
K_e	Mean turbulent energy of the flow near the free surface
M_L	Cumulative amount of erosion
L	Distance between two boundaries
n_d	Number of water droplets
Pd	Probability of a certain diameter
P_{max}	Impact intensity of the shock wave
P_v	Probability of a certain droplet velocity
Q_a, Q_w	Volume flows of air and water, respectively
R_a	Equivalent radius of the air bubble
Re	Flow Reynolds number
R_{max}	Maximum radius of the cavitation bubble
r	Curvature radius of the local deformation
r_C	Critical curvature radius of the free-surface
r_m	Curvature radius at the bottom endpoint with the maximum deformation
T_1 and T_2	Times needed by the two CBs to complete their first collapse, respectively

u_0	Cross-sectional mean velocity of the inflow
V_e	Entrainment velocity of air into the water
V_r	Bubble rising velocity of air in the water
v'	Turbulent velocity
v^*	Local characteristic velocity near the vortex
v_τ	Mesoscale friction velocity
We	Flow Weber number
y_2	Characterized flow depth where local air concentration is 0.02
y_{50}	Characterized flow depth where local air concentration is 0.50
y_{90}	Local flow depth where local air concentration is 0.90
α	Channel slope
α_s	Shape parameter of the probability distribution of water droplets.
β	Angle between the outlet nappe and the streamwise direction
γ_{bw}	Dimensionless distance between the cavitation bubble and the boundary
γ_{bb}	Dimensionless relative distance between the two CBs
γ_{bp}	Dimensionless distance between a CB and a particle
γ_0	Critical distance required for the microjet to penetrate the boundary
ω	Dimensionless distance between the centroids of air bubbles and cavitation bubbles
ε	Ratio between the radii of the air bubble and cavitation bubble
ξ	Local head loss coefficient
θ	Angle between the line of the air bubble-cavitation bubble and the normal line from the cavitation bubble center to the wall with the cavitation bubble center as the apex.
ζ	Correction coefficient
λ	Criterion indicators for identifying vortex blobs
η_{Fr}	Ratio of the Froude number of the upstream and downstream of the hydraulic jump
Δt_0	The difference between the inception times of the two CBs

List of Main Acronyms

CB	Cavitation bubble
FDA	Flood discharge atomization
FFSD	Flash flood and sediment disaster
SP	Sound pressures

Chapter 1
Introduction

In nature and engineering, when the water flow velocity reaches a certain high level, a series of special water flow phenomena such as cavitation erosion, strong air entrainment, splashing, severe fluctuations, and severe scour and abrasion may occur. High-velocity hydraulics is a hydraulic research area that targets these special flow phenomena.

In hydraulic and hydropower engineering projects, these flow phenomena are often concentrated due to high flow velocity, complex boundaries, and free surfaces, posing a particularly prominent threat of destruction. In this book, these water flow phenomena are studied at the mesoscale level in the context of hydraulic and hydropower engineering, aiming at better application of high-velocity hydraulics in engineering guidance.

1.1 Definition of Mesoscale

In terms of research methods, high-velocity hydraulics has undergone two research stages, namely, a stage combining theoretical analysis and physical experimentation and a stage combining theoretical analysis, physical experimentation, and numerical simulation. The theoretical analysis is mainly based on fluid mechanics and hydraulics theory (Pope 2001), the physical experimentation includes mechanism testing, scale model testing, and engineering prototype testing (Brennen 2005), and the numerical simulations are based on the Navier–Stokes equations and take advantages of numerical methods and modern computing technology (Lee et al. 1990; Bernard and Wallace 2002).

In terms of research scale, the past high-velocity hydraulics is mainly categorized as macroscale research, which is characterized by the description of the motion of water flow with macroscopic parameters such as flow rate, water depth, flow velocity, pressure, and concentration (Boes and Hager 2003; Hager 2013). In the early stage, the concept of total flow was largely adopted, using the integral forms of

W. Xu, *Mesoscale Analysis of Hydraulics*,
https://doi.org/10.1007/978-981-15-9785-5_1

the continuity equations, equations of motion, and momentum equations as the main theoretical tools and supplemented by a large amount of experimental measurements and analyses (Hibbeler 2007; Crowe et al. 2011). In the late stage, with the development of measurement and computing technologies, detailed descriptions of the flow field became possible, the differential forms of the water flow equations started to play an increasingly prominent role, and the detailed spatiotemporal distribution of the macroscopic parameters could be obtained through physical experimentation and numerical simulation (Xu et al. 2002).

In theory, high-velocity hydraulics problems are actually multiscale problems ranging from the macroscopic to microscopic scale. The microscale here refers to the molecular scale of water and the medium interacting with water (Crowe et al. 1998). For example, the main energy dissipation in water flow follows the cascade of the mean flow, large vortex (energy-containing vortex), small vortex (energy-dissipating vortex), smaller vortex, and the so-called minimum vortex, which is unable to overcome the viscous effect of the water flow. Eventually, the energy is dissipated by the minimum vortex into the thermal energy of the water body through the viscous effect of the water flow, that is, the thermal motion of molecules. Another example is the dissolution and evaporation in the air–water two-phase flow at the microscopic scale, regardless of air bubbles in the water or water droplets in the air. A third example is the formation of cavitation erosion and scour, which, at the microscopic scale, is ultimately attributed to the breaking of bonds between molecules in solid materials under water flow. From this perspective, as research methods continue to advance, the study of high-velocity hydraulics may eventually expand to the microscale in the future.

It has become increasingly difficult to meet current engineering needs by relying only on macroscale research (which is especially unsatisfactory for revealing underlying mechanisms), while the necessity of microscale research has not yet been fully justified. Therefore, mesoscale research has become an area that urgently needs to be explored. The mesoscale here refers to the scale of cavitation bubbles, air bubbles, water droplets, particles, and small vortex blobs between macroscopic flow and microscopic molecules. The role of mesoscale research is to more clearly reveal the underlying mechanism and trends of the special hydraulic phenomena of high-velocity water flow and to better predict the occurrence and development of these phenomena in order to better provide theoretical and methodological guidance for engineering applications.

1.2 Necessity of Mesoscale Research

Although various mechanical phenomena specific to high-velocity water flow exhibit remarkable macroscopic characteristics on the surface, they are essentially the macroscopic aggregation of mesoscopic phenomena. Cavitation is the process of the generation, development, movement, and collapse of cavitation bubbles (Rayleigh 1917; Plesset 1949). Cavitation erosion is the result of cavitation bubbles acting on a solid

surface (Knapp et al. 1979). Aerated water flow is a result of water entraining air bubbles and water droplets spalling into the air (Ervine and Falvey 1987). Aeration and erosion protection is the interaction between cavitation bubbles, air bubbles, and a solid surface (Russell and Sheehan 1974). Flood discharge atomization is the diffusion of water droplets or clusters of water droplets in the air (Ibrahim and Przekwas 1991). Energy dissipation is the process by which small vortex blobs eventually dissipate the energy of water flow into thermal energy (Kolmogorov 1962).

Therefore, if we only study the various mechanical phenomena specific to high-velocity flow from the macroscopic scale, it is inevitably difficult to clarify the complex underlying mechanisms. In fact, the in-depth understanding of cavitation erosion so far has been mostly originated from research on bubble dynamics, which itself is mesoscopic research. Nevertheless, the previous studies on bubble dynamics have mostly focused on cavitation bubbles but have rarely involved the effects of factors such as the two-phase flow that is of concern to hydraulics. The first thing to understand regarding aerated water flow is the mechanism of air entrainment in water flow, which is the basis for revealing the concentration distribution pattern. Although the previous understanding of this aspect has been limited by experimental techniques, the research on aerated water flow has consistently been committed to forming a complete chain ranging from the origin of aeration to prediction methods. Aeration and erosion protection is a more typical example. Due to the lack of a direct experimental basis for understanding the mechanism of aeration and erosion protection, there have been a variety of explanations for this mechanism for a long time. In addition, mesoscale analysis plays a very important role in the study of the calculation methods and the scale effect of flood discharge atomization as well as the local vortex structures of flood discharge and energy dissipation.

The development of contemporary experimental and computing techniques provides a powerful basis for the mesoscale analysis of high-velocity hydraulics. The early film-based high-speed cameras have been replaced by digital counterparts, which not only have faster shutter speeds and higher image quality but also reduce the cost of image analysis and improve the analysis efficiency. The development and popularization of many pieces of specialized equipment such as the spark-induced cavitation generating device, laser-induced cavitation generating device, and ultrasonic cavitation device have greatly facilitated the mesoscopic study of cavitation erosion. Various advanced light source systems also enable more in-depth and detailed mesoscale observations. Additionally, the development of numerical simulation techniques not only opens up a new path for mesoscale analysis but also provides an effective means for clarifying the mechanics behind the phenomena because of its complete and detailed simulation results.

1.3 Main Contents of Mesoscale Research

Overall, mesoscale research mainly includes mesoscopic mechanisms, mesoscopic trends, and mesoscopic predictions.

The study of mesoscopic mechanisms aims to answer the “what” questions. Traditional macroscale studies fail to provide definitive answers to the mechanisms for many well-known high-velocity hydraulic phenomena. A typical example is aeration and erosion protection. Cavitation reduction by aeration has been verified in engineering practice for decades and has even become the last line of defense for the reduction of cavitation damage in hydraulic and hydropower projects. However, there is still a lack of direct evidence-based answers to the most fundamental question of why aeration can reduce cavitation damage. Consequently, multiple explanations coexist, which affects the establishment of basic principles and critical control conditions for the design of aeration and erosion protection facilities in engineering. A similar problem has also occurred in the study of self-aerated water flow, that is, how high-velocity water flow is self-aerated. Only by accurate exposure of the mechanism for self-aeration of high-velocity water flow can various self-aeration theories be unified in order to lay a solid and reliable foundation for the research on self-aerated water flow.

The research on mesoscopic trends are expected to answer the “why” questions. The study of mesoscopic trends is intended to expand and quantify the study of mesoscopic mechanisms. Still taking the aeration and erosion protection as an example, research on mesoscopic trends aims to further reveal the physical factors that influence the effects of aeration and erosion protection as well as the conditions of aeration and erosion protection based on the study of the mesoscopic mechanisms. The same is also true for the example of the self-aeration of high-velocity water flow as described above, that is, how the various factors of high-velocity water flow interact with each other and what level these interactions need to reach to lead to self-aeration. There are many other similar examples. For instance, for cavitation caused by the flow around a convex body, why is cavitation damage to the solid surface induced under some conditions while there is no cavitation damage under other conditions? In this situation, it is certainly difficult to provide an accurate answer by relying only on the incipient cavitation number and flow cavitation number of a convex body, as adopted in macroscopic studies. Another example is the local vertical vortex occurring in flood discharge and energy dissipation. Why is cavitation damage sometimes induced on the floor, but on other occasions, no cavitation damage is induced at all? All of these questions need to be answered through the research on mesoscopic trends.

The core of research on mesoscopic predictions is to answer the “how” questions. Aeration and erosion protection is again taken as an example. To predict aeration and erosion protection, not only the flow field calculation method but also the coupling of the flow field calculation and bubble calculation are needed so that the aeration concentration distribution and the bubble movement can be predicted. Similarly, for self-aerated water flow, it is necessary to establish a systematic calculation method for self-aerated water flow on the basis of elucidating the self-aeration mechanism and conditions of the high-velocity water flow. Obviously, calculation methods (including theoretical calculations and numerical simulations) play very important roles in mesoscopic prediction research.

Specifically, the mesoscale analysis of high-velocity hydraulics in this book includes the following six parts, namely, cavitation erosion, aeration and erosion protection, air–water two-phase flow, energy dissipation and scour, flood discharge atomization, and flash flood and sediment disasters, which have clear mesoscopic characteristics and correspond to Chaps. 2–7 of the book.

References

Bernard, P. S., & Wallace, J. M. (2002). *Turbulent flow: analysis, measurement, and prediction.* New York: Wiley.

Boes, R. M., & Hager, W. H. (2003). Hydraulic design of stepped spillways. *Journal of Hydraulic Engineering, 129*(9), 671–679.

Brennen, C. E., & C. E. Brennen (2005). *Fundamentals of multiphase flow*. Cambridge university press.

Crowe, C., Sommerfeld, M., Tsuji, Y., & Crowe, C. (1998). *Multiphase flows with droplets and particles CRC*. Boca Raton, FL.

Crowe, C. T., Schwarzkopf, J. D., Sommerfeld, M., & Tsuji, Y. (2011). *Multiphase flows with droplets and particles.* CRC press.

Ervine, D., & Falvey, H. (1987). Behaviour of turbulent water jets in the atmosphere and in plunge pools. *Proceedings of the Institution of Civil Engineers, 83*(1), 295–314.

Hager, W. H. (2013). *Energy dissipators and hydraulic jump.* Berlin: Springer Science & Business Media.

Hibbeler, R. C. (2007). *Engineering mechanics: statics.* Pearson Education India.

Ibrahim, E., & Przekwas, A. (1991). Impinging jets atomization. *Physics of Fluids a: Fluid Dynamics, 3*(12), 2981–2987.

Knapp, R. T., Daily, J. W., & Hammitt, F. G. (1979). *Cavitation.* Institute of hydraulic research, University of Iowa.

Kolmogorov, A. N. (1962). A refinement of previous hypotheses concerning the local structure of turbulence in a viscous incompressible fluid at high Reynolds number. *Journal of Fluid Mechanics, 13*(1), 82–85.

Lee, M. J., Kim, J., & Moin, P. (1990). Structure of turbulence at high shear rate. *Journal of Fluid Mechanics, 216,* 561–583.

Plesset, M. S. (1949). The dynamics of cavitation bubbles. *Journal of Applied Mechanics, 16,* 277–282.

Pope, S. B. (2001). *Turbulent flows.* IOP Publishing.

Rayleigh, L. (1917). VIII. On the pressure developed in a liquid during the collapse of a spherical cavity. *The London, Edinburgh, and Dublin Philosophical Magazine and Journal of Science, 34*(200), 94–98.

Russell, S., & Sheehan, G. (1974). Effect of entrained air on cavitation damage. *Canadian Journal of Civil Engineering, 1*(1), 97–107.

Xu, W., Liao, H., Yang, Y., & Wu, C. (2002). Turbulent flow and energy dissipation in plunge pool of high arch dam. *Journal of Hydraulic Research, 40*(4), 471–476.

Chapter 2
Mesoscale Analysis of Cavitation and Cavitation Erosion

2.1 Background

Cavitation is one of the most common types of damage in hydraulic and hydropower engineering projects. In 1941, the spillway of the Boulder Dam in the U.S. suffered cavitation and developed a deep cavitation pit of 35 m in length, 9.5 m in width, and 13.7 m in depth at the end of its ogee section as a result of the washing away of over 4500 m^3 of concrete and rock. In 1967, the spillway of the Yellowtail Dam in the U.S. discharged floodwater at the maximum flow rate of 560 m^3/s and the maximum flow velocity of 48.8 m/s. This led to damage to an area of 38 m in length, 7.3 m in width, and 2.1 m in depth in the ogee section of this spillway as well as its downstream region. In 1967, the overflow section of the Bratsk Hydroelectric Power Station in the former Soviet Union sustained cavitation damage after 11 consecutive days of overflow. As a consequence, a cavitation pit of 1.2 m in depth and approximately 12 m^3 in volume was formed on the surface of the overflow dam. During the flood season of 1964, the Yanguoxia Hydropower Station discharged floodwater at a rate of 4900 m^3/s. Its bottom discharge outlets as well as both sides of the energy-dissipation piers in its stilling basin sustained significant cavitation damage. Approximately 2600 m^3 of the floor of its stilling basin was destroyed by the rush of water. In 1987, the chute of the Longyangxia Hydropower Station sustained damage to varying degrees at both its floor and sidewalls after discharging through the bottom discharge outlets. In 1989, the sidewalls of the chute of the Longyangxia Hydropower Station again sustained damage in a large area. In 2001, the downstream sidewalls and floor of the No. 2 aerator at the end of the ogee section of the No. 1 spillway of the Ertan Hydropower Station were found to have suffered cavitation damage in large areas during the postflood season inspection. In 2006, both sidewalls of the sand-flushing tunnel of the Zipingpu Dam approximately 7.0 m downstream of the exit of the service gate suffered relatively significant cavitation damage.

All of the abovementioned severe cavitation damage resulted from interactions between cavitation bubbles (CBs) and boundaries. In other words, while cavitation results in extensive erosion of solid structures, in essence, cavitation is the mesoscale

W. Xu, *Mesoscale Analysis of Hydraulics*,
https://doi.org/10.1007/978-981-15-9785-5_2

mechanical behavior of CBs. Hence, to investigate cavitation and cavitation erosion in depth, it is imperative to extend the focus to the mesoscale. In fact, the well-known CB dynamics occur at the mesoscale (Philipp and Lauterborn 1998; Brennen 2014). Overall, CB dynamics has always drawn great attention in fields such as naval engineering. In comparison, the attention paid by the hydraulic and hydropower engineering field to CB dynamics is notably inadequate. In the hydraulic and hydropower field, the total flow parameters, such as the flow cavitation number and incipient cavitation number, have been used for a long time to study and predict cavitation (Russell and Ball 1967; Pan et al. 2001). As a result, there have been numerous failures to correctly address engineering problems.

One typical example is the orifice plate-type spillways of the Xiaolangdi Dam. Three-level energy dissipation orifice plates were designed to achieve energy dissipation within these spillways. An ultimate spillway design, including orifice plates, a tunnel, and a middle gate chamber, was formulated based on extensive experimental studies conducted in various scientific research institutions in China. Reduced-pressure test results showed that the ultimate design could allow cavitation-free operation of the spillways. However, high-frequency cavitation noise was detected during the operational observation of the spillways after construction. This suggested that significant cavitation had occurred within the spillways. This phenomenon was not particularly surprising, because the scale effect of cavitation and cavitation erosion was already very well known. What was beyond expectation was that no traces of cavitation were found upon inspection of the spillways after lowering the gate. Thus, important questions arose—is the orifice plate-type internal-flow energy dissipation technique safe? Should the orifice plate-type internal-flow energy dissipation technique be further popularized or eschewed in subsequent similar projects?

Regarding this question, the consensus among researchers is that the CBs formed within the orifice plate-type spillways of the Xiaolangdi Dam fail to reach their walls and all collapse in the flow far from its walls. This explanation is obviously sensible. Then, under what conditions do CBs reach the walls of a spillway? This question is difficult to answer simply using the total flow parameters, such as the flow cavitation number and incipient cavitation number, in the analysis. It is necessary to study the motion and collapse patterns of CBs on the mesoscale. This question has not been covered in previous research on cavitation dynamics or cavitation and cavitation erosion in hydraulic and hydropower structures but needs to be addressed with mesoscale hydraulic analysis.

In addition, the mesoscale analysis of cavitation and cavitation erosion includes the analysis of interactions between CBs and boundaries made of various materials, interactions between CBs in strong cavitation conditions, and interactions between CBs and solid particles.

2.2 Interactions Between Cavitation Bubbles and Rigid Boundaries

Cavitation is a process in which microair nuclei in a body of water expand when the water pressure is lower than the saturated vapor pressure and form CBs, which ultimately collapse after leaving the low-pressure region. CBs produce shock waves when collapsing. When collapsing near a solid boundary, CBs can also produce microjets oriented to the boundary. Microjets and shock waves can damage solid boundaries. This is so-called cavitation.

In as early as 1917, Rayleigh (1917) believed that CBs would generate a very high pressure and radiate shock waves to the surrounding water at the final stage of collapse. Later, Harrison (1952), Güth (1954), and Shutler and Mesler (1965) verified Rayleigh's shock wave theory using acoustic measurement techniques, the striation technique, and an electric spark-induced air bubble system, respectively. Jones and Edwards (1960), Shima (1981), and Vogel and Lauterborn (1988) believed that the shock-wave pressure released by CBs under collapse could be as high as 1 GPa.

Benjamin and Ellis (1966) were the first to discover the asymmetrical collapse of CBs near boundaries. This type of asymmetrical collapse results in the formation of boundary-oriented microjets and, thereby, causes cavitation damage. Vogel et al. (1989) found that the velocity and impact pressure of a microjet could reach 100 m/s and 450 MPa, respectively.

2.2.1 Shock Waves and Microjets Generated from the Collapse of CBs

A CB will radiate a shock wave to the surrounding water when contracting to its minimum volume during the collapse process. Figure 2.1 shows a shock wave radiated by an electric spark-induced CB. The velocity of this shock wave reached as high as approximately 1800 m/s as it propagated towards the surrounding water. Figure 2.2 shows the impact intensity of the shock wave on the boundary on the right side of the image upon arrival, which was measured using a high-response frequency pressure measurement system. As demonstrated in Fig. 2.2, a peak pressure of approximately

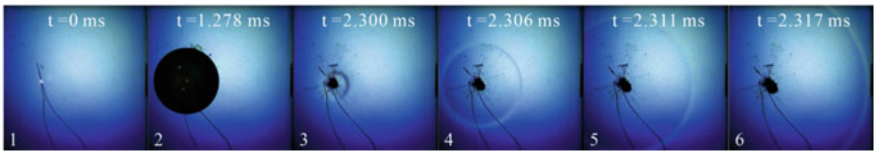


Fig. 2.1 Shock wave generated by an electric spark-induced CB near a boundary (frame rate = 180,000 fps; frame width = 41 mm; exposure time = 0.25 µs; maximum radius $R_{\max}$ of the CB = 9.83 mm; dimensionless distance between the CB and the boundary γ_{bw} = 2.95)

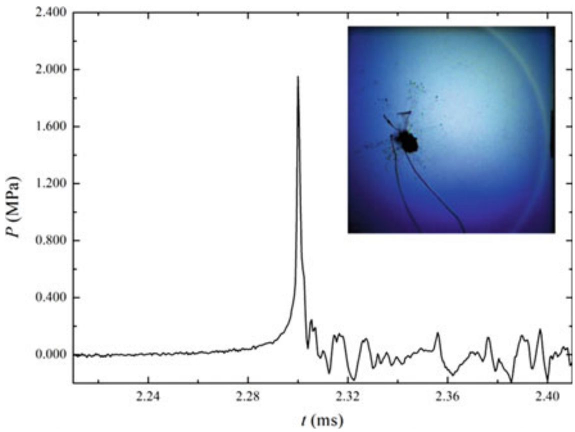


Fig. 2.2 Impact of the shock wave generated by an electric spark-induced CB near a boundary on the boundary

2.0 MPa was generated by the shock wave. As the distance between a CB and a boundary decreases, there is a further increase in the intensity of the shock wave.

When a CB collapses near a boundary, its far side relative to the boundary contracts much faster than its near side. This results in the formation of a microjet that punctures the CB. After puncturing the CB, the microjet continues to move towards the boundary at a high velocity and ultimately impacts the boundary (Fig. 2.3).

The abovementioned shock wave and microjet each exert a strong impact on the boundary. Under this high-intensity impact, the boundary suffers fatigue failure in a local area and, thereby, cavitation damage.

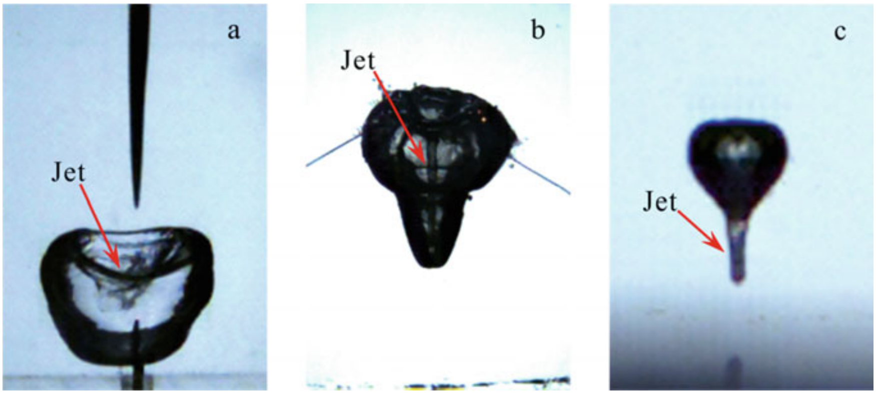


Fig. 2.3 Formation of a microjet from the collapse of a CB near a boundary. **a** CB induced by a high voltage near a boundary; **b** CB induced by a low voltage near a boundary; **c** CB induced by a laser near a boundary

2.2.2 *Effects of the Geometric Shape of a Boundary on the Collapse Behavior of a CB*

In the real world, a boundary is not an infinite slab. The way a CB collapses near a boundary varies with the geometric shape of the boundary.

First, the collapse behavior of a CB between two parallel boundaries is examined. Figure 2.4 shows a schematic diagram depicting the spatial locations of a CB and two parallel boundaries. In the experiment, the two electrodes and the left and right boundaries were fixed by a horizontal stand. The two electrodes were connected by wires to a high-voltage single-pulse circuit. The left and right boundaries could be adjusted based on the experimental requirements. CBs of varying sizes were generated by adjusting the resistance and voltage in the circuit. The deformation and collapse direction of each CB were recorded by high-speed photography. In Fig. 2.4, D_l is the minimum distance between the surface of the CB and the left boundary when the CB has expanded to its maximum volume, and D_r is the minimum distance between the surface of the CB and the right boundary when the CB has expanded to its maximum volume. To describe the positional relationships between the whole CB and the two boundaries, the ratio $\gamma_{bw,l}$ of the minimum distance between the center of the CB and the left boundary to the maximum radius $R_{\max}$ of the CB is selected as the positional relationship parameter between the CB and the left boundary, while the ratio $\gamma_{bw,r}$ of the minimum distance between the center of the CB and the right boundary to the $R_{\max}$ of the CB is selected as the positional relationship parameter between the CB and the right boundary.

Figure 2.5 shows the decomposition of the collapse of each CB between two parallel boundaries. The distance L between the left and right boundaries was 8.537 mm. Each column shows photographs of one CB. From left to right, the CBs are denoted a to g, respectively. The $R_{\max}$ values of CB a (2.413 mm) to CB g (3.830 mm) increased, as shown in Table 2.1. The $R_{\max}$ value of CB a was 2.413 mm. The dimensionless $\gamma_{bw,l}$ and $\gamma_{bw,r}$ for CB a were both less than 3. CB a collapsed simultaneously towards both boundaries. As $R_{\max}$ gradually increased, a "∞"-shaped CB was formed during the collapse process as a result of the action of the two boundaries.

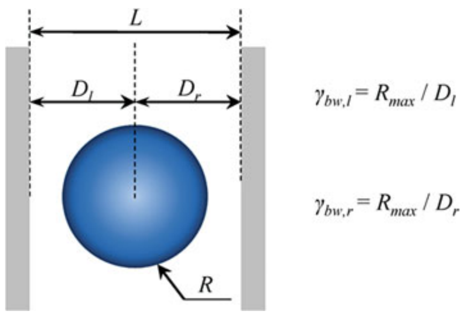


Fig. 2.4 Schematic diagram of a model consisting of a CB between two parallel boundaries and the parameter settings

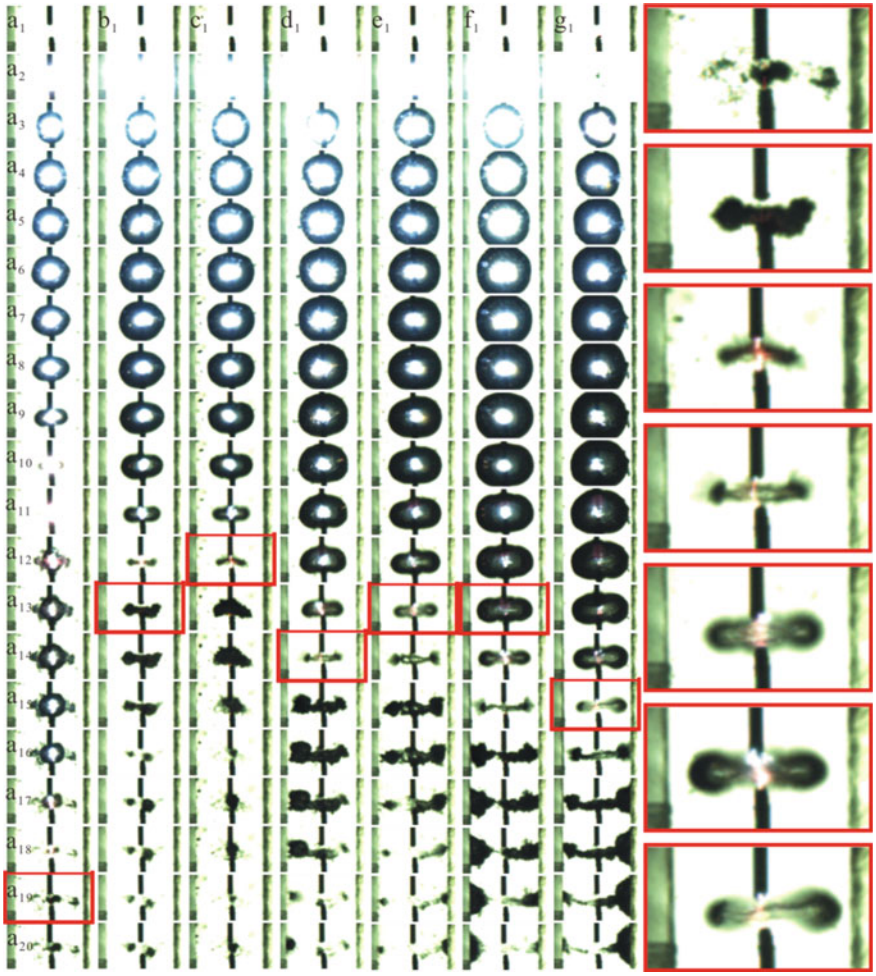


Fig. 2.5 Decomposition of the collapse of CBs between two parallel boundaries (frame rate: 19,700 fps; exposure time: 48 μs; image size: 10.394 mm × 6.310 mm)

Table 2.1 Experimental parameters for the collapse of CBs between two parallel boundaries

CB	R_{max} (mm)	$\gamma_{bw,l}$	$\gamma_{bw,r}$
a	2.413	1.846	1.692
b	3.016	1.373	1.343
c	3.109	1.462	1.354
d	3.155	1.412	1.324
e	3.341	1.347	1.222
f	3.712	1.175	1.150
g	3.830	1.187	1.018

Second, the collapse behavior of a CB at the corner of the intersection of two perpendicular boundaries. Figure 2.6 shows a schematic diagram depicting the spatial locations of a CB and two perpendicular boundaries. In the experiment, the distance D_v between the bottom boundary and the center of the CB was maintained unchanged. The distance D_h between the right boundary and the center of the CB was adjustable. The effects of the two perpendicular boundaries on the collapse direction of the CB were investigated by gradually reducing D_h. The size of the CB was varied by adjusting the distance between the resistance and the discharge needle plate in the circuit.

Figure 2.7 shows the corner effect observed during the collapse of CBs at the corner of the intersection of two perpendicular boundaries. Each row shows photographs of one CB. From top to bottom, the CBs are denoted a to h, respectively. For CBs a to d, D_h was relatively large and exceeded the distance required for a microjet to form, whereas D_v was relatively small. Ultimately, these CBs collapsed towards the

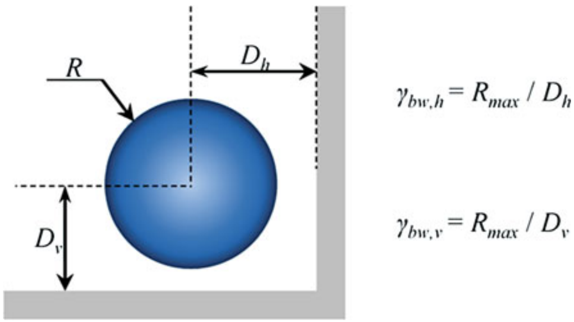


Fig. 2.6 Schematic diagram of a model composed of a CB at the corner of the intersection of two perpendicular boundaries as well as the parameter settings

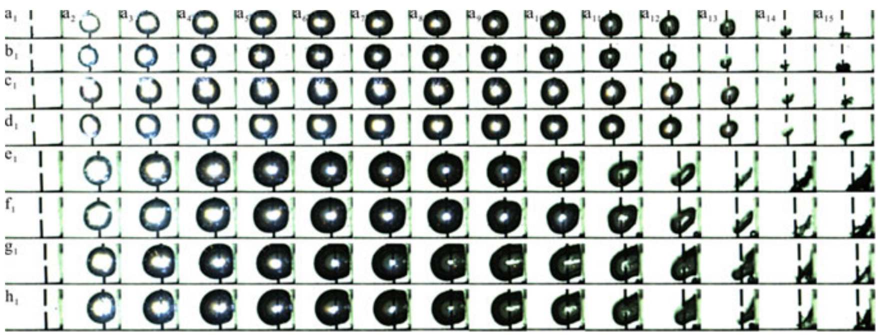


Fig. 2.7 Corner effect in the collapse of the CBs at the corner of the intersection of two perpendicular boundaries [frame rate: 17,500 fps; exposure time: 55 μs; image sizes: 17.333 mm × 8.667 mm (a and b), 15.600 mm × 8.667 mm (c and d), 12.133 mm × 8.667 mm (e and f), and 12.133 mm × 8.667 mm (g and h)]

Table 2.2 Experimental parameters for the collapse of CBs at the corner of the intersection of two perpendicular boundaries

CB	$R_{\max}$ (mm)	$\gamma_{bw,h}$	$\gamma_{bw,v}$
a	4.008	2.257	1.108
b	3.792	2.500	1.171
c	4.008	1.932	1.135
d	3.900	1.986	1.348
e	4.008	0.973	1.108
f	3.900	1.056	1.139
g	4.171	0.792	1.026
h	4.171	0.753	1.039

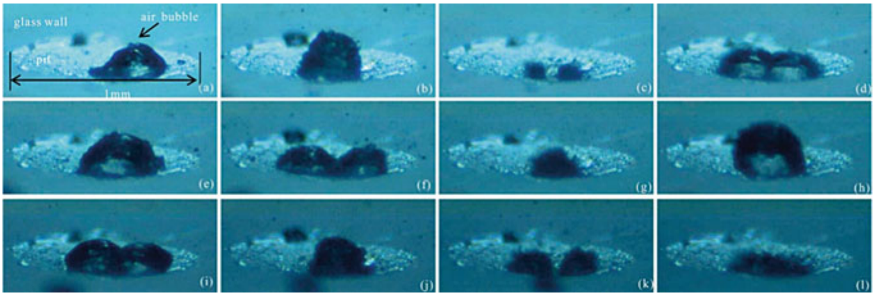


Fig. 2.8 Collapse and recovery of a single CB in an ultrasonic field

bottom boundary. For CBs e to h, D_h was comparable to D_v. As a result, these CBs collapsed towards the corner of the intersection of the two boundaries (Table 2.2).

Finally, the collapse behavior of a CB within a pit is examined. Different from the previous two experiments in which CBs were formed by electric sparks, the CBs in this experiment were formed by ultrasonic waves. Figure 2.8 shows the collapse and recovery of one CB within a pit on a glass boundary. In the continuous periodic ultrasonic field, the development and collapse of the CB exhibited notable periodic characteristics. Within one ultrasonic period, the spherical CB collapsed to its minimum volume and then recovered to form an annular CB (or two independent CBs). In the following ultrasonic period, the annular CB (or two independent CBs) collapsed to its minimum volume (or their minimum volumes) and then recovered to form a spherical CB. In addition, as demonstrated in Fig. 2.8, in contrast to a flat boundary where a CB moves about, a pit is capable of gathering and immobilizing CBs.

2.3 Interactions Between Cavitation Bubbles and Elastic Boundaries

Compared to rigid boundaries, the collapse behavior of CBs near elastic boundaries is more complex. Sankin and Zhong (2006) measured the impact force of CBs near a silicon rubber membrane and analyzed the factors that affected the impact force. Brujan et al. (2001) and Vogel et al. (2001) studied the interactions between a CB and an elastic boundary as well as the dependence of their interactions on their distance. However, overall, relatively few studies have been conducted to date to examine the interactions between CBs and elastic boundaries.

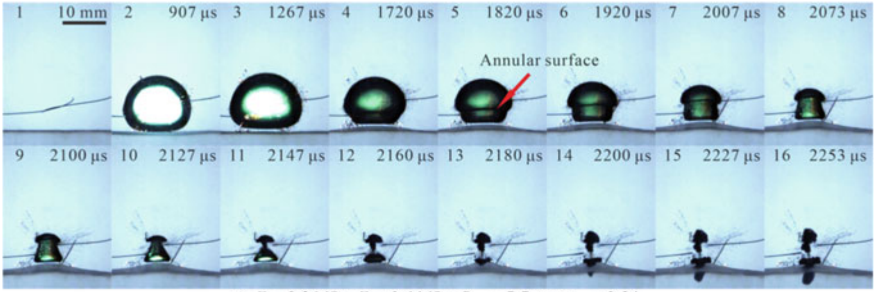
2.3.1 *Morphology of CBs Near Elastic Boundaries During the Collapsing Process*

Two-component transparent liquid silicone rubbers manufactured by Quantum Silicones, Inc. (U.S.) were used to prepare boundary specimens. Specifically, the components were mixed and stirred at various mass ratios and then were degassed under vacuum. The mixtures were subsequently placed in polytetrafluoroethylene molds at a constant temperature to fabricate specimens sized 30 mm × 30 mm × 12 mm. Each specimen was then glued onto a polymethylmethacrylate plate with a liquid silicone rubber with the same mass ratio as that of the specimen. The transmittance of the specimens was above 95% after curing. In addition, the specimens had relatively high hydrolytic stability, did not turn yellow, and exhibited stable mechanical performance for a relatively long period of time (Zhai et al. 2019). An Instron 5567 (Instron, U.S.) universal material testing machine was used to test the specimens. Based on the properties of the specimens, a sensor with a measuring range of 30 kN was selected for testing. The error was 0.3%. Table 2.3 summarizes the mechanical parameters of the flexible materials. The compressive modulus of elasticity E_c of each specimen material was determined by cyclic loading and unloading at a rate of 10 mm/min until 20% of the maximum strain was reached. The tensile modulus of elasticity E_t was determined by a tensile failure test at a loading rate of 500 mm/min.

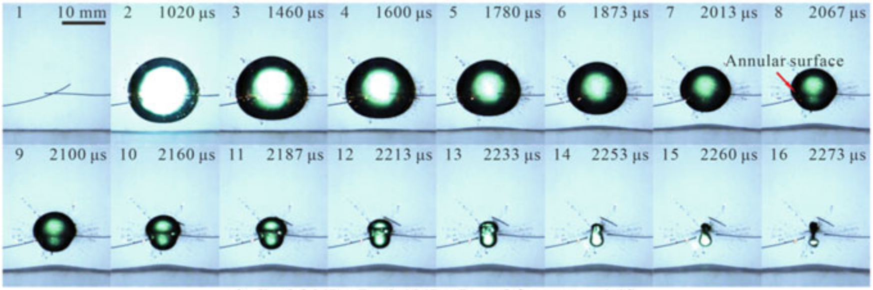
Figure 2.9 shows the variation in the CB collapse process with the modulus of elasticity E. At a low E and a small γ_{bw}, the boundary was compressed as the CB expanded and recovered as the CB contracted. In addition, the CB became flat at the bottom when contracting. As the CB contracted, the boundary gradually protruded

Table 2.3 Mechanical parameters of the specimen materials

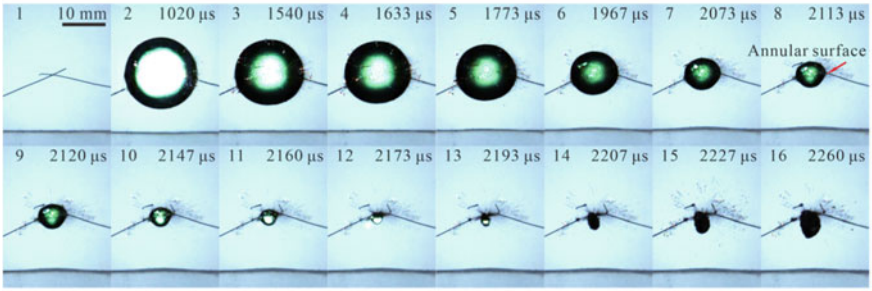
Specimen No.	1	2	3	4	5	6
E_t/MPa	0.3	1.0	2.5	4.6	8.2	9.7
E_c/MPa	0.4	2.3	3.3	4.3	6.5	7.5



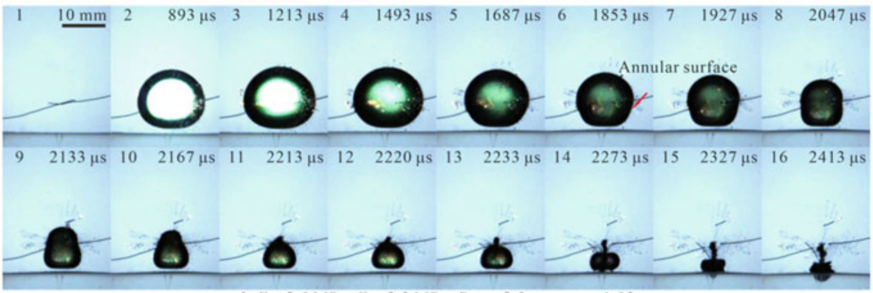
a. $E_t = 0.3$ MPa, $E_c = 0.4$ MPa, $R_{max} = 7.7$ mm, $\gamma_{bw} = 0.84$



b. $E_t = 0.3$ MPa, $E_c = 0.4$ MPa, $R_{max} = 8.3$ mm, $\gamma_{bw} = 1.13$

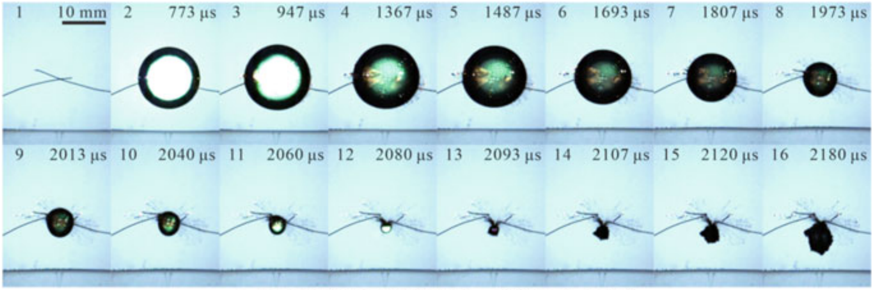


c. $E_t = 0.3$ MPa, $E_c = 0.4$ MPa, $R_{max} = 8.5$ mm, $\gamma_{bw} = 1.58$

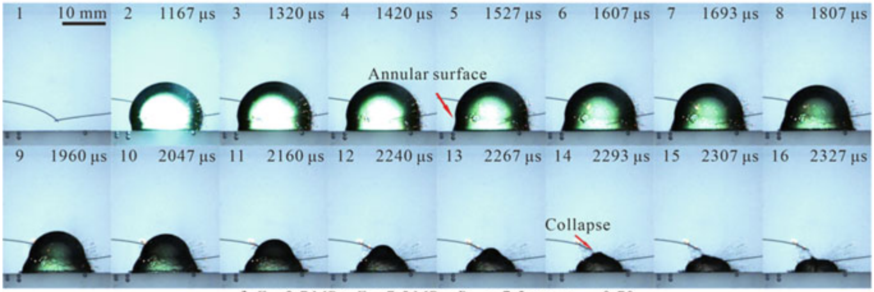


d. $E_t = 2.5$ MPa, $E_c = 3.3$ MPa, $R_{max} = 8.0$ mm, $\gamma_{bw} = 1.03$

Fig. 2.9 Images captured by a high-speed camera of the collapse of CBs near boundaries with different elastic moduli



e. $E_t = 2.5$ MPa, $E_c = 3.3$ MPa, $R_{max} = 8.0$ mm, $\gamma_{bw} = 1.56$



f. $E_t = 9.7$ MPa, $E_c = 7.5$ MPa, $R_{max} = 7.5$ mm, $\gamma_{bw} = 0.70$

Fig. 2.9 (continued)

and remained in a relatively stable state after protruding to a certain extent until the CB collapsed. As a result of the deformation of the boundary, the CB gradually acquired a mushroom shape as it contracted. At the time of collapse, the cap and stem of the "mushroom" became separated from one another and collapsed in opposite directions. The impact of the boundary-oriented microjet reached the inside of the boundary, causing relatively significant deformation of the boundary (Xu et al. 2019). As γ_{bw} increased or the E of the boundary increased, the abovementioned characteristics gradually became less notable.

The experiment showed that the critical distance γ_r required for a CB to develop an annular surface when contracting was closely related to the E_t of the boundary material (Fig. 2.10). As the CB contracted, some of the space initially occupied by the CB was refilled by the surrounding water. The delay in refilling by the surrounding water resulted in a low local pressure, which in turn caused the boundary to protrude. As the CB contracted, the uneven refilling of the spaces below it, above it, and at its sides led to the formation of an annular surface. The annular surface caused the CB to acquire a mushroom shape during the collapse process. As the E_t of the boundary gradually increased, the cap of the "mushroom" gradually decreased in size and its stem gradually increased in size until it eventually disappeared. The lower the E_t of the boundary material was, the larger the γ_r affecting the development of an annular CB surface was.

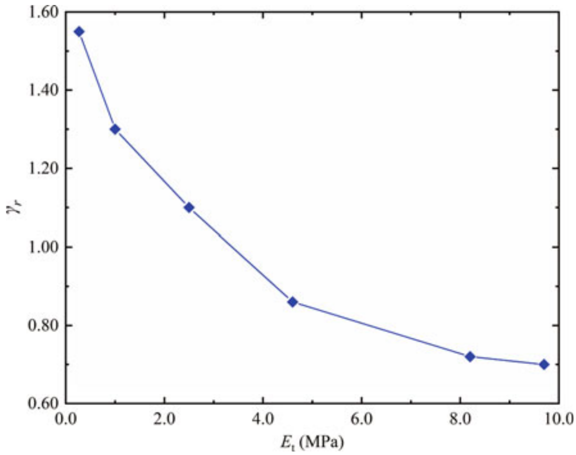


Fig. 2.10 Effects of the E_t of the boundary material on the critical condition required for the development of an annular CB surface

2.3.2 Shock Waves Generated by CBs Near Elastic Boundaries When Collapsing

Figure 2.11 shows the shock waves generated by CBs near elastic boundaries when collapsing. As demonstrated in Fig. 2.11, not only did the shock wave generated by each CB propagate rapidly in water, but it also penetrated the elastic boundary. An analysis of the images found that the shock waves propagated at a velocity of approximately 1485 m/s in water. In comparison, the shock waves propagated at a notably lower velocity in the elastic boundaries. In addition, as shown in Fig. 2.11, the intensity of each shock wave propagating inside a boundary remained relatively high after it was reflected by the boundary. Moreover, each shock wave was reflected again upon returning to the liquid–solid interface but basically did not penetrate the liquid–solid interface and propagate in the water again.

2.3.3 Cavitation Erosion Resistance of Elastic Materials

The deformation behavior of the experimental materials during the CB collapse process was analyzed by measuring their tensile and compressive deformation. Figure 2.12 shows the relationship between the amount of deformation H of each material and γ_{bw} (a positive H value signifies tensile deformation, while a negative H value signifies compressive deformation). At a relatively low modulus of elasticity E, H gradually decreased as γ_{bw} increased. As E gradually increased, H became increasingly insensitive to γ_{bw}. For each of the six boundary materials, its compressive H first increased and then decreased as γ_{bw} increased. As E increased, there was a gradual decrease in the maximum H ($H_{\max}$) and a gradual increase in the corresponding γ_{bw}.

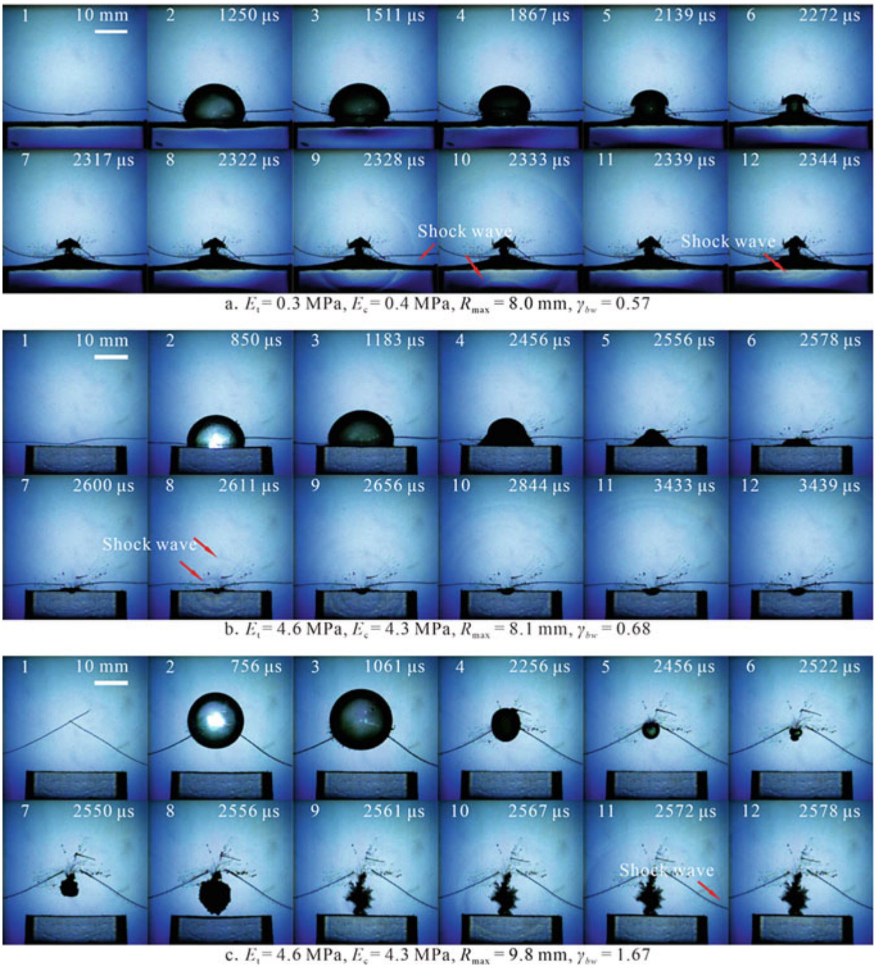


Fig. 2.11 Evolution of the shock waves generated by CBs near flexible materials when collapsing

To further analyze the effects of the collapse of a CB on the boundary material, $H_{\max}$ was extracted from Fig. 2.12. Figure 2.13a and b shows the $H_{\max}$–E_c and $H_{\max}$–E_t relationships, respectively. The dimensionless maximum deformation $\alpha_{\max}$ ($\alpha_{\max} = H_{\max}/R_{\max}$) is used to represent the amount of deformation in a material caused by a CB. Figure 2.13c and d shows the relationships of $\alpha_{\max}$ with the dimensionless E_c ($E_c{}'$) and dimensionless E_t ($E_t{}'$), respectively. As demonstrated in Fig. 2.13, as E_c increased, there was a gradual decrease in the compressive $H_{\max}$ ($H_{p_\max}$). When $H > H_{p_\max}$, the microjet caused the boundary material to undergo brittle deformation. Consequently, the boundary material sustained cavitation damage. A boundary made of a material with a very high E [e.g., aluminum (Al) ($E = 70$ GPa)] can be considered a rigid boundary. It is difficult for a CB to cause a rigid boundary to protrude when

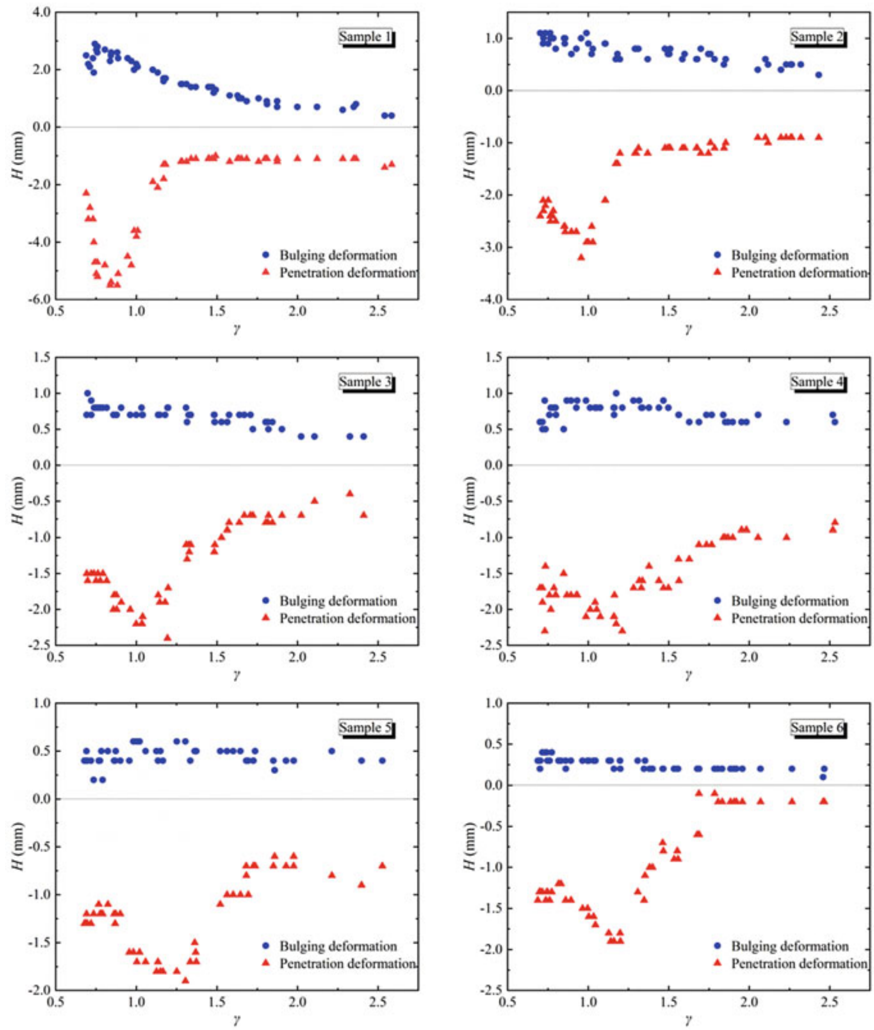
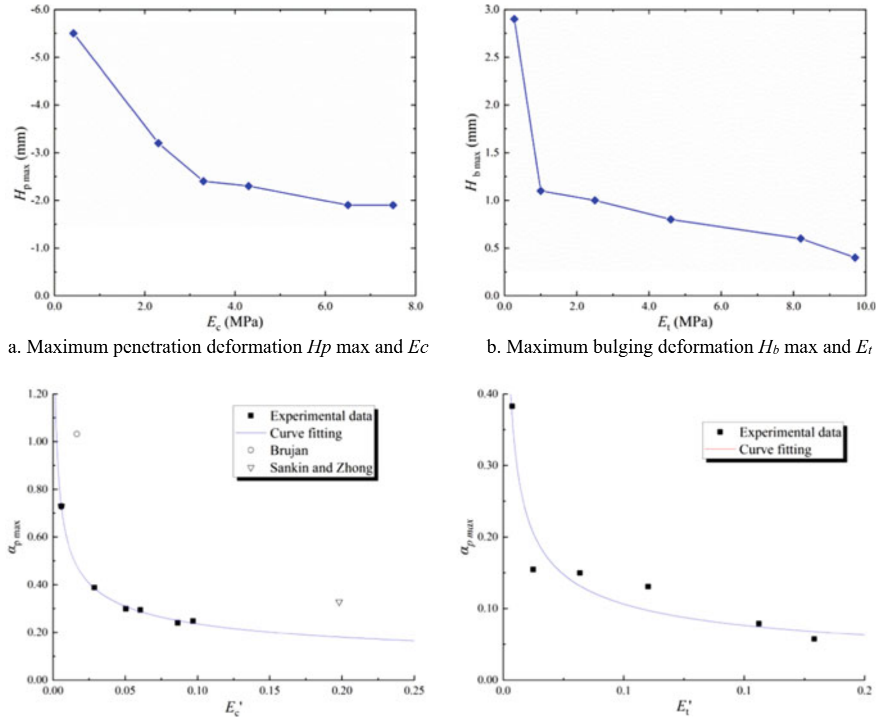


Fig. 2.12 Relationships between the tensile and compressive deformation H and dimensionless CB-boundary distance γ_{bw} for various elastic materials

collapsing. This increases the impact of the collapse of the CB on the boundary and, thereby, causes cavitation damage to the boundary. For a low-E boundary, when $H < H_{\max}$, the deformation of the boundary slows the contraction and impact of the CB. As a result, the boundary is not prone to cavitation. However, when $H > H_{\max}$, the protruding material is eroded. Therefore, a reasonable elastic material can effectively allow the boundary to resist cavitation damage caused by CBs. A material has optimal cavitation erosion resistance when its E falls in a certain range.



a. Maximum penetration deformation *Hp* max and *Ec*

b. Maximum bulging deformation H_b max and E_t

c. $\alpha_{p\,max}$ and $E_c{}'$

d. $\alpha_{b\,max}$ and $E_t{}'$

Fig. 2.13 *H*–*E* and *α*–*E*′ relationships under the action of CBs

To quantitatively analyze the *H*–*E* relationship under the action of CBs, the dimensionless modulus of elasticity E' is defined as follows:

$$E' = \frac{E}{R_{\max}\rho g} \tag{2.1}$$

where ρ is the density of the liquid and g is gravitational acceleration.

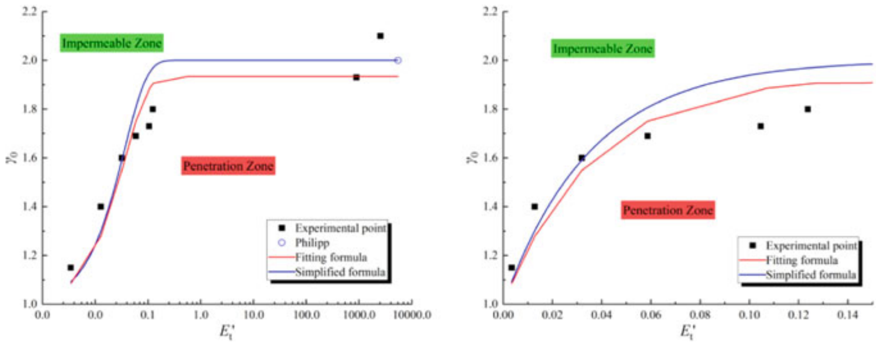
The relationships between the dimensionless deformation α and E' are derived from Fig. 2.13c and d:

$$\alpha_{p\max} = -0.0954 \times E_c'^{-0.393} \tag{2.2}$$

$$\text{and}\, \alpha_{b\max} = 0.0256 \times E'^{-0.475_t} \tag{2.3}$$

Based on the above equations, α and E' can be employed to approximately evaluate a material's risk of sustaining cavitation erosion.

The depth penetrated in a boundary by the microjet generated by a CB when collapsing as well as the critical distance γ_0 required for the microjet to penetrate



a. Experimental and fitting results b. Some results for elastic boundaries

Fig. 2.14 Relationship between the critical distance required for the microjet to penetrate the boundary (γ_0) and the dimensionless tensile modulus of elasticity ($E_t{}'$)

the boundary increased as the $E_t{}'$ of the boundary material increased (Fig. 2.14). γ_0 and $E_t{}'$ satisfied the exponential relationship below:

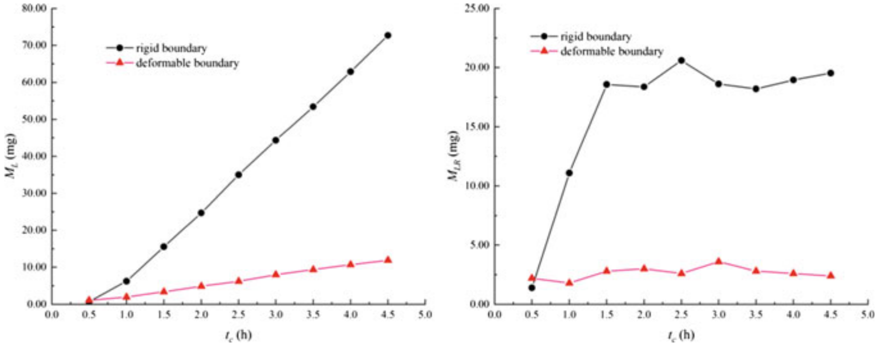
$$\gamma_0 = 1.933 - 0.933 \times e^{-27.802 \times E_t'} \tag{2.4}$$

Considering the experimental accuracy, the above relationship can be approximately represented by the following equation:

$$\gamma_0 = 2 - e^{-28 \times E_t'} \tag{2.5}$$

As demonstrated in Fig. 2.14, there was a characteristic value of $E_t{}'$ near 0.1. As $E_t{}'$ exceeded this characteristic value, there was an insignificant change in γ_0. However, when $E_t{}'$ was below this characteristic value, $E_t{}'$ changed significantly with γ_0. Therefore, the penetrable and impenetrable regions of a boundary can be determined based on the properties of the boundary material as well as the distance between the CB and the boundary. This division can help determine the cavitation erosion resistance of an elastic material.

On the basis of the above analysis, ultrasonic waves were used to induce cavitation erosion to directly determine the cavitation erosion resistance of elastic materials. Figure 2.15a shows the variations in the cumulative amount of erosion M_L and the rate of erosion M_{LR} of a rigid material and an elastic material with time. The M_L of the rigid material reached 72.60 mg after 4.5 h. In comparison, the M_L of the elastic material reached only 11.90 mg after 4.5 h, far less than that of the rigid material. The variation in M_{LR} with time of the two materials also differed notably. The M_{LR} of the rigid material underwent three stages, namely, an embryonic stage, an acceleration stage, and a stable stage. In the beginning of the experiment, the rigid material had a smooth and flat surface and exhibited relatively high cavitation erosion resistance. This was the embryonic stage. As the cavitation erosion progressed, cavitation pits



a. Variation in the cumulative amount of erosion M_L with time

b. Variation in the erosion rate M_{LR} with time

Fig. 2.15 Comparison of the cavitation erosion behavior of a rigid material and an elastic material

began to appear. As the number of cavitation pits gradually increased, the surface of the rigid material coarsened, and its M_{LR} increased significantly. This was the acceleration stage. As the cavitation erosion further advanced, the surface roughness of the rigid material became relatively stable, and its M_{LR} stabilized. This was the stable stage. The M_{LR} of the elastic material underwent no significant changes and remained at a relatively low level.

A further observation of the elastic material found that its surface was basically as smooth and flat as before the experiment and was free of notable pits or damage. Measurements showed that the elastic material sustained a natural weight loss of approximately 1.00 mg/d under exposure to air. In the experiment, the time intervals were set to 1 d. The cumulative weight loss sustained by the elastic material amounted to 11.90 mg at 9 d. Thus, the M_L of the elastic material was basically attributed to its natural weight loss. The elastic material underwent no actual cavitation erosion. Hence, a reasonable elastic material is capable of avoiding cavitation erosion even when subjected to long-term cavitation.

2.4 Interactions Between Cavitation Bubbles

Multiple CBs often coexist when cavitation occurs in the real world. Numerous studies have been conducted to investigate the interactions between two CBs. As a result, there is a relatively clear understanding of the interactions between two CBs as well as their related collapse behavior. In contrast, few studies on interactions between multiple CBs have been reported. Van Wijngaarden (1966) investigated the dynamic behavior of a group of CBs. Morch (1981) treated a group of CBs as a single-degree-of-freedom system and described its motion in a generalized coordinate system. Chahine (1981) examined the collapse of multiple CBs when the ratio of the initial radius of each CB to its distance from the center of the CBs was relatively low and

analyzed the motion of each CB using the singular perturbation method. In view of the slow propagation of a pressure wave in a group of CBs in a liquid, Huang and Ni (1987) linked the collapse of each CB within a group of CBs with that of the group of CBs and studied the dynamic characteristics of a group of CBs while taking into consideration the liquid compressibility based on the research results for CB dynamics.

2.4.1 Interactions Between Two CBs

During the interactions between two CBs, the collapse directions of the two CBs depend closely on whether their inception times are synchronized (Fig. 2.16). If the two CBs do not have synchronized inception times, the CB with early inception will collapse in a direction diverging from that of the other CB. If the two CBs have synchronized inception times, they will collapse towards each. If the two CBs have synchronized inception times but differ in size, not only will they collapse towards one another, but the smaller CB will also be absorbed by the larger CB. If the sum of the radii of the two CBs is greater than the center-to-center distance between them, their adjacent surfaces will be compressed flat as they expand, and they will merge into one CB when they contract to their respective minimum sizes.

Figure 2.17 compares the collapse of a single CB near a boundary with that of two CBs near a boundary. As demonstrated in Fig. 2.17, in the two-CB case, the presence of the smaller CB disturbed the development and collapse of the larger CB. (1) In the single-CB case, it took 166.7 μs for the CB to contract to its minimum size. This time increased to 177.8 μs in the presence of a smaller CB. (2) The smaller CB generated a microjet that impacted the larger CB and, thereby, altered the morphology of the larger CB. (3) After being disturbed by the smaller CB, the larger CB was unable to

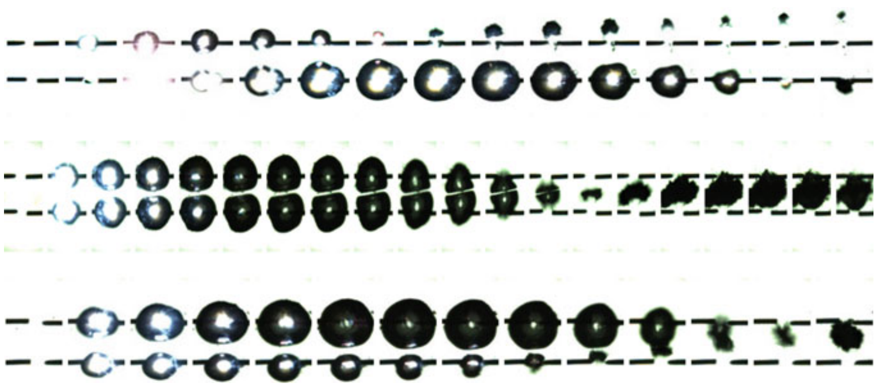
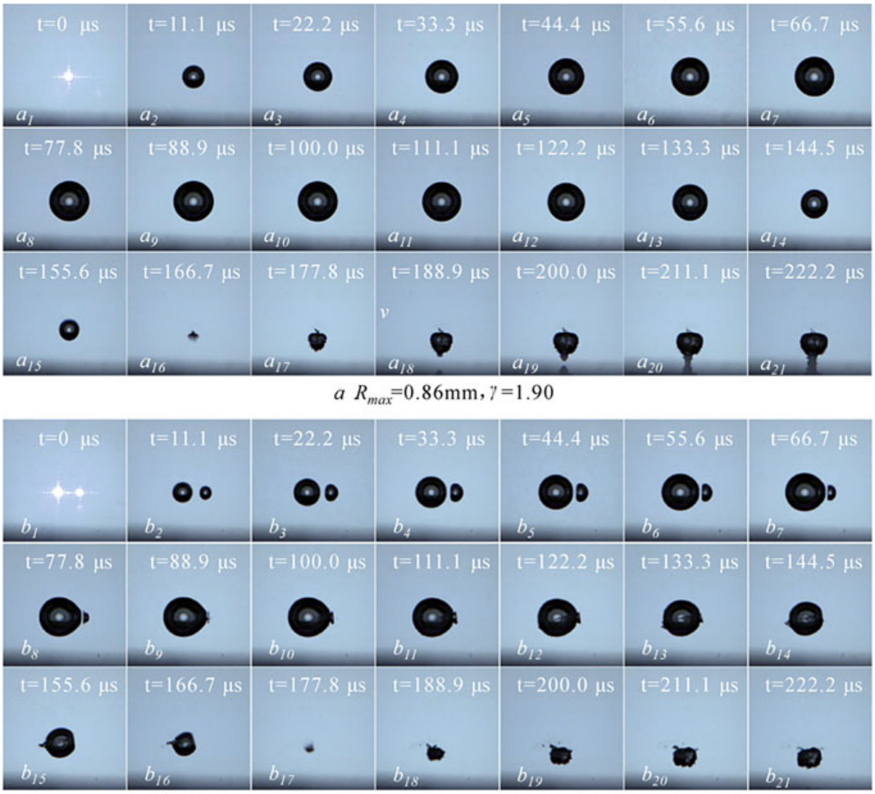


Fig. 2.16 Interactions between two CBs



a R_{max}=0.86mm, γ=1.90

b. L=0.96mm, $R_{max\text{-}1}$=0.33mm, $R_{max\text{-}2}$=0.86mm, γ_1=4.82, γ_2=1.85

Fig. 2.17 Impacts of a single CB and two CBs near a boundary on the boundary

generate a boundary-impacting microjet during recovery and regeneration. Instead, the larger CB only shifted towards the boundary as a whole.

The variations in the collapse pattern of two CBs with the difference in their inception time and the distance between them are further analyzed. Let T_1 and T_2 be the times needed by the two CBs to complete their first collapse, respectively, Δt_0 be the difference between the inception time of the two CBs, and γ_{bb} be the dimensionless relative distance between the two CBs, i.e., the ratio of the center–to–center distance between the two CBs to the $R_{\max}$ of the CBs. Figure 2.18 shows the $\Delta t_0/T_2$ (dimensionless difference in the inception time between the two CBs)–γ_{bb} plots for two scenarios, namely, in a free field and near a boundary. As demonstrated in Fig. 2.18, the collapse patterns of two CBs near a boundary were similar to those in a free field. Four relatively notable collapse pattern zones can be observed in Fig. 2.18, namely, a "towards" zone, a diverging zone, a catapulting zone, and a merging zone.

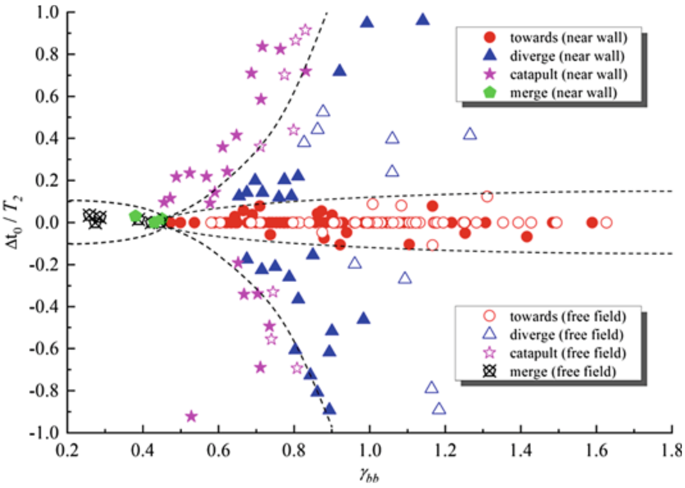
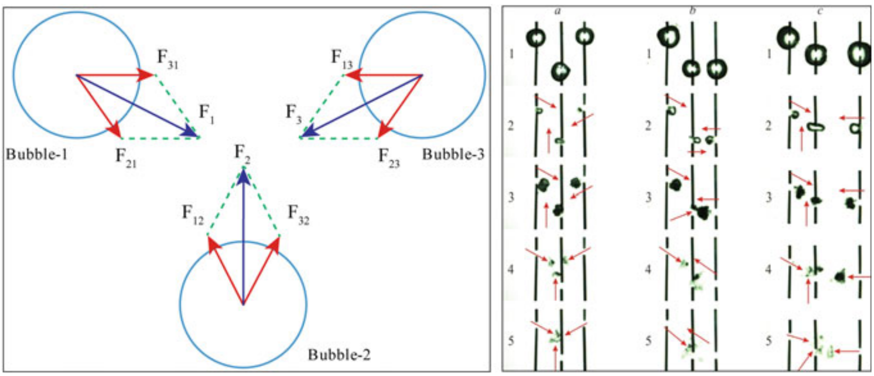


Fig. 2.18 Effects of dimensionless parameters on the collapse pattern of two CBs near a boundary

2.4.2 Interactions Between Multiple CBs

Here, the interactions between three CBs are primarily examined. As demonstrated in Fig. 2.19, for three adjacent CBs, the collapse direction of any one of the CBs is the result of the vector composition of its interactions with the other two CBs. For three synchronous CBs with the same maximum radius $R_{\max}$, their velocity vectors intersect at one point. For three CBs, if the γ_{bb} between any two of them remains



(a) Vector composition model (b) Experimental results

Fig. 2.19 Vector composition of interactions between three CBs (group *a*: $R_{\max,1} = 2.29$ mm, $R_{\max,2} = 2.33$ mm, $R_{\max,3} = 2.18$ mm, and $\theta = 72.0°$; group *b*: $R_{\max,1} = 2.81$ mm, $R_{\max,2} = 2.26$ mm, $R_{\max,3} = 2.56$ mm, and $\theta = 127.5°$; group *c*: $R_{\max,1} = 2.87$ mm, $R_{\max,2} = 2.72$ mm, $R_{\max,3} = 3.14$ mm, and $\theta = 146.3°$)

a constant, they will collapse towards one point, which is referred to as "collapse merging point". For three CBs that differ in γ_{bb} or size, there is a weakened "collapse merging point" effect.

2.5 Interactions Between Cavitation Bubbles and Particles

Sediment-laden flows are ubiquitous in nature and engineering. Hence, it is imperative to determine the effects of sediment particles on cavitation and cavitation erosion. Some researchers have conducted relevant studies. Liu (1983) studied the effects of suspended sediment on the cavitation conditions of a flow. Lu and Xu (1990) investigated the calculation of the collapse of CBs near a rigid flat side boundary in a solid–liquid two-phase flow. Huang et al. (1998) examined the effects of the sediment concentration on the expansion and contraction of a single CB in liquids with different surface tension. Tian et al. (1999) studied the erosion of gate slots caused by a sediment-laden flow through an experiment. These studies have expanded the understanding of cavitation and cavitation erosion. However, overall, research on cavitation and cavitation erosion relating to sediment-laden flows has been, to date, notably inadequate. There is an even more significant lack of mesoscale research on the interactions between CBs and particles.

2.5.1 Effects of Particles on the Collapse Directions of CBs

The effects of particles on the collapse directions of CBs were investigated with electric spark-induced CBs. In the experiment, particles of four radii R_p, namely, 1.0, 1.5, 3.0, and 5.0 mm, were used. The CB size was adjusted by altering the resistance ratio in the circuit. Let γ_{bp} be the dimensionless distance between a CB and a particle. Figure 2.20 shows the rest of the parameters.

The observation and analysis of the variation in the collapse of a CB with γ_{bp} (Fig. 2.21) yielded the following. (1) At a relatively large γ_{bp}, the effects of the

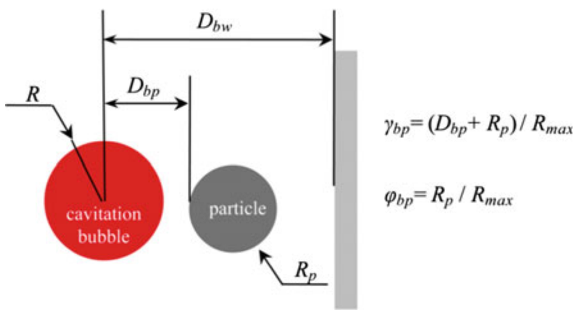


Fig. 2.20 Schematic diagram of the relative positions of a CB and a particle

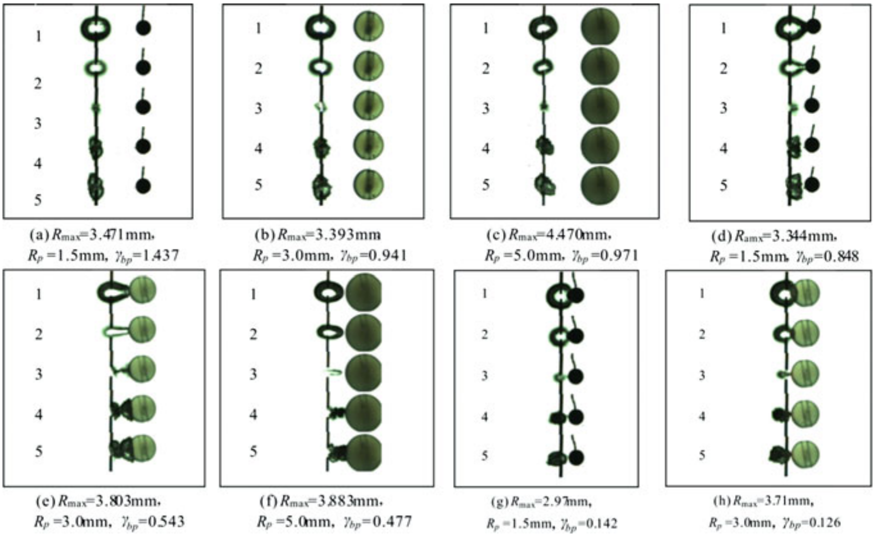


Fig. 2.21 Variation in the collapse direction of a CB with γ_{bp}

particle on the CB were extremely insignificant. The CB basically maintained a spherical shape while contracting and collapsed at the original location. (2) At a relatively small γ_{bp}, the presence of the particle altered the flow field and pressure surrounding the CB. As a result, the CB collapsed towards the particle. (3) At a very small γ_{bp}, the CB exhibited a droplet-like shape when collapsing. The CB first collapsed towards the particle and then recovered.

To quantitatively analyze the collapse direction of a CB in the presence of a particle, 1 and 0 are used to represent when the CB collapses towards the particle and when the CB collapses at its original location, respectively. Figure 2.22 and Table 2.4 show the collapse direction–γ_{bp} relationships corresponding to various R_p values.

(1) R_p = 1.0 mm. When $\gamma_{bp} < 0.77$, the CB collapsed towards the particle. The zone where $\gamma_{bp} < 0.77$ was the “towards” zone. When $0.77 < \gamma_{bp} < 2.5$, the CB partially collapsed towards the particle and partially collapsed at its original location. The zone where $0.77 < \gamma_{bp} < 2.5$ was the transition zone. When $\gamma_{bp} > 2.5$, the CB collapsed at its original location, and the particle exerted no impact on the collapse direction of the CB. The zone where $\gamma_{bp} > 2.5$ was the impact-free zone.
(2) R_p = 1.5 mm. The zone where $\gamma_{bp} < 1.15$ was the “towards” zone. The zone where $1.15 < \gamma_{bp} < 2.5$ was the transition zone. The zone where $\gamma_{bp} > 2.5$ was the impact-free zone.
(3) R_p = 3.0 mm. The zone where $\gamma_{bp} < 0.7$ was the “towards” zone. The zone where $0.7 < \gamma_{bp} < 1.65$ was the transition zone. The zone where $\gamma_{bp} > 1.65$ was the impact-free zone.

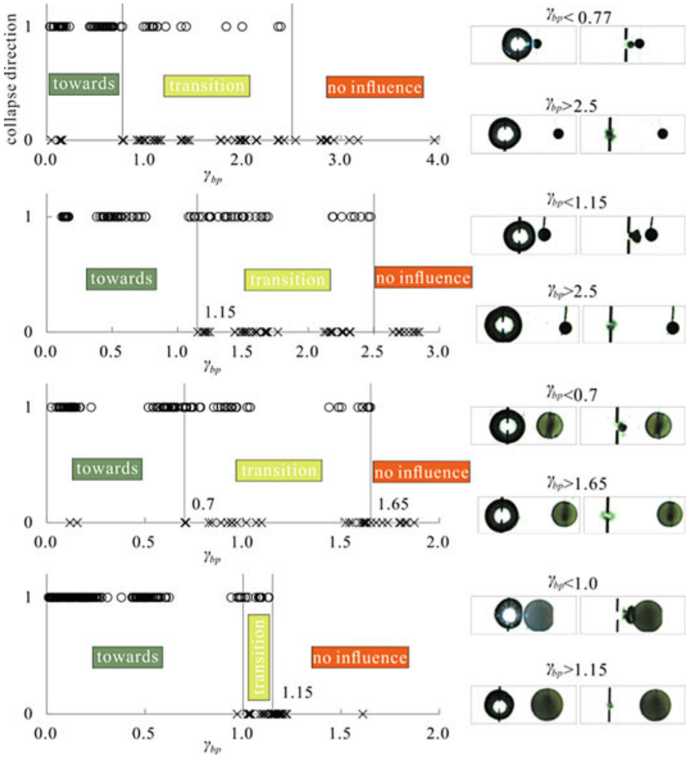


Fig. 2.22 Effects of γ_{bp} on the collapse direction of a CB

Table 2.4 Zones where the collapse direction of a CB was affected by a particle

No.	Affected zone	Collapse direction	γ_{bp} range			
			$R_p = 1.0$ mm	$R_p = 1.5$ mm	$R_p = 3.0$ mm	$R_p = 5.0$ mm
A	"Towards" zone	The CB collapsed towards the particle	0–0.77	0–1.15	0–0.7	0–1.0
B	Transition zone	The CB collapsed partially towards the particle and partially away from the partially	0.77–2.5	1.15–2.5	0.7–1.65	1.0–1.15
C	Impact-free zone	The CB collapsed at its original location	>2.5	>2.5	>1.65	>1.15

(4) $R_p = 5.0$ mm. The zone where $\gamma_{bp} < 1.0$ was the "towards" zone. The zone where $1.0 < \gamma_{bp} < 1.15$ was the transition zone. The zone where $\gamma_{bp} > 1.15$ was the impact-free zone.

Thus, under the above experimental conditions, the "towards" and transition zones were separated by γ_{bp} values of approximately 0.7–1.1, and the transition and impact-free zones were separated by γ_{bp} values of approximately 1.1–2.5. The transition zone narrowed as R_p increased. Hence, a particle affects the collapse direction of a CB within a certain distance and, thereby, can help reduce the impact and damage exerted by a CB on the boundary.

Furthermore, extensive experiments (Xu et al. 2017) were conducted to analyze the collapse behavior of a CB near a particle. Let φ_{bp} be the ratio of R_p to $R_{\max}$. Figure 2.23 shows a γ_{bp}– φ_{bp} plot. As demonstrated in Fig. 2.23, approximately three zones (separated by dashed lines) can be distinguished based on the collapse directions of the CBs. The zone to the left side of the green dotted line ($\varphi_{bp} = 0.45/(\gamma_{bp} - 0.45) - 1$) is the "towards" zone. In the "towards" zone where γ_{bp} was relatively small, the CB near the particle collapsed towards the particle under the action of the particle in each case. The zone between the green and blue dotted lines ($\varphi_{bp} = 4/(\gamma_{bp} + 0.45) - 1$) is the transition zone. In the transition zone where γ_{bp} was larger than that in the "towards" zone, the CB sometimes collapsed towards the particle and sometimes was unaffected by the particle. The zone to the right side of the blue dotted line is the impact-free zone. In the impact-free zone where γ_{bp} was even larger than that in the transition zone, the collapse direction of the CB was no longer affected by the particle. The black solid line in the middle ($\varphi_{bp} = 2/\gamma_{bp} - 1$) was plotted based on the critical distance L ($L = 2R_{\max}$) required for the CB to impact the boundary when collapsing and can be treated as a simplified boundary between the "towards" and impact-free zones.

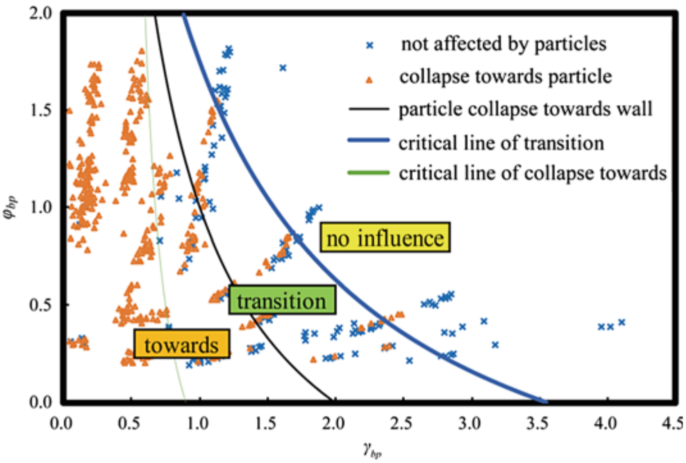


Fig. 2.23 Statistics of the collapse directions of a CB near a particle

2.5.2 Effects of a Particle on the Shock Wave Generated by a CB When Collapsing

Figure 2.24 shows images captured by a high-speed camera that demonstrate the effects of a particle on the shock wave generated by a CB. The black circle in each image is a particle. Seven R_p values (1.00, 1.50, 3.00, 4.00, 5.00, 7.50, and 10.00 mm) were used in the experiment.

The following can be observed from Fig. 2.24. (1) When R_p was very small, the particle basically exerted no impact on the morphology of the CB during its expansion and collapse. When expanding, the CB encapsulated the particle. However, the presence of the particle led to an additional shock wave. Two shock waves, which were very close to one another, were clearly visible on the side far from the particle. (2) As R_p increased, the effects of the particle on the morphology of the CB during its expansion and collapse became increasingly pronounced, and there was also a significant increase in the distance between the two shock waves. (3) As R_p gradually approached $R_{\max}$, the effects of the particle on the morphology of the CB during its expansion and collapse became even more pronounced. However, the shock waves became extremely weak. It was impossible to distinguish the traces of the shock waves. In addition, as demonstrated in Fig. 2.24, the particle diffracted the shock waves. The shock waves were able to maintain their continuity after passing by the particle. However, as R_p increased, the shock waves were notably delayed and weakened in the zone blocked by the particle.

The weakening effect of a particle on the shock wave generated by a CB when collapsing can be more clearly reflected by measuring the impact pressure of the shock wave. Thus, a pressure sensor was placed behind each particle to collect pressure data. Figure 2.25 shows the pressure time-histories of the shock waves behind particles of different size. At a relatively small R_p, a relatively high peak pressure of the shock wave occurred when the CB collapsed. Peak pressure values of 1.895 and 1.690 MPa can be seen in Fig. 2.25a and b, respectively. As R_p gradually increased, there was a gradual decrease in the peak pressure of the shock wave. Peak pressure values of 0.865 and 0.539 MPa can be seen in Fig. 2.25d and e, respectively. In addition, the time-history curve of the impact pressure became flatter as R_p increased. As shown in Fig. 2.25f, the peak pressure almost disappeared, and the whole process was very gentle with a maximum impact pressure of only 0.185 MPa.

In the presence of a solid boundary, while maintaining the CB–solid boundary distance unchanged, placing particles of varying sizes between the CB and the solid boundary can help determine the blocking effect of a particle on the shock wave generated by the CB under various conditions. Let $P_{\max}$ and $P'_{\max}$ be the impact intensity of the shock wave generated by a CB on a boundary when the CB is collapsing in the presence of a particle and the impact intensity of the shock wave generated by a CB on a boundary when the CB collapsing in the absence of a particle, respectively. Figure 2.26 shows a $P_{\max}/P'_{\max} - \gamma_{bp}$ plot. At a relatively small R_p, the relative intensity (i.e., $P_{\max}/P'_{\max}$ ratio) varied within a relatively small range. The $P_{\max}/P'_{\max}$ ratio decreased to approximately 0.8–0.9 only at a relatively small γ_{bp}.

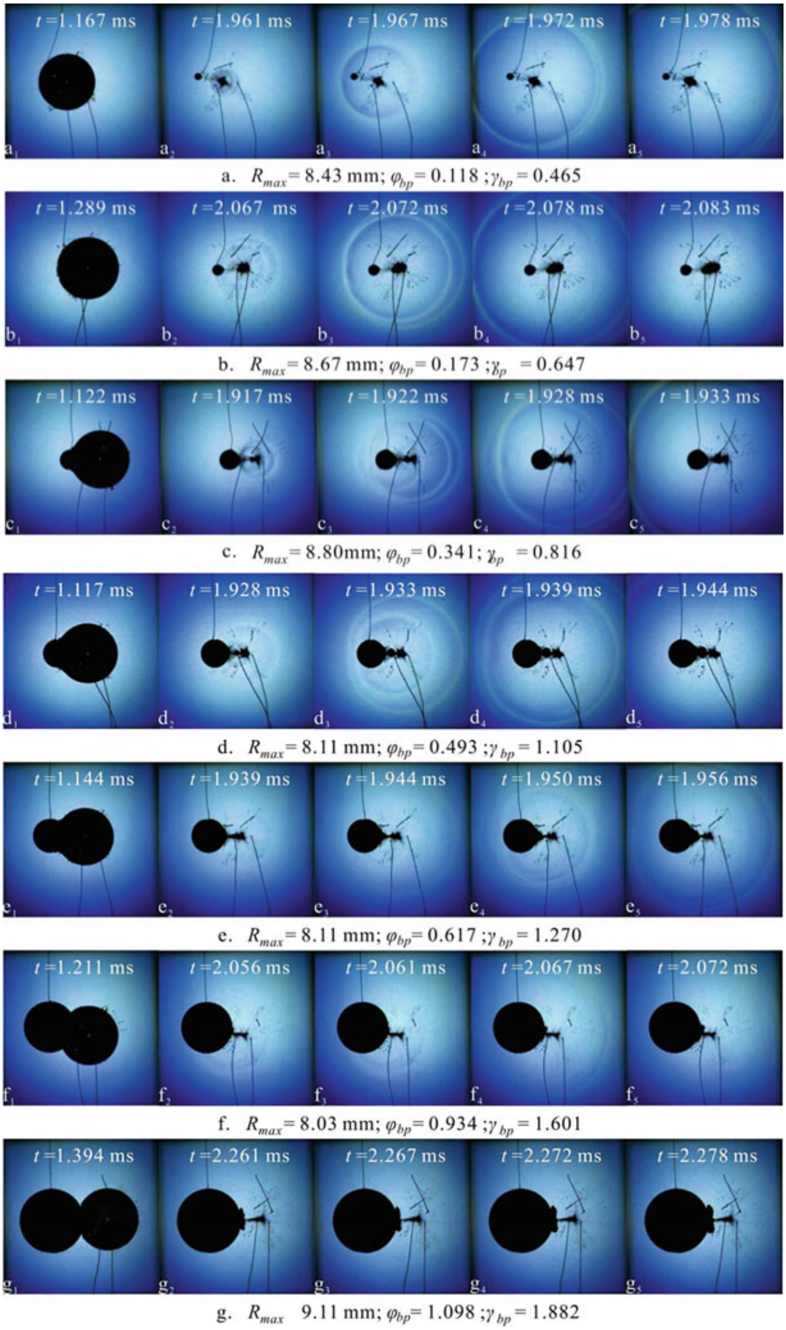


Fig. 2.24 Effects of the relative sizes of a particle and a CB on the shock wave generated by the CB when collapsing

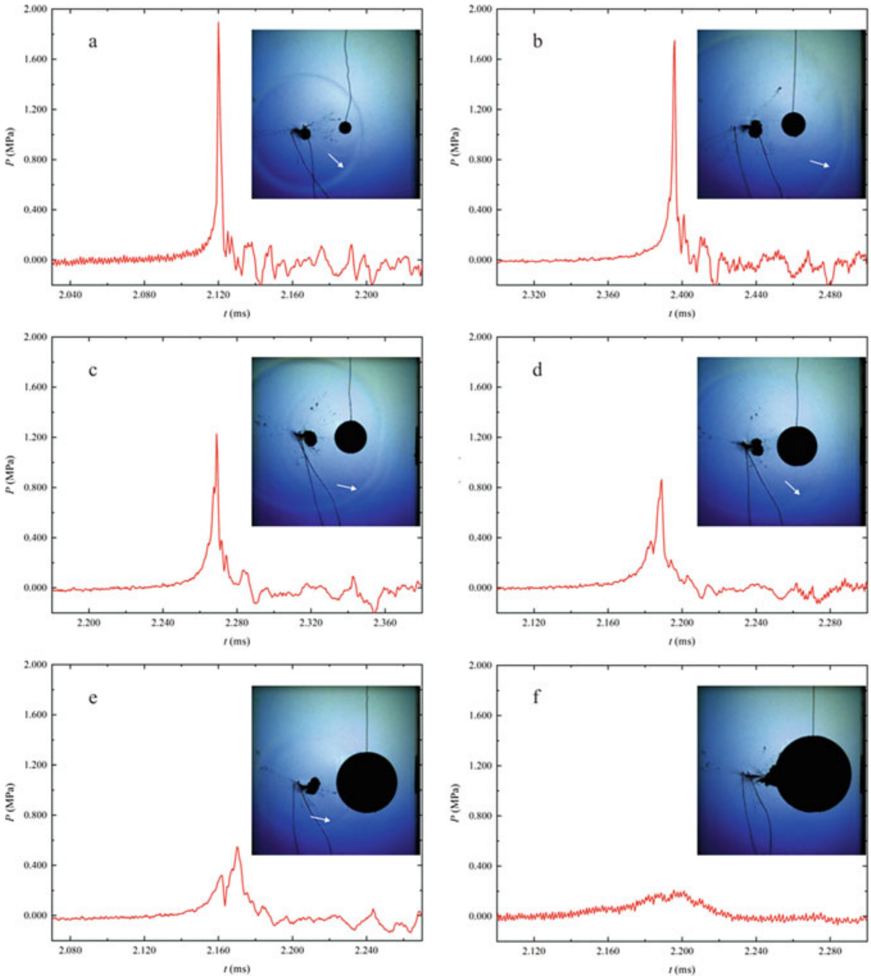


Fig. 2.25 Blocking effect of a particle on the shock wave generated by a CB when collapsing

However, when $\gamma_{bp} = 0.5–2.5$, the $P_{\max}/P'_{\max}$ ratio decreased significantly as R_p increased from 3.0 through 4.0 to 5.0 mm. When $R_p = 7.5$ and 10.0 mm, the particle significantly obstructed the shock wave.

2.5.3 Effects of Particles on Cavitation Erosion

To study the effects of particles on cavitation erosion, the erosion of Al specimens caused by quartz sand particles of six mean diameters d_{50} (0.0018, 0.0352, 0.0804, 0.1583, 0.3022, and 0.6601 mm) at five concentrations C_p (1, 7, 20, 50, and 85 kg/m^3)

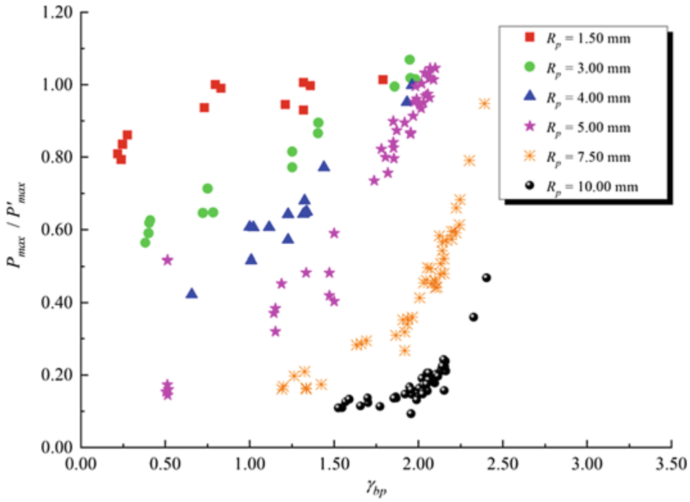
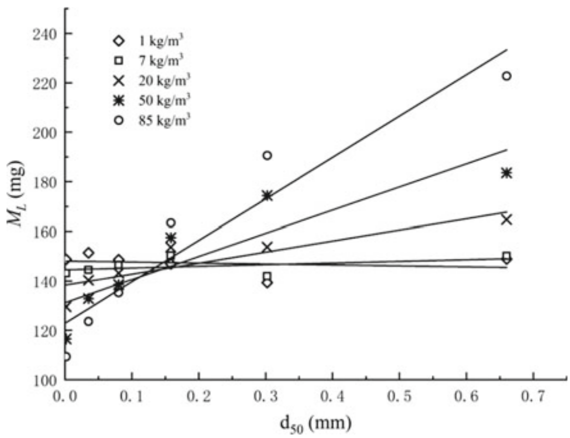


Fig. 2.26 Variation in the effects of γ_{bp} on the peak shock-wave intensity with R_p

was determined using an ultrasonic cavitation erosion analyzer. A total of 30 experiments were conducted. Each experiment lasted for 5 h. Prior to each experiment, the Al specimen was first weighed using an electronic balance. Then, during the experiment, the Al specimen was removed every 30 min and subsequently dried and weighed. The cumulative amount of erosion M_L was calculated based on the mass measurements taken before and after the experiment (accurate to 0.01 mg).

First, the effects of particle size on M_L were examined. Figure 2.27 shows the M_L–d_{50} relationships for the Al specimens. As demonstrated in Fig. 2.27, at a relatively low C_p, M_L varied insignificantly with d_{50} and remained close to that (144.24 mg) in clear water. As C_p increased, the effects of d_{50} on M_L gradually became pronounced.

Fig. 2.27 Relationships between the 5-h cumulative amount of erosion M_L and particle diameter d_{50} for Al specimens



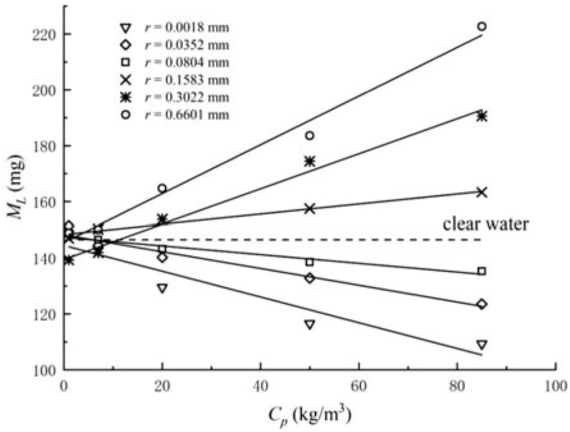


Fig. 2.28 Relationships between the 5-h cumulative amount of erosion M_L and sediment concentration C_p for Al specimens

Relatively small particles (those with a d_{50} approximately less than 0.15 mm) relatively significantly inhibited cavitation erosion. For example, at a C_p of 50 kg/m^3, M_L reached 116.53, 132.82, and 138.53 mg when $d_{50} = 0.0018$, 0.0352, and 0.0804 mm, respectively, which was 19%, 8%, and 4% lower than that (144.24 mg) in clear water, respectively. However, when d_{50} was relatively large (d_{50} approximately greater than 0.15 mm), the presence of particles increased the mass loss of the Al specimen. For example, when $d_{50} = 0.6601$ mm, M_L reached 183.56 mg, which was 27% higher than that in clear water. This should be attributed to the abrasive effect of large particles. Manifestly, there was a critical d_{50} (approximately 0.15 mm) for particles to mitigate cavitation erosion.

Second, the effects of C_p on M_L were examined. Figure 2.28 shows the M_L–C_p relationships corresponding to the d_{50} values, which were determined based on the above experimental results. As demonstrated in Fig. 2.28, within the above experimental range, M_L basically increased linearly as C_p increased.

2.6 Collapse Locations of Cavitation Bubbles and Cavitation Erosion Control in Engineering Practice

As mentioned in the background section in the beginning of this chapter, the orifice plate-type spillways of the Xiaolangdi Dam on the Yellow River have suffered cavitation and cavitation erosion. The orifice plates cause sudden contraction and subsequent sudden diffusion of the flow. As a result, cavitation can easily occur. However, if cavitation occurs in the core region of the flow far from the boundaries, the boundaries will not sustain cavitation damage. Then, under what conditions will the cavitation that occurs past an orifice plate cause cavitation erosion in the boundaries? This question is vitally important for cavitation erosion control in engineering design. To answer it, it is necessary to study the collapse locations of CBs past a convex body in depth.

2.6.1 Collapse Location Distribution Pattern of CBs in a Flow Past a Convex Body

The observations of the motion and evolution of CBs downstream of a convex body showed that the shape, size, and range of CBs varied significantly with the conditions. Let β and u_0 be the contraction ratio of the convex body and the cross-sectional mean velocity of the inflow, respectively. Figure 2.29 shows the formation, development, and collapse of a near-spherical CB downstream of an orifice plate when $\beta = 0.799$ and $u_0 = 7$ m/s. Figure 2.30 shows a banded group of CBs formed downstream of an orifice plate when $\beta = 0.799$ and $u_0 = 10$ m/s.

The collapse location of a CB can be determined by image analysis and synchronous noise measurements (Li et al. 2013). Based on the analysis of the impact exerted by CBs when they are collapsing on the boundary in the experiment, if a CB collapsed at a location within 2 cm from the boundary, this CB is considered to have collapsed in the near-boundary region. For example, none of the CBs shown in Fig. 2.31 collapsed in the near-boundary region, whereas some of the CBs shown in Fig. 2.32 collapsed in the near-boundary region ("o" and "*" signify the formation and collapse locations of CBs, respectively).

First, the effects of β on the collapse locations of CBs at a constant u_0 were investigated. Figures 2.33, 2.34 and 2.35 show the collapse location distributions of CBs downstream of a convex body when $\beta = 0.60$, 0.70, and 0.80 at a u_0 of 7 m/s, respectively. When $\beta = 0.60$, some CBs collapsed in the near-boundary region. Under

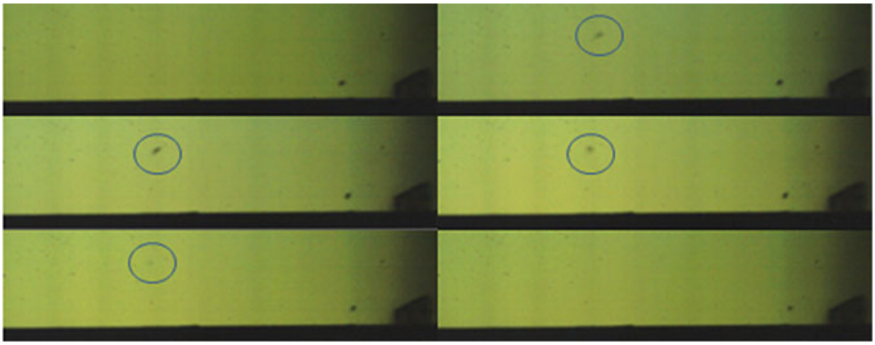
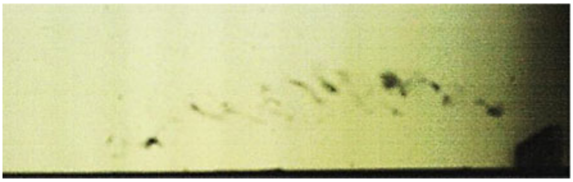


Fig. 2.29 CB formed when contraction ratio $\beta = 0.799$ and mean inflow velocity $u_0 = 7$ m/s

Fig. 2.30 Group of CBs formed when $\beta = 0.799$ and $u_0 = 10$ m/s



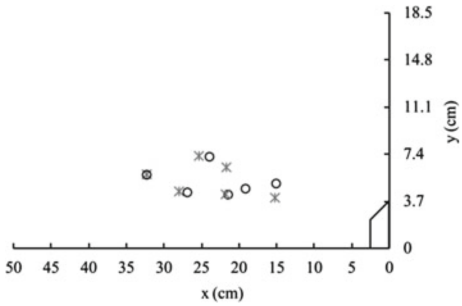


Fig. 2.31 Formation and collapse locations of CBs when $\beta = 0.799$ and $u_0 = 7$ m/s

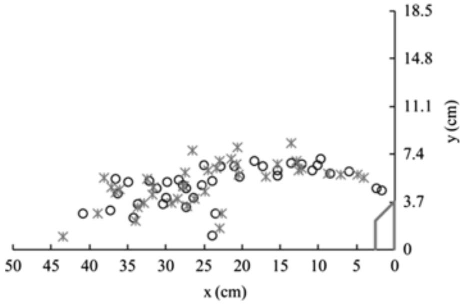


Fig. 2.32 Formation and collapse locations of CBs when $\beta = 0.799$ and $u_0 = 10$ m/s

this condition, the boundary ran the risk of sustaining cavitation damage. When $\beta = 0.70$, an extremely small number of CBs collapsed in the near-boundary region. Under this condition, the boundary was basically in a critical state. When $\beta = 0.80$, there was a significant decrease in the cavitation intensity and the number of CBs. In addition, all the CBs collapsed in the core region of the flow far away from the boundary, and no CBs collapsed in the near-boundary region. Under this condition, the boundary ran no risk of sustaining cavitation damage.

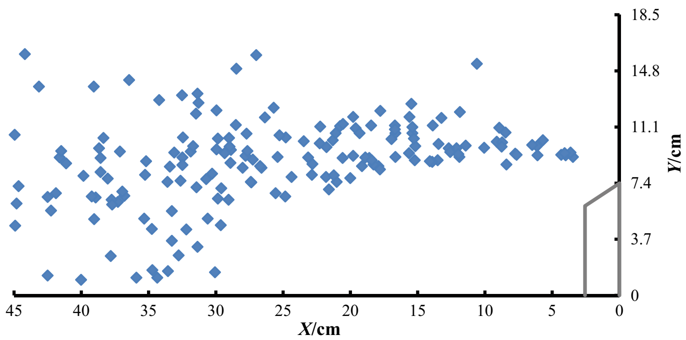


Fig. 2.33 Collapse location distribution of CBs when $\beta = 0.60$ and $u_0 = 7$ m/s

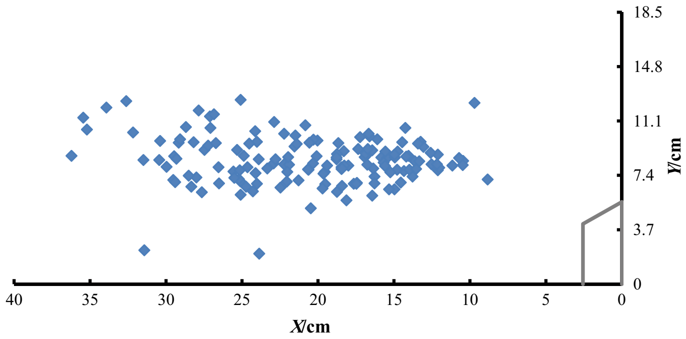


Fig. 2.34 Collapse location distribution of CBs when $\beta = 0.70$ and $u_0 = 7$ m/s

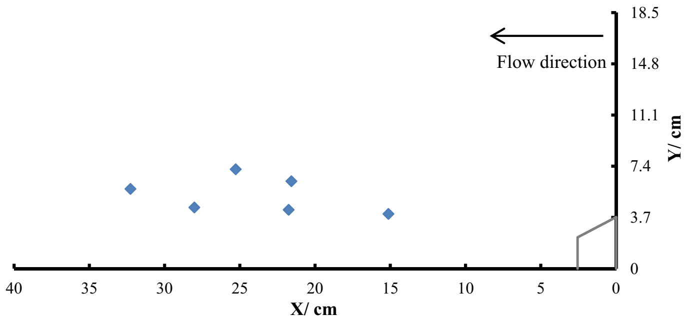


Fig. 2.35 Collapse location distribution of CBs when $\beta = 0.80$ and $u_0 = 7$ m/s

Second, the effects of u_0 on the collapse locations of CBs at a constant β are investigated. Figures 2.36 and 2.37 show the collapse location distributions of CBs downstream of a convex body when $u_0 = 6$ and 8 m/s at a β of 0.6, respectively.

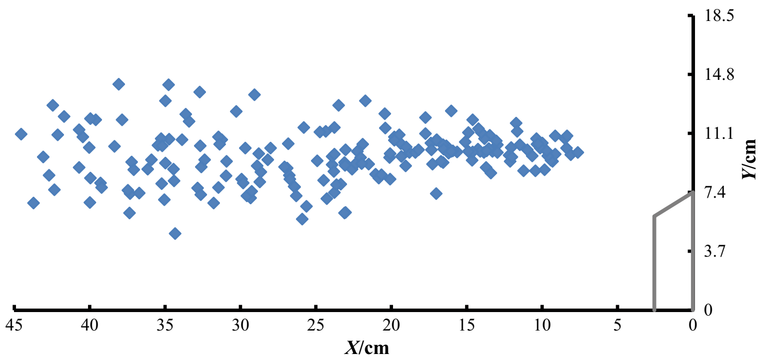


Fig. 2.36 Collapse location distribution of CBs when $\beta = 0.60$ and $u_0 = 6$ m/s

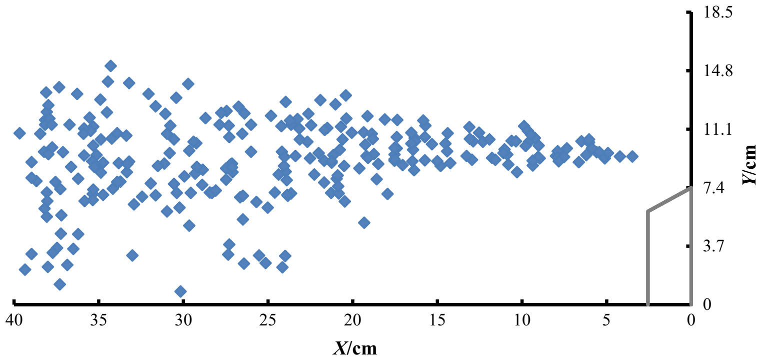


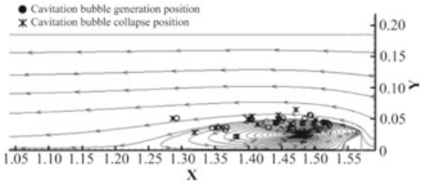
Fig. 2.37 Collapse location distribution of CBs when $\beta = 0.60$ and $u_0 = 8$ m/s

When $u_0 = 6$ m/s, all the CBs collapsed in the core region of the flow far from the boundary, and no CBs collapsed in the near-boundary region. Under this condition, the boundary ran no risk of sustaining cavitation damage. When $u_0 = 8$ m/s, some CBs collapsed in the near-boundary region. Under this condition, the boundary ran the risk of sustaining cavitation damage.

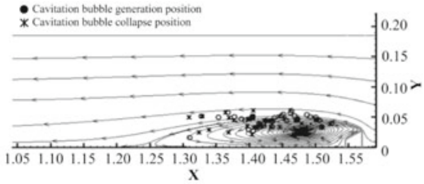
2.6.2 Relationship of the Collapse Locations of CBs in a Flow Past a Convex Body with the Flow Field

The collapse locations of CBs are closely related to the flow field. Thus, a comparative analysis of the flow field and the collapse locations of CBs can help determine the intrinsic cause of the collapse location distribution of CBs. Figure 2.38 shows the streamline patterns (obtained from numerical simulations of turbulence) at various mean inflow velocities u_0 with contraction ratio $\beta = 0.85$ overlaid with the formation and collapse locations of CBs (similarly, "o" and "*" signify the formation and collapse locations of CBs, respectively).

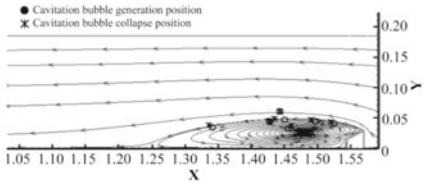
As demonstrated in Fig. 2.38, CBs were formed near the outer edge of the vortex region. At a relatively low u_0, CBs were primarily formed on the outer edge of the vortex region closer to the upstream region and moved downstream along the streamline. These CBs lasted for a short period of time and had collapsed before reaching the tail of the vortex region. As a result, no CBs collapsed in the near-boundary region. At a relatively high u_0, there was an increase in the cavitation intensity of the flow, and CBs were formed at locations closer to the downstream region. Some CBs were able to move over a relatively long distance along the streamline and even reached locations very close to the boundary and then collapsed.



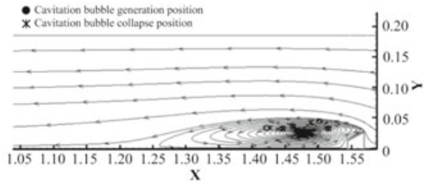
a. Simulated streamline pattern when $u_0 = 9$ m/s and $\beta = 0.85$



b. Simulated streamline pattern when $u_0 = 8$ m/s and $\beta = 0.85$



c. Simulated streamline pattern when $u_0 = 7$ m/s and $\beta = 0.85$



d. Simulated streamline pattern when $u_0 = 6$ m/s and $\beta = 0.85$

Fig. 2.38 Relationship of the collapse locations of CBs downstream of a convex body with the flow field (direction unit: cm)

2.6.3 Critical Conditions Required for Near-Boundary Collapse of CBs in a Flow Past a Convex Body

Based on the above analysis, the collapse locations of CBs downstream of a convex body are controlled by the inflow conditions and the geometry of the boundary. Thus, a dimensionless parameter $\Delta P/\rho gh$ ($\Delta P/\rho g$ is the pressure head loss after passing the convex body, and h is the height of the convex body) is used to comprehensively reflect the effects of the inflow conditions and the geometry of the boundary.

Figure 2.39 shows the experimental results for $\Delta P/\rho gh$ at seven β values (0.5–0.85) and seven u_0 values (4–10 m/s) [the x-axis is the dimensionless u_0 ($u_0^2/2gh$)]. As demonstrated in Fig. 2.39, $\Delta P/\rho gh = 20$ is a notable boundary. Basically, when $\Delta P/\rho gh > 20$, some CBs collapsed in the near-boundary region. In contrast, when $\Delta P/\rho gh < 20$, no CBs collapsed in the near-boundary region.

Thus, the following expression of the critical conditions required for the near-boundary collapse of CBs downstream of a convex body is obtained:

$$\frac{\Delta P}{\rho gh} > 20 \tag{2.6}$$

where h is the height of the convex body and $\Delta P/\rho g$ is the pressure head loss from passing the convex body, which can be calculated using the equation below:

$$\frac{\Delta P}{\rho g} = \xi \frac{u_0^2}{2g} \tag{2.7}$$

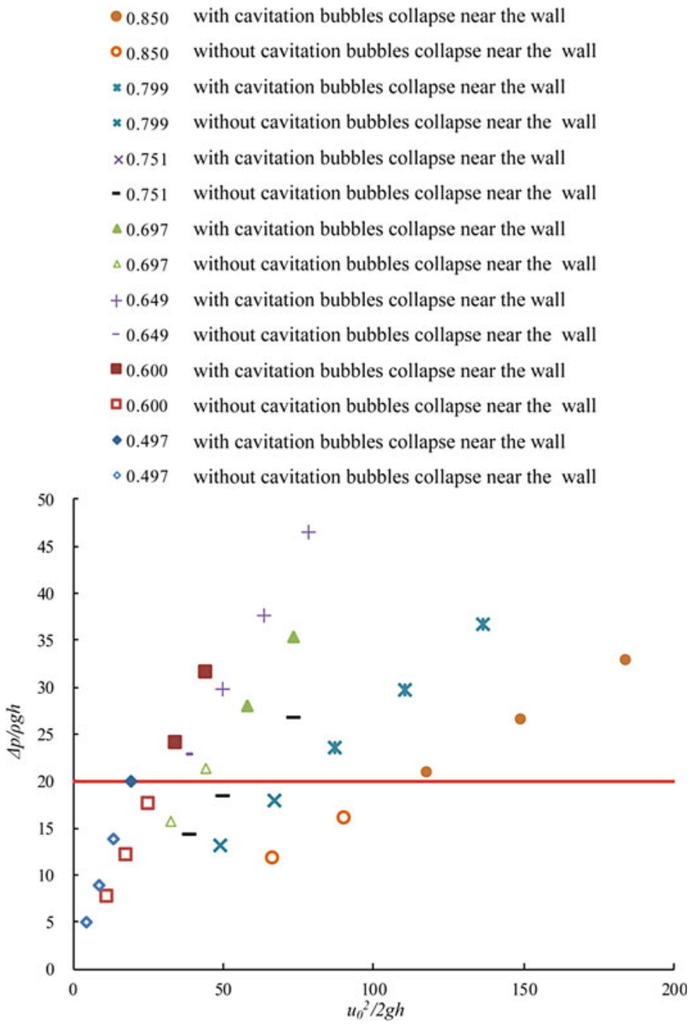


Fig. 2.39 Critical conditions required for the near-boundary collapse of CBs downstream of a convex body

where ξ is the local head loss coefficient. The ξ for an orifice plate is as follows:

$$\xi = \left(1 + 0.707\sqrt{1-\beta} - \beta\right)^2 \tag{2.8}$$

where β is the contraction of the orifice plate.

On this basis, the real-world operational data for the spillways of the Xiaolangdi Dam can be analyzed. Figure 2.40 shows the $\Delta P/\rho gh$–$u_0^2/2gh$ plot for the spillways of the Xiaolangdi Dam. As demonstrated in Fig. 2.40, the maximum $\Delta P/\rho gh$

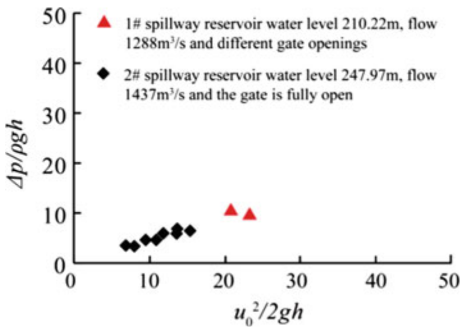


Fig. 2.40 $\Delta P/\rho gh - u_0^2/2gh$ relationship under the real-world operation conditions of the Xiaolangdi Dam

collected under the operational conditions of the spillways of the Xiaolangdi Dam was only 1.04, far lower than the critical value of 20. Even if the reduced-scale effect of cavitation is taken into consideration, the collapse locations of CBs in the spillways of the Xiaolangdi Dam will be far from their boundaries. As a result, the collapse of CBs will not cause cavitation damage to these spillways. This result is in complete agreement with the real-world situation. This suggests that the above critical conditions can be used a reference for engineering design and operational guidance.

2.7 Conclusions

The main conclusions derived from the analysis in this chapter are summarized as follows:

(1) The geometric shape of the boundary and the presence of other CBs both significantly affect the collapse behavior of a CB.
(2) Elastic materials are capable of resisting cavitation erosion to varying degrees by responding to the collapse of CBs by undergoing protruding deformation as well as by absorbing shock waves.
(3) Solid particles are able to attract CBs within a certain distance such that CBs collapse towards them. Thus, solid particles can help mitigate the damage caused by CBs to boundaries.
(4) There are critical conditions for the collapse locations of CBs downstream of a convex body. When the flow parameters and the geometric parameters of the boundary meet the critical conditions, even if cavitation occurs downstream of the convex body, CBs will not collapse near the boundary. Under these conditions, the boundary will not suffer cavitation damage.

References

Benjamin, T. B., & Ellis, A. T. (1966). The collapse of cavitation bubbles and the pressures thereby produced against solid boundaries. In *Philosophical Transactions for the Royal Society of London. Series A, Mathematical and Physical Sciences* (pp. 221–240).

Brennen, C. E. (2014). *Cavitation and bubble dynamics*. Cambridge University Press.

Brujan, E.-A., Nahen, K., Schmidt, P., & Vogel, A. (2001). Dynamics of laser-induced cavitation bubbles. *Journal of Fluid Mechanics, 433,* 283–314.

Chahine, G. (1981). Asymptotic theory of collective bubble growth and collapse. In *Proceeding of 5th International Symposium on Water Column Separation*, IAHR, Obernach, Germany, September.

Güth, W. (1954). Kinematographische aufnahmen von wasserdampfblasen. *Acta Acustica United with Acustica, 4*(4), 445–455.

Harrison, M. (1952). An experimental study of single bubble cavitation noise. *The Journal of the Acoustical Society of America, 24*(6), 776–782.

Huang, J., Chen, J., & Ding, T. (1998). Effect of sediment concentration on bubble expansion and collapse process in fluids with different surface tension. *Journal of Hydraulic Engineering, 000*(2), 12. (In Chinese with English abstract).

Huang, J., & Ni, H. (1987). Collapse pressure of moving groups of cavitation bubbles in compressible liquids. *Journal of Hydrodynamics, 03,* 5–15. (In Chinese).

Jones, I., & Edwards, D. (1960). An experimental study of the forces generated by the collapse of transient cavities in water. *Journal of Fluid Mechanics, 7*(4), 596–609.

Li, Y., Xu, W.-L., Zhang, Y.-L., Zhang, J.-W., & Chen, C.-Q. (2013). Cavitation bubbles collapse characteristics behind a convex body. *Journal of Hydrodynamics, 25*(6), 886–894.

Liu, Y. (1983). Effects of suspended sediments on the cavitation conditions of flows. *Journal of Hydraulic Engineering, 000*(003), 55. (In Chinese).

Lu, L., & Xu, X. (1990). Numerical investigation of bubble collapse near a rigid boundary in solid-liquid two-phase fluid. *Journal of Hydrodynamics, 4,* 108–119. (In Chinese with English abstract).

Morch, K. (1981). Cavity cluster dynamics and cavitation erosion. *Cavitation Polyphase Flow Forum.*

Pan, S., Xiang, T., & Wu, B. (2001). *Investigating to cavitation behavior of orifice tunnel*. http://resolver.caltech.edu/cav2001:sessionA9.002.

Philipp, A., & Lauterborn, W. (1998). Cavitation erosion by single laser-produced bubbles. *Journal of Fluid Mechanics, 361,* 75–116.

Rayleigh, L. (1917). VIII. On the pressure developed in a liquid during the collapse of a spherical cavity. *The London, Edinburgh, and Dublin Philosophical Magazine and Journal of Science, 34*(200), 94–98.

Russell, S. O., & Ball, J. W. (1967). Sudden-enlargement energy dissipater for Mica dam. *Journal of the Hydraulics Division, 93*(4), 41–56.

Sankin, G., & Zhong, P. (2006). Interaction between shock wave and single inertial bubbles near an elastic boundary. *Physical Review E, 74*(4), 046304.

Shima, A. (1981). *The collapse of a spheroidal bubble near a solid wall.*

Shutler, N., & Mesler, R. (1965). *A photographic study of the dynamics and damage capabilities of bubbles collapsing near solid boundaries.*

Tian, L., Huang, J., & Ding, T. (1999). Experimental research of cavitation damage and erosion in gate slots in laden flow. *Water Resources and Hydropower Engineering, 05,* 14–16. (In Chinese with English abstract).

Van Wijngaarden, L. (1966). *On the collective collapse of a large number of gas bubbles in water* (pp. 854–861). Applied Mechanics: Springer.

Vogel, A., Brujan, P. Schmidt and K. Nahen (2001). Interaction of laser-produced cavitation bubbles with elastic boundaries. In *IUTAM symposium on free surface flows.* Springer.

Vogel, A., & Lauterborn, W. (1988). Acoustic transient generation by laser-produced cavitation bubbles near solid boundaries. *The Journal of the Acoustical Society of America, 84*(2), 719–731.
Vogel, A., Lauterborn, W., & Timm, R. (1989). Optical and acoustic investigations of the dynamics of laser-produced cavitation bubbles near a solid boundary. *Journal of Fluid Mechanics, 206,* 299–338.
Xu, W., Zhai, Y., Luo, J., Zhang, Q., & Li, J. (2019). Experimental study of the influence of flexible boundaries with different elastic moduli on cavitation bubbles. *Experimental Thermal and Fluid Science, 109,* 109897.
Xu, W., Zhang, Y., Luo, J., Zhang, Q., & Zhai, Y. (2017). The impact of particles on the collapse characteristics of cavitation bubbles. *Ocean Engineering, 131,* 15–24.
Zhai, Y., Xu, W., Luo, J., & Zhang, Q. (2019). Experimental study on the effect of a deformable boundary on the collapse characteristics of a cavitation bubble. *Thermal Science, 23*(4), 2195–2204.

Chapter 3
Mesoscale Analysis of Aeration for Cavitation Erosion Protection

3.1 Background

Cavitation often occurs in high-velocity water flows. Cavitation-induced erosion is a major threat facing many engineering projects. For hydraulic and hydropower engineering projects, the major methods for alleviating and preventing cavitation erosion can be classified as follows. The first method is to optimize the geometric design of water passages to minimize intense water flow separation, which leads to the formation of negative pressure, the necessary condition for cavitation to occur. However, water flow separation cannot be completely prevented in real-world projects due to the performance, cost-efficiency, and construction efficiency required of water passages. The second method is to improve the surface roughness of water passages when water flow separation is difficult to avoid, thereby reducing the source of cavitation. However, even with the best control of the surface roughness, the surface of water passages cannot be absolutely smooth. Thus, cavitation may occur when the cavitation number of the water flow is lower than a certain value. The third method is to use erosion- and wear-resistant materials. However, no materials have been found that can sufficiently and effectively resist cavitation erosion. In addition, the bounding between an erosion-resistant surface material and the substrate has remained a challenge. The fourth method is to aerate the water flow to reduce and prevent cavitation erosion. Because the first three methods cannot sufficiently prevent cavitation erosion, the fourth method is actually the major means used in real-world engineering to reduce and prevent cavitation erosion (Peterka 1953; Vischer and Hager 1998).

The engineering practice of aeration for cavitation erosion protection was introduced as early as the 1960s. The Grand Coulee Dam in the United States was modified by adding chute aerators after frequent cavitation erosion was observed downstream of the tapered exits of the flood discharge outlets. No cavitation erosion has occurred since the modification, demonstrating that aeration is an effective means for preventing cavitation erosion. Aeration measures have also been successfully implemented in later engineering projects, such as the Glen Canyon Dam and the

W. Xu, *Mesoscale Analysis of Hydraulics*,
https://doi.org/10.1007/978-981-15-9785-5_3

Yellowtail Dam in the United States and the Mica Dam in Canada. Currently, aeration has been incorporated as a mandatory requirement in design specifications for high-velocity discharge structures and, as a result, has been widely adopted for cavitation erosion protection. However, there been a lack of a clear understanding of the mechanism of aeration for cavitation erosion protection, and there are inconsistent explanations for why aeration can prevent cavitation erosion (Ivany and Hammitt 1965; Hammitt 1980; Auret et al. 1993; Xu et al. 2010; Brennen 2014). The lack of experimental research into the mechanism of aeration for cavitation erosion protection is the main reason for this gap. Almost all the existing explanations lack the support of experimental data.

Due to inadequate research into the mechanism, the effectiveness of aeration-based cavitation erosion protection technology in engineering applications has been compromised to different degrees (Rasmussen 1956; Pfister et al. 2011). As a typical example, aeration-based cavitation erosion protection technology was adopted for the spillway tunnel of an engineering project, but the structure still suffered severe cavitation erosion. The upstream section of the spillway tunnel was constructed with a relatively high elevation to facilitate the configuration of the inlet gate, while the downstream section was constructed with a relatively low elevation to facilitate the connection with the outlet. The upstream and downstream sections were connected with a steep-slope section. The connection between the steep-slope and downstream sections had a concave-curve streamwise section. The flow velocity inside the tunnel was higher than 35 m/s. To prevent cavitation erosion, two bottom aerators were constructed, one in the steep-slope section and one at the end of the concave-curve section. However, after the project was commissioned, severe cavitation erosion occurred in an approximately 400-m long section downstream of the end of the concave-curve section. After repeated investigations were conducted on the root cause of the erosion, the sidewalls at the end of the concave-curve section—a dead corner that cannot be protected by the two aerators nor free-surface aeration—became the focus. An effective solution for the problem was to add an aeration structure on the sidewalls. However, only a very small flip bucket could be constructed on the sidewalls, because an excessive lateral contraction might cause the water flow to jump up and impact the tunnel roof. Because a very small flip bucket was expected to entrain air to a very low concentration, a question arises: Can such a low air concentration effectively prevent cavitation erosion? Only with a clear understanding of the inherent mechanism of aeration for cavitation erosion protection can this question be answered scientifically.

In fact, similar to cavitation and cavitation erosion, aeration for cavitation erosion protection is essentially a mesoscale phenomenon. Its effectiveness depends on the interaction between three factors: cavitation bubbles, air bubbles, and solid walls. Only with an in-depth understanding of the inherent mesoscale mechanism of aeration for cavitation erosion protection can reliable theoretical input be provided for the research and development of aeration-based cavitation erosion protection technology and the design of aeration structures for cavitation erosion protection of engineering projects.

3.2 Attenuation Effect of Air Bubbles on the Collapse Intensity of Cavitation Bubbles

The collapse of a cavitation bubble is accompanied by a strong acoustic effect (Vogel et al. 1989). Therefore, the collapse intensity of cavitation bubbles can be comprehensively evaluated using underwater noise monitoring techniques. In the following, the effects of the following factors on the collapse intensity of cavitation bubbles are analyzed: the relative position, relative size, and quantity of air bubbles interacting with the cavitation bubbles.

3.2.1 Intensity of the Collapse Noise of a Cavitation Bubble Interacting But Not Connected with Air Bubbles

First, the attenuation of the intensity of the collapse noise of a cavitation bubble interacting with a single air bubble is examined.

The effect of an air bubble on the attenuation of the collapse intensity of cavitation bubbles varies with the distance between the air bubble and cavitation bubble. Here, the sound pressures on the air bubble side and the other side of a cavitation bubble measured using a hydrophone are designated SP_1 and SP_2, respectively. $SP_{max,1}$ and $SP_{max,2}$ are the maximum noise measurements obtained by a hydrophone at the corresponding sides. Figure 3.1 shows high-speed images of the evolution of a

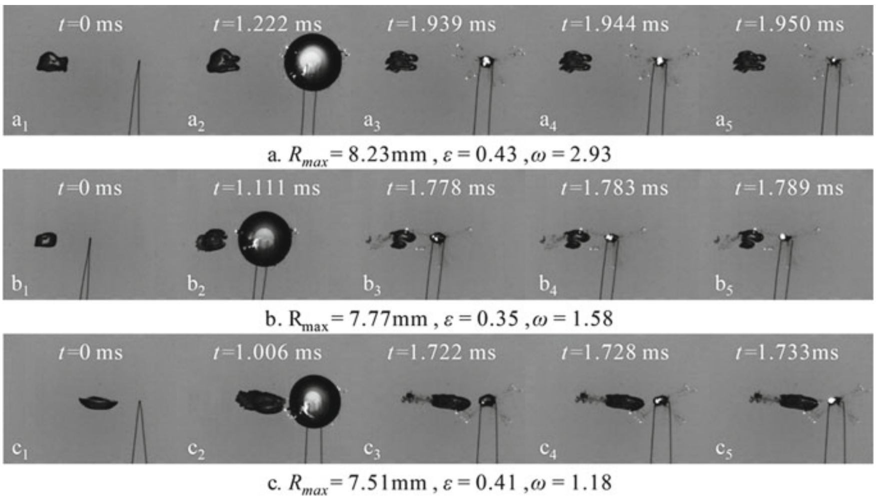


Fig. 3.1 High-speed images of the collapse of a cavitation bubble interacting with an air bubble at different air bubble-cavitation bubble distances (frame rate: 180,000 fps; frame width: 48.31 mm; exposure time: 3.95 μs)

cavitation bubble interacting with an air bubble obtained from a series of experiments, in which the air bubble-cavitation bubble distance was gradually decreased but not to the extent that the two bubbles merged. In experiment a (Fig. 3.1a), the initial equivalent radius of the air bubble $R_a = 3.54$ mm, the cavitation bubble expanded to a maximum radius of $R_{\max} = 8.23$ mm at $t = 1222$ μs, and the dimensionless distance between the centroids of the air bubble and cavitation bubble $\omega = 2.93$. The peak sound pressures on the air bubble side and the other side of the cavitation bubble measured using a hydrophone, $SP_{\max,1}$ and $SP_{\max,2}$, were 55.49 and 57.89 kPa, respectively.

Similarly, in experiment b (Fig. 3.1b), $R_a = 3.08$ mm, $R_{\max} = 7.77$ mm, $\omega = 1.58$, $SP_{\max,1} = 59.22$ kPa, and $SP_{\max,2} = 59.76$ kPa. In experiment c (Fig. 3.1c), $R_a = 3.079$ mm, $R_{\max} = 7.51$ mm, $\omega = 1.18$, $SP_{\max,1} = 26.00$ kPa, and $SP_{\max,2} = 28.45$ kPa.

The dimensionless distance between the air bubble and cavitation bubble gradually decreased from experiment a to c. In the development phase of the cavitation bubble, the air bubble underwent extremely complex morphological changes and certain degrees of size oscillations. These size oscillations of the air bubble under the effect of the cavitation bubble served to effectively absorb part of the cavitation bubble's energy and decrease the collapse intensity of the cavitation bubble. The peak sound pressures measured using a hydrophone illustrate this effect well.

In an experiment in which a cavitation bubble interacted with an air bubble in the absence of a boundary effect, the peak collapse sound pressure of the cavitation bubble measured using a hydrophone was $SP = 60.0$ kPa. We first examine the first phase of a cavitation bubble, or the scenario in which a cavitation bubble does not merge an air bubble to form a gas-containing cavitation bubble.

Figure 3.2 shows the sound pressures (measured using a hydrophone) produced by the collapse of a cavitation bubble interacting with a large air bubble under the

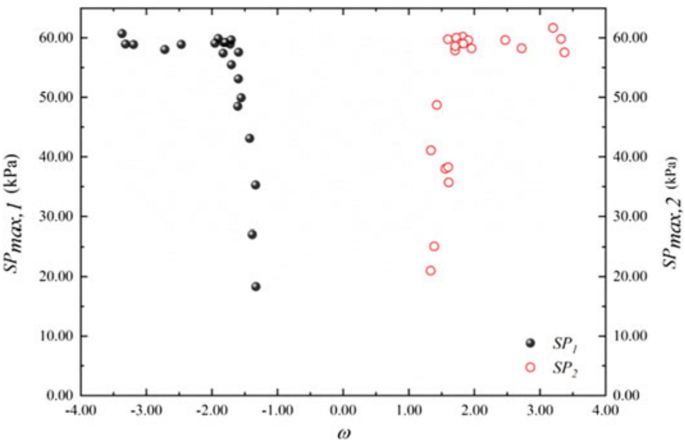
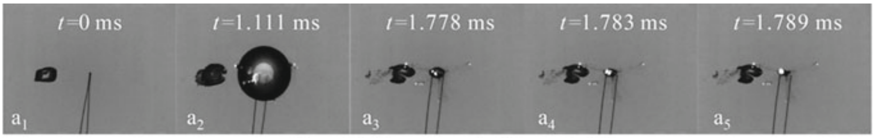


Fig. 3.2 Collapse noise of a cavitation bubble interacting with an air bubble at different air bubble-cavitation bubble distances (with the size of the air bubble held constant)

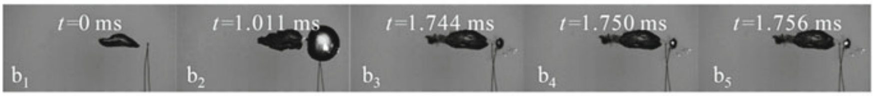
following conditions: position of cavitation bubble $\omega = 0$, position of air bubble $\omega < 0$, and positions of the two hydrophones $\omega > 11$. As the dimensionless air bubble-cavitation bubble distance ω increased, the collapse sound pressure of the cavitation bubble gradually increased to 60 kPa. At $\omega > 4$, the sound pressure decreased slightly. This occurs because when an air bubble is close to a hydrophone probe, the air bubble has a shielding effect on the probe.

The effect of an air bubble on the attenuation of the collapse intensity of cavitation bubbles varies with the air bubble-to-cavitation bubble size ratio. Figure 3.3 shows the high-speed images of the collapse of a cavitation bubble interacting with an air bubble obtained from a series of experiments, in which the air bubble-to-cavitation bubble size ratio gradually increased. In experiment a (Fig. 3.3a), $R_{\max} = 7.77$ mm, $\varepsilon = 0.35$, $\omega = 1.58$, $SP_{\max,1} = 58.58$ kPa, and $SP_{\max,2} = 60.56$ kPa. In experiment b (Fig. 3.3b), $R_a = 3.08$ mm, $R_{\max} = 7.51$ mm, $\omega = 1.58$, $SP_{\max,1} = 26.00$ kPa, and $SP_{\max,2} = 28.45$ kPa. In experiment c (Fig. 3.3c), $R_a = 4.62$ mm, $R_{\max} = 7.34$ mm, $\omega = 1.74$, $SP_{\max,1} = 12.95$ kPa, and $SP_{\max,2} = 21.43$ kPa. The results of the above series of experiments showed that as the air bubble-to-cavitation bubble size ratio gradually increased, the effect of the air bubble on the attenuation of the collapse noise of the cavitation bubble became more pronounced. In addition, the peak sound pressure on the air bubble side (measured with a hydrophone) was considerably lower than that on the other side. This result indicates that the air bubble not only attenuated the collapse noise of the cavitation bubble but also partially shielded the transmission of the cavitation bubble's collapse noise toward the air bubble side.

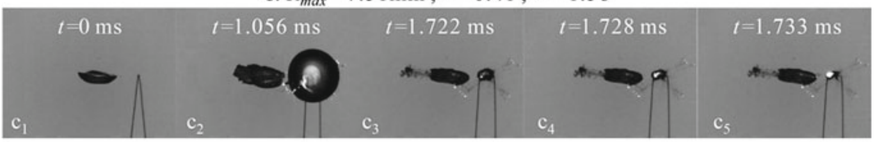
A comparison of the collapse sound pressures of the cavitation bubble interacting with an air bubble of three different sizes (small, medium, and large) showed that as ω increased, the effect of the air bubble on the attenuation of the collapse noise



a. $R_{max} = 7.77$mm, $\varepsilon = 0.35$, $\omega = 1.58$



b. $R_{max} = 7.51$mm, $\varepsilon = 0.41$, $\omega = 1.58$



c. $R_{max} = 7.34$mm, $\varepsilon = 0.63$, $\omega = 1.74$

Fig. 3.3 High-speed images of the collapse of a cavitation bubble interacting with an air bubble of different relative sizes and distances

of the cavitation bubble gradually decreased. In addition, as the volume of the air bubble increased, the range of influence of the air bubble on ω increased (Fig. 3.4).

Next, we investigate the effect of two air bubbles on the attenuation of the intensity of the collapse noise of a cavitation bubble.

The first scenario is that two air bubbles are located on the same side of a cavitation bubble. Figure 3.5 shows the collapse sound pressure (measured with a hydrophone) of a cavitation bubble interacting with two large air bubbles on the same side. The ratio between the distances from the two air bubbles to the cavitation bubble was 1:2. The horizontal axis shows the values of the smaller ω. As ω increased, the sound pressure on the SP_1 side first gradually increased to 40 kPa and then gradually decreased. Our explanation for this result is as follows: When an air bubble is close to a cavitation bubble, the air bubble has a shielding effect on the collapse sound pressure of the cavitation bubble, whereas when an air bubble is relatively far from a cavitation bubble, the air bubble has a shielding effect on the hydrophone probe. Because of the absence of the shielding effect of an air bubble on this side, the collapse sound pressure on the SP_2 side was approximately equal to that produced by the cavitation bubble in the absence of a boundary effect.

A comparison of the collapse sound pressures of cavitation bubbles interacting with two air bubbles of three different sizes (small, medium, and large) located on the same side showed that as ω increased, the effect of the air bubbles on the attenuation of the collapse noise of the cavitation bubble gradually weakened. In addition, as the volume of the air bubbles increased, the range of influence of the air bubbles on ω increased (Figs. 3.6 and 3.7).

Another scenario is that a cavitation bubble interacts with two air bubbles located on opposite sides. Figure 3.8 shows the collapse sound pressures (measured with a

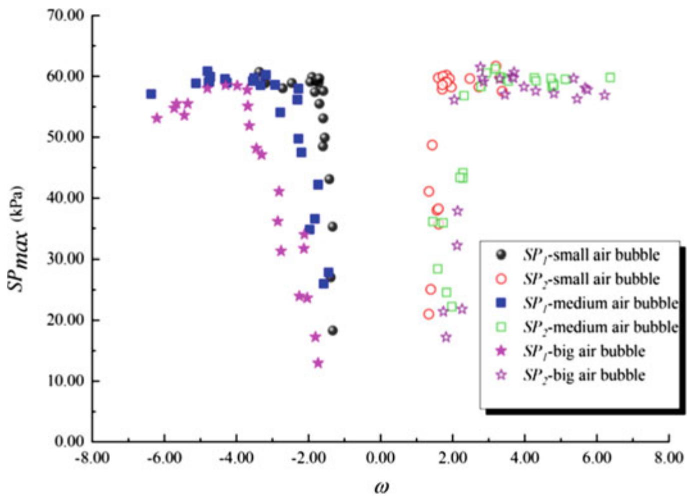


Fig. 3.4 Collapse noises of a cavitation bubble interacting with an air bubble of different relative sizes at the same air bubble-cavitation bubble distance

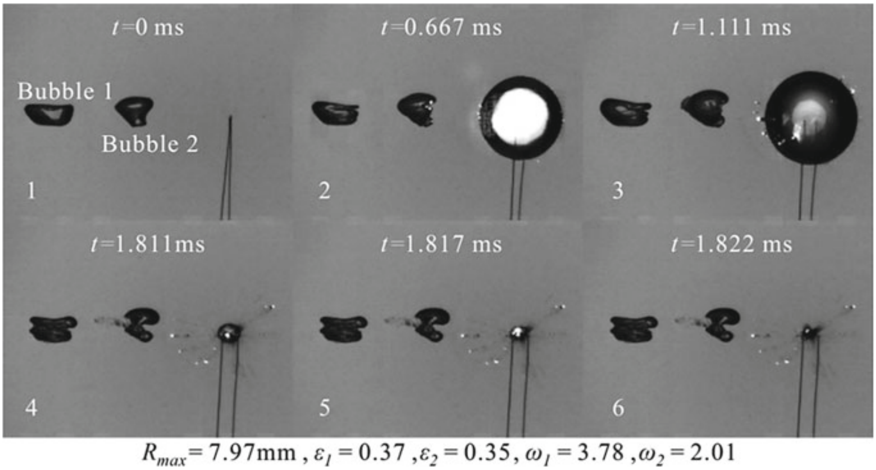


Fig. 3.5 High-speed images of the collapse of a cavitation bubble interacting with two air bubbles located on the same side (frame rate: 180,000 fps; frame width: 48.31 mm; exposure time: 3.95 μs; $R_{\max} = 7.97$ mm; $\varepsilon_1 = 0.37$; $\varepsilon_2 = 0.35$; $\omega_1 = 3.78$; $\omega_2 = 2.01$)

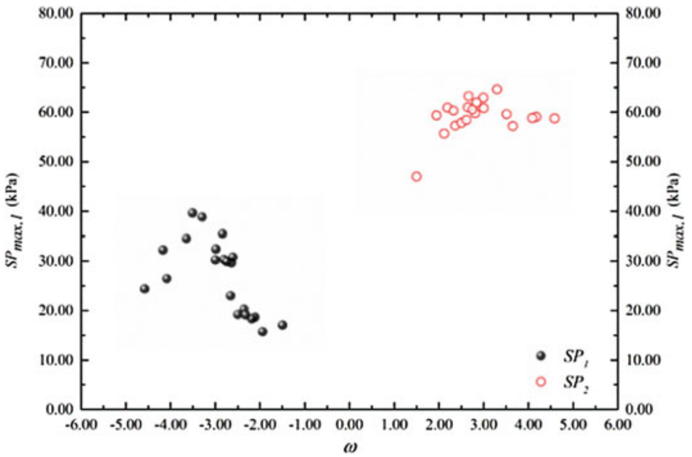


Fig. 3.6 Collapse noise of a cavitation bubble interacting with two air bubbles on the same side at different air bubble-cavitation bubble distances

hydrophone) of a cavitation bubble interacting with two large air bubbles located symmetrically on opposite sides at different air bubble-cavitation bubble distances. As the dimensionless distance from the air bubbles to the cavitation bubble increased, the collapse sound pressure first gradually increased to 40 kPa and then gradually decreased. Our explanation of this result is as follows: When close to a cavitation bubble, the two air bubbles have a shielding effect on the collapse sound pressure of

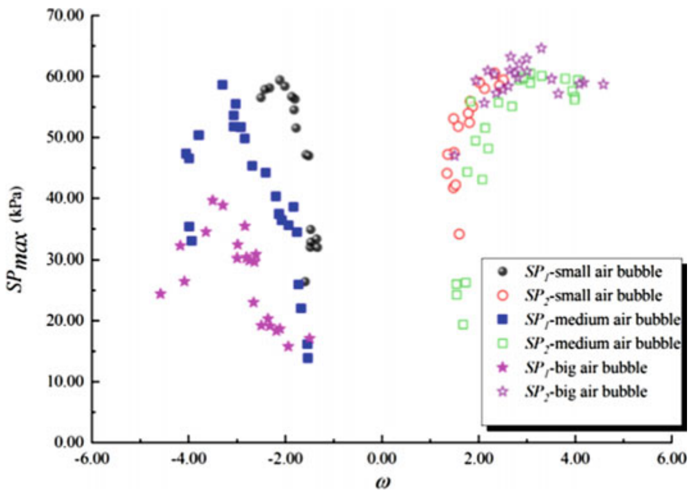


Fig. 3.7 Variation in the collapse noise of a cavitation bubble interacting with two air bubbles located on the same side with the radii of the air bubbles

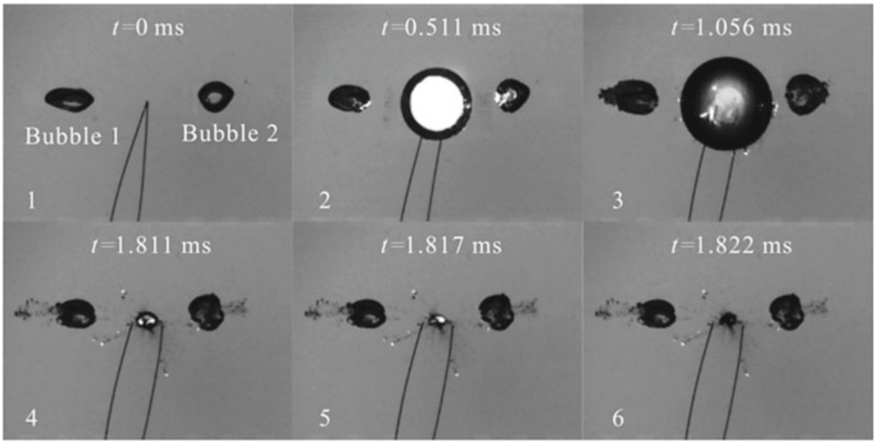


Fig. 3.8 High-speed images of the collapse of a cavitation bubble interacting with two air bubbles located on opposite sides (frequency of images: 180,000 fps; frame width: 48.31 mm; exposure time: 3.95 μs; $R_{\max} = 7.97$ mm; $\varepsilon_1 = 0.36$; $\varepsilon_2 = 0.35$; $\omega_1 = 1.61$; $\omega_2 = 1.46$)

the cavitation bubble, whereas when far from a cavitation bubble, the two air bubbles have a shielding effect on the hydrophone probe.

A comparison of the collapse sound pressures of a cavitation bubble interacting with two air bubbles of three different sizes (small, medium, and large) located on opposite sides showed that as ω was increased, the effect of the air bubbles on the attenuation of the collapse noise of the cavitation bubble gradually weakened. In

addition, as the volume of the air bubbles increased, the range of influence of the air bubbles on ω increased (Figs. 3.9 and 3.10).

Finally, we investigate the intensity of the collapse noise of a cavitation bubble interacting with four air bubbles.

A comparison of the collapse sound pressures of a cavitation bubble interacting with four air bubbles of two different sizes (small and medium) showed that as

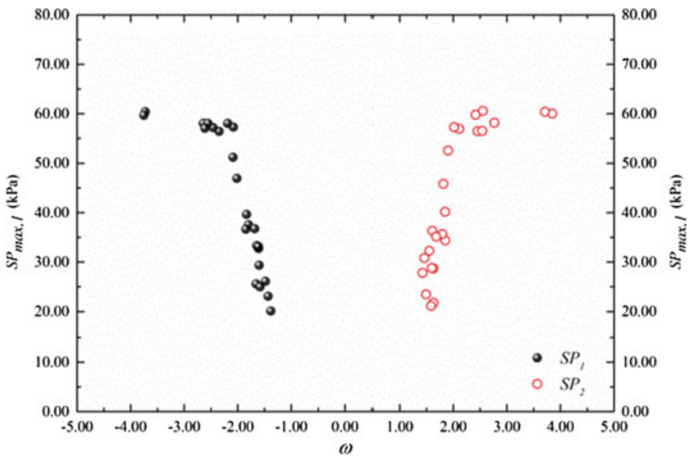


Fig. 3.9 Collapse noise of a cavitation bubble interacting with two air bubbles located symmetrically on opposite sides at different air bubble-cavitation bubble distances

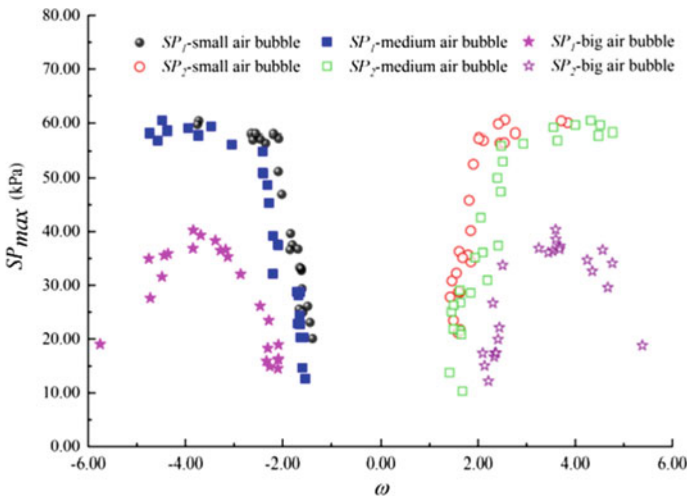


Fig. 3.10 Collapse noise of a cavitation bubble interacting with two air bubbles of three different sizes located symmetrically on opposite sides

ω increased, the effect of the air bubbles on attenuating the collapse noise of the cavitation bubble gradually decreased (Fig. 3.11).

The collapse sound pressure of a cavitation bubble interacting with four air bubbles was experimentally investigated by varying the size of the air bubbles from small to medium only due to the difficulty of conducting experiments at three different sizes with desirable experimental accuracy (Figs. 3.12 and 3.13). The collapse sound pressure of a cavitation bubble interacting with four air bubbles gradually increased as the dimensionless distance from the air bubbles to the cavitation bubble increased.

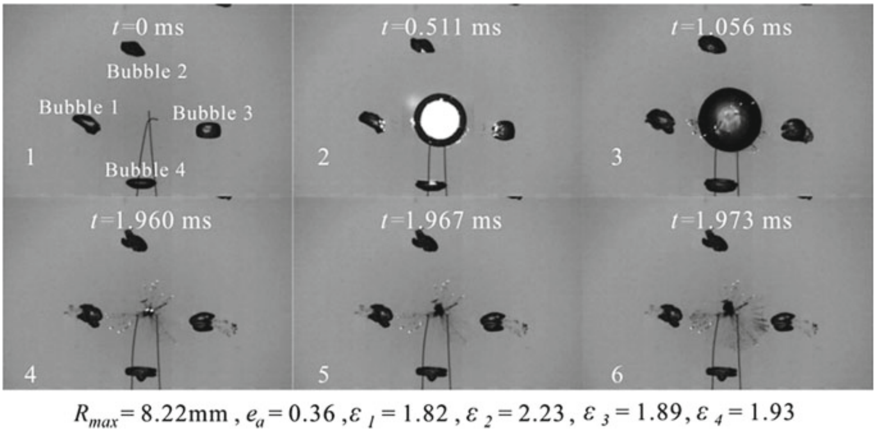


Fig. 3.11 High-speed images of the collapse of a cavitation bubble interacting with four air bubbles (frequency of images: 180,000 fps; frame width: 48.31 mm; exposure time: 3.95 μs; $R_{\max} = 8.22$ mm; $\varepsilon_a = 0.36$; $\omega_1 = 1.82$; $\omega_2 = 2.23$; $\omega_3 = 1.89$; $\omega_4 = 1.93$)

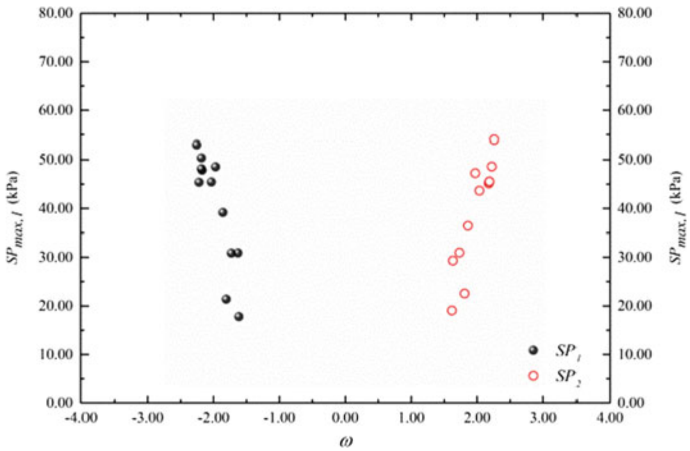


Fig. 3.12 Collapse noises of a cavitation bubble interacting with four air bubbles

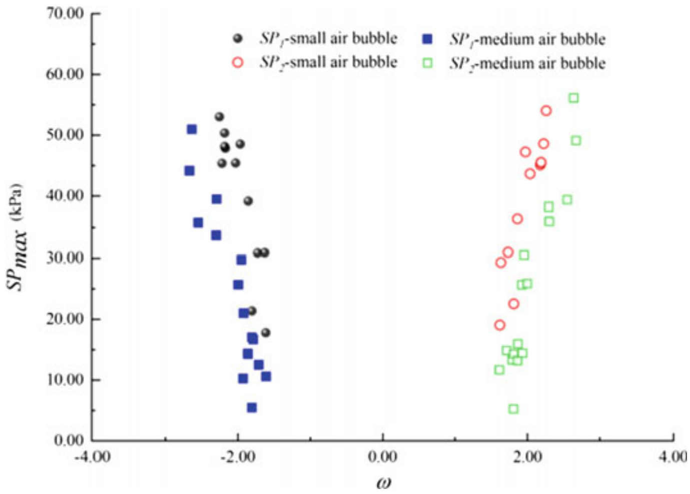


Fig. 3.13 Variation in the collapse noise of a cavitation bubble interacting with four air bubbles as the air bubble size increases from small to medium

The collapse sound pressure of a cavitation bubble interacting with a single air bubble was compared with that of the cavitation bubble interacting with two air bubbles located on the same side to investigate the effect of the quantity of air bubbles on the collapse noise of a cavitation bubble (Fig. 3.14). The sound pressure of a cavitation bubble interacting with two air bubbles located on the same side was generally lower than that of the cavitation bubble interacting with a single air bubble. However, the difference was small, indicating that an increase in the quantity of air bubbles did not result in a considerable decrease in the sound pressure.

Fig. 3.14 Collapse noise of a cavitation bubble interacting with different quantities of air bubbles

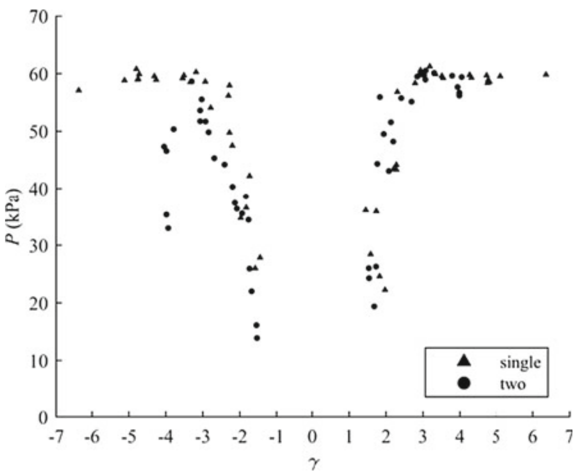
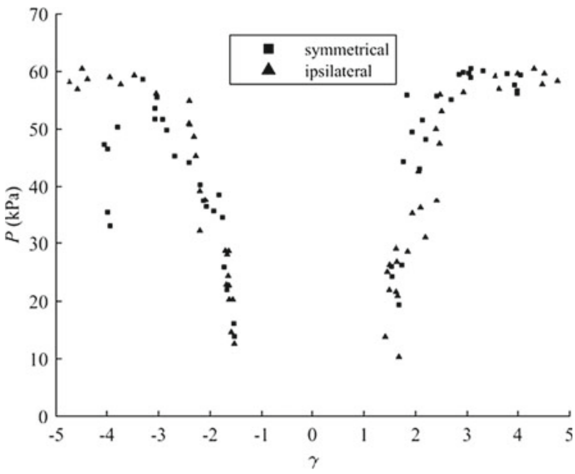


Fig. 3.15 Collapse noise of a cavitation bubble interacting with air bubbles in different air bubble-cavitation bubble configurations



The sound pressure of a cavitation bubble interacting with air bubbles symmetrically located on opposite sides was compared that of a cavitation bubble interacting with air bubbles located on the same side to investigate the effect of the position of air bubbles on the collapse noise of a cavitation bubble (Fig. 3.15). The sound pressure in the first air bubble-cavitation bubble configuration was larger or smaller than that in the second configuration, but the difference was not large. Changing the position of air bubbles did not result in a significant change in the sound pressure.

When the distance between an air bubble and a cavitation bubble is small enough, they will thread together and air goes into the cavitation bubble, therefore the collapse noise decreases further as shown in Fig. 3.16.

3.2.2 Intensity of the Collapse Noise of a Cavitation Bubble Interacting and Connected with an Air Bubble

Figure 3.17 shows high-speed image of a cavitation bubble interacting with, absorbing, and merging an air bubble obtained a series of experiments conducted under the same conditions. In the experiments, the dimensionless radius of the air bubble (the ratio between the radii of the air bubble and cavitation bubble) ε was varied in the range of 0.213–0.217; the maximum radius of the cavitation bubble R_{max} was varied in the range of 3.575–4.063 mm; the dimensionless distance from the cavitation bubble center to the nearest air bubble surface ω was varied in the range of 0.721–1.012. The images in column 1 show the position of the center of the electrode pair before the inception of the cavitation bubble relative to the position of an air bubble. A cavitation bubble emerged at the moment shown by the images in column 4. The cavitation bubble kept expanding up to the moment shown in column 6, when the air bubble was penetrated by the principal shock wave of the cavitation

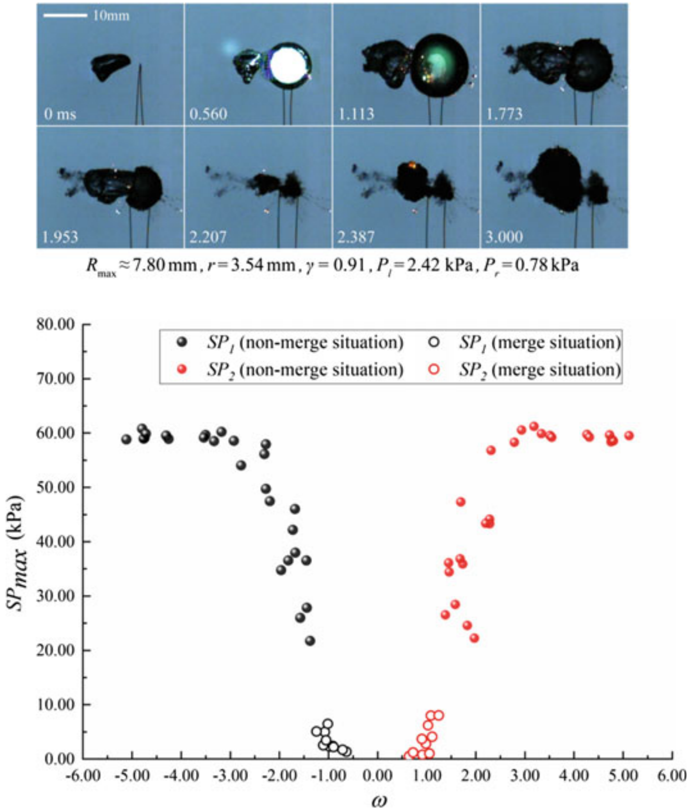


Fig. 3.16 Collapse noise of a cavitation bubble interacting with air bubbles in different air bubble-cavitation bubble distances

bubble. In experiment b, in which the dimensionless radius of the air bubble was the smallest among the four experiments, not only was the air bubble penetrated, but it also split to form new, small bubbles, as shown near the bottom edge of image b6. As the cavitation bubble expanded further, the intensity of the principal shock wave decreased, and the outer size of the air bubble increased due to the high compressibility of the noncondensed gas inside the air bubble, as shown by the images in columns 7–9. From columns 10–17, the cavitation bubble kept shrinking. During the course, the rapid shrinking of the cavitation bubble was accompanied by the emptied space rapidly refilling with the surrounding water. Under the effect of the refilling flow, the air bubble elongated, with the shape of the main body of the air bubble changing from flat in the buffering phase to thin and long. As the cavitation bubble further shrank, the liquid in the original path of the jet that penetrated the air bubble moved toward the cavitation bubble center more quickly than the liquid surrounding the cavitation bubble. At this moment, the air bubble exhibited a stepped morphology at the original position of the penetrating jet. This phenomenon can be

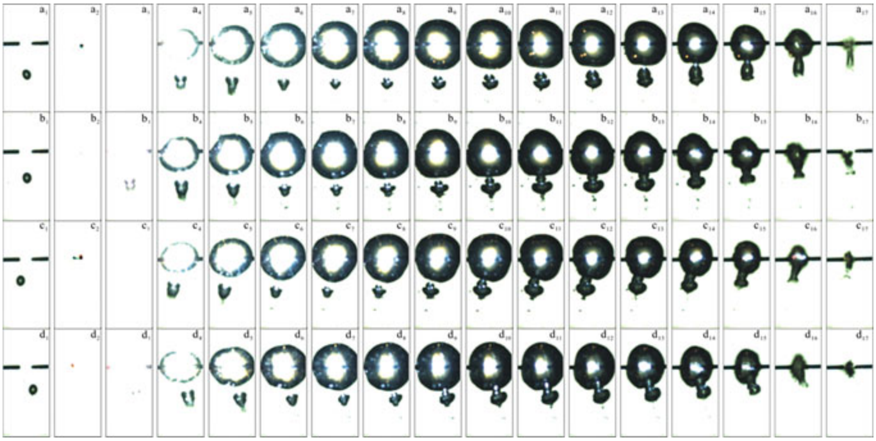
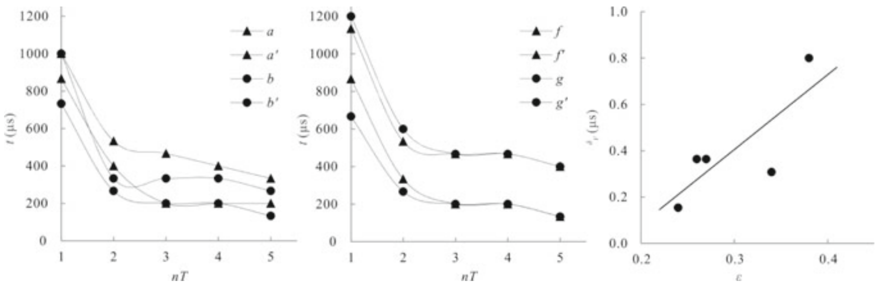


Fig. 3.17 High-speed images of a cavitation bubble interacting and merging with an air bubble (frame rate: 19,700 fps; exposure time: 48 us; image size: 17.333 * 7.367 mm; **a** $R_{\max} = 4.008$ mm; $\omega = 1.012$; $\varepsilon = 0.218$; **b** $R_{\max} = 4.063$ mm; $\omega = 0.721$; $\varepsilon = 0.213$; **c** $R_{\max} = 3.575$ mm; $\omega = 0.864$; $\varepsilon = 0.227$; **d** $R_{\max} = 3.958$ mm; $\omega = 0.734$; $\varepsilon = 0.219$)

mainly explained by the following mechanism: A volume of liquid without an air bubble in the vicinity cannot be easily placed under tension, whereas the air bubble can be easily pulled toward the cavitation bubble center due to the high compressibility of the noncondensed gas inside the air bubble, thereby developing stepped morphology. In addition, as shown in Fig. 3.17, the refilling flow-induced stepped air bubble surface developed markedly slower in experiment a (in which the ω value was the largest among the four experiments) than in the other three experiments. In experiments b–d, the air bubble was connected with the cavitation bubble in the later collapse phase of the cavitation bubble.

As shown by the above analyses of the morphological evolution of the cavitation bubble and air bubble throughout the expansion-collapse life cycle of the cavitation bubble, in the expansion phase of the cavitation bubble, the air bubble surface was concave on the cavitation bubble side due to the effect of the principal shock wave. The concave region developed gradually and ultimately developed into a jet penetrating the air bubble, which underwent a shrinkage-expansion mode of morphological evolution. As the cavitation bubble collapsed, the air bubble was elongated by the refilling flow and exhibited a stepped surface on the side near the cavitation bubble center. The morphological evolution of an air bubble has the following effects: First, as the air bubble is tensioned to a stepped shape, it greatly buffers the shrinkage and collapse of the cavitation bubble. Second, the cavitation bubble and air bubble merge to form a gas-containing cavitation bubble.

Figure 3.18 compares the life cycles of a gas-containing cavitation bubble and its nongas-containing counterpart. In Fig. 3.18a, b, the solid lines show the life cycle (phases 1–5) of a gas-containing cavitation bubble; the dashed lines show the life cycle of its nongas-containing counterpart. The radius of the air bubble in Fig. 3.18a,



(a) Air bubble $r = 0.96$ mm (b) Air bubble $r = 1.49$ mm (c) Relationship between the increase in the life cycle and the bubble radius ratio

Fig. 3.18 Comparison of the life cycles of a gas-containing cavitation bubble and its nongas-containing counterpart

b is Ra = 0.96 and 1.49 mm, respectively. As shown clearly in the figure, the durations of all the five life-cycle phases of a gas-containing cavitation bubble are longer than those of its nongas-containing counterpart. This result indicates that the presence of an air bubble serves to extend the life cycle and reduce the velocity and collapse intensity of cavitation bubbles. A comparison of Fig. 3.18a, b shows that an increase in the radius of the air bubble, or an increase in the gas content of the gas-containing cavitation bubble, leads to a marked increase in the life cycle of the cavitation bubble. Therefore, a larger air bubble has a greater effect on the buffering of the expansion and collapse of a cavitation bubble.

Figure 3.18c shows the relationship between the duration of the first life-cycle phase of a gas-containing cavitation bubble over that of its nongas-containing counterpart and the bubble radius ratio (the ratio of the radius of the air bubble to that of the cavitation bubble). In the figure, the horizontal axis is the bubble radius ratio, and the vertical axis is the duration of the first life-cycle phase. As the bubble radius ratio ε, or the gas content of the gas-containing cavitation bubble, increased, the ratio of the life cycle of the gas-containing cavitation bubble to that of its nongas-containing counterpart increased. This result indicates that a higher gas content leads to a greater effect on the buffering of the expansion and collapse of a cavitation bubble.

Figure 3.19 compares the volumetric evolution of a gas-containing cavitation bubble and its nongas-containing counterpart. Figure 3.19a, b show the temporal volumetric evolution of a gas-containing cavitation bubble formed by a small air bubble and its nongas-containing counterpart. Figure 3.19c, d show the temporal volumetric evolution of a gas-containing cavitation bubble formed by a large air bubble and its nongas-containing counterpart.

In Fig. 3.19a, the nongas-containing cavitation bubble (a′) starts rapidly expanding upon its inception, with its radius increasing to the maximum value in a very short period of time, then rapidly shrinks and collapses, with its volume decreased sharply to 3.51 mm^3. This is followed by two or three rounds of rebound of the cavitation bubble, as shown by the smaller peaks after the major peak in the figure. The

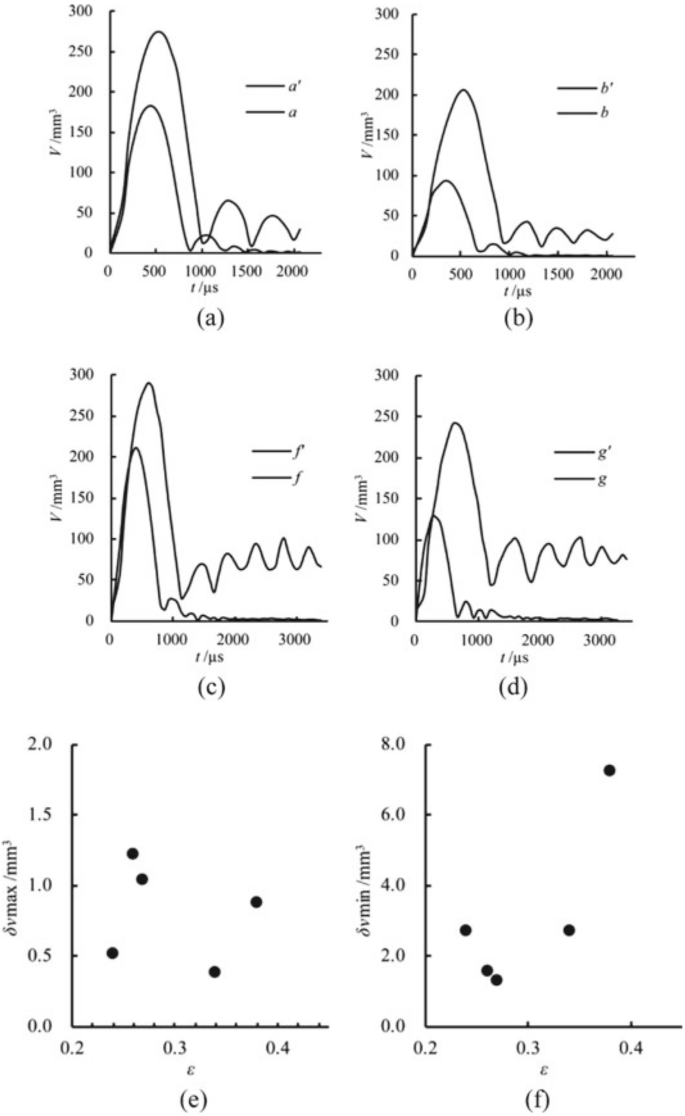


Fig. 3.19 Comparison of the temporal volumetric evolution of a gas-containing cavitation bubble and its nongas-containing counterpart

maximum volumes of the cavitation bubble at the expansion and the first and second rebounds are 182.45, 22.06, and 8.22 mm^3, respectively. The gas-containing cavitation bubble (a), which has the same volume as the air bubble (3.68 mm^3) upon its inception, emerges and rapidly expands to the maximum volume, which is much larger than that of its nongas-containing counterpart. Then, it rapidly shrinks and collapses, with the volume decreased to 13.02 mm^3. Similarly, the gas-containing

cavitation bubble undergoes two or three rounds of rebound. The maximum volumes at the expansion and the first and second rounds of rebound are 275.40, 64.53, and 45.29 mm^3, respectively. The gas-containing cavitation bubble has a much larger volume than that of its nongas-containing counterpart at all the corresponding rebounds. This result indicates that the presence of an air bubble leads to a larger volume of a cavitation bubble in the expansion (to the maximum volume) and the following rebounds. The nongas-containing cavitation has an extremely small volume of 3.51 mm^3 at the first collapse, which has a high intensity and a strong damaging effect. The gas-containing cavitation bubble has a volume of 13.02 mm^3 at the first collapse, indicating that the volume of the cavitation bubble does not shrink as much as that in the case of the nongas containing cavitation bubble due to the presence of the air bubble. Thus, the collapse of the gas-containing cavitation bubble has a markedly lower intensity and a markedly weaker damaging effect. Figure 3.19b shows the similar temporal volumetric evolution processes of a gas-containing cavitation bubble (b) formed by a smaller air bubble and its nongas-containing counterpart (b′).

In Fig. 3.19c, the nongas-containing cavitation bubble (f′) rapidly expands to the maximum volume then rapidly shrinks and collapses. It has an extremely small volume at the first collapse, which is followed by several rounds of rebound and recollapse. After $t = 1500$ μs, its volume gradually approaches 0. Compared with its nongas-containing counterpart, the gas-containing cavitation bubble (f) rapidly expands to a much larger maximum volume after a slightly longer time and has a larger volume at the first collapse. Similarly, this is followed by several rounds of rebound and recollapse. However, as shown in the figure, during the rounds of rebound and recollapse, the volume of the gas-containing cavitation bubble (which varies in the range of 40–100 mm^3) is much larger than that of its nongas-containing counterpart and does not show a decreasing trend. Figure 3.19d shows the similar collapse characteristics of a smaller gas-containing cavitation bubble and its nongas-containing counterpart. A larger air bubble leads to a significant increase in both the maximum volume and the volume at the rebounds of the cavitation bubble. In addition, the volume at the rebounds does not show a decreasing trend. A comparison of the behaviors of a cavitation bubble interacting with large and small air bubbles indicates that a larger air bubble has a more significant effect on the buffering of the expansion and collapse of a cavitation bubble.

In Fig. 3.19e, f, the horizontal axis is the bubble radius ratio; the vertical axis is the volumetric increase, which is defined as the ratio of the difference between the volume of a gas-containing cavitation bubble and that of its nongas-containing counterpart at the same life-cycle phase to the volume of the nongas-containing cavitation bubble. Figure 3.19e shows the increase in the maximum volume, $\delta_{V\max}$. Figure 3.19f shows the increase in the volume at the first collapse, $\delta_{V\min}$. A higher gas content has a more significant effect on the buffering of the expansion and collapse of a cavitation bubble. The increase in the maximum volume of a cavitation bubble is larger than 0.4. This result is due to the following mechanism: A cavitation bubble has a negative pressure when expanded to the maximum volume. A gas-containing cavitation bubble has a much larger pressure than its nongas-containing counterpart expanded to the same

volume. In addition, a cavitation bubble with a higher gas content can be expanded to a larger maximum volume. In other words, when the contained gas changes from a gas nucleus to a large air bubble, the volume of the cavitation bubble increases sharply. However, a further increase in the gas content does not lead to a large increase in the volumetric increase of the cavitation bubble. In summary, a higher gas content leads to a significantly longer life cycle, a larger maximum volume, and a larger volume at the collapse of a cavitation bubble. However, the relationship between the increases and the bubble radius ratio is subject to further investigation.

Figure 3.20 shows the maximum collapse sound pressures $SP_{\max}$ of a cavitation bubble in two different scenarios: (1) interacting with an air bubble at different dimensionless air bubble-cavitation bubble distances and (2) evolving in the absence of an air bubble.

As shown in Fig. 3.20, in the absence of an air bubble, the maximum collapse sound pressure $SP_{\max}$ of a cavitation bubble stays at approximately 60 kPa. The collapse sound pressure of a cavitation bubble interacting with but not merged with an air bubble is completely different from that of a cavitation bubble evolving in the absence of an air bubble. Specifically, as the dimensionless cavitation bubble-air bubble distance is decreased, the collapse sound pressure of the cavitation bubble decreases continuously from approximately 60 to approximately 10 kPa. As the cavitation bubble-air bubble distance further decreases, the cavitation bubble evolves and finally absorbs the air bubble, forming a gas-containing cavitation bubble. The gas-containing cavitation bubble has a larger minimum volume at collapse and a longer life cycle, thus radiating a markedly smaller energy at collapse. The collapse sound pressure decreases to below 10 kPa.

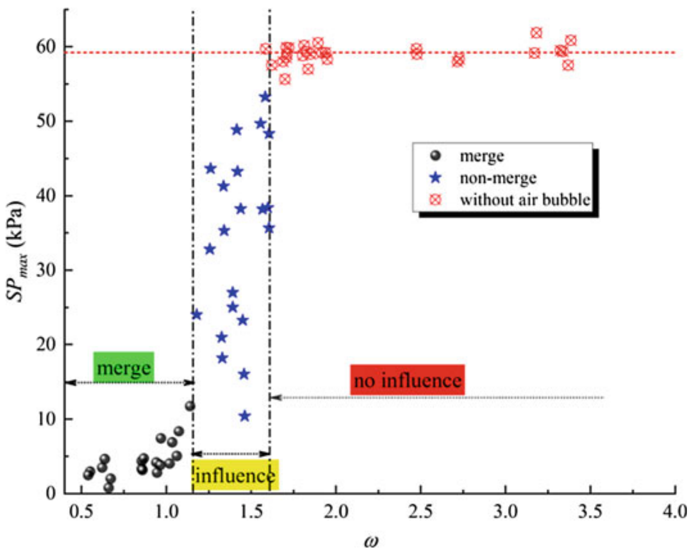


Fig. 3.20 Collapse noise of a gas-containing cavitation bubble

As shown clearly in Fig. 3.20, the presence of an air bubble contributes to an effective decrease in the collapse intensity of cavitation bubbles. In addition, the effect of an air bubble on a cavitation bubble is much stronger when they are merged than when they are not merged. An air bubble's effect on the attenuation of the intensity of the collapse noise of a cavitation bubble is closely related to the air bubble's mechanism of influence.

3.3 Direction-Changing Effect of an Air Bubble on the Collapse of a Cavitation Bubble

An air bubble not only can attenuate the collapse intensity of cavitation bubbles but also can influence the direction of collapse of a cavitation bubble. The latter effect is referred to as the direction-changing effect.

3.3.1 Direction-Changing Effect of an Air Bubble on the Collapse of a Cavitation Bubble

First, we examine the direction of collapse a cavitation bubble near a free surface. A free surface can be a normal water surface, an air bubble with an infinite radius, or an elastic boundary. The collapse of a cavitation bubble near a free surface produces a microjet moving away the free surface. This characteristic has been experimentally investigated and demonstrated by Gibson and Blake (1982).

A cavitation bubble collapses away from a free surface when the distance between the cavitation bubble and the free surface is small. The collapse is not affected by the free surface at large cavitation bubble-free surface distances. To determine the critical condition for a cavitation bubble to collapse away from a free surface, a large amount of data on the direction of collapse of a cavitation bubble collapsing near a free surface has been collected, as shown in Fig. 3.21, where the horizontal axis is the maximum radius of air bubble $R_{\max}$ and the vertical axis is the dimensionless air bubble-free surface distance ω_s.

As shown in the figure, the critical condition for a cavitation bubble to collapse away from a free surface is $\omega_s \approx 5$; i.e., the distance from the cavitation bubble center to the free surface is approximately 5 times that of the maximum radius of the cavitation bubble. When the ratio of the distance between the cavitation bubble center and free surface to the maximum radius of the cavitation bubble is larger than 5, the direction of collapse of the cavitation bubble is not affected by the free surface, and the cavitation bubble collapses in the original place. When the ratio of the distance between the cavitation bubble center and free surface to the maximum radius of the cavitation bubble is smaller than 5, the direction of collapse of the cavitation bubble

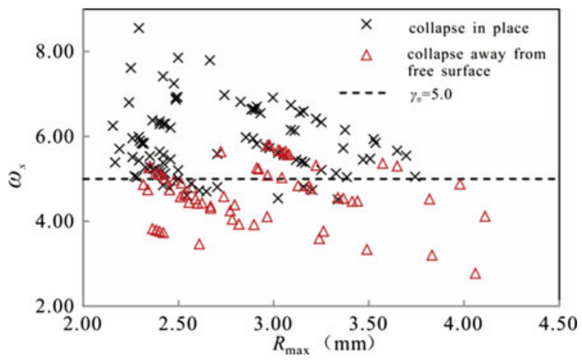


Fig. 3.21 Critical condition for a cavitation bubble to collapse away from a free surface

is affected by the free surface, and the cavitation bubble collapses away from the free surface.

First, we investigate the mesoscale mechanism behind an air bubble's effect on the alleviation of cavitation erosion by examining the air bubble-cavitation bubble interaction, particularly the effect of an air bubble on the collapse characteristics of a cavitation bubble.

The dimensional distance between a cavitation bubble and an air bubble is defined as follows:

$$\omega = S/R_{\max} \tag{3.1}$$

the ratio of the radius of an air bubble to that of a cavitation bubble is defined as follows:

$$\varepsilon = R_a/R_{\max} \tag{3.2}$$

where S is the distance between the centers of the air bubble and cavitation bubble (mm), R_a is the radius of the air bubble (mm), and $R_{\max}$ is the maximum radius of the cavitation bubble (mm).

In the following, we discuss the effect of these two parameters on the air bubble-cavitation bubble interaction and analyze the collapse characteristics of a gas-containing cavitation bubble.

To investigate the effect of the air bubble-cavitation bubble distance on the direction of collapse of a cavitation bubble, a series of four experiments were conducted by varying the distance between the centers of the cavitation bubble and air bubble S, the maximum radius of the cavitation bubble $R_{\max}$, and the radius of the air bubble R_a.

The same electric voltage and resistance were used to generate the cavitation bubbles in the four experiments (Fig. 3.22), but the cavitation bubbles had different maximum radii. The difference between the maximum radii of cavitation bubbles a and b was only 0.001 mm, but the differences between the radii of cavitation bubbles

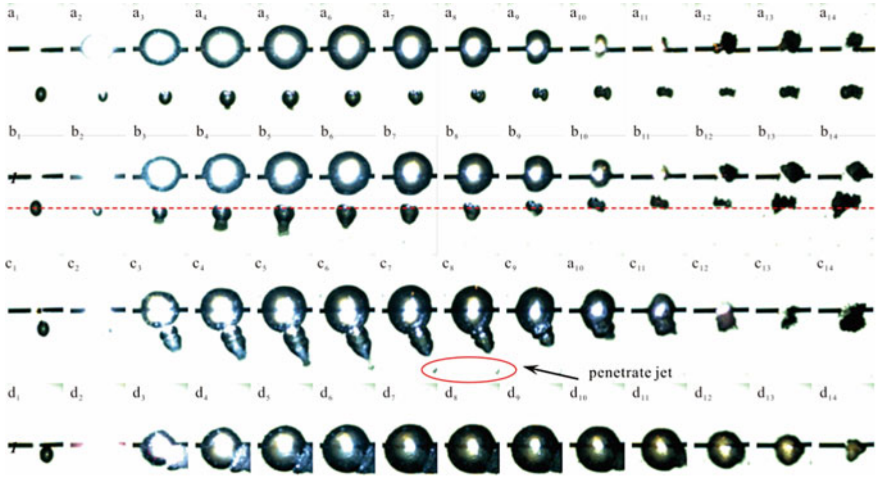


Fig. 3.22 Interaction between a cavitation bubble and an air bubble at different distances (frame rate: 19,700 fps; exposure time: 48 us; image size: 17.333 * 7.367 mm; **a** $R_{\max} = 2.926$ mm; $\delta = 1.810$; $\varepsilon = 0.333$; **b** $R_{\max} = 2.925$ mm; $\delta = 1.204$; $\varepsilon = 0.389$; **c** $R_{\max} = 2.004$ mm; $\delta = 0.996$; $\varepsilon = 0.405$; **d** $R_{\max} = 3.146$ mm; $\delta = 0.194$; $\varepsilon = 0.362$)

c and d and those of cavitation bubbles a and b were large. This is due to the following mechanism: When a cavitation bubble is close to an air bubble, the cavitation bubble is connected with the air bubble in the expansion phase, as shown in images c5 and d3. At this moment, the cavitation bubble contains a large amount of noncondensed gas and is a gas-containing cavitation bubble.

In Fig. 3.22, column 1 shows the distance between the air bubble and the center of the electrode pair at the moment just before the inception of the cavitation bubble. Column 2 shows the dazzling light produced by the electric discharge between the electrodes. The distance between the air bubble and the center of the electrode pair in experiment a was larger than that in experiment d. As shown in the figure, the intensity of the light produced by the electric discharge was high near the center of the electrode pair but gradually decreased with the distance from the center. Cavitation bubbles a and b expanded to the maximum volume before the moment shown in column 6, whereas cavitation bubbles c and d expanded to the maximum volume in the moments shown in columns 7 and 8, respectively. In this phase, in experiments a and b (in which the distance between the air bubble and the center of the electrodes pair was large), the air bubble was penetrated by the principal shock wave produced by the expansion of the cavitation bubble. Comparing experiments a and b, the air bubble was penetrated at a later moment in experiment a than in experiment b (as shown in images a4 and b3, respectively). In experiments c and d (in which the distance between the air bubble and the center of the electrode pair was small), the air bubble was penetrated in the early expansion phase of the cavitation bubble in experiment c, whereas the air bubble completely merged the cavitation bubble and formed a gas-containing cavitation bubble in experiment d. In experiment c, not only was the

air bubble penetrated by the principal shock wave but also a part of the air bubble separated from the parent air bubble to form a small separate bubble, as highlighted in the figure.

After the cavitation bubble entered the collapse phase, while the space occupied by the cavitation bubble was freed by the collapse, the freed space was quickly refilled by the surrounding water, and the air bubble was driven by the centralizing flow to move toward the cavitation bubble center by a very small distance, as shown by the images from experiment b. Compared with experiment a, the air bubble moved toward the cavitation bubble center more noticeably in experiment b than in experiment a. Because of the combined effect of the shock wave and the centralizing flow produced by the collapse of the cavitation bubble, the air bubble surface was concave on the side far from the cavitation bubble and on the side near the cavitation bubble, exhibiting an overall dumbbell shape. In addition, the air bubble had a more typical dumbbell shape in experiment a (in which the air bubble-cavitation bubble distance was larger than that in experiment b) than in experiment b. In experiments a and b, the cavitation bubble did not move toward the air bubble in the collapse phase. In addition, rebound bubbles emerged after the complete collapse of the cavitation bubble in both experiments. These rebound bubbles moved away from the air bubble, and the movement was more noticeable at a larger distance between the air bubble and the center of the electrode pair. Compared with experiments a and b, the cavitation bubble exhibited a longer expansion-collapse life cycle in experiments c and d, although the same needle-plate electric voltage was used for both experiments. This phenomenon is due to the following mechanism: At a small distance between an air bubble and the center of an electrode pair, part or even all of the noncondensed gas inside the air bubble enters the cavitation bubble in its expansion or collapse phase, thereby forming a gas-containing cavitation bubble. In addition, the cavitation bubble has a longer expansion-collapse life cycle if a larger amount of noncondensed gas entered the cavitation bubble in its expansion phase. As analyzed above, the direction of collapse of a cavitation bubble does not change in the final collapse phase regardless of whether the cavitation bubble has absorbed noncondensed gas or has interacted with an air bubble in the expansion or collapse phase.

As revealed by the investigation of a cavitation bubble interacting with an air bubble at different distances, as the distance between the centers of the cavitation bubble and air bubble gradually decreased, in the expansion phase of the cavitation bubble, the intensity and length of the jet penetrating the air bubble gradually increased, and the air bubble and cavitation bubble merged when the distance between the centers of the cavitation bubble and air bubble was very small; in the collapse phase of the cavitation bubble, the penetrating jet was pulled toward the air bubble center at a higher rate, and the air bubble underwent more drastic morphological changes.

As the air bubble-to-cavitation bubble size ratio was varied, the effect of the air bubble on the direction of collapse of the cavitation bubble varied markedly. Figure 3.23 shows the entire process of the air bubble-cavitation bubble interaction. Figure 3.23a shows the interaction between a cavitation bubble and a small air bubble. Figure 3.23b shows the interaction between a cavitation bubble and a large air bubble.

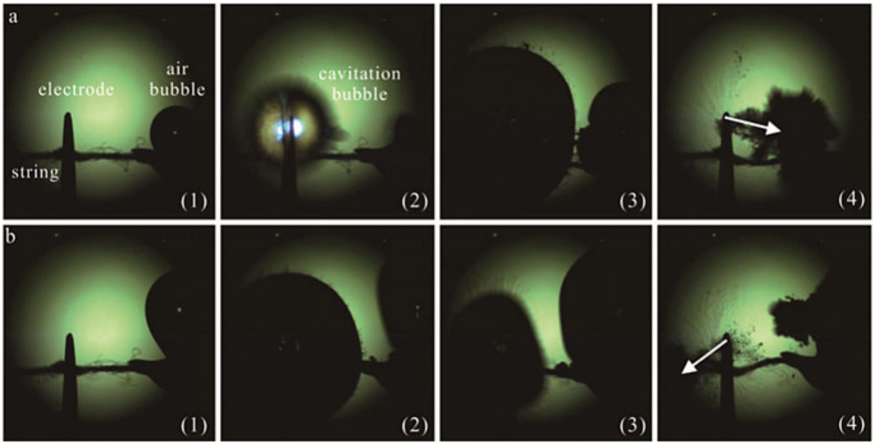
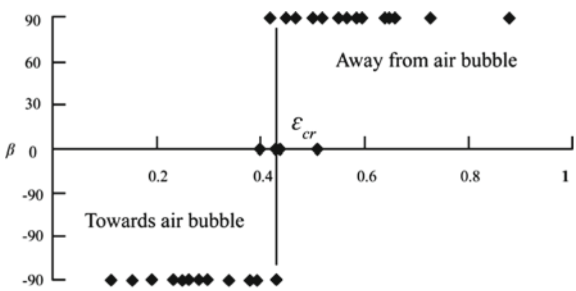


Fig. 3.23 Cavitation bubble-air bubble interaction (frame rate: 3000 fps; exposure time: 42 μs; image size: 9 × 9 mm; $\delta = 0.91$; $R = 3.4$ mm; **a** $\varepsilon = 0.31$; **b**: $\varepsilon = 0.89$)

The dimensionless radius of an air bubble is defined as $\varepsilon = r/R$, where r is the radius of the air bubble and R is the maximum radius of the cavitation bubble. When the air bubble is small (Fig. 3.23a), the cavitation bubble and air bubble attract each other, the cavitation bubble collapses toward the air bubble, and the two bubbles are merged into one in the rebound phase. When the air bubble is large (Fig. 3.23b), the cavitation bubble and air bubble repel each other, and the cavitation bubble collapses away from the air bubble.

As shown in Fig. 3.23, ε is a critical parameter influencing the direction of collapse of a cavitation bubble. Figure 3.24 shows the relationship between the direction of collapse of a cavitation bubble β and ε (40 experimental observations). The midpoint of the line connecting a cavitation bubble and an air bubble is designated as the pole, and the line passing through the centers of the cavitation bubble and air bubble is designated as the polar axis; then, the direction of the cavitation bubble is defined as the positive direction of angle β. As shown in the figure, the cavitation bubble always collapses at a position on the line connecting the centers of the cavitation bubble and air bubble. In the figure, a positive value of β indicates that the cavitation

Fig. 3.24 Relationship between the direction of collapse of a cavitation bubble and ε ($\delta = 0.91$, $R =$ 3.4 mm)



bubble collapses away from the air bubble, whereas a negative value indicates that the cavitation bubble collapses toward the air bubble. At $\delta = 0.91$ and $R = 3.4$ mm, the critical value of ε, $\varepsilon_{cr} \approx 0.42$. When $\varepsilon < \varepsilon_{cr}$, the cavitation bubble and air bubble attract each other, and the cavitation bubble collapses toward the air bubble. When $\varepsilon > \varepsilon_{cr}$, the cavitation bubble and air bubble repel each other, and the cavitation bubble collapses away from the air bubble. This phenomenon can be explained by momentum conservation and the effect of a cavitation bubble's shock wave on the deformation of an air bubble. Because the density of air is lower than that of water, the momentum of the cavitation bubble on the air bubble side is smaller than that on the opposite side. However, under the effect of the cavitation bubble's shock wave, the air bubble shrinks, rebounds, and reshrinks, and the reshrinkage of the air bubble occurs simultaneously with the collapse of the cavitation bubble, resulting in the momentum of the cavitation bubble on the air bubble side being higher than that on the opposite side. These are two opposing effects. To maintain momentum conservation, the cavitation bubble collapses toward the side with the higher momentum. Therefore, there exists an ε_{cr}, where when $\varepsilon < \varepsilon_{cr}$, the momentum of the cavitation bubble on the air bubble side is higher than that on the opposite side. The extreme condition of this scenario is that the air bubble is a very small gas nucleus and is similar to a cavitation bubble (two interacting cavitation bubbles attract each other). When $\varepsilon > \varepsilon_{cr}$, the momentum of the cavitation bubble on the air bubble side is lower than that on the opposite side. The extreme condition of this scenario is that the air bubble has an infinite volume and is similar to a free surface (a cavitation bubble evolving near a free surface collapses away from the free surface). The direction of the collapse of a cavitation bubble can also be explained directly from the perspective of the pressure gradient.

Generally, the direction of collapse of a cavitation bubble near an air bubble is shown in Fig. 3.25 (Xu et al. 2020), where ε is the relative size of the air bubble (the radius of the air bubble/the maximum radius of the cavitation bubble), γ is the relative distance between the cavitation bubble and the air bubble (the distance between two sphere centers/the maximum radius of the cavitation bubble). The figure can be divided into four areas: no direction, away from the air bubble, towards the air bubble, and merged air bubble.

3.3.2 Direction-Changing Effect of an Air Bubble on a Cavitation Bubble Evolving Near a Wall

The position of a cavitation bubble relative to a wall is measured using the dimensionless parameter $\gamma_{bw} = D/R_{\max}$, where D is the smallest distance from the cavitation bubble center to the wall and $R_{\max}$ is the maximum radius of the cavitation bubble during its evolution. The size of an air bubble relative to that of a cavitation bubble is measured using a dimensionless parameter, $\varepsilon = R_a/R_{\max}$, where R_a is the radius of the air bubble and $R_{\max}$ is the maximum radius of the cavitation bubble during

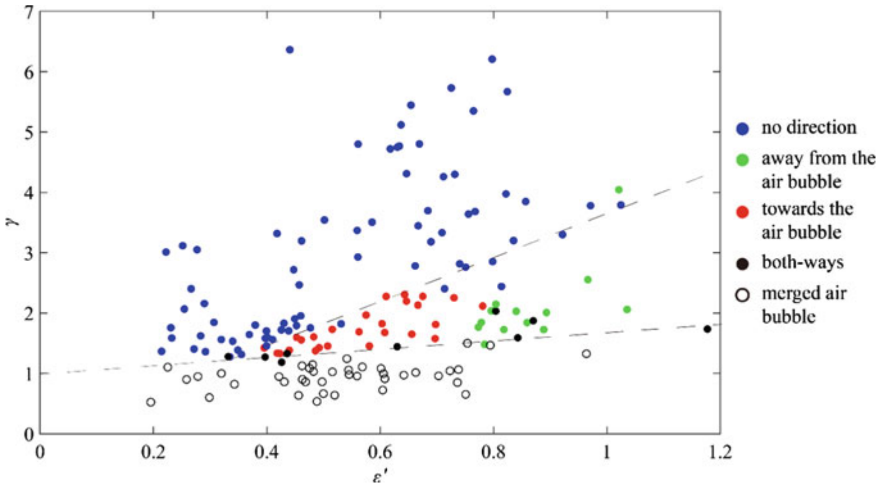
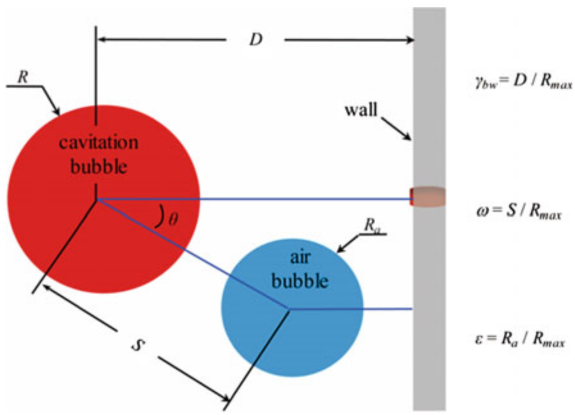


Fig. 3.25 The direction of collapse of a cavitation bubble near an air bubble

its evolution. In addition, the position of an air bubble relative to that of a cavitation bubble is measured using the dimensionless parameter $\omega = S/R_{\max}$, The S is the distance from the center of cavitation bubble to the center of air bubble and $R_{\max}$ is the maximum radius of the cavitation bubble during its evolution. The positional relationship between the air bubble, cavitation bubble, and wall is measured with the angle θ between the line connecting the centers of the air bubble and cavitation bubble and the normal line from the cavitation bubble center to the wall, with the cavitation bubble center as the apex. The spatial relationship between the cavitation bubble, air bubble, and wall can be determined using the four parameters γ, ε, ω, and θ, defined above, as shown in Fig. 3.26.

Fig. 3.26 Definition of parameters for describing the spatial relationship between an air bubble, a cavitation bubble, and a wall



We first investigate the effect of the air bubble-cavitation bubble distance on the collapse characteristics of a cavitation bubble near a wall.

Figure 3.27 shows high-speed images of a cavitation bubble interacting with an air bubble obtained from a series of five experiments, in which the cavitation bubble-air bubble distance was varied and the cavitation bubble-wall distance was held constant. In the five experiments, the maximum radius of the cavitation bubble $R_{\max}$ was varied in the range of 2.275–2.817 mm, and the dimensionless radius of the air bubble was varied in the range of 0.300–0.548. Table 3.1 shows the parametric settings for the experiments.

As shown in Fig. 3.27, in experiment a (in which the air bubble-cavitation bubble distance was small, with the dimensionless distance from the cavitation bubble center

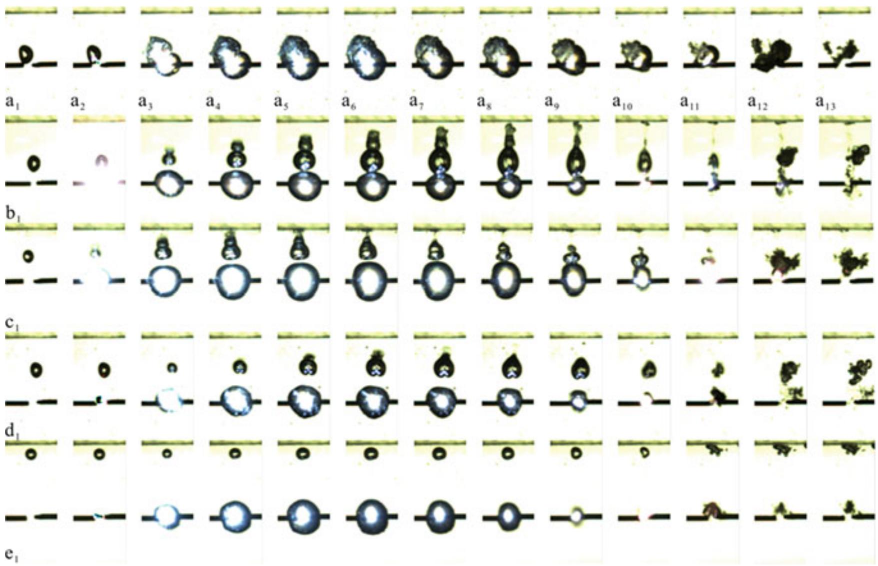


Fig. 3.27 Air bubble-cavitation bubble-wall interaction at different ω values (frame rate: 19,700 fps; exposure time: 48 us; image size: 17.333 * 7.367 mm; spatial relationship between the air bubble, cavitation bubble, and wall is shown in Table 3.1)

Table 3.1 Parametric settings for experiments of air bubble-cavitation bubble-wall interaction at different ω values

	$R_{\max}$ (mm)	γ	ε	ω	θ
Experiment a	2.600	2.729	0.500	0.088	22.932
Experiment b	2.275	3.976	0.548	0.882	1.909
Experiment c	2.817	2.558	0.327	0.924	1.762
Experiment d	2.383	3.773	0.477	1.420	6.189
Experiment e	2.708	3.760	0.300	3.020	0

to the air bubble surface set at 0.088), after its inception, the cavitation bubble rapidly merged with the air bubble and further evolved into a gas-containing cavitation bubble. In experiment b (in which the dimensionless distance from the cavitation bubble center to the nearest air bubble surface was set at 0.882), a cavitation bubble was generated by an electric discharge between the electrodes, and the air bubble was penetrated under the effect of the principal shock wave of the cavitation bubble, forming a penetrating jet. In addition, the air bubble had a volume smaller than its volume before the inception of the cavitation bubble. This result is mainly due to the effect of the principal shock wave. As the cavitation bubble developed further through the expansion-collapse life cycle, the penetrating jet continued to develop into a long jet. Prior to the moment shown in Row 7, the jet penetrating the air bubble continued to grow and gradually developed toward the wall. When the cavitation bubble developed to the moments shown in Rows 8 and 9, the jet penetrating the air bubble reached the wall, and the cavitation bubble entered its later collapse phase, when the cavitation bubble radiated a strong collapse shock wave. Under the effect of the collapse shock wave, the overall outer size of the penetrated air bubble decreased. At this moment, part of the penetrating jet detached from the air bubble and adhered to the wall, and the nondetached part of the penetrating jet began to move toward the cavitation bubble center, as shown in images b10 and b11 (Fig. 3.27). When the cavitation bubble completed the first collapse, the air bubble shrank to the minimum volume and exhibited an irregular spatial morphology. In experiment c (Fig. 3.27), in which the dimensionless distance from the center of the air bubble to the nearest air bubble surface was 0.924, the bubbles underwent evolution similar to that in experiment b. Under the effect of the principal shock wave radiated by the cavitation bubble, a jet emerged and penetrated the air bubble. The penetrating jet reached the wall at the moment shown in image c5, earlier than in experiment b. This result is mainly because of the smaller γ and larger ω. In the later collapse phase of the cavitation bubble, under the effect of the collapse shock wave of the cavitation bubble, the overall outer size of the air bubble decreased. Similarly, part of the penetrating jet detached from the air bubble and adhered to the wall, but the nondetached part of the penetrating jet did not move toward the cavitation bubble center along with the parent air bubble. The difference between the results of experiments c and b was that the penetrating jet developed at a much slower rate in experiment c than in experiment b.

In experiment d (Fig. 3.27), in which the air bubble-cavitation bubble distance was further increased, a jet also developed to penetrate the air bubble. However, different from experiments b and c, the penetrating jet did not reach the wall and did not detach from the air bubble. Before the moment shown in row 7, the jet penetrating the air bubble continued to grow. After the cavitation bubble entered the collapse phase, the space freed by the collapse of the cavitation bubble was quickly refilled by the surrounding water. Under the effect of the refilling flow, the outer size of the air bubble quickly increased, as shown in image d9. In the later collapse phase, the cavitation bubble radiated a strong collapse shock wave into the surrounding water. Under the effect of the shock wave, the outer size of the air bubble decreased, indicating that the air bubble was being compressed. The penetrating jet gradually

disappeared. Being surrounded by a complex flow field, the air bubble exhibited an irregular spatial morphology. In experiment e (Fig. 3.27), in which the dimensionless distance from the cavitation bubble center to the nearest air bubble surface was further increased to 3.020, no jet developed to penetrate the air bubble. The outer size of the air bubble throughout the expansion-collapse life cycle of the cavitation bubble was the smallest among the five experiments, indicating that the air bubble played a considerable role in the buffering of the principal and collapse shock waves but did not experience severe deformation.

In summary, for an air bubble located between a wall and a cavitation bubble, as the cavitation bubble evolves through the expansion-collapse life cycle, the air bubble is subjected to three motions, namely, merging with the cavitation bubble, forming a penetrating jet, and experiencing overall deformation, if the air bubble-cavitation bubble distance is small. For a ω value in the range of 1–1.5, a jet develops to penetrate the air bubble; a decrease in ω leads to a stronger penetrating jet, and vice versa. At $\omega > 1.5$, no jet develops to penetrate the air bubble; the air bubble undergoes a shrinkage-expansion-reshrinkage mode of morphological evolution but does not experience severe surface deformation.

Figure 3.28 shows high-speed images of the interaction between an air bubble, a cavitation bubble of similar size, and a wall obtained from a series of experiments in which the cavitation bubble-wall distance was held constant and the distance between the cavitation bubble center and the air bubble surface was varied. In the series of experiments, the maximum radius of the cavitation bubble $R_{\max}$ was varied in the range of 1.679–2.004 mm; the radius of the air bubble was varied in the range of 0.974–0.975 mm, and the distance between the cavitation bubble center and the wall was kept constant at 3.684 mm. In experiment a (in which the distance from the cavitation bubble center to the nearest air bubble surface was 1.661 mm and the radius of the air bubble was 0.975 mm), the cavitation bubble radiated a principal shock wave in the expansion phase. Under the effect of the principal shock wave, the air bubble experienced shrinkage deformation and its surface near the cavitation bubble center was compressed and concave. When the principal shock wave was strong, the air bubble was penetrated, and a penetrating jet formed, as shown in image a4. As the cavitation bubble further developed, the principal shock wave radiated by the cavitation bubble into the surrounding water weakened, and the jet penetrating the air bubble continued to develop outward. A comparison of images a4–a7 shows that the penetrating jet gradually developed, resulting in an increasing part of the air bubble being penetrated. After the cavitation bubble entered the shrinkage phase (image a7), the length of the penetrating jet continued to increase, but the penetrating jet thinned. Because of the long penetrating jet, the cavitation bubble gradually radiated a collapse shock wave into the surrounding water after entering the collapse phase. Under the effect of the collapse shock wave, the parent air bubble began to undergo shrinkage deformation, as shown by a comparison of images a7 and a8. As the cavitation bubble continued to radiate a collapse shock wave into the surrounding water, the slender penetrating jet gradually detached from the parent air bubble, as shown by the black mass shown in the left part of image a9 (Table 3.2).



Fig. 3.28 Air bubble-cavitation bubble-wall interaction at the same value of γ and different values of ω (frame rate: 19,700 fps; exposure time: 48 us; image size: **a** 12.133 * 7.367 mm; **b**–**f** 13.867 * 7.367 mm; the spatial relationship between the air bubble, cavitation bubble, and wall is shown in Table 3.2)

In experiment b (in which the smallest distance from the cavitation bubble center to the air bubble surface was increased to 1.901 mm), the air bubble also underwent a shrinkage-expansion-reshrinkage mode of deformation and was penetrated by a jet. However, the penetrating jet had a different morphology in experiment b than in experiment b. More specifically, the penetrating jet in experiment b was wider and had a sharper frontal end and larger overall length than those in experiment a, as shown by a comparison of images b6 and a7. After the cavitation bubble entered the collapse phase, the principal shock wave attenuated drastically to a very weak level.

Table 3.2 Parametric settings for experiments of air bubble-cavitation bubble-wall interaction at the same value of γ and different values of ω

	R_{max} (mm)	γ	ε	ω	θ
Experiment a	1.679	2.194	0.581	0.989	189.462
Experiment b	1.842	1.824	0.500	1.032	176.698
Experiment c	2.004	1.784	0.378	1.569	166.349
Experiment d	2.058	1.632	0.447	2.124	193.610
Experiment e	1.950	1.667	0.444	2.543	185.870
Experiment f	2.004	1.703	0.486	2.645	205.016

At that moment, the frontal section of the jet penetrating the air bubble detached from the parent air bubble, as shown in image b7. As the cavitation bubble further collapsed, the intensity of the collapse shock wave increased. At this moment, the air bubble experienced more drastic deformation, as shown in image b8.

In experiment c (in which the smallest distance from the cavitation bubble center to the air bubble surface was further increased to 3.144 mm), the air bubble shrank, expanded, and reshrank under the effect of the principal shock wave of the cavitation bubble, and a penetrating jet developed. However, compared with experiments a and b, the penetrating jet in experiment c was much shorter and thinner, as shown by a comparison of images c4 and c5 with the images for the corresponding moments in the previous two experiments. In addition, the penetrating jet was slenderer. When the cavitation bubble developed to the maximum volume (c6), the penetrating jet detached from the parent air bubble to form separate small bubbles. In the later collapse phase of the cavitation bubble, the air bubble experienced larger deformation in experiment c. However, the color of the severely deformed air bubble in experiment c was darker than those in experiments a and b at the corresponding moment. For an air bubble that has experienced severe deformation and energetic motion, a dark color indicates that minimal liquid is present inside the air bubble, whereas a light color indicates that there is a large amount of liquid inside the air bubble. Based on this criterion, in experiment c, the air bubble experienced severe deformation, but its surface was not severely concave, and there was not a large amount of liquid inside it.

In experiments d, e, and f, the smallest distances from the cavitation bubble center to the bubble surface were further increased to 4.371, 4.959, and 5.301 mm, respectively. At these smallest distances from the cavitation bubble center to the air bubble surface, the air bubble experienced a shrinkage-expansion-reshrinkage mode of deformation throughout the expansion-collapse life cycle of the cavitation bubble, but no penetrating jet developed. In the expansion phase of the cavitation bubble, the air bubble surface was concave on the cavitation bubble side, which was mainly due to the expansion shock wave. In the final collapse phase of the cavitation bubble, the air bubble surface was concave to different degrees on the side away from the cavitation bubble, and the volume of the air bubble shrank. As analyzed in the previous chapters, this result is due to the strong collapse shock wave radiated by the cavitation

bubble into the surrounding water in the final phase of collapse. The concave surface of the air bubble on the side near the cavitation bubble in the early phase and on the side away from the cavitation bubble in the later phase served to greatly buffer the principal and collapse shock waves of the cavitation bubble.

To summarize the above analyses, in the series of experiments on the interaction between a cavitation bubble and an air bubble of similar sizes near a wall with the distance from the cavitation bubble center to the wall held constant and the smallest distance from the cavitation bubble center to the air bubble surface varied, at smaller cavitation bubble-air bubble distances, the air bubble experienced larger deformation, a more energetic jet developed to penetrate the air bubble, and the penetrating jet ultimately detached from the parent air bubble. As the distance between the cavitation bubble center and air bubble surface increased, the penetrating jet gradually weakened, or no penetrating jet developed; the air bubble surface was concave on the side near the cavitation bubble in the expansion phase of the cavitation bubble and was concave on the side away from the cavitation bubble in the collapse phase of the cavitation bubble.

In the following, we investigate the effect of the size of an air bubble relative to that of a cavitation bubble on the collapse characteristics of a cavitation bubble near a wall. Figure 3.29 shows high-speed images of air bubble-cavitation bubble-wall interactions obtained from a series of experiments, in which the distance between the cavitation bubble center and the wall and the same size of the cavitation bubble were held constant and the size of the air bubble was varied. In the series of experiments, the maximum radius of the air bubble $R_{\max}$ was varied in the range of 1.950–2.600 mm, the dimensionless distance from the cavitation bubble center to the wall was varied in the range of 2.068–2.792, and the dimensionless radius of the air bubble was varied in the range of 0–0.545. In experiment a, a cavitation bubble was allowed to interact with a wall in the absence of an air bubble. This experimental setting simulated the extreme scenario of a cavitation bubble interacting with an air bubble of a very small radius near a wall. The radius of the air bubble was gradually increased from experiment b and f. In experiment b (in which the dimensionless radius of the air bubble was 0.295), the cavitation bubble after its inception radiated a principal shock wave into the surrounding water. Under the effect of the principal shock wave, the air bubble was compressed and deformed, as shown in image b3. While the air bubble was being further subjected to the effect of the principal shock wave, a jet developed to penetrate the air bubble. As shown in image b4, as the effect of the principal shock wave weakened, the penetrating jet developed further and finally reached the wall, at which time the air bubble exhibited a spherical outer profile, as shown in images b1–b6. After the cavitation bubble entered the later collapse phase, the air bubble was elongated under the effect of the refilling flow. However, owing to the collapse shock wave radiated by the cavitation bubble into the surrounding water, the air bubble exhibited a slenderer overall morphology in this final phase than in the previous phases. As discussed in the previous section, the wall has an adsorbing effect on the jet penetrating the air bubble. Thus, in the later collapse phase of the cavitation bubble, the air bubble was elongated, while the penetrating jet was

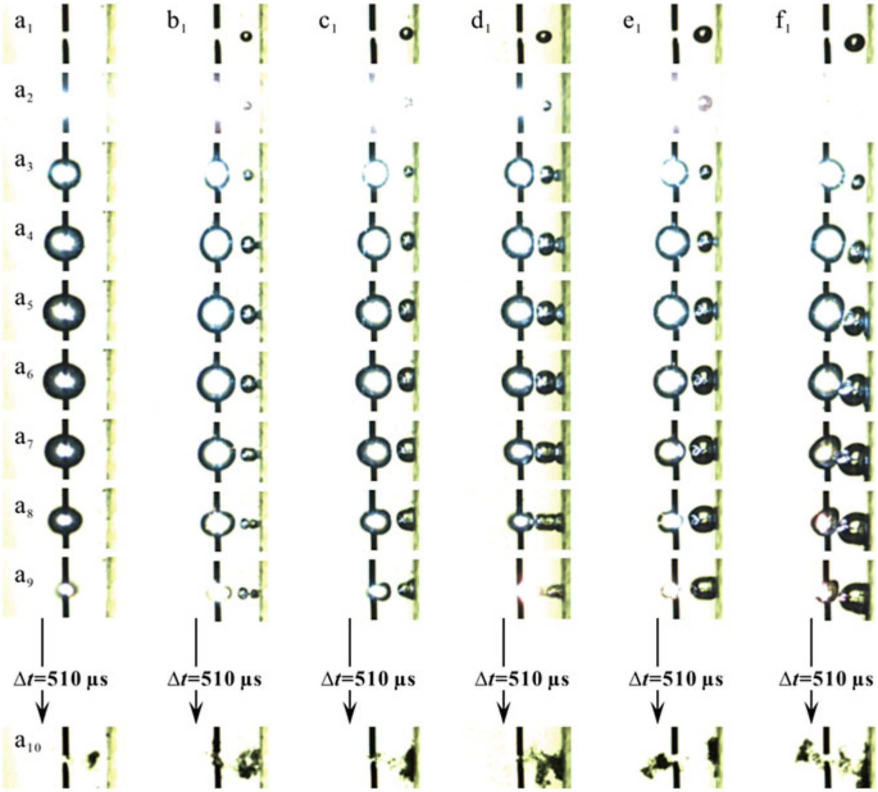


Fig. 3.29 Air bubble-cavitation bubble-wall interaction at different air bubble sizes ($-90° < \theta < 90°$; frame rate: 19,700 fps; exposure time: 48 us; image size: 13.867 * 7.367 mm; the parametric settings for the experiments are shown in Table 3.3)

being adsorbed on the wall, thereby detaching the penetrating jet from the parent air bubble, as shown in image b9.

In experiment c, the volume of the air bubble was further increased, with its dimensionless radius increased to 0.400. After its inception, the cavitation bubble radiated a shock wave into the surrounding water. The air bubble was compressed and shrank because of the principal shock wave, as shown in image c3. As the principal shock wave weakened, the volume of the air bubble increased. Owing to the small air bubble-wall distance, the air bubble was compressed flat by the principal shock wave. After the cavitation bubble entered the collapse phase, the space freed by the volumetric shrinkage of the cavitation bubble was quickly refilled by the surrounding water. The air bubble was elongated by the effect of the rapid refilling flow while being adsorbed on the wall, resulting in a conical morphology of the air bubble, as shown in images c8 and c9. In experiment d (in which the radius of the air bubble was further increased), owing to the small air bubble-cavitation bubble distance, not only was the air bubble compressed under the effect of the principal shock wave

of the cavitation bubble, but a penetrating jet also developed and reached the wall. As the cavitation bubble expanded further, the penetrating jet developed further. However, the development of the penetration was blocked by the wall, resulting in the frontal part of the penetrating jet spread onto the wall, while the parent air bubble still maintained a spherical morphology. As the cavitation bubble collapsed, the air bubble was elongated, and the penetrating jet was adsorbed to the wall, resulting in the air bubble elongating into a cylindrical structure.

In experiments e and f (in which the radius of the air bubble was further increased), the air bubble was compressed under the effect of the principal shock wave of the cavitation bubble, a penetrating jet developed, and the penetrating jet spread onto the wall after being blocked by the wall. Compared with the previous experiments, the air bubble was elongated in the later collapse phase of the cavitation bubble in experiments e and f but to markedly lower degrees. After the cavitation bubble collapsed, rebound bubbles emerged under the effect of the surrounding high-turbulence water flow, and the development of the rebound bubbles was affected by the continuously deformed air bubble. In experiments a–d, the residual of the collapsed cavitation bubble moved toward the wall, whereas in experiments e and f, the residual moved into the surrounding water. This is mainly due to the following mechanism: With the distance from the center of a cavitation bubble center to a wall held constant (that is, with the effect of the wall on the cavitation bubble held constant), a smaller air bubble has a weaker effect on the cavitation bubble, resulting in the cavitation bubble moving toward the wall. A larger air bubble has a larger buffering effect on a cavitation bubble, resulting in the cavitation bubble moving into the surrounding water. Therefore, with the size of the cavitation bubble and the distance from the cavitation bubble enter to the wall held constant, there exists a critical value of the radius of the air bubble. An air bubble with a radius larger than the critical value not only can buffer the shock wave radiated by the cavitation bubble toward the wall but can also change the direction of collapse of the cavitation bubble, thereby having two effects that protect the wall. An air bubble with a radius smaller than the critical value only has the effect of buffering the shock wave of the cavitation bubble.

In summary, with the size of the cavitation bubble and the cavitation bubble-wall distance held constant, the air bubble was compressed, and a penetrating jet developed and was elongated under the effect of the principal shock wave of the cavitation bubble. When the penetrating jet reached the wall, the wall had a strong adsorbing effect on the penetrating jet. In the later collapse phase of the cavitation bubble, not only did the part of the air bubble absorbed on the wall buffer the refilling flow between the wall and cavitation bubble but the air bubble also had a strong buffering effect on the collapse shock wave radiated by the cavitation bubble. A larger air bubble not only had a buffering effect on the shock wave radiated by the cavitation bubble but also caused the cavitation bubble to ultimately collapse away from the wall into the surrounding water, thereby preventing the microjet from impacting the wall and protecting the wall (Table 3.3).

Figure 3.30 shows high-speed images of air bubble-cavitation bubble-wall interactions obtained from a series of five experiments, in which the cavitation bubble center-wall distance and the size of the cavitation bubble were held constant and the

Table 3.3 Parametric settings for the experiments on the air bubble-cavitation bubble-wall interaction at the same values of R_{max} and γ and different values of ε

	R_{max} (mm)	γ	ε	δ	θ
Experiment a	2.600	2.792	0	–	–
Experiment b	2.383	2.227	0.295	1.252	2.526
Experiment c	2.167	2.225	0.400	1.377	2.420
Experiment d	1.950	2.667	0.500	1.087	4.014
Experiment e	2.275	2.452	0.525	1.214	0.796
Experiment f	2.383	2.068	0.545	0.885	17.571

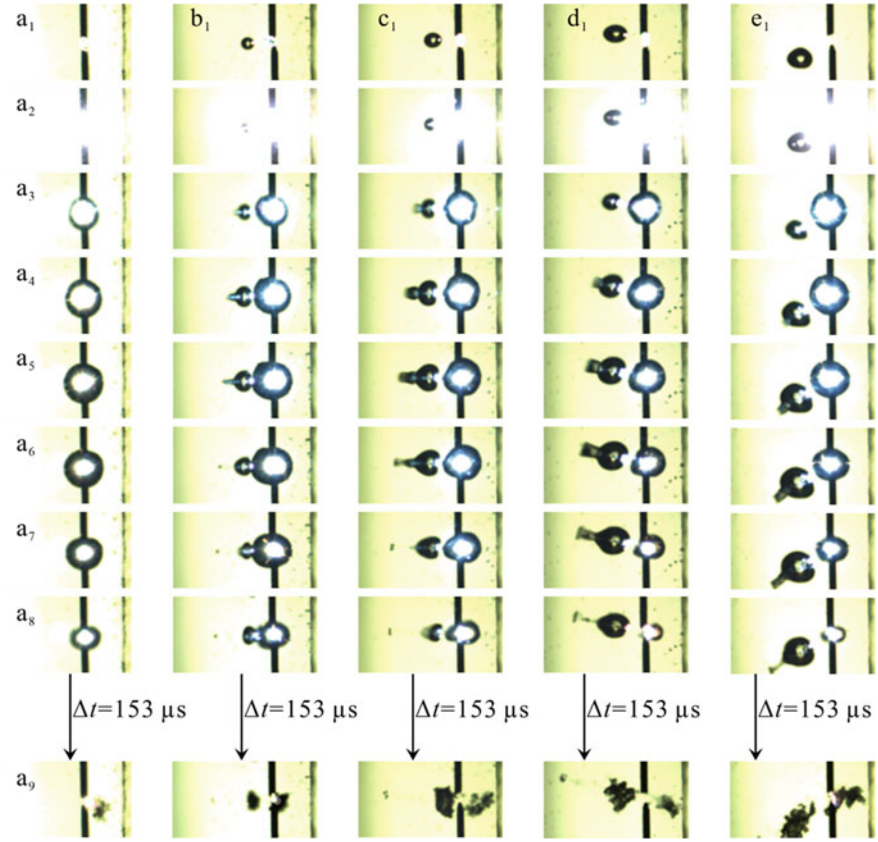


Fig. 3.30 Air bubble-cavitation bubble-wall interaction at different air bubble sizes (90° < θ < 270°; frame rate: 19,700 fps; exposure time: 48 us; image size: **a** 12.133 * 7.367 mm; **b–e** 13.867 * 7.367 mm; air bubble-cavitation bubble-wall spatial relationship is shown in Table 3.4)

size of the air bubble was varied. In experiment a, the cavitation bubble was allowed to interact with the wall in the absence of an air bubble. This experiment setting simulated the extreme scenario of a cavitation bubble interacting with an air bubble with a radius of 0 near a wall. In the experiments, the radius of the cavitation bubble was varied in the range of 1.786–2.004 mm; the radius of the air bubble was varied in the range of 0–1.246 mm; the distance from the cavitation bubble center to the wall was kept constant at approximately 3.5 mm. In experiment a, the dimensionless vertical distance from the cavitation bubble center to the wall γ_{bw} was 1.972. As discussed above, the cavitation bubble collapses toward the wall under this condition. In the experiment, the cavitation bubble did collapse toward the wall, as shown in image a9.

In experiment b, the cavitation bubble interacted with an air bubble with a radius of 0.650 mm on the left side. In the expansion phase of the cavitation bubble, not only did the overall volume of the air bubble shrink under the effect of the principal shock wave of the cavitation bubble, but the air bubble surface was also penetrated, compressed, and forced into a concave shape by the principal shock wave on the side near the cavitation bubble. Under the continuous effect of the principal shock wave, the concave surface gradually developed into a jet to penetrate the surface on the opposite side, as shown in image b4. As the cavitation bubble expanded further, the penetrating jet developed further, and the left part of the jet became slender, as shown in image b5. As the cavitation bubble expanded to the maximum volume and entered the collapse phase, the space freed by the volumetric shrinkage of the cavitation bubble was quickly refilled by the surrounding water, generating an energetic refilling flow. Under the effect of the refilling flow, the frontal section of the penetrating jet gradually detached from the parent air bubble, forming a separate small bubble, as shown in image b6. The part of the air bubble near the cavitation bubble was elongated and deformed by the refilling flow between the cavitation bubble and air bubble, and the air bubble as a whole was elongated and deformed. As the cavitation bubble rapidly collapsed, it radiated a collapse shock wave into the surrounding water. The volume of the elongated air bubble further shrank because of the effect of the collapse shock wave. During this course, the air bubble had an active effect of buffering the collapse shock wave. In the later collapse phase, the cavitation bubble also collapsed toward the wall.

In experiment c, the radius of the air bubble was 0.866 mm, larger than that in experiment b. Compared with experiment b, the air bubble also experienced a shrinkage-expansion-reshrinkage mode of evolution, and a penetrating jet developed. However, the penetrating jet was wider and emerged later in experiment c than in experiment b, as shown in image c7. In the later collapse phase, the cavitation bubble also collapsed toward the wall.

In experiment d, the radius of the air bubble increased to 1.191 mm, larger than those in experiments b and c. Compared with experiments b and c, the air bubble also experienced a shrinkage-expansion-reshrinkage mode of evolution, and a penetrating jet developed. However, the penetrating jet was wider than that in experiments b and c and emerged later than in experiment c. In the later collapse phase, the cavitation bubble also collapsed toward the wall. In experiment e, the radius of the air

Table 3.4 Parametric settings for experiments on air bubble-cavitation bubble-wall interaction at the same value of γ but different values of ε

	R_{max} (mm)	γ	ε	δ	θ
Experiment a	1.950	1.972	0		
Experiment b	2.058	1.816	0.316	0.819	176.009
Experiment c	1.896	1.742	0.457	1.000	178.877
Experiment d	1.786	1.939	0.667	0.992	170.538
Experiment e	2.004	1.838	0.622	1.066	215.218

bubble was increased to 1.246 mm, larger than that in experiments b–d. Compared with experiments b–d, the air bubble in experiment e also experienced a shrinkage-expansion-reshrinkage mode of evolution, and a penetrating jet developed. However, the penetrating jet was slenderer in experiment e than in experiment d. This is mainly due to the following mechanism: The distance from the cavitation bubble center to the air bubble surface was 2.136 mm in experiment e and 1.771 mm in experiment d. Because the shock wave rapidly attenuates in the direction of radiation, an air bubble farther from a cavitation bubble receives less energy. Thus, the penetrating jet was weaker in experiment e than in experiment d. In addition, the penetrating jet emerged later in experiment e than in experiment d. In the later collapse phase, the cavitation bubble collapsed toward the wall, but the motion of the residual of the collapse toward the wall weakened (Table 3.4).

In the following, we investigate the effect of the cavitation bubble-wall distance on the collapse characteristics of a cavitation bubble near a wall.

Figure 3.31 shows high-speed images of the cavitation bubble-air bubble-wall interaction obtained from a series of experiments, in which the cavitation bubble-wall distance was varied. In the five experiments, the maximum radius of the cavitation bubble R_{max} was varied in the range of 1.842–2.383 mm, ε was varied in a small range, and the value of γ_{bw} was gradually increased from experiments a to d. In experiment a, a cavitation bubble emerged immediately after the electric discharge between the electrodes. At this moment, the cavitation bubble radiated a principal shock wave into the surrounding water. Because of the small cavitation bubble-wall distance, the wall had a large effect on the cavitation bubble. Meanwhile, the air bubble (which was located between the cavitation bubble and wall) underwent shrinkage deformation under the effect of the principal shock wave of the cavitation bubble, as shown in images a2–a4. At the moment shown in image a4, the cavitation bubble expanded to the maximum volume, and a jet emerged to penetrate the air bubble. While being penetrated by the principal shock wave of the cavitation bubble, the air bubble reached the wall and, under the effect of the cavitation bubble, spread over the wall, as shown in images a5 and a6. For the morphological evolution of the cavitation bubble in experiment a (in which the air bubble was located between the cavitation bubble and wall), when the cavitation bubble radiated a principal shock wave into the surrounding water, the air bubble was compressed, and the volume of water between the wall and cavitation bubble moved toward the wall, and the

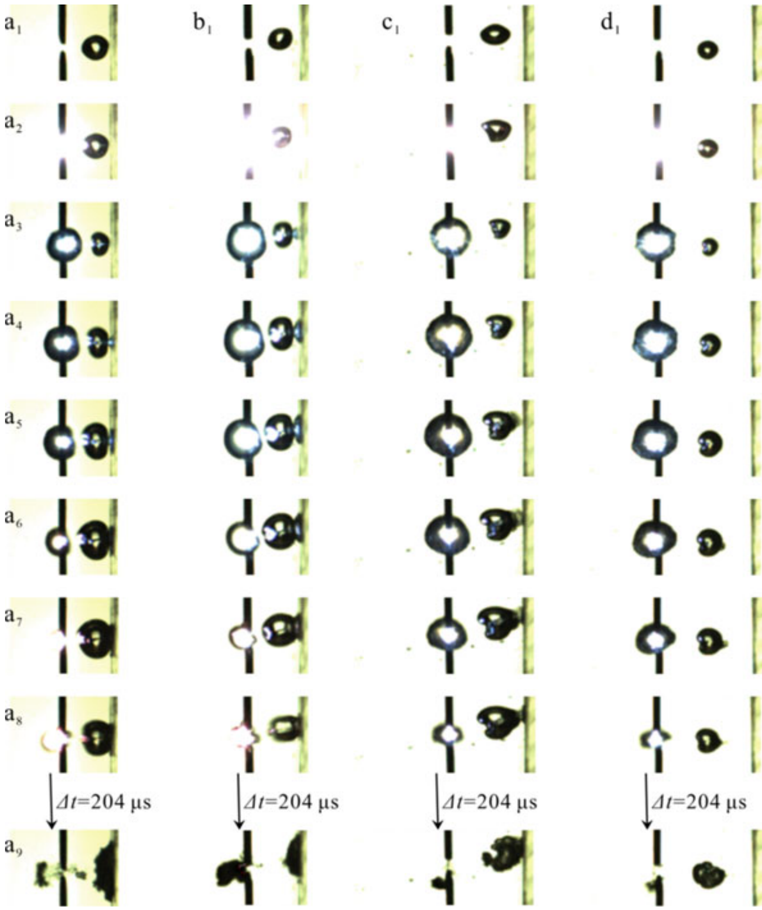


Fig. 3.31 Cavitation bubble-air bubble-wall interaction at different cavitation bubble-wall distances (−90° < θ < 90°; frame rate: 19,700 fps; exposure time: 48 us; image size: **a** 10.400 * 7.367 mm; **b** 13.867 * 7.367 mm; **c** 17.333 * 7.367 mm; **d** 17.333 * 7.367 mm; **e** 17.333 * 7.367 mm: positional relationship between the cavitation bubble, air bubble, and wall is shown in Table 3.5)

cavitation bubble surface became flat on the air bubble side. This result is due to the following mechanism: The air bubble is compressed, and the volume of liquid between the cavitation bubble and air bubble and the air bubble itself are subjected to the blocking effect of the wall. Under the effect of the high-pressure medium, the cavitation bubble evolves into an irregular spherical morphology, as shown in image a5. The cavitation bubble continues to have this irregular morphology up to the later collapse phase of the cavitation bubble. At the moment shown in image a5, the cavitation bubble entered the shrinkage phase. From a5–a8, the cavitation bubble was in the collapse phase, when the air bubble was elongated under the effect of the refilling flow. In addition, subjected to the wall's adsorbing effect, the

air bubble continued to expand in the later collapse phase of the cavitation bubble up to the moment when the cavitation bubble had evolved through the complete expansion-collapse life cycle.

In experiment b, in which the dimensionless cavitation bubble-wall distance was increased to 2.771 (from 2.256 in experiment a), the air bubble also shrank and a penetrating jet developed under the effect of the principal shock wave of the cavitation bubble. When the air bubble was completely penetrated, the penetrating jet quickly reached the wall, as shown in image b3. In the expansion phase of the cavitation bubble, subjected to the blocking effect of the wall after reaching the wall, the penetrating jet immediately spread over the wall and evolved into a conical morphology, as shown in images b4–b6. As the cavitation bubble developed further and entered the collapse phase, as shown in image b5, the main body of the air bubble was elongated continuously by the refilling flow and evolved into a morphology where the width of the main body of the air bubble was smaller than that of the penetrating jet, as shown in images b7 and b8. In experiment c (in which the distance from the cavitation bubble center to the wall was further increased), when the cavitation bubble expanded to the maximum volume, a jet developed to penetrate the air bubble, but the penetrating jet had a much lower intensity than that in experiments a and b. In the collapse phase of the cavitation bubble, the air bubble was elongated by the effect of the refilling flow, and its outer size gradually increased, as shown in images c3–c8. In the final collapse phase, the cavitation bubble radiated a strong shock wave into the surrounding water. Under the effect of the collapse shock wave, the air bubble began to undergo shrinkage deformation. Meanwhile, the penetrating jet reached the wall and, under the adsorbing effect of the wall, was elongated but did not completely detach from the wall. In experiment e (in which the distance from the cavitation bubble center to the wall was increased to 3.773), the cavitation bubble was subjected to a weak effect of the wall, and the interaction between the air bubble, cavitation bubble, and wall was similar to the interaction between an air bubble and cavitation bubble in the absence of a wall. In the experiment, a jet developed to penetrate the air bubble, but the penetrating jet did not reach the wall. The air bubble also experienced a shrinkage-expansion-reshrinkage mode of evolution. However, owing to the large dimensionless distance from the cavitation bubble center to the nearest air bubble surface, the air bubble had a regular profile in the final collapse phase of the cavitation bubble. When the cavitation bubble-wall distance was increased to four times that of the maximum radius of the cavitation bubble $R_{\max}$, the air bubble adhered to the wall and, under the effect of the principal shock wave and collapse shock wave of the cavitation bubble, only experienced shrinkage-expansion-reshrinkage deformation. In addition, the air bubble shrank to the minimum volume in the final collapse phase of the cavitation bubble.

In summary, as the dimensionless distance from the cavitation bubble center to the wall γ_{bw} decreased, the effect of the wall on the expansion-shrinkage life cycle of the cavitation bubble increased. Under the combined effect of the wall and air bubble, the cavitation bubble surface on the air bubble side was blocked by the unbalanced pressure gradient around the wall, and the air bubble gradually exhibited nonspherical expansion. Under the effect of the principal and collapse shock waves

Table 3.5 Parametric settings for experiments of air bubble-cavitation bubble-wall interaction at different values of γ

	R_{max} (mm)	γ	ε	ω	θ
Experiment a	1.842	2.256	0.676	1.118	0
Experiment b	2.004	2.771	0.622	1.080	8.820
Experiment c	2.383	3.5	0.614	1.318	8.797
Experiment d	2.275	3.773	0.452	1.794	4.865

of the cavitation bubble, the air bubble exhibited a shrinkage-expansion-reshrinkage mode of morphological evolution. In addition, at a small air bubble-cavitation bubble distance, a jet developed to penetrate the air bubble under the effect of the principal shock wave, and the wall had an adsorbing effect on the penetrating jet (Table 3.5).

Figure 3.32 shows high-speed images of the air bubble-cavitation bubble-wall interactions obtained from a series of experiments with different distances between the cavitation bubble center and wall. In experiment d, a cavitation bubble was allowed to interact with an air bubble in the absence of a wall. This parametric setting simulated the air bubble-cavitation bubble-wall interactions at a very large cavitation bubble-wall distance. As the cavitation bubble-wall distance increases, the effect of a wall on the expansion-collapse characteristics and direction of collapse of a cavitation bubble gradually weakens. At $\gamma > 3$, the effect of the wall on the cavitation bubble basically disappears. In the series of experiments, the maximum radius of the cavitation bubble R_{max} was varied in the range of 1.896–2.438 mm; the distances from the cavitation bubble center to the wall for experiments a–c were

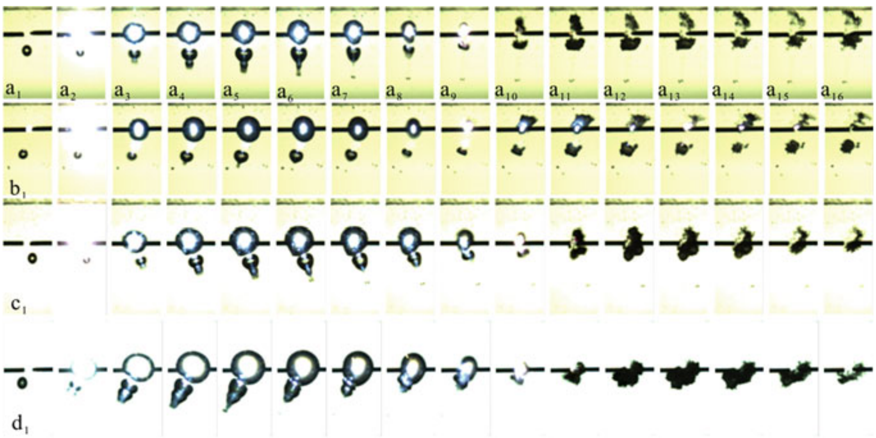


Fig. 3.32 Cavitation bubble-air bubble-wall interaction at different cavitation bubble-wall distances (90° < θ < 270°; frame rate: 19,700 fps; exposure time: 48 us; image size: **a** 13.867 * 7.367 mm; **b** 13.867 * 7.367 mm; **c** 17.333 * 7.367 mm; **d** 17.333 * 7.367 mm; the air bubble-cavitation bubble-wall spatial relationship is shown in Table 3.6)

3.305, 3.521, and 5.418 mm, respectively. Experiment d can be considered to use a cavitation bubble-wall distance of ∞.

In experiments a and b, the distance between the cavitation bubble center and wall was set at two small values with a small difference between them. During the whole expansion-collapse life cycle of the cavitation bubble and the evolution of the rebound bubbles, the air bubble exhibited a shrinkage-expansion-reshrinkage mode of deformation. The cavitation bubble radiated a principal shock wave into the surrounding water in its expansion phase. Under the effect of the principal shock wave, a jet developed to penetrate the air bubble, and a part of the penetrating jet detached from the air bubble, as shown by the images for experiment a. In addition, the penetrating jet developed to a greater length and width in experiment a than in experiment b. The different penetrating jets were mainly caused by the different cavitation bubble-air bubble distances. However, the air bubble exhibited similar modes of morphological evolution. In the two experiments, after the cavitation bubble entered the collapse phase, the space freed by the volumetric shrinkage of the cavitation bubble was quickly refilled by the surrounding water. Under the effect of the refilling flow, the air bubble with the penetrating jet experienced volumetric shrinkage, while the penetrating jet moved toward the cavitation bubble center, as shown in images a7, a8, b7, and b8. In experiments a and b, because distance between the cavitation bubble center and the wall in experiment a was smaller than that in experiment b, the rebound bubbles emerged in the rebound phase of the cavitation bubble and moved toward the wall more quickly in experiment a than in experiment b, as shown in images a10–a16 and b10–b16.

In experiment c, the air bubble experienced morphological evolution similar to that in experiments a and b. More specifically, the air bubble also underwent a shrinkage-expansion-reshrinkage mode of evolution and was also penetrated by a jet to form separate bubbles. In experiment c, in which the dimensionless distance from the cavitation bubble center to the wall γ_{bw} was 2.500, the cavitation bubble was still in the range of influence of the wall. However, owing to the presence of the air bubble, the evolution of the cavitation bubble was mainly influenced by the air bubble. The residual of the collapsed cavitation bubble showed the potential to move toward the wall in the later collapse phase. However, owing to the very small distance and weak energy of the motion, the residual of the collapsed cavitation bubble did not move toward the wall in the later collapse phase. As shown by the above experiments, as the distance from the cavitation bubble center to the wall was gradually increased, the effect of the wall on the cavitation bubble gradually weakened, and the velocity at which the residual of the collapsed cavitation bubble moved toward the wall gradually decreased (Table 3.6).

Table 3.6 Parametric settings for experiments of air bubble-cavitation bubble-wall interaction at different values of γ

	R_{max} (mm)	γ	ε	ω	θ
Experiment a	1.896	1.743	0.486	1.000	178.898
Experiment b	2.004	1.757	0.351	1.569	166.159
Experiment c	2.167	2.500	0.375	0.906	197.021
Experiment d	2.438	∞	0.378	0.621	159.146

3.3.3 Combined Direction-Changing Effects of a Wall and an Air Bubble on the Collapse of a Cavitation Bubble

A cavitation bubble interacting with an air bubble and a wall is subjected simultaneously to two effects: (1) the effect of the wall on attracting the collapse of the cavitation bubble and (2) the effect of the air bubble on repelling or attracting the collapse of the cavitation bubble. In this section, we will analyze the interaction between a cavitation bubble, an air bubble, and a wall in two different scenarios of their spatial relationship: (1) the air bubble is located between the cavitation bubble and wall; and (2) the cavitation bubble is located between the air bubble and wall.

Figure 3.33 shows the direction of collapse of a cavitation bubble interacting with an air bubble and a wall obtained from a series of experiments, in which the cavitation bubble was located between the air bubble and wall (image a1 and a2) or the air bubble

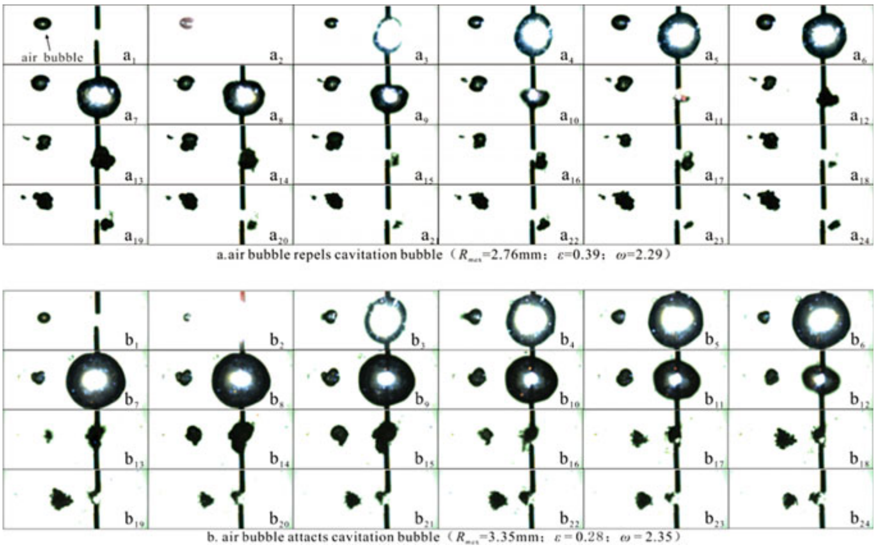


Fig. 3.33 Repelling and attracting effects of an air bubble on a cavitation bubble

was located between the cavitation bubble and wall (a3 and a4). As shown by the experimental results presented in the figure, the cavitation bubble moved away from the air bubble due to the repelling effect of the air bubble, while the wall had an attracting effect on the evolving cavitation bubble. Under the combined effect of these two different forces, the cavitation bubble finally collapsed in the direction of the combined vector of the two forces. Images b1 and b2 show the results of the experiment in which the cavitation bubble was located between the air bubble and wall. Images b3 and b4 show the results of the experiment in which the air bubble was located between the cavitation bubble and wall. Similar to experiment a (in which the air bubble exerted a repelling force on the cavitation bubble), in experiment b (in which the air bubble exerted an attracting force on the cavitation bubble and the cavitation bubble collapsed near a rigid wall), the final direction of collapse of the cavitation bubble depended on the direction of the combined vector of the two forces.

As shown by significant experimental observations of cavitation bubble-air bubble-wall interaction in which a cavitation bubble was located between an air bubble and a wall or an air bubble was located between a cavitation bubble and a wall, the final direction of collapse of a cavitation bubble depends on the direction of the combined effect of the repelling or attracting force exerted by the air bubble on the cavitation bubble and the attracting force exerted by the wall exerted on the cavitation bubble. In addition, an air bubble more often has a repelling effect on a cavitation bubble than an attracting effect on a cavitation bubble. Understanding the combined effect of an air bubble and wall on a cavitation bubble has important implications for cavitation erosion protection-purposed aeration of high-velocity water flows (Fig. 3.34).

3.4 Retarding Effect of an Air Bubble on the Collapse Shock Wave of a Cavitation Bubble

In this section, we analyze another effect an air bubble has on a cavitation bubble—the retardation of the collapse shock wave of a cavitation bubble.

3.4.1 Retarding Effect of an Air Bubble on the Collapse Shock Wave of a Cavitation Bubble

Before analyzing an air bubble's effect of retarding the collapse shock wave of a cavitation bubble, we investigated the effect of a free surface on the collapse shock wave of a cavitation bubble through a series of experiments (Fig. 3.35).

In experiment a (Fig. 3.35), in which the dimensionless distance from the cavitation bubble to the free surface $\varphi_s = 0.95$, the cavitation bubble completed the first round of oscillations at 0 ms < t < 2.056 ms. During the first round of oscillations,

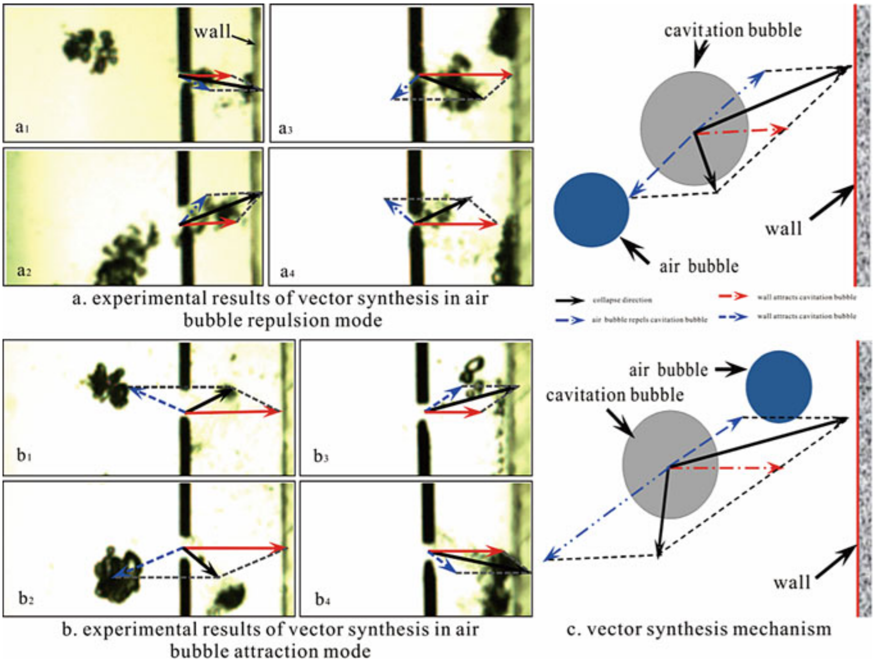


Fig. 3.34 Combined effect of an air bubble and wall on the collapse of a cavitation bubble

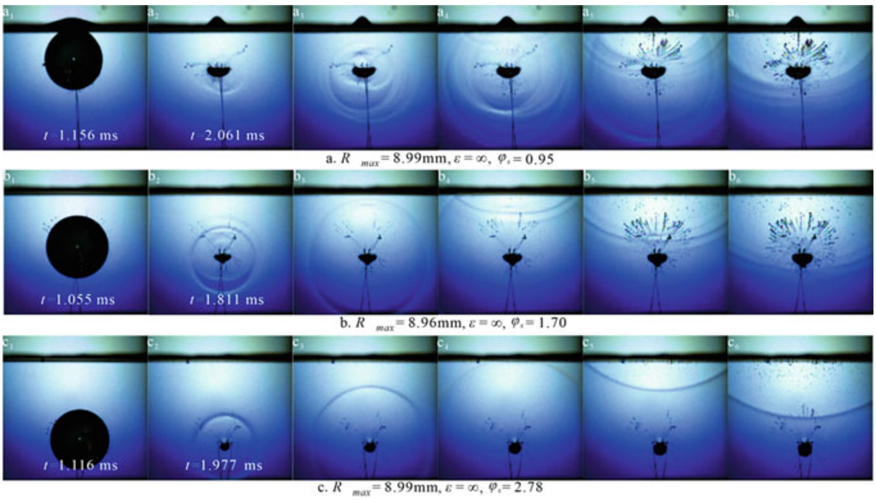


Fig. 3.35 Reflection of a cavitation bubble's shock wave by a free surface

because of the small cavitation bubble-wall distance, the cavitation bubble expanded to occupy part of the free surface's space, causing the free surface to become convex. At this moment, the cavitation bubble no longer had the original regular spherical morphology, as shown in image a1 (Fig. 3.35). When the cavitation bubble shrank to the minimum volume, the free surface remained convex, as shown in image a2 (Fig. 3.35). During the course of collapse, the cavitation bubble radiated a shock wave into the surrounding water. At such a small free surface-cavitation bubble distance, the cavitation bubble's collapse shock wave exhibited a clear multilevel structure, as shown in image a3 (Fig. 3.35). As this dispersed multilevel shock wave propagated outward, it was reflected by the free surface, generating a reflecting wave that propagated into the water, as shown in image a5 (Fig. 3.35). The reflecting wave passed through the cavitation bubble and caused secondary cavitation around the cavitation bubble, as shown in image a6 (Fig. 3.35). In experiment b (Fig. 3.35), the dimensionless distance from the cavitation bubble to the free surface φ_s increased to 1.70. Compared with that of experiment a (Fig. 3.35), the shock wave radiated by the collapse of the cavitation bubble in experiment b also exhibited a clear multilevel structure, as shown in image b2 (Fig. 3.35). However, the degree of dispersion of the shock wave was smaller in experiment b than in experiment a (Fig. 3.35), as shown by a comparison of images a3 and b3 (Fig. 3.35). The dispersed shock wave propagated to the free surface to generate a reflecting wave, which also had a multilevel structure. In experiment c (Fig. 3.35), the dimensionless distance from the cavitation bubble to the free surface φ_s further increased to 2.78. The collapse shock wave of the cavitation bubble in experiment c did not have a multilevel structure and did not have a multilevel structure after being reflected by the free surface.

In the following, we investigate the effect of the air bubble-cavitation bubble distance on a cavitation bubble's collapse shock wave.

Figure 3.36 shows high-speed images of the collapse shock wave of a cavitation bubble obtained from a series of experiments, in which a cavitation bubble was allowed to interact with an air bubble at different air bubble-cavitation bubble dimensionless distances ω in a free field. In experiment a (Fig. 3.36a), a cavitation bubble was allowed to evolve in a free field without an air bubble, thereby enabling a comparison of the shock wave morphological evolution of a cavitation bubble interacting with an air bubble and that of a cavitation bubble not interacting with an air bubble. In Fig. 3.36b–g (for experiments b–g), the black mass shown in the left part of the images is an air bubble.

In experiment a, the cavitation bubble had a maximum radius $R_{\max}$ of 9.83 mm when expanded to the maximum volume and shrank to the minimum volume at $t =$ 2.344 ms. Because the cavitation bubble evolved in a free field, the cavitation bubble did not show a clear direction of collapse during the course of shrinkage, as shown in image a4 (Fig. 3.36). During the course of collapse, the cavitation bubble radiated into the surrounding water a strong shock wave, which rapidly propagated outward. Because the cavitation bubble evolved in a free field (that is, in the absence of any external interferences), the collapse shock wave exhibited a regular spherical spatial morphology.

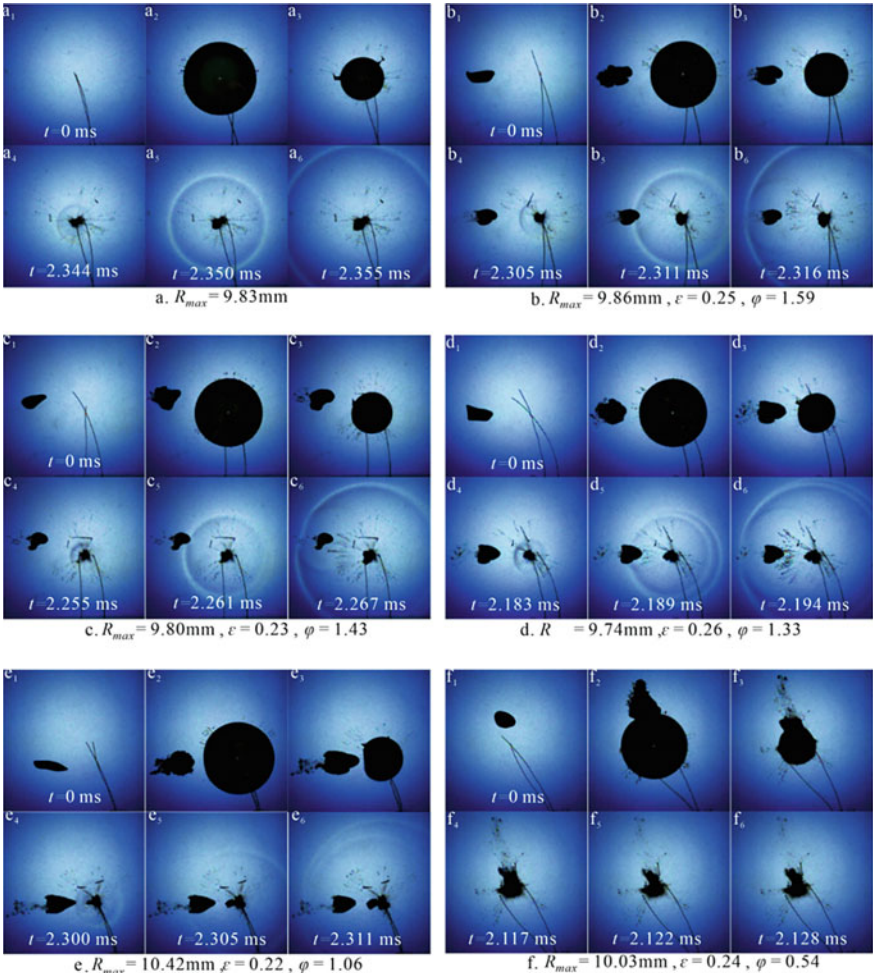


Fig. 3.36 Effect of the air bubble-cavitation bubble distance on the collapse shock wave of a cavitation bubble

In experiment b (Fig. 3.36b), the air bubble-cavitation bubble distance increased to a relatively large value of 1.59. The cavitation bubble completed the first collapse at approximately 2.305 ms and radiated a shock wave at collapse. As shown by the high-speed images, the collapse shock wave had a regular morphology similar to that of the shock wave produced by the collapse of the cavitation bubble in the free field without an air bubble. In experiment b (Fig. 3.36b), when the cavitation bubble's shock wave propagated to the air bubble, a dark-colored wave radiated from the air bubble surface in the reverse direction, as shown in image b6 (Fig. 3.36). After passing through the air bubble, the cavitation bubble's collapse shock wave was lighter in color on the left side of the air bubble than in other areas.

In experiments c–e (Fig. 3.36c–e), the air bubble-cavitation bubble distances were gradually reduced to 1.43, 1.33, and 1.06, respectively. In all three experiments, the cavitation bubble radiated a shock wave into the surrounding water during the course of collapse. Because of the small air bubble-cavitation bubble distances, the shock waves produced by the collapse of the cavitation bubble in these three experiments had different morphologies than that in experiment a (Fig. 3.36). First, the shock wave radiated by the cavitation bubble exhibited a very clear multilevel structure in experiments c–e. As the dispersed waves propagated outward, the interwave distance increased with decreasing dimensionless cavitation bubble-air bubble distance ω, as shown in Fig. 3.36c–e. Second, when the shock waves propagated to the air bubble surface, a clear wave was reflected from the air bubble surface and propagated in the reverse direction, as shown in Fig. 3.36c, d. Finally, when the collapse shock wave of the cavitation bubble passed through the air bubble and continued to propagate, the shock wave considerably deformed in the area shielded by the air bubble, as shown in image c6 (Fig. 3.36), and the degree of deformation gradually decreased with decreasing cavitation bubble-air bubble dimensionless distance (Fig. 3.36d) and finally became unidentifiable (Fig. 3.36e).

In experiment f (Fig. 3.36), in which the cavitation bubble-air bubble distance was further decreased, the cavitation bubble absorbed the air bubble during its course of development, forming a gas-containing cavitation bubble, as shown in image f2 (Fig. 3.36). When the cavitation bubble shrank to the minimum volume, it completely merged with the air bubble, as shown in image f4 (Fig. 3.36). In addition, compared with the results of other experiments (Fig. 3.36), the cavitation bubble shrank to a markedly larger minimum volume in experiment f. Another important phenomenon observed in experiment f was that the cavitation bubble did not radiate a clear shock wave into the surrounding water during its course of collapse.

In the following, we investigate the effect of the air bubble-to-cavitation bubble size ratio on the collapse shock wave of the cavitation bubble.

Figure 3.37 shows high-speed images of the collapse shock wave of a cavitation bubble obtained from a series of experiments in which cavitation bubbles were allowed to interact with air bubbles of different dimensionless sizes ε in a free field. In the experiments, the radius of the air bubble R_a was varied in the range of 1.30–2.71 mm, and the air bubble-cavitation bubble dimensionless distance was kept constant at approximately 1.30. The black mass shown in the left part of images a1–e1 (Fig. 3.37) is an air bubble.

In experiment a (Fig. 3.37a), in which the air bubble had a very small volume, the air bubble did not have a considerable effect on the morphology of the cavitation bubble throughout its expansion-shrinkage life cycle, as shown in images a2 and a3 (Fig. 3.37). During the course of the cavitation bubble's evolution, the air bubble was compressed, elongated, and split. During the course of collapse, the cavitation bubble radiated a shock wave into the surrounding water that had a spherical morphology similar to that in experiment a. However, compared that in with experiment a, a markedly different phenomenon was observed in experiment b: The shock wave produced by the collapse of the cavitation bubble propagated to the back side of the air bubble and experienced considerable deformation there, as shown in

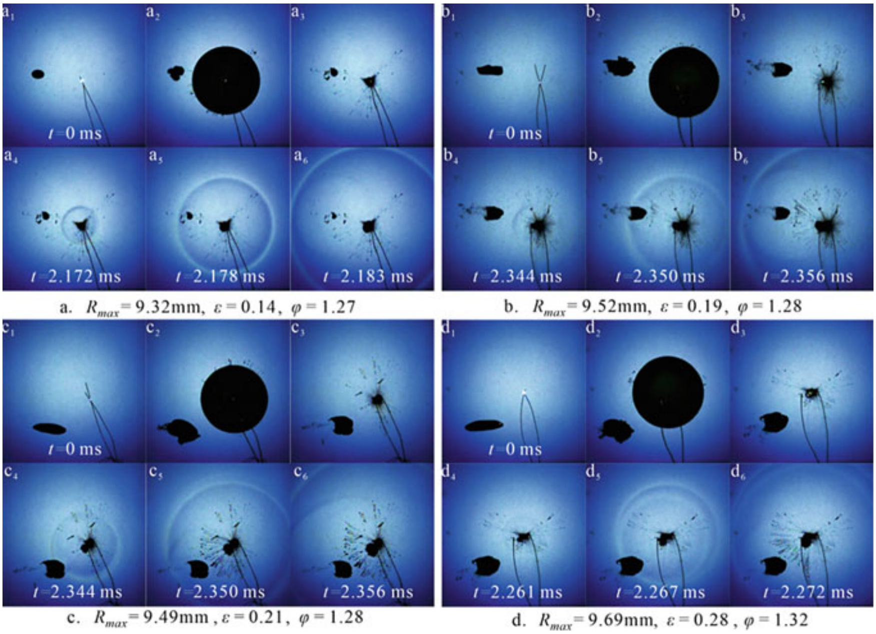


Fig. 3.37 Effect of the air bubble size on the collapse shock wave of a cavitation bubble

image b6 (Fig. 3.37). In both experiments a and b (Fig. 3.37), the evolution of the cavitation bubble was influenced by the air bubble, but the shock wave produced by the cavitation bubble did not have a clear multilevel structure.

In experiment c (Fig. 3.37), the relative size of the air bubble ε was further increased to 0.21. Similar to experiments a and b, the cavitation bubble did not experience considerable deformation throughout its expansion-shrinkage life cycle and did not show considerable movement toward the air bubble in the collapse phase. However, the cavitation bubble in experiment c produced a markedly different collapse shock wave than those in experiments a and b. In experiment c (Fig. 3.37), the shock wave radiated by the cavitation bubble during the course of collapse exhibited a degree of dispersion, as shown in image c4 (Fig. 3.37), and experienced deformation in the spatial morphology in the area shielded by the air bubble, as shown in image c5 (Fig. 3.37).

Finally, in experiment d (Fig. 3.37), the radius of the air bubble R_a was increased to approximately 2.72 mm. Throughout its expansion-shrinkage life cycle, the cavitation bubble did not experience deformation under the effect of the air bubble, as shown in images d2 and d3 (Fig. 3.37). In experiment d, the shock wave radiated by the collapse of the cavitation bubble exhibited a considerable degree of dispersion; in addition, the shock wave was reflected by the air bubble surface to generate a wave that propagated in the reverse direction toward the cavitation bubble center.

3.4.2 Impact Intensity of the Collapse Shock Wave of a Cavitation Bubble Interacting with an Air Bubble Near a Wall

First, we investigate the effect of the air bubble-cavitation bubble distance on the collapse shock wave of a cavitation bubble interacting with an air bubble near a wall.

Figure 3.38 shows high-speed images of the collapse shock waves of cavitation bubbles obtained from a series of experiments, in which a cavitation bubble was allowed to interact with an air bubble at different air bubble-cavitation bubble distances ω near a wall. In experiment a (Fig. 3.38a), a cavitation bubble was allowed to evolve near a wall without interacting with an air bubble, thereby enabling a

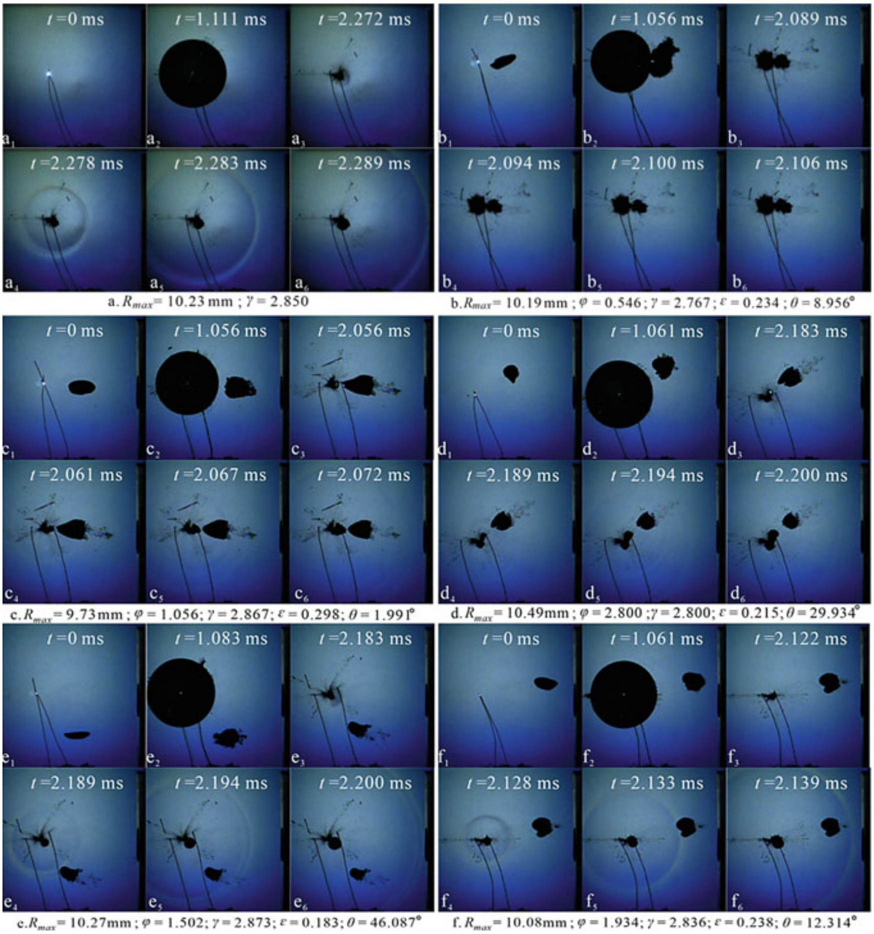


Fig. 3.38 Shock wave of a cavitation bubble interacting with an air bubble at different air bubble-cavitation bubble distances near a wall

comparison of the shock wave of a cavitation bubble interacting with an air bubble near a wall and that of a cavitation bubble evolving near a wall without interacting with an air bubble. In Fig. 3.38b–f, the black mass shown in the middle part of the images is an air bubble (after the inception of a cavitation bubble, the black mass shown in the left part of the images is a cavitation bubble); the boundary on the right side of the images is a rigid wall.

In experiment a (Fig. 3.38), in which the cavitation bubble-wall dimensionless distance γ_{bw} was 2.850, the wall did not interfere with the evolution of the cavitation bubble, and the cavitation bubble did not show any signs of moving toward the wall during the first collapse. The collapse of the cavitation bubble radiated a shock wave with a regular spherical morphology into the surrounding water. The shock wave rapidly propagated outward and reached the wall, exerting a large transient impact on the wall.

In experiment b (Fig. 3.38), in which there was an air bubble between the cavitation bubble and wall and the air bubble-cavitation bubble distance was small, the cavitation bubble was connected with the air bubble in the expansion phase of the cavitation bubble, forming a gas-containing cavitation bubble, as shown in image b4 (Fig. 3.38). The gas-containing cavitation bubble shrank to a minimum volume that was markedly larger than that in experiment a (Fig. 3.38). In addition, the gas-containing cavitation bubble did not radiate a shock wave into the surrounding water, as shown in images b4–b6 (Fig. 3.38).

From experiments c–e (Fig. 3.38), the air bubble-cavitation bubble distance gradually increased. In experiment c (Fig. 3.38), when the cavitation bubble shrank to the minimum volume, the air bubble-cavitation bubble distance became very small, the air bubble experienced considerable deformation, and the part of the bubble near the cavitation bubble center exhibited a conical morphology, as shown in image c3 (Fig. 3.38). At this moment, the cavitation bubble and air bubble were not merged. As the cavitation bubble further evolved, it radiated a shock wave into the surrounding water that exhibited a very clear multilevel structure, as shown in image c5 (Fig. 3.38). The multilevel shock wave propagated outward and ultimately reached the wall. The cavitation bubble exhibited evolution in experiment d (Fig. 3.38) similar to that in experiment c (Fig. 3.38) and radiated a shock wave of a multilevel structure during the course of collapse. In experiment e (Fig. 3.38), the cavitation bubble exhibited morphological evolution basically similar to that in experiment d (Fig. 3.38) and radiated a shock wave with a multilevel structure. What was different among experiments c–e was that as the air bubble-cavitation bubble distance ω increased, the degree of dispersion of the shock wave varied. In experiment c (Fig. 3.38), the shock wave dispersed into three levels, as shown in image c5 (Fig. 3.38); in experiment d, the shock wave dispersed into two levels, as shown in image d5 (Fig. 3.38), and the distance between the two levels was large; in experiment e, the shock wave was dispersed into two levels, but the distance between the two levels was very small, as shown in image e5 (Fig. 3.38).

In experiment f (Fig. 3.38), the air bubble-cavitation bubble distance was large. When the cavitation bubble shrank to the minimum volume, it radiated a shock wave that did not exhibit considerable deformation in the area between the air bubble

and wall and maintained a regular spherical morphology, similar to experiment a (Fig. 3.38).

As shown by the collapse shock waves of cavitation bubbles interacting with air bubbles at different air bubble-cavitation bubble distances, an air bubble has an effect on the dispersion of the collapse shock wave of a cavitation bubble. However, the high-speed images in Fig. 3.38 only show that the shock wave is dispersed but do not show the intensity of the dispersed shock wave. In the experiments, the pressure caused by the shock wave on the wall was measured using a pressure gage buried inside the wall. Figure 3.39 shows the measurements of the shock wave-induced pressure on the wall obtained from the experiments shown in Fig. 3.38.

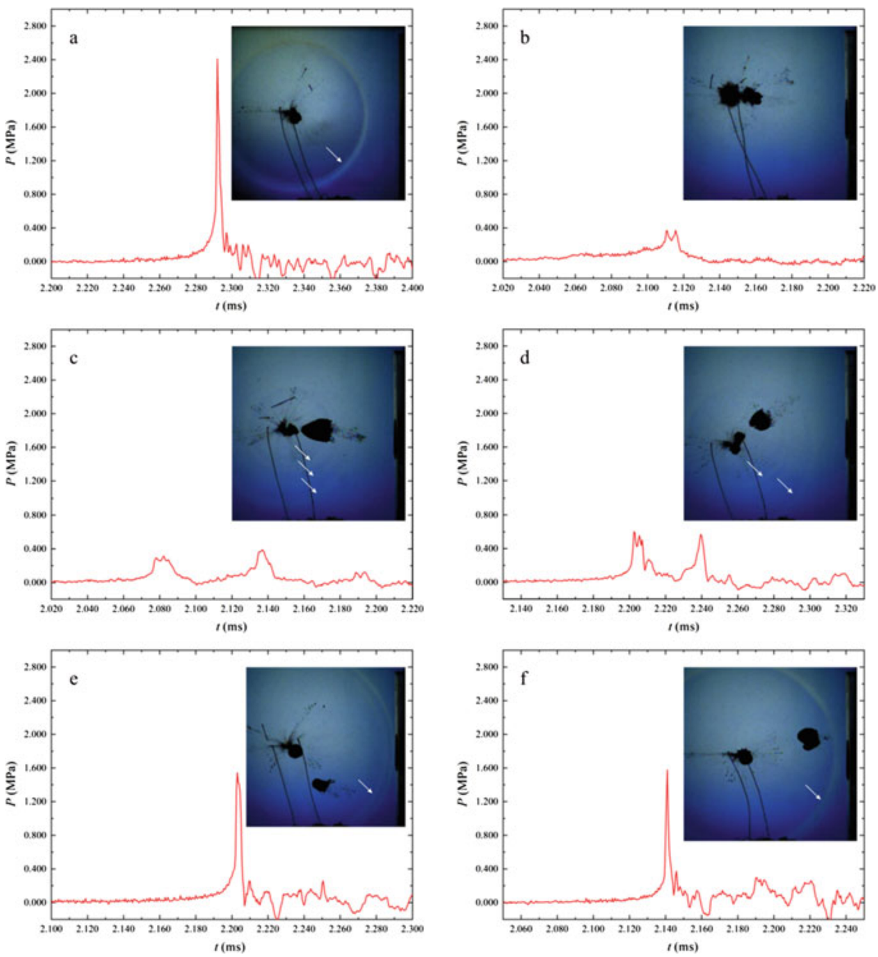


Fig. 3.39 Impact of a cavitation bubble collapse shock wave on a wall at different air bubble-cavitation bubble distances

In experiment a (Fig. 3.39), the temporal variations in the impact of the regular spherical shock wave on the wall in the collapse phase of the cavitation bubble exhibited a single-peak patten, with the peak pressure at 2.930 MPa. In experiment b (Fig. 3.39), the cavitation bubble evolved into a gas-containing cavitation bubble, as shown by the high-speed images above, and shrank to a relatively large minimum volume. In addition, the cavitation bubble did not radiate a shock wave in the collapse phase, as shown by the high-speed images above. However, the measurements of the impact of the cavitation bubble on the wall in the collapse phase of the cavitation bubble showed two small peaks, which were close to each other and measured 0.366 and 0.372 MPa.

In experiment c (Fig. 3.39), the measurements of the impact of the cavitation bubble's collapse shock wave on the wall exhibited three small peaks, which measured 0.309, 0.390, and 0.0119 MPa. These three peaks matched the high-speed images. In experiment d (Fig. 3.39), the cavitation bubble's collapse shock wave was dispersed into two levels, as clearly shown by the high-speed images. The two levels of the wave reached the wall and exerted impact pressures of 0.589 and 0.548 MPa on the wall. In experiment e (Fig. 3.39), in which the air bubble-cavitation bubble distance was large, the cavitation bubble's collapse shock wave exhibited a two-level structure. However, the distance between the two levels was small, and the measurements of their impact on the wall exhibited only one major peak (1.54 MPa). The presence of a second peak following this major peak could be confirmed from the high-speed images. However, owing to the limited frame rate of the high-speed images, the exact value of the second peak was difficult to identify. Because the distance between the two peaks was very small, we were able to estimate that the intensity of impact of the second wave on the wall was approximately 0.257 MPa. In addition, for the duration of the impact of a dispersed shock wave on the wall, the presence of an air bubble led to a slight increase in the duration of impact, as shown in Fig. 3.39b–d.

In experiment f (Fig. 3.39), the high-speed images showed that the shock wave radiated by the cavitation bubble in the collapse phase was similar to that in experiment a (Fig. 3.38). The shock wave did not have a clear stratified structure. The shock wave reached the wall and exerted a peak pressure of approximately 1.58 MPa on the wall. Although the cavitation bubble's collapse shock wave did not have a clear stratified structure in experiment f (Fig. 3.38), the peak impact of the shock wave on the wall was markedly lower than that (2.930 MPa) in experiment a, in which a cavitation bubble evolved near a wall without interacting with an air bubble. As shown in image f6 (Fig. 3.38), the cavitation bubble's collapse shock wave had an integrated nonstratified structure in the area between the air bubble and wall but had a lighter color in the area shielded by the air bubble. This result indicates that at a large air bubble-cavitation bubble distance, an air bubble does not have a considerable effect on the dispersion of the collapse shock wave of a cavitation bubble but does have an effect on the buffering of the impact of the shock wave, thereby resulting in a smaller impact from the shock wave on the wall compared with the impact of the shock wave of a cavitation bubble evolving at the same cavitation bubble-wall distance in the absence of an air bubble.

In the following, we analyze the effect of the air bubble-cavitation bubble size ratio on the collapse shock wave of a cavitation bubble interacting with an air bubble near a wall.

Figure 3.40 shows the evolution of the collapse shock wave of a cavitation bubble interacting with an air bubble near a wall obtained from a series of experiments, in which the air bubble-cavitation bubble size ratio was gradually increased.

In experiment a (Fig. 3.40), the equivalent radius of the air bubble r was very small relative to the maximum radius of the cavitation bubble $R_{\max}$. Throughout the expansion-shrinkage life cycle, the cavitation bubble did not experience considerable deformation. When at the minimum volume, the cavitation bubble radiated a shock wave into the surrounding water. As shown in image a3 (Fig. 3.40), the shock wave consisted of two levels with a very small interlevel distance. As the shock wave propagated outward, the interlevel distance remained very small. The shock wave finally passed through the air bubble and impacted the wall. In experiment b (Fig. 3.40),

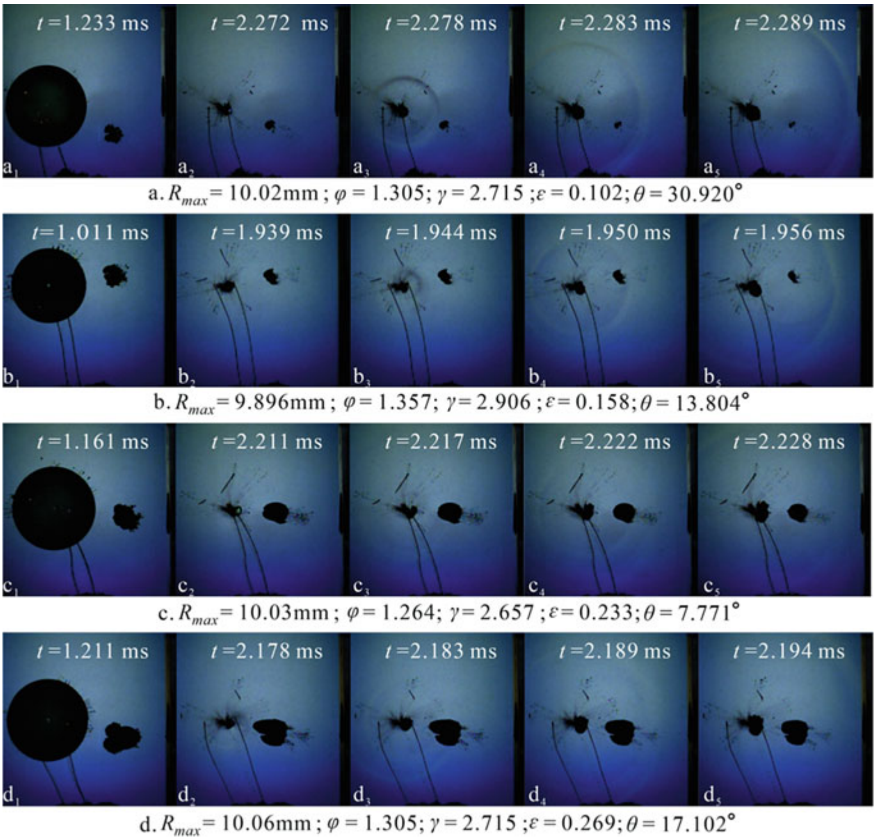


Fig. 3.40 Morphology of the shock wave of a cavitation bubble interacting with an air bubble of different relative sizes near a wall

the shock wave radiated into the surrounding water by the cavitation bubble in the collapse phase was multilevel, as shown in image b4 (Fig. 3.40). In addition, the cavitation bubble's collapse shock wave impacted the air bubble surface and was reflected there, generating a rebound wave, as shown in image b5 (Fig. 3.40). Furthermore, the collapse shock wave exhibited a slightly flat shape in the area behind the air bubble, different than the case in experiment a (Fig. 3.40). In experiment c (Fig. 3.40), in which the relative size of the air bubble ε was increased to 0.233, the cavitation bubble radiated a multilevel shock wave into the surrounding water. However, there were no clear high-speed images of the shock wave, in contrast with experiments a and b (Fig. 3.40). In addition, the shock wave behind the air bubble could hardly be identified in the high-speed images. In experiment d (Fig. 3.40), in which the relative size of the air bubble was increased to 0.269, the cavitation bubble also radiated a multilevel shock wave during the course of collapse. However, the brightness of the shock wave in the high-speed images decreased further. Similarly, the cavitation bubble's collapse shock wave could hardly be identified in the area between the air bubble and wall, as shown in image d5 (Fig. 3.40). In addition, in experiments c and d (Fig. 3.40), when the cavitation bubble radiated a shock wave, the air bubble experienced morphological changes to different degrees, with the cavitation bubble side of the air bubble being compressed to different degrees as the shock wave developed, as shown in images c3–c6 and d3–d6 (Fig. 3.40).

Figure 3.41 shows the measurements of the impact of the cavitation bubble's collapse shock wave on the wall obtained from the experiments shown in Fig. 3.40. In experiment a (Fig. 3.40), the shock wave had a two-level structure, as shown in image a4 (Fig. 3.40). However, the two-level structure became less identifiable as the shock wave propagated toward the wall. The measurements of the impact pressure exerted by the shock wave on the wall (Fig. 3.41a) exhibited only a single peak, which measured 2.480 MPa. In experiment b (Fig. 3.40), the cavitation bubble's collapse shock wave had a two-level structure, as could easily be identified in image b5 (Fig. 3.40). The cavitation bubble's collapse shock wave propagated to the air bubble and was reflected there, generating a rebound wave. The rebound wave and the collapse shock wave of the cavitation bubble propagated toward the wall together and ultimately impacted the wall, exerting two peak pressures of 1.420 and 0.308 MPa, respectively. In experiment c (Fig. 3.40), the measurements of the impact exerted by the cavitation bubble collapse on the wall clearly exhibited two peaks, which measured 0.737 and 0.656 MPa and matched the two-level structure, as shown in image c5 (Fig. 3.40). In experiment d (Fig. 3.40), the multilevel shock wave exerted a peak pressure of 0.702 MPa on the wall. As the relative size of the air bubble increased gradually from experiment a to d (Fig. 3.41), the peak impact pressure of the cavitation bubble's shock wave on the wall exhibited a clear decreasing trend, and the duration of the shock wave's impact on the wall gradually increased.

Figure 3.42 shows the relationship between the relative intensity of the shock wave, P_{max}/P'_{max} (where P_{max} is the peak impact pressure on a wall exerted by the collapse shock wave of a cavitation bubble interacting with an air bubble and P'_{max} is the peak impact pressure on a wall exerted by the collapse shock wave of a cavitation bubble evolving in the absence of an air bubble), and $\theta_{\omega}/\varepsilon_{\gamma bw}$. The figure shows

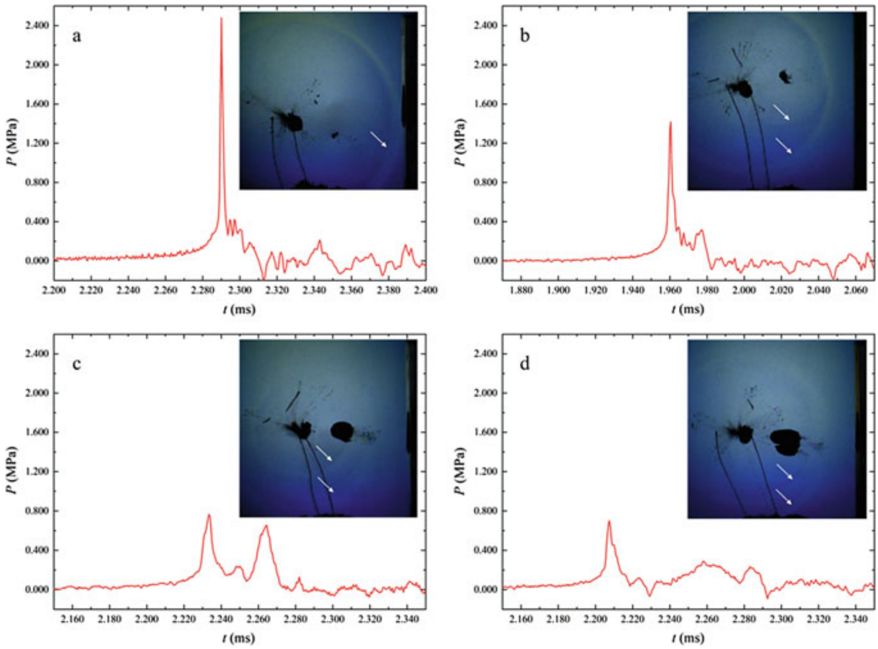


Fig. 3.41 Impacts on a wall exerted by the collapse shock waves of cavitation bubbles interacting with air bubbles of different sizes

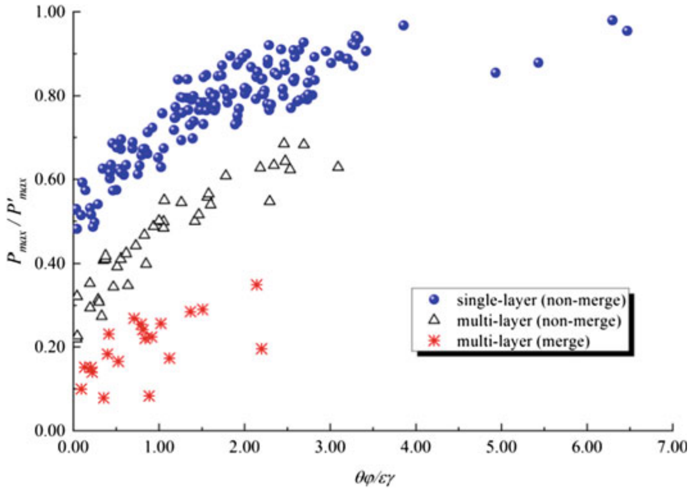


Fig. 3.42 Effect of dimensionless parameter $\theta_{\omega}/\varepsilon_{\gamma}$ on the intensity of the impact of a cavitation bubble's collapse shock wave

the combined effect of the air bubble size ε, cavitation bubble-wall distance γ_{bw}, air bubble-cavitation bubble distance ω, and angle θ on the relative intensity of the cavitation bubble's collapse shock wave at a given point on the wall. For a cavitation bubble interacting with an air bubble near a wall, the impact exerted by the collapse of the cavitation bubble on the wall is the smallest when the cavitation bubble has merged with the air bubble. At a small cavitation bubble-air bubble distance, the air bubble serves to effectively reduce the impact exerted by the collapse of the cavitation bubble on the wall mainly through the dispersion of the cavitation bubble's collapse shock wave. At a large cavitation bubble-air bubble distance, the air bubble can retard the direct impact of the cavitation bubble's shock wave on the wall to a certain degree, thereby reducing the intensity of the impact to a certain degree.

3.5 Forced Aeration for Cavitation Erosion Protection of High-Head Dams

For the open-channel discharge structures of high-head dams, the water flow needs to be aerated to protect the channel surface from cavitation erosion. For the air entrained in a high-velocity water flow through surface self-aeration to diffuse across the entire cross-section, appropriate conditions need to be provided, and the channel needs to be long enough to allow streamwise diffusion to occur. Therefore, to ensure the effectiveness of cavitation erosion protection, forced-aeration structures are necessary (Wood 1991; Pfister and Hager 2010). The design of forced-aeration structures is an important task in the cavitation erosion protection of high-head dams.

3.5.1 Mesoscale Mechanism of Forced Aeration

Forced-aeration structures for high-head dams are typically configured at the bottom of flow channels (Fig. 3.43). Such a structure usually consists of a flip bucket, an aerator, air vent holes on the sidewalls of the aerator, and an air supply duct connecting the air vent holes and the environmental air (or the nonwater flow space in the upper part of the channel). When passing through a flip bucket and aerator, a high-velocity water flow separates, resulting in local pressures lower than the atmospheric pressure. Thereby, the air is automatically sucked into the aerator through the air supply ducts, forming an aeration cavity. The air in the aeration cavity is entrained into the water flow, thereby aerating the water flow.

Figure 3.44 shows the mesoscale mechanism of forced aeration. As shown in the figure, when the water comes into contact again with the wall boundary at the wall-attachment point, the intense flow-wall interaction generates a water-air mixed zone. Further observations show that bulky volumes of aerated water gradually emerge

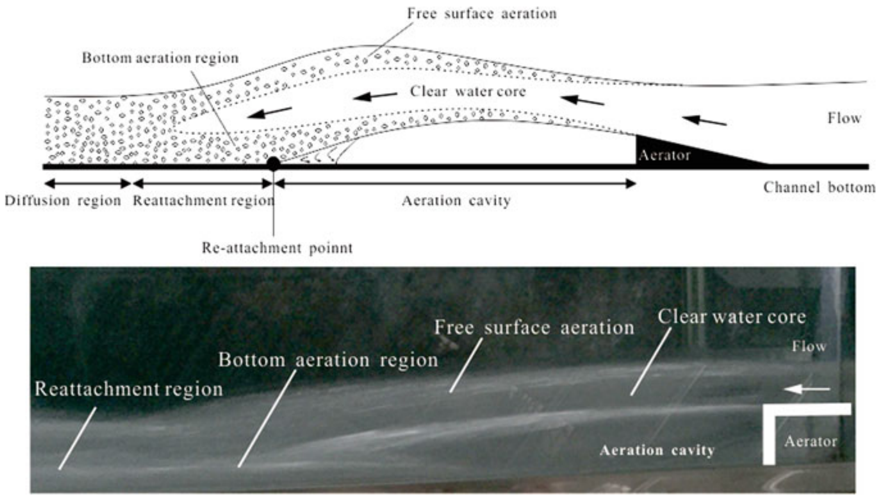


Fig. 3.43 Illustration of aeration through an aerator at the bottom of a water channel

downstream of the wall-attachment point of the water flow. These water-air mixed volumes gradually diffuse into the flow while moving downstream.

As air is entrained into the water at the wall-attachment point, the water flow surface in the aeration cavity becomes instable and deforms, thereby entraining air into the flow. However, the quantity of air bubbles entrained at the water flow surface is much lower than that at the wall-attachment point. Therefore, forced aeration functions mainly through the air entrainment at the wall-attachment point, with the free-surface aeration in the aeration cavity playing only a minor role.

As shown in Fig. 3.45a, the cross-sectional distribution of the air concentration in the high-velocity water flow at the front of the flip bucket is consistent with that of self-aeration. In the aeration cavity, because the bottom surface of the water flow is also a free surface, the air concentration in that zone is the result of self-aeration at two free surfaces. At the wall-attachment point at the end of the aeration cavity, the bottom part of the water flow cross-section has a high air concentration. As the water flow moves further downstream, the air entrained in the aeration cavity gradually diffuses upward, and the peak air concentration at the bottom gradually decreases.

The mesoscale mechanism of forced aeration can be better understood through the spatial distribution of the air bubble frequency (Fig. 3.45b). In the aeration cavity, the air bubble frequency distribution in the vertical direction exhibits a two-peak characteristic. At the wall-attachment point and in the wall-attachment zone behind it, the air bubble frequency contributed by the bottom aerator significantly increases to a level even higher than that contributed by the self-aeration at the upper surface of the water flow. As the water flow moves further downstream of the wall-attachment zone, the air bubbles contributed by the bottom aerator gradually float upward and diffuses.

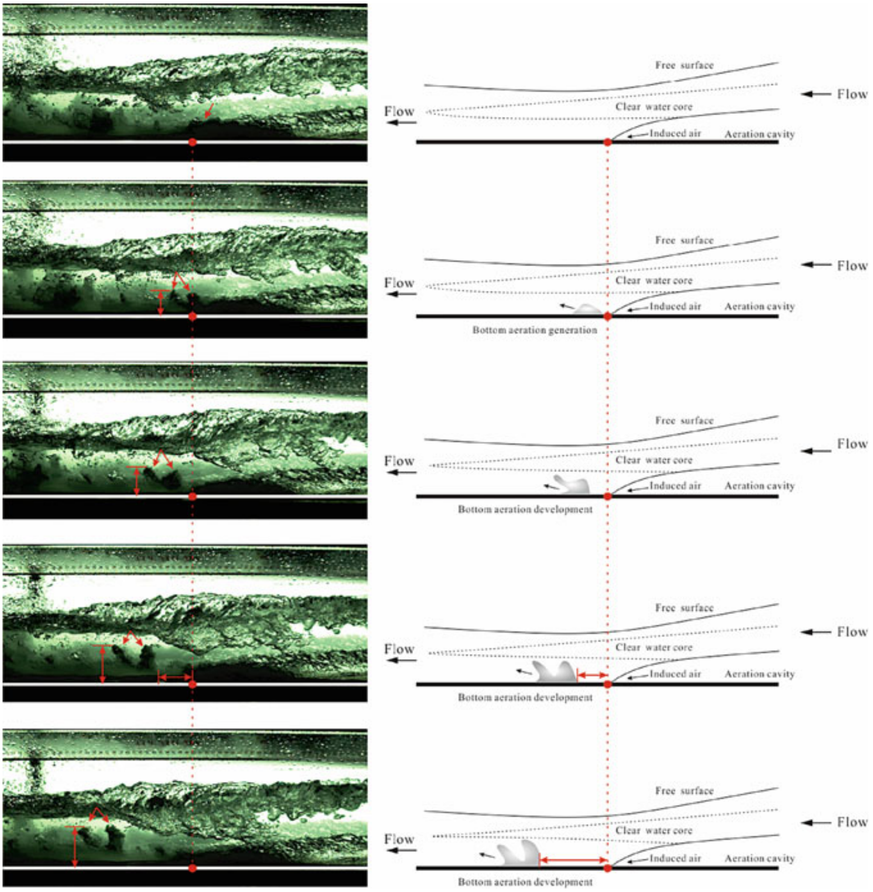
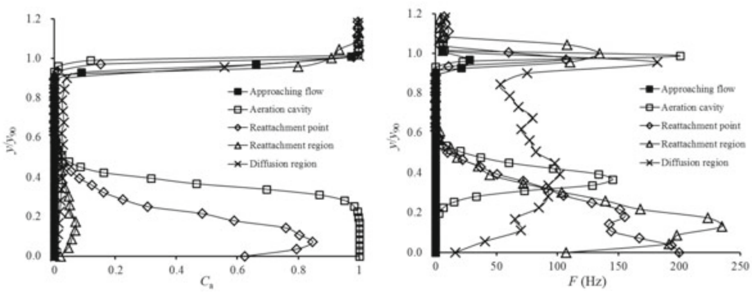


Fig. 3.44 Illustration of aeration using an aerator at the bottom of a flow channel



(a) Cross-sectional distribution of the air concentration (b) Cross-sectional distribution of the air bubble frequency

Fig. 3.45 Streamwise evolution of air entrained with a bottom aerator

From the perspective of the air bubble size, experimental observations show that the air bubbles in the vicinity of the wall-attachment point are larger, with a mean diameter d_{mean} above 20 mm (Fig. 3.46). This is mainly because the water flow at the wall-attachment has a high turbulence, resulting in the relatively large air bubble sizes at the wall-attachment point. As the water flow moves further downstream, the air bubble size gradually decreases, indicating that the originally large air bubbles entrained in the water gradually split to form small air bubbles as the large air bubbles move with, float up, and diffuse into the water flow. The air bubbles near the bottom wall maintain stable sizes in the range of 1–2 mm for a long streamwise distance. Figure 3.47 clearly shows the streamwise evolution in the air bubble mean diameter and frequency.

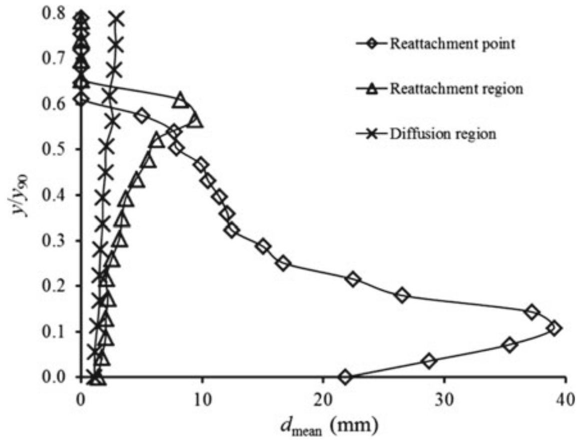


Fig. 3.46 Streamwise evolution of the size of air bubbles entrained through a bottom aerator

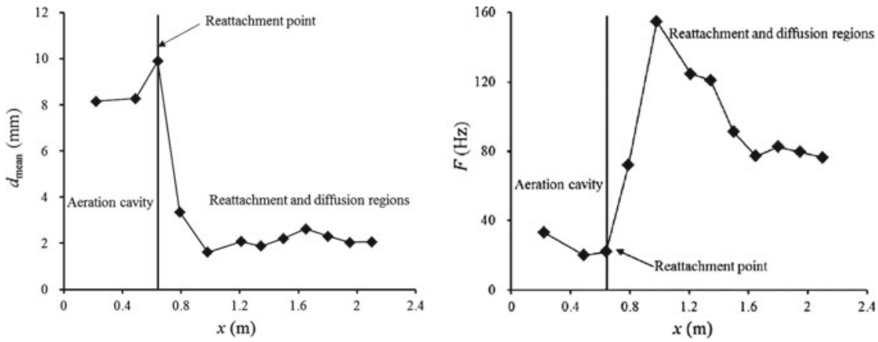


Fig. 3.47 Streamwise evolution in the mesoscale characteristics of air bubbles entrained through a bottom aerator

3.5.2 Design Principles of Forced-Aeration for Cavitation Erosion Protection Structures of High-Head Dams

Traditionally, to ensure effective cavitation erosion protection, the forced-aeration structures of high-head dams generally must be designed to be capable of achieving a sufficiently high air concentration. However, as analyzed in the previous sections, the mechanism of aeration-based cavitation erosion protection lies in the ability of the air bubbles to attenuate the collapse intensity, change the direction of collapse, and retard the collapse shock wave of cavitation bubbles. Therefore, for cavitation erosion protection-purposed aeration, the quantity of air bubbles is more important than the air concentration. For a given air concentration, a large quantity of small air bubbles is more effective in cavitation erosion protection than a small quantity of large air bubbles.

For high-head dams, because the high flow velocity makes it difficult for large air bubbles to exist stably in the water, the air bubbles have very small sizes. Under this condition, only if air can be continuously entrained into the water can aeration be effective for protection from cavitation erosion at a very low air concentration.

Therefore, forced-aeration structures for cavitation erosion protection of high-head dams should be designed based on a principle ensuring that aeration channels are unimpeded without being blocked by backwater, aeration cavities maintain their integrity, and the water flow regime is regular.

The above principles can be demonstrated by the engineering practices mentioned in Sect. 3.1 of this chapter.

Traditional aeration structures were built at the bottom of the spillway of a project, but the spillway suffered severe cavitation erosion in a section approximately 400 m long (Fig. 3.48). Repeated investigations of the root cause of the erosion put the focus on the sidewalls at the end of the concave-curve section—a dead corner that cannot be protected by the two aerators nor free-surface aeration. To solve this problem, an



Fig. 3.48 Cavitation erosion of a spillway

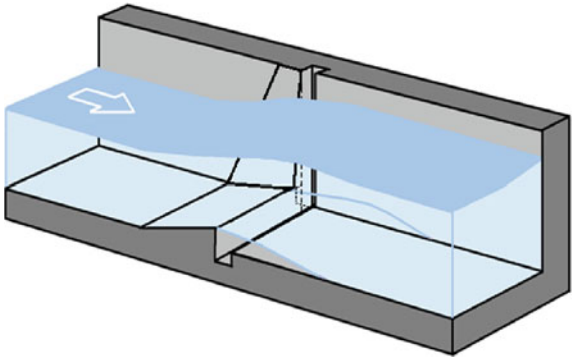


Fig. 3.49 Aeration structures built at the bottom and sidewalls of a spillway

aeration structure was built on the sidewalls at the position of the bottom flip bucket, as shown in Fig. 3.49.

However, model tests showed that the flip bucket on the sidewall could be built with only a maximum height of approximately 20 cm. Otherwise, the water flow would jump up due to the lateral contraction, thereby impacting the tunnel roof. Because a small flip bucket can only achieve a low air concentration, then the following question arises: Can such a low air concentration effectively prevent cavitation erosion?

The results demonstrated an affirmative answer. The first solution adopted after the cavitation erosion was repair according to the original design. However, erosion occurred again after 300 h of operation. Since the aeration structures were added to the sidewalls, cavitation erosion has been completely prevented.

3.6 Conclusions

The following conclusions can be drawn based on the analyses in this chapter:

1. The mechanism of aeration-enabled cavitation erosion protection lies in the ability of air bubbles to attenuate the collapse intensity, change the direction of collapse, and retard the collapse shock wave of cavitation bubbles.
2. A forced-aeration structure works mainly by entraining air bubbles into the water at the wall-attachment point of the water flow, with the air entrained through free-surface aeration in the aeration cavity playing only a minor role.
3. Forced-aeration structures for cavitation erosion protection of high-head dams should be designed based on a principle ensuring that aeration channels are unimpeded without being blocked by backwater, aeration cavities maintain their integrity, and the water flow regime is regular. Whenever these conditions are satisfied, the so-called “minimum air concentration” is not necessary for cavitation erosion protection.

References

Auret, J., Damm, O., Wright, G., & Robinson, F. (1993). The influence of water air content on cavitation erosion in distilled water. *Tribology International, 26*(6), 431–433.
Brennen, C. E. (2014). *Cavitation and bubble dynamics*. Cambridge University Press.
Gibson, D., & Blake, J. R. (1982). The growth and collapse of bubbles near deformable surfaces. *Applied Scientific Research, 38*(1), 215–224.
Hammitt, F. G. (1980). *Cavitation and multiphases flow phenomena*. McGraw-Hill.
Ivany, R. D., & Hammitt, F. G. (1965). Cavitation bubble collapse in viscous, compressible liquids—Numerical analysis.
Peterka, A. J. (1953). The effect of entrained air on cavitation pitting. In *Proceedings: Minnesota International Hydraulic Convention*. ASCE.
Pfister, M., & Hager, W. H. (2010). Chute aerators. II: Hydraulic design. *Journal of Hydraulic Engineering, 136*(6), 360–367.
Pfister, M., Lucas, J., & Hager, W. H. (2011). Chute aerators: Preaerated approach flow. *Journal of Hydraulic Engineering, 137*(11), 1452–1461.
Rasmussen, R. (1956). Some experiments on cavitation erosion in water mixed with air. In *Proceedings of the International Symposium on Cavitation in Hydrodynamics*. London: National Physical Laboratory.
Vischer, D., & Hager, W. H. (1998). *Dam hydraulics*. UK: Wiley Chichester.
Vogel, A., Lauterborn, W., & Timm, R. (1989). Optical and acoustic investigations of the dynamics of laser-produced cavitation bubbles near a solid boundary. *Journal of Fluid Mechanics, 206*, 299–338.
Wood, I. (1991). Air entrainment in free-surface flows. IAHR hydraulic structures design Manual No. 4, Hydraulic Design Considerations (p. 149). Balkema, Rotterdam.
Xu, W.-l., Bai, L.-x., & Zhang, F.-x. (2010). Interaction of a cavitation bubble and an air bubble with a rigid boundary. *Journal of Hydrodynamics, Series B, 22*(4), 503–512.
Xu, W. L., Li, J. B., Luo, J., & Zhai, Y. W. (2020). Effect of a single air bubble on the collapse direction and collapse noise of a cavitation bubble. *Experimental Thermal and Fluid Science, 120*(24), 110218.

Chapter 4
Mesoscale Analysis of Air-Water Two-Phase Flow

4.1 Background

In nature and engineering, a free-surface flow entraps air through its free surface when moving at a relatively high velocity, forming an air-water two-phase flow, which has both positive and negative effects. On the one hand, the air bubbles entrained into the flow can reduce cavitation erosion and enhance water reaeration (Russell and Sheehan 1974; Geist et al. 2013). On the other hand, air entrainment will increase the flow depth and, thereby, will require an increase in the height of the tunnel or the sidewalls of the spillway (Falvey 1980). In addition, an overly high concentration of entrained air C_a can pose a threat to the fish in the downstream waters (Weitkamp and Katz 1980). Regardless of the perspective, it is important to understand and grasp the causes and development of air-water two-phase flow.

With regard to the physical mechanism of air entrainment and aeration, there were once two main theoretical explanations. (1) The falling of the water droplets that leap from the surface (Lane 1939; Volkart 1980). This aeration theory states the following. After the boundary of turbulence inside a flow formed by solid boundaries moves to the surface and exposes the turbulence to the air, as the turbulence continues to evolve, the water in the local regions of the free surface of the flow will overcome gravity and surface tension and subsequently leave the free surface and leap into the air in the form of droplets. When the water droplets fall back into the flow, the air entrained by them will move with the flow in the form of bubbles, forming an air-water two-phase flow. (2) Surface waves (Ervine and Falvey 1987). This air entrainment and aeration theory states the following. After an open-channel flow develops into a turbulent regime across its full cross-section, undulating waves will be formed at the surface. As they fall or break, these waves will entrain air into the flow. Then, what is the true cause of flow aeration? How can the free-surface aeration at the bottom of a jet flow be explained?

Apart from the cause of the formation of aerated flows, there remains a need to further investigate the methods used to calculate aerated flows, particularly the parameter C_a. With regard to the C_a distribution, Wu (1988) provided a complete

W. Xu, *Mesoscale Analysis of Hydraulics*,
https://doi.org/10.1007/978-981-15-9785-5_4

set of calculation methods, which was an important contribution to aerated-flow calculations. Due to the limitations in the experimental techniques, there are several unknown parameters in Wu's calculation model, which necessitates the use empirical equations. In addition, the model used to directly calculate the C_a distribution in the aerated region based on turbulent diffusion equations (Chanson 1997) contains empirical parameters and the cross-section-averaged C_a (C_{mean}). In other words, this model is directly correlated to the amount of entrained air, for which there is a lack of corresponding calculation methods.

An air-water two-phase flow is essentially formed by the air bubbles in a flow, and the free-surface aeration and C_a distribution both depend on the formation and motion of air bubbles. Therefore, mesoscale analysis will undoubtedly play a vital role in the study of air-water two-phase flows.

4.2 Mesoscale Mechanism for Surface Aeration of High-Velocity Flows

Ehrenberge (1927) was the first to describe the physical cross-sectional structure of a self-aerated flow along the flow depth direction. Later, researchers basically followed Ehrenberger's stratification method for self-aerated flows and believed that a typical self-aerated flow can be divided into four layers, namely, a water-droplet leaping layer (top layer), an air-water mixture layer (middle layer), an air-bubble suspension layer (bottom layer), and a possible bottommost clear-water layer (Fig. 4.1).

Numerous researchers have described the stratified structure of self-aerated flows in more detail through extensive experiments. They believe that the distribution of the volume proportion of air (C_a) transported with a flow varies between the upper and lower regions. Water droplets leap in the upper region. In this region, the water droplets that leap from the surface are random and follow a Gaussian (normal) distribution. The lower region contains suspended air bubbles. The motion of the air bubbles in the flow conforms to the law of material diffusion. There is no notable separation between the upper and lower regions. The development and application of high-speed photography in recent years have rendered it possible to directly observe

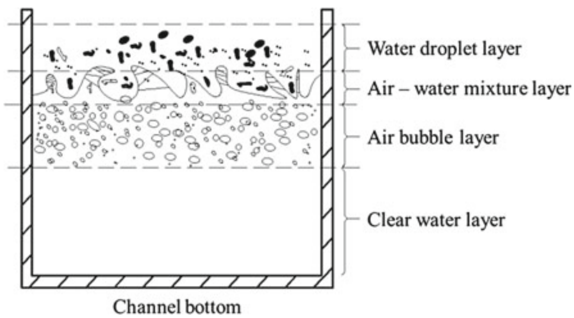


Fig. 4.1 Schematic diagram of the distribution of the water and air regions in the cross-section of a self-aerated flow (Ehrenberger 1927)

self-aerated open-channel flows. It has been discovered that the free surface of a self-aerated flow is highly deformed, irregularly undulating, and continuous and that there are an extremely small number of moving water droplets over the surface.

A self-aerated flow has three notable cross-sectional regions along the streamwise direction, namely, an air-free clear-water region, which is located before the inception point of self-aeration, an aeration development region (consisting of a developing, partially aerated region and a full-cross-sectional, fully aerated region), and a fully aerated region, as shown in Fig. 4.2. Specifically, when the turbulence intensity in the surface of an open-channel flow reaches the aeration condition, the flow develops into an air-water two-phase regime after the inception point of self-aeration. Air enters the flow in the form of bubbles, which, under turbulence, overcome buoyancy and continue to diffuse towards the inner region of the flow. The aerated region gradually increases in size along the course. There is a clear-water region in the cross-section of this region, where the air bubbles have yet to diffuse to the bottom of the open channel. As a result, this region is a developing, partially aerated region. As the air bubbles diffuse to the wall at the bottom of the open channel, the clear-water region disappears, forming a full-cross-sectional air-water two-phase flow. However, as the air bubbles have yet to reach equilibrium under turbulence and buoyancy, there is a gradual increase in the extent of aeration along the course. As a result, this is a developing, fully aerated region. Further down, as the interaction between the water and air phases continues to evolve and reach equilibrium, the extent of aeration gradually becomes stable along the course, as reflected by the fact that there is basically no change in the macroscopic amount of entrained air as well as the mesoscopic number and size of air bubbles. This is considered a fully aerated region in the self-aerated flow.

The concentration of entrained air is the most straightforward parameter depicting the air-water structure of a self-aerated flow. The parameter refers to the amount of air contained in a certain amount of water. The local volume ratio (i.e. the concentration of entrained air, C_a, in hydraulics) is often used as an evaluation index for an air-water two-phase flow.

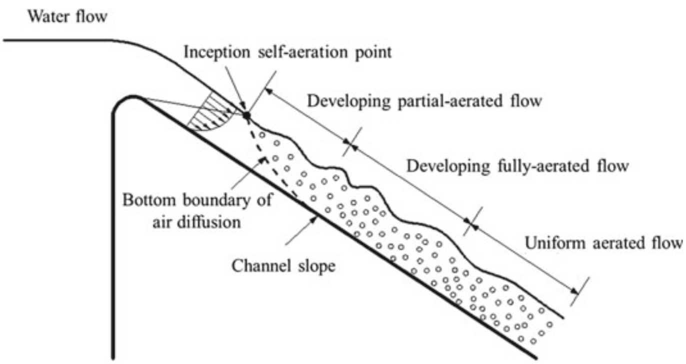


Fig. 4.2 Typical streamwise structure of a self-aerated open-channel flow

$$C_a = \frac{V_{\mathrm{La}}}{V_{\mathrm{Lm}}} = \frac{V_{\mathrm{La}}}{V_{\mathrm{La}} + V_{\mathrm{Lw}}} \tag{4.1}$$

where V_{La} and V_{Lw} are the volumes of air and water in the aerated flow, respectively, and V_{Lm} is the volume of the air-water mixture flow. The volume flow (rate) (i.e. the common concept of flow in hydraulic engineering) is the volume of the fluid that flows through per unit time. Let Q_{a}, Q_{w}, and Q_{m} be the volume flows of air, water, and mixture, respectively. Thus, we have the following relation:

$$Q_m = Q_a + Q_w \tag{4.2}$$

For an open-channel air-water two-phase flow, it can be assumed that water and air move at basically the same velocity in the streamwise direction. The flow concentration (i.e. C_a) refers to the ratio of the volume flow of air in the air-water mixture to the total flow, i.e.

$$C_a = \frac{Q_a}{Q_m} = \frac{Q_a}{Q_a + Q_w} \tag{4.3}$$

The aeration coefficient β refers to the ratio of the microvolume of air, $\mathrm{d}V_{\mathrm{L}a}$, to the microvolume of water, $\mathrm{d}V_{\mathrm{Lw}}$, in the mixture:

$$\beta = \frac{dV_{\mathrm{L}a}}{dV_{\mathrm{L}w}} \tag{4.4}$$

Evidently, the relationship between C_a and β at a certain point follows the equation below:

$$C_a = \frac{\beta}{\beta + 1} \tag{4.5}$$

4.2.1 Mesoscale Characteristics of the Free-Surface Shape of Flows

For an open-channel flow, the mesoscale of its free-surface shape is relatively small under turbulence. In addition, its free-surface shape changes at an extremely high rate within an extremely short duration (generally on the order of 10^{-2} s). As the turbulence intensity of the flow increases and aeration develops along the course, its free-surface shape changes within a relatively large range (Volkart 1980; Medwin et al. 1990; Pfister and Hager 2011), which is on the order of 10^{-3}–10^{-1} m. In this book, a dynamic image acquisition system with a high-speed camera as its core and image processing techniques are used to analyze the location of the free-surface

boundary as well as the shape, size, and velocity of air bubbles to prevent errors caused by human judgment. In addition, the local mesoscale characteristics of the free-surface shape are quantitatively described. New quantification parameters are proposed to describe the characteristics of the free-surface shape in an accurate and reasonable manner. Moreover, the quantitative patterns of the evolution of the free-surface shape under various conditions are investigated.

Typical free-surface depression shapes were extracted, and their distribution was studied. In real-world conditions, there is a certain unavoidable angle between the direction of the downward fluctuation velocity near the free surface of a flow and its free surface. In addition, under random turbulence, a depression may either turn in the upstream direction or the downstream direction. Therefore, for the analysis in this book, all free-surface shapes are treated as depressed deformations perpendicular to the streamline direction of the free surface, and the angle of each free-surface shape is first corrected horizontally. Thus, the characteristics of the free-surface shape are determined and subsequently further analyzed.

Figure 4.3 shows the shape characteristics of a series of typical free-surface depressions. The flow moves from the right side of the image to its left side. In the photographic process, a stream was formed close to the wall above the surface as a result of the interaction between the surface tension of the flow and the shear stress exerted by the sidewalls of the steep channel, to some extent affecting the deformation above the surface. However, the deformation of the surface towards the inner region of the flow was relatively clearly observed, and the surface was found to be obviously uneven. Relatively intact depression shapes when no notable instabilities occurred

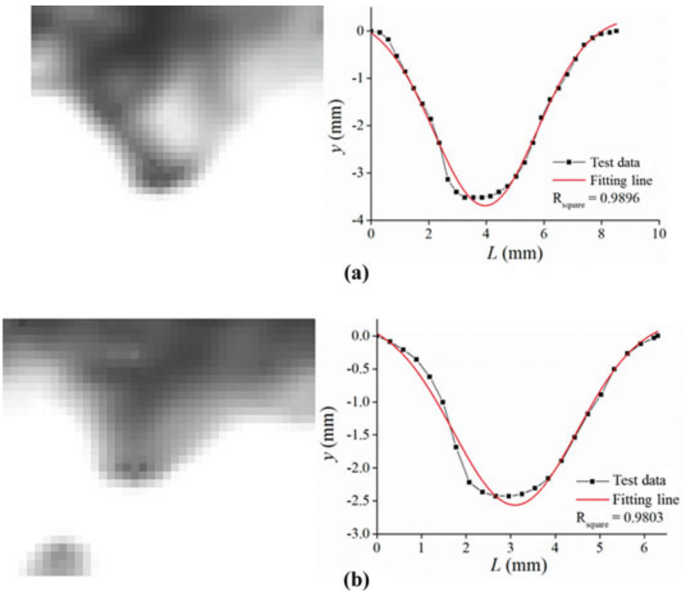


Fig. 4.3 Characteristic comparison of free-surface depression shapes

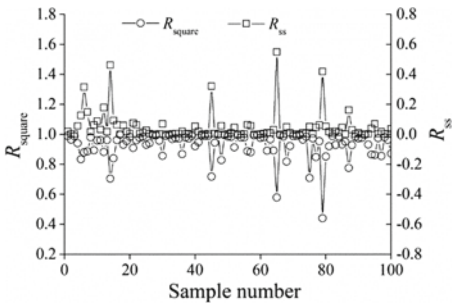


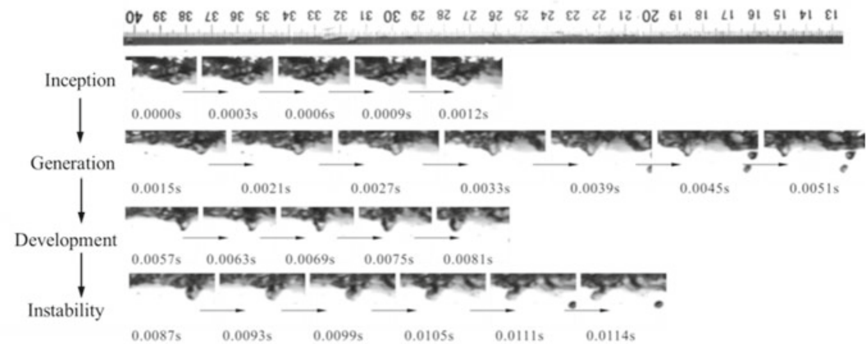
Fig. 4.4 Correlation analysis of free-surface depression shapes and the Gaussian curve

were selected for analysis. In addition, for each depression whose boundaries on the two sides were relatively smooth and that was insignificantly disturbed by the shape of the adjacent free-surface regions, notable inflection points and discontinuous locations were selected as its boundaries on the two sides.

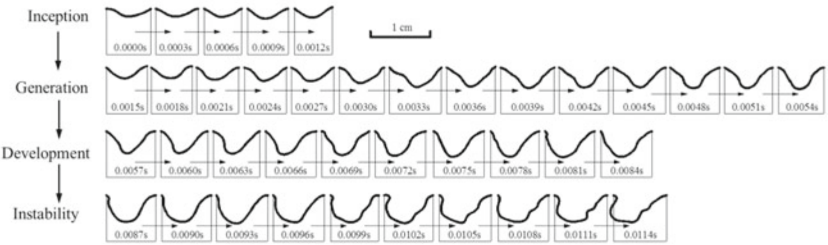
The local free-surface depression shapes were extracted from the images and subsequently subjected to discrete analysis. Fitting and comparative analysis were performed using a symmetric Gaussian distribution curve. The results show the following. On the one hand, under complex three-dimensional turbulence in the surrounding water, some local free-surface depressions were unable to achieve a completely symmetrical shape on the two sides. In addition, it was impossible for the air-water interface in the depressed region to be absolutely smooth. On the other hand, free-surface depression shapes as well as their variation trends basically followed the Gaussian distribution curve. The results obtained by fitting 100 extracted depression shapes to the Gaussian distribution curve (Fig. 4.4) show that the correlation coefficient R_{square} was above 0.95 for 58 shapes, above 0.90 for 74 shapes, and below 0.80 for six shapes. Thus, the assumption used in the analysis of the air entrainment and aeration mechanism of the free-surface depressions—that the shape of a depression follows a Gaussian distribution curve— can be considered relatively reasonable.

4.2.2 *Mesoscale Free-Surface Aeration Process of Flows*

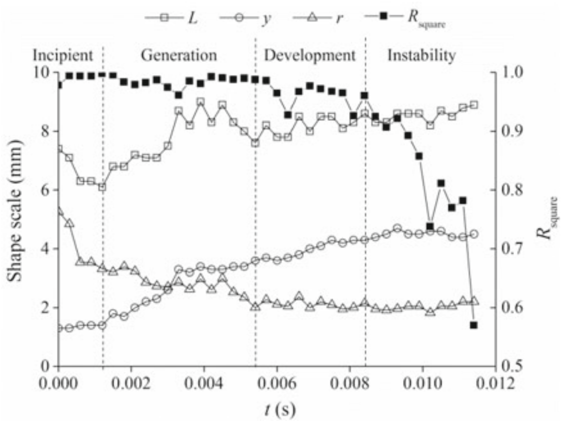
Figure 4.5a, b shows the process in which the free surface of a flow moving at a velocity of 5.5 m/s underwent deformation and became unstable in a time series as well as a generalized diagram depicting the corresponding air entrainment and aeration process, respectively. At the initial time point ($t = 0.000$ s), the free surface of the flow had a relatively smooth local region with a basically stable shape. The curvature radius r of the local deformation was calculated with the straight-line distance between the two boundary points and the vertical distance between the lowest point of the depression and the line connecting the boundary points as the width L and depth y of the depression, respectively. At this time point, the extent of the deformations of the flow in the x- and y-directions (L_σ and y_σ) were 7.4 and 1.3 mm,



(a) Photographed process



(b) Generalized process



(c) Changes in the parameters with time

Fig. 4.5 Shape evolution of a free-surface depression

respectively, and the r at the endpoint of the depression was 5.3 mm. At the following time point ($t = 0.0003$ s), there was a sudden decrease in L. As demonstrated in Fig. 4.5c, L decreased significantly with r. This suggests that in this time period ($t = 0.0003$–0.0012 s), the free surface was locally significantly depressed under the action of the downward fluctuation velocity. This time period can be treated as the incipient stage of the shape evolution of the free-surface depression. Subsequently, the depression shape further evolved. In the time period of $t = 0.0015$ to 0.0051 s, the depression developed towards the inner region of the flow along the flow depth direction, i.e. there was a gradual increase in y (from 1.8 to 3.4 mm). In addition, there was a gradual increase in L (from 6.8 to 8.0 mm) in the flow direction. However, in this time period, there was a gradual decrease in the r of the depressed free surface (from 3.2 to 2.4 mm). This suggests a gradual increase in the concave extent of the depression as well as a notable increase in the extent of deformation with time and shape development. This time period can be treated as the formation stage of the shape evolution of the free-surface depression. The R_{square} values for the depression shape at the corresponding location and the Gaussian curve at these two stages were both above 0.95. This indicates that the overall shape of the free surface remained relatively stable and intact at the inception and formation stages of evolution of the depression. In the following time period ($t = 0.0054$ to 0.0081 s), L and y evolved and changed to a significantly smaller extent. Specifically, L increased from 7.6 to 8.1 mm, while y increased from 3.6 to 4.2 mm. The corresponding r remained basically unchanged at approximately 2.0 mm. In addition, the R_{square} for the depression shape and the Gaussian curve fluctuated significantly and decreased to a certain extent but remained above 0.90, indicating that the shape became significantly unstable at this stage. The analysis of r and the stable shape characteristics shows that at this stage, the local depressed deformation developed close to the limit extent under flow conditions and the action of the surrounding water. The ultimate capacity of the depression to maintain a relatively stable shape also approached its limit. This time period can be treated as the development stage of the shape evolution of the free-surface depression. Afterwards, the shape of the depressed deformation further evolved with time. In the time period of $t = 0.0084$–0.0114 s, the three shape parameters (L, y, and r) of the depression basically remained stable. However, the shape of the depression underwent significant changes, and its correlation with the Gaussian curve decreased considerably. With time and shape development, the R_{square} value decreased to 0.5702 ($t = 0.0114$ s). This suggests that the shape of the depression changed significantly and became highly twisted at this stage compared to the first three stages. As demonstrated in Fig. 4.5a, there was a decrease in the continuity of the free surface on the two sides of the depression. In addition, the free surface on the two sides of the depression became loose and fluctuated ($t = 0.0105$–0.0114 s). The depression was no longer able to maintain the stable shape seen in the previous stages. This corresponds to the previous theoretical analysis—that the surface tension was unable to overcome the turbulent action. As a result, the free surface had already become unstable at this stage. This stage can be treated as the instability stage of the shape evolution of the free-surface depression. At this stage, the shape of the free-surface depression could no longer be treated as a Gaussian curve for analysis.

Moreover, the total duration of the four stages lasted for only 0.0114 s. This suggests that a local free-surface depression becomes unstable in an extremely short period of time and that the duration of each process is on the order of 10^{-3} s.

Based on the theoretical analysis and the captured images, the characteristics of the four processes—inception, formation, development, and instability—involved in the shape evolution of a local free-surface depression in a flow are summarized as follows.

Inception: The depressed deformation is insignificant and has a stable shape.
Formation: The depressed deformation increases in extent and has a stable shape.
Development: The extent of the depressed deformation approaches the limit, and there is a decrease in the stability of its shape.
Instability: The depressed deformation is loose, and its stability decreases sharply.

4.2.3 Quantitative Analysis of the Free-Surface Aeration of Flows

A certain vortex near the free surface and the corresponding local region of the free surface are selected for analysis. At a certain time point, the vortex moves towards the inner region of the flow under turbulence. Let E_e be the turbulent energy of the vortex. At this time point, the free surface responds to the turbulent action by undergoing depressed deformation. This deformation results in the formation of the surface free energy E_σ in the depressed free surface. As the turbulence of the vortex overcomes the surface tension during the deformation process, the scale of the free-surface shape continues to increase in the transverse and streamwise directions. If the depression formed on the free surface contains sufficient E_σ to absorb E_e, then the free-surface depression remains smooth and stable throughout its evolution.

If the depression formed on the free surface does not contain sufficient E_σ to absorb E_e, then the free-surface depression is unable to maintain a smooth and stable shape throughout its evolution. The surface tension is unable to balance the pressure. This leads to instability, which causes the water on the two sides of the depressed region to converge towards the center. During this process, if the free-surface regions on the two sides of the depression are closed, an air bubble is formed and entrained into the water. This results in the formation of an aerated flow.

Figure 4.6 shows the generalized process of the free-surface deformation of an open-channel flow and the entrainment of an air bubble into the water. The physical process is generalized as follows: (1) a free-surface depression is formed under transverse fluctuations; (2) this destabilizes the deformed free surface; (3) during irregular shape evolution, the free surface is closed and entrains air.

If E_e equals E_σ, E_e can be just completely converted to E_σ, which can be used as the critical air-bubble entrainment condition for a free surface, i.e.

$$E_e = E_\sigma \tag{4.6}$$

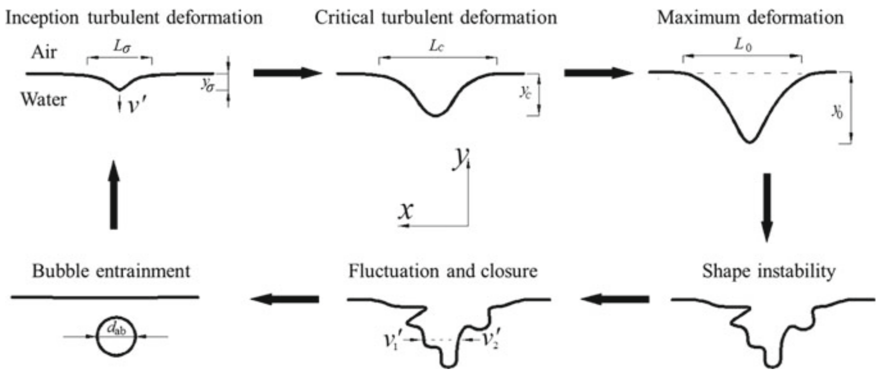


Fig. 4.6 Generalized process of air entrainment and aeration associated with a free-surface depression

with E_e and E_σ expressed as:

$$E_e = \frac{1}{2} \cdot \rho \cdot \frac{4}{3}\pi (\frac{D}{2})^3 \cdot v'^2 \tag{4.7}$$

$$E_\sigma = \pi r_C^2 \cdot \sigma_\rho \tag{4.8}$$

where v' is the fluctuation velocity of the vortex in the vertical (y) direction, σ_ρ is surface tension, ρ is the density of water, D is the characteristic size of the vortex, and r_C is the curvature radius of the free-surface depression under the critical condition.

D represents the turbulence intensity of a flow. The greater D is, the higher the turbulence intensity of the flow is. For the free surface of an open-channel flow, considering the effects of gravity and the surface tension formed after free-surface deformation on a vortex (Brocchini and Peregrine 2001), the D of a vortex and the local characteristic velocity v_* near the vortex should satisfy the following relationship:

$$v_*^2 \approx 0.13gD + \frac{1.57\sigma_\rho}{\rho D} \tag{4.9}$$

where $0.13gD$ is the gravity term and $1.57\sigma_\rho/(\rho D)$ is the E_σ term formed as a result of free-surface deformation. For the free surface of an open-channel flow, at the initial time point of the transverse action of a vortex, the free surface has yet to undergo deformation, and $E_\sigma = 0$. The above equation can be approximated to $v_*^2 \approx 0.13gD$. v_* can be approximately treated as the mesoscale friction velocity v_τ when the bottom turbulence boundary layer of the open channel moves to the free surface.

r_C is the curvature radius at the bottom endpoint of a depression on the free surface of a flow under the critical condition and is used to depict the deformed shape of the

flow. The smaller r_C is, the more significant the depressed deformation is. The larger r_C is, the gentler the shape of the depression is. Based on the analysis of the free-surface deformation under turbulence (Davies 1972; Rein 1998), it can be assumed that the free-surface shape follows a Gaussian curve. r_C under the critical condition is expressed as:

$$r_C = \frac{L_C^2}{8y_C} \tag{4.10}$$

where L_C and y_C are the critical width and depth, respectively, of the free-surface depression in the critical state. Thus, the expression of r_C can be rewritten as follows:

$$r_C = \left(\frac{\rho D^3 v'^2}{12\sigma_\rho} \right)^{\frac{1}{2}} \tag{4.11}$$

When the curvature radius of a local free-surface depression, r_0, is less than r_C, the free surface is more significantly deformed, and the motion of the vortex near the free surface is more intense. Under this condition, the surface tension is insufficient to balance the turbulent motion of the vortex. The deformed free surface is unable to continue to remain smooth and intact and will further become loose. Under the action of the transverse fluctuation velocity, the free surface will be closed at a certain location. This results in the formation of an air bubble, which subsequently enters the water. Overall, the entrainment of an air bubble into the free surface can be viewed as a process of forming an individual air bubble from the "entrapped air" and can also be treated as the self-aeration mechanism of open channels. When $r_0 > r_C$, the free surface is relatively insignificantly deformed. The surface tension is able to balance the turbulent motion of the vortex during the deformation process. The free surface is able to maintain an intact shape. Under this condition, it is assumed that no air bubbles will be entrained into the water. Clearly, air-bubble entrainment is significantly affected by the free-surface deformation caused by the turbulent motion of vortices in real-world conditions. Next, the free-surface deformation of flows in real-world turbulent conditions is analyzed.

It is assumed that surface tension is able to balance the vertical turbulent action of a vortex throughout the turbulent deformation of the free surface of a flow. Thus, there is a theoretical equilibrium location where E_e can be completely converted to E_σ. Under this condition, the deformation of the free surface reaches the maximum. At this time point, according to mechanical equilibrium conditions, the fluctuation pressure p' at the bottom endpoint equals the sum of the surface tension ($2\sigma_\rho/r_\mathrm{m}$, where r_m is the curvature radius at the bottom endpoint when the maximum deformation is reached) and the static pressure ($y_\mathrm{m}\rho g$, where y_m is the maximum depth of depression when the maximum deformation is reached). Davie (1972) noted that the free-surface p' and friction velocity v_τ follow a quadratic relationship, i.e., $p' = C_1\rho v_\tau^2$. Therefore, when the theoretical maximum deformation is reached, the bottom endpoint of the free surface satisfies the following mechanical equilibrium condition:

$$C_1 \rho v_\tau^2 = \frac{2\sigma}{r_\mathrm{m}} + y_\mathrm{m} \rho g \tag{4.12}$$

When $C_1 = 1$, $v_\tau = v'$ passes the first-order hypothesis test. The cross-section-averaged flow velocity V and the corresponding v_τ satisfy the following logarithmic distribution:

$$V = \frac{v_\tau}{\kappa} \ln \frac{H v_\tau}{\nu} \tag{4.13}$$

where v is the kinematic viscosity of the flow and H is the mean flow depth. Previous theoretical and experimental studies on the turbulent free-surface deformation of open-channel flows have shown that y_m meets the following empirical condition:

$$y_\mathrm{m} \approx \frac{K_e}{g} \tag{4.14}$$

where K_e is the mean turbulent energy of the flow near the free surface and is equal to $0.5(v')^2$. Thus, based on the above relationships, the curvature radius of the theoretical turbulent free-surface deformation of a flow under the turbulent action of a vortex is determined as:

$$r_\mathrm{m} = \frac{4\sigma_\rho}{\rho v'^2} \tag{4.15}$$

where r_m is the maximum extent of free-surface deformation without considering the free-surface instability.

The basic physical process of formation of a self-aerated flow is summarized as follows: The aeration development in a self-aerated flow along the course is a continuous equilibrium process between the air entrained in the water and the air that continuously escapes from the water due to buoyancy, as shown in Fig. 4.7.

The mathematical expression of air entrainment and aeration in the direction vertical to the free surface of an equal-width open-channel flow is as follows:

$$\mathrm{d}q_a = (V_\mathrm{e} - V_\mathrm{r} \cdot \cos\alpha)\mathrm{d}s \tag{4.16}$$

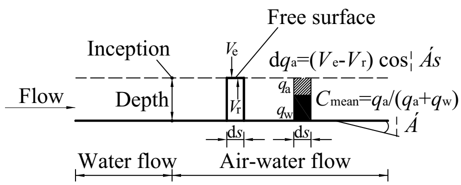


Fig. 4.7 Generalized physical process of self-aeration development

where V_e is the entrainment velocity of air into the water, V_r is the rising velocity of air in the water, and α is the slope of the channel.

Next, the method for determining the generalized V_e is discussed.

According to the generalized physical process, the air entrainment and self-aeration condition is that the turbulent energy E_e of a turbulent vortex that acts on a local region of the free surface of the flow is greater than the surface free energy E_σ corresponding to the deformation, i.e.,

$$E_e > E_\sigma \tag{4.17}$$

Based on the relevant equations in Chap. 2, the surface tension $(E\sigma)_C$ that needs to be overcome for air entrainment and aeration to occur can be calculated. Thus, the remaining energy $\triangle E$ when free-surface aeration occurs in a real-world flow is as follows:

$$\Delta E = E_e - (E_\sigma)_C \tag{4.18}$$

It is assumed that this energy acts on the water that encapsulates air and brings the entrained "air bubble" to move inwardly, as shown in Fig. 4.8.

Thus, this energy should be reflected by the generalized V_e. Based on the E_e equation for a vortex, V_e can be calculated:

$$V_e = \sqrt{\frac{12 \cdot \Delta E}{\pi \rho D^3}} \tag{4.19}$$

Figure 4.9 shows the calculated values of V_e under various conditions.

Next, the method used to determine the generalized rising velocity V_r is discussed.

Figure 4.10 shows the V_r–size (i.e., diameter d_{ab}) relationship for air bubbles. Mendelson (1967) found the following. There is a notable extreme-value inflection point for V_r at a d_{ab} of 7–8 mm. Compared to the surface tension and buoyancy, the

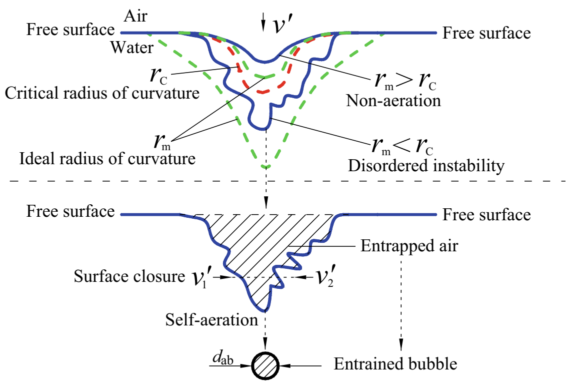


Fig. 4.8 Generalized diagram of the turbulent deformation of a free surface as well as the corresponding air entrainment and aeration process

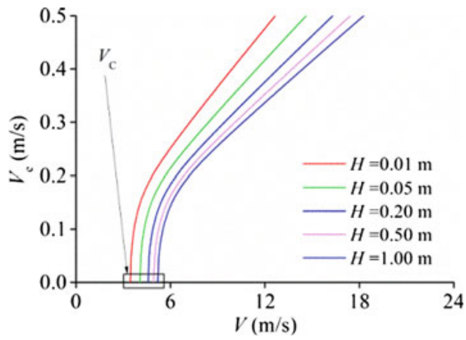


Fig. 4.9 Theoretical calculated values of the entrainment velocity V_e

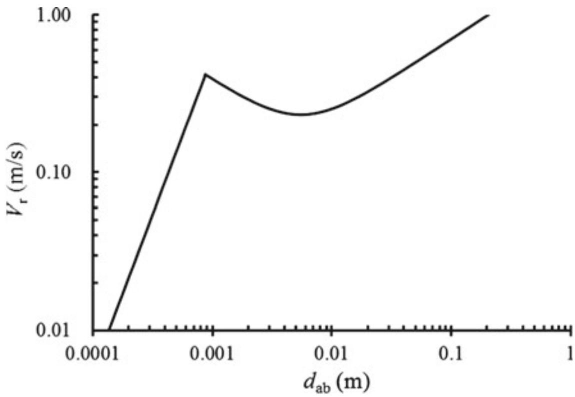


Fig. 4.10 Relationship between the rising velocity V_r and size d_{ab} of air bubbles (Mendelson 1967)

fluid viscosity is the primary factor that affects relatively small air bubbles ($d_{ab} < 7$–8 mm). For air bubbles of this critical size (i.e. $d_{ab} = 7$–8 mm), the effects of the fluid viscosity on the rising motion of air bubbles are negligible. As d_{ab} increases beyond 7–8 mm, the surface tension and buoyancy become the primary factors that affect V_r. As d_{ab} continues to increase within a certain range, the surface tension plays a main role in V_r. As d_{ab} further increases, the buoyancy that acts on air bubbles gradually plays a chief role in V_r, whereas the effects of the surface tension gradually weaken.

Previous studies on the relationship between V_r and the macroscopic flow conditions have shown that at various slope α values, the component of V_r ($V_r \cdot \cos\alpha$) in the direction vertical to the flow direction characterizes the extent of the escape of air from the flow. Due to the differences in the measurement methods and experimental conditions, the V_r values obtained in various studies under the same flow velocity and α conditions vary to some extent. Thus, by averaging the V_r values obtained under basically the same flow velocity and α conditions, the following approximate linear relationship between V_r and the flow velocity is determined:

$$V_r \cdot \cos\alpha = a \cdot (V_0 - V_C) \tag{4.20}$$

where a is a coefficient ($a = 0.025$ based on the experimental results) and V_C is the critical entrainment velocity at a certain flow depth.

The above shows the variation pattern of V_r from mesoscopic and macroscopic perspectives. A combined analysis finds that the macroscopic velocity of a self-aerated flow affects V_r by altering the mesoscopic size of the air bubbles. In a self-aerated flow, V_r increases with the flow velocity, suggesting that the mean size of the air bubbles in a self-aerated flow increases with the flow velocity. An increase in the turbulence intensity of a flow can allow its free surface to entrain air and produce relatively large air bubbles. Additionally, the internal air-carrying capacity of a flow increases with the velocity. Relatively large air bubbles can exist more stably in a flow and move with it.

The generalized V_r can be considered to characterize the intensity of the continuous escape of the entrained air through the free surface of the flow under buoyancy. Previous studies have demonstrated that the air-bubble size is the factor that directly affects the generalized V_r. Current studies on the air-bubble size probability distribution in self-aerated flows show that d_{ab} ranges mainly from 0.5 to 10 mm in water. The corresponding V_r ranges from 0.1 to 0.3 m/s, as shown in Fig. 4.10.

Based on the above-determined generalized V_e and V_r combined with the basic equations for self-aerated flows, the cross-section-averaged concentration of entrained air, C_{mean}, in a self-aerated flow along the course can be calculated. The amount of entrained air q_a at a distance of x from the inception point of self-aeration is calculated as follows:

$$q_a = \int_0^{s=x} (V_e - V_r \cdot \cos\alpha) \mathrm{d}s \tag{4.21}$$

C_{mean} at the corresponding location is defined as $\overline{C_{mean}} = q_a/(q_a + q_w)$.

For a real-world aerated flow, the air-water structure resulting from aeration is very complex and consists of nonspherical, irregular granular air bubbles, water-bearing air pockets, and a highly twisted air-entraining free surface. Killen (1969) as well as Wilhelms and Gulliver (2005) proposed a generalized vertical self-aerated flow structure based on the various forms of open-channel flow aeration. They noted that the air carried by a self-aerated flow should consist of two components, namely, the granular air bubbles (entrained air) and "entrapped air" between the depressions and the deformed free surface. The total amount of these two components constitutes the concentration of entrained air C_a in the flow. Thus, it is necessary to modify the abovementioned theoretical calculated value of C_{mean}:

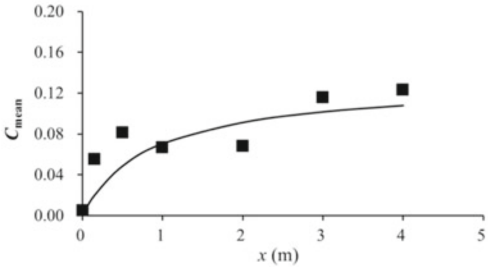
$$C_{mean} = K_C \cdot \overline{C_{mean}} = K_C \cdot \frac{q_a}{q_a + q_w} \tag{4.22}$$

where K_C is a correction coefficient. Based on previous measurements of C_{mean} directly related to the slope α of the open channel (Killen 1969; Cain 1978; Xi 1988; Chanson 1997; Wei et al. 2016), the relationship between K_C and α is established:

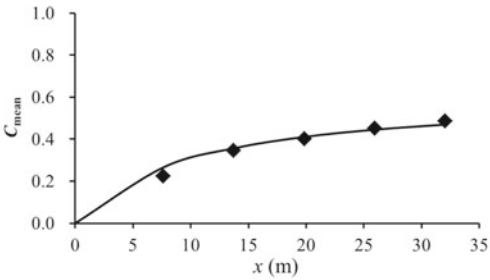
$$K_C = 1.68 \cdot [\tanh(\sin\alpha)]^3 + 0.15 \quad (4.23)$$

K_C increases as α increases. This means that the impact of the difference in the air-water structure on the theoretical analysis of C_a gradually weakens. An increase in α can facilitate the formation of a more uniform air-water mixture. This is in line with the previous findings on the effects of α on aeration.

Figure 4.11 compares the values of C_{mean} along the course calculated using Eq. (4.21) and experimental measurements. As demonstrated in Fig. 4.11, the calculated and measured values exhibit basically consistent trends. Specifically, the gradient of change in C_{mean} is relatively large during the initial self-aeration development. As the self-aeration continues to develop along the course, there is a gradual decrease in the gradient of change in C_{mean}, and uniform aeration is gradually reached. In addition, the errors in C_{mean} are relatively small. This suggests that it is, to some extent, reasonable to analyze the development of and variation in self-aeration based on this generalized model and that this model can reflect the basic physical process of the formation of an air-water two-phase flow as a result of the free-surface aeration in an open-channel flow.



(a) Experimental data obtained from Chanson (1997): flow velocity V_0=5.00 m/s, slope α=4°, and q_w=0.15 m^2/s



(b) Prototype data obtained from Cain (1978): flow velocity V_0=14.21 m/s, slope α=45°, and q_w=2.16 m^2/s

Fig. 4.11 Comparison of calculated and measured values of C_{mean} in self-aerated flows

4.3 Critical Condition for Surface Aeration of High-Velocity Flows

4.3.1 Critical Condition for Air Entrainment of Free-Surface Depressions in Flows

The above analysis shows that mean flow velocity and flow depth are flow conditions that affect the free-surface deformation. When the theoretical maximum extent of the free-surface deformation exceeds the critical condition required for aeration, air entrainment and aeration occur. This critical condition is represented by the following equation:

$$r_{\mathrm{m}} \leq r_{\mathrm{C}} \tag{4.24}$$

Figure 4.12 shows two types of free-surface shape evolution under turbulence. (1) When the maximum extent of deformation of a local region of the free surface of an open-channel flow under the action of the transverse fluctuation velocity exceeds the extent of deformation required for air entrainment and aeration (i.e. $r_{\mathrm{m}} < r_{\mathrm{C}}$), the depressed free surface will become unstable and loose after exceeding the critical aerated state and will become closed as a result of the difference between the local fluctuation velocities of the upstream and downstream regions. This will lead to the entrainment of an air bubble in the water. (2) When the maximum extent of deformation of a local region of the free surface of an open-channel flow under the action of the transverse fluctuation velocity is smaller than the extent of deformation required for air entrainment and aeration, the free surface will remain smooth and intact throughout the depression process and will not become loose and disorderly.

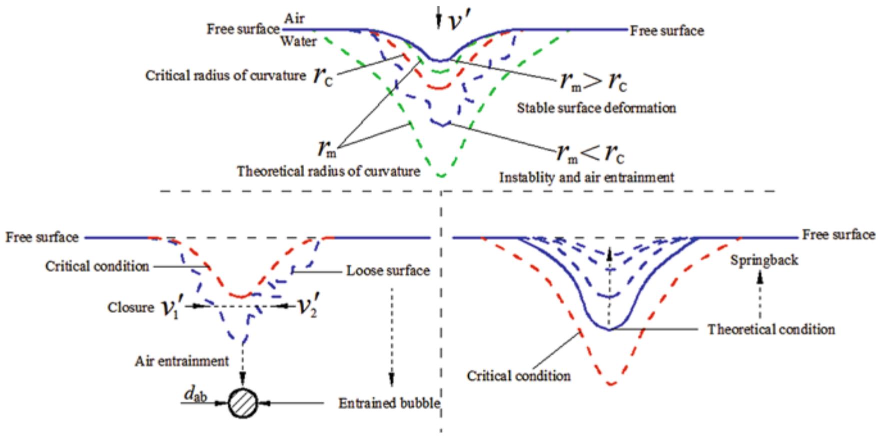


Fig. 4.12 Two development and variation processes of free-surface depressions

The free surface will recover to the initial depressed state under the action of surface tension after reaching the maximum deformation. While the free surface is deformed, air entrainment and aeration will not occur.

Figure 4.13 shows the patterns of change in the critical curvature radius r_C (Eq. (4.11)) and the theoretical maximum curvature radius r_m (Eq. (4.15)) corresponding to air-bubble entrainment in a flow at various mean flow velocity and flow depth values. The following can be derived from the patterns of change in r_C and r_m:

(1) As the mean flow velocity and flow depth increase, there is a gradual decrease in r_m. This suggests a gradual increase in the theoretical extent of deformation of the free surface and is reflected by the increasingly notable development of an "uneven" free-surface shape and a continuous increase in the surface roughness.

(2) There is an extremely small r_C at a relatively low flow velocity. This suggests that it is relatively difficult for free-surface aeration to occur under this condition. As the flow velocity increases, there is a rapid increase in r_C. This suggests a gradual decrease in the dependence of the free-surface aeration on the deformation. An increase in the flow velocity is accompanied by an increase in the turbulence intensity of the flow, making self-aeration easier. At a constant flow velocity, as the flow depth increases, there is a gradual decrease in r_C. This indicates that an increase in the flow depth will raise the critical condition required for free-surface aeration and render self-aeration more difficult. This is because at a constant mean flow velocity, according to the equation for the cross-sectional distribution of the friction velocity v_τ, as the flow depth increases, there is a decrease in the v_τ near the free surface, a decrease in the fluctuation velocity, a decrease in the turbulence intensity, a decrease in the corresponding turbulent energy, and a decrease in the surface free energy E_σ of a single depression formed under turbulent action to entrain air into and aerate the free surface (i.e. the turbulent action can destabilize a depression and entrain air bubbles into

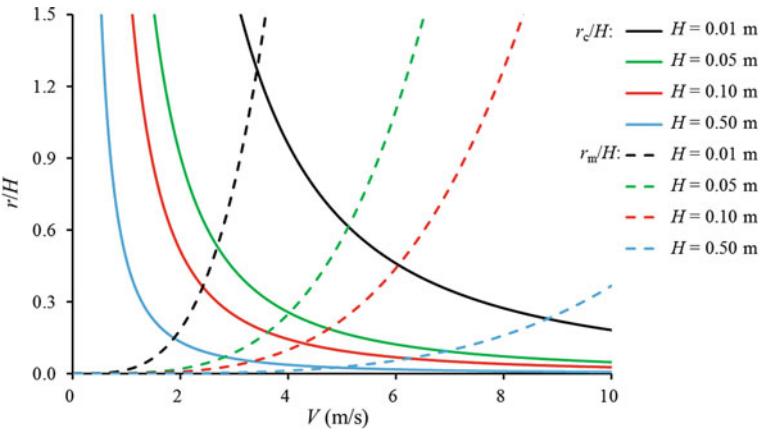


Fig. 4.13 Comparison of the critical and theoretical values of the curvature radius of a free-surface depression

the water only when the depression is significant). Thus, a stricter free-surface deformation condition is required for aeration at a relatively large flow depth.

(3) A comparison of the r_C and r_m curves in Fig. 4.13 finds the following. At a relatively low mean flow velocity (V < 2.5 m/s), the r_m curve is above the r_C curve, i.e. $r_\mathrm{m} > r_C$. This suggests that the theoretical maximum extent of deformation of the free surface of the flow is smaller than the critical extent of deformation required for aeration, and consequently, no free-surface aeration will occur. At a relatively high mean flow velocity (V > 3.5 m/s), the r_m curve is below the r_C curve. This suggests that the theoretical maximum extent of deformation of the free surface of the flow is greater than the critical extent of deformation required for aeration. The theoretical deformation of the free surface can become more significant. During the deformation process, as the free surface is unable to overcome the turbulent energy and becomes unstable in local regions, free-surface aeration will occur. Here, the mean flow velocity corresponding to the point of intersection of the two curves of each pair is treated as the critical flow velocity (V_C) required for self-aeration (Wei et al. 2017), i.e. $r_\mathrm{m} = r_C$. For a mean flow depth H in the range of 0.05–1.00 m, the V_C under theoretical conditions ranges from approximately 3.36–5.19 m/s. This is consistent with the phenomena observed in experiments and engineering practice— self-aeration can be observed in an open channel at flow velocities of 3–4 m/s. Figure 4.14 shows the V_C–H relationship obtained based on this generalized self-aeration model for open channels. As demonstrated in Fig. 4.14, as H increases, there is an increase in V_C, suggesting that an increase in H is unfavorable to self-aeration. This is consistent with the phenomenon observed in engineering practice— the inception point of self-aeration moves downstream as the hydraulic head increases; i.e. as the flow depth increases, an increase in flow velocity is required for self-aeration to occur. V_C and H approximately satisfy the following equation:

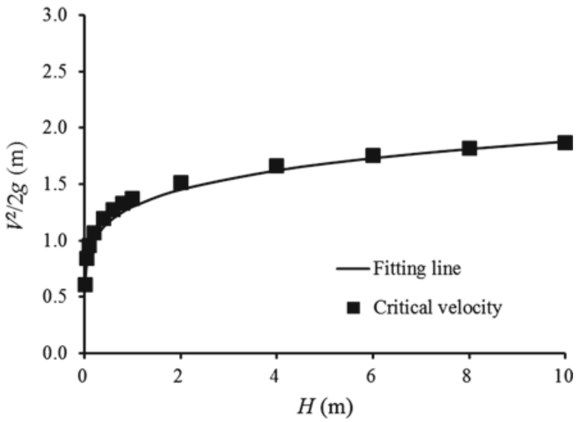


Fig. 4.14 Pattern of change in the critical velocity of free-surface aeration

$$\frac{V_C^2}{2g} = 1.3 \cdot H^{0.16} \tag{4.25}$$

It is worth noting that the above two-dimensional (2D) generalized turbulent deformation and air entrainment and aeration models for the free-surface of an open channel are only theoretical results. The critical aeration conditions obtained using these models reflect the capacity of the free surface to deform and become unstable as well as to entrain air and become aerated under flow conditions. However, the entry of the air bubbles formed as a result of aeration in the water is affected by the randomness of turbulence. Consequently, after becoming depressed and unstable, the free surface exhibits a loose shape. Air bubbles can be entrained into the water only if the surfaces on the two sides of a depression are closed when moving in a disordered manner. During this process, if the free surfaces on the two sides of the depression are not closed, no air bubbles will be entrained into the water. Thus, the process in which a turbulent surface depression becomes unstable and entrains air bubbles is also affected by the intrinsic properties of the turbulent flow.

4.3.2 Air-Bubble Entrainment Characteristics of Free-Surface Depressions in Flows

Figure 4.15 shows three typical air entrainment and aeration processes resulting from a free-surface closure when local free-surface depressions in a flow became depressed and unstable. These three processes led to the formation of air bubbles of various sizes ((a) $d_{ab} = 4.3$ mm, (b) $d_{ab} = 2.5$ mm, and (c) $d_{ab} = 8.6$ mm), which

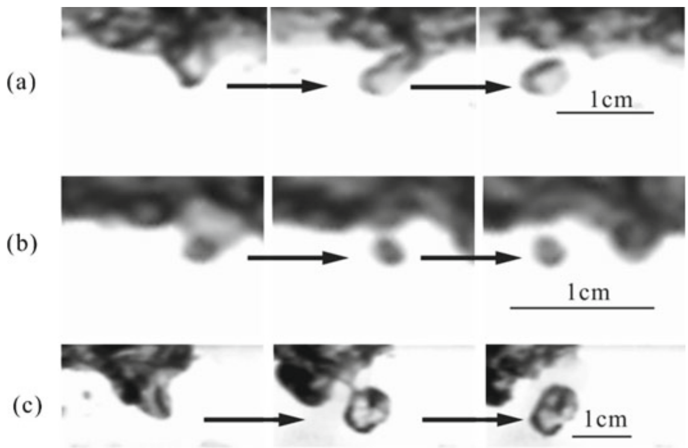


Fig. 4.15 Instability of the free-surface depressions and formation of air bubbles: **a** $d_{ab} = 4.3$ mm; **b** $d_{ab} = 2.5$ mm; **c** $d_{ab} = 8.6$ mm

subsequently entered the water. As demonstrated in Fig. 4.15, during the closure-induced air-bubble entrainment process, the closure could either occur in the middle of the depression along the flow depth direction or near the free surface. The form of each free-surface depression became unstable as it developed from the incipient state to beyond the limit state. Within an extremely short period of time (approximately 10^{-3}–10^{-2} s), the shape of each depression changed significantly. This suggests that the surface tension was unable to overcome the action of turbulence and the difference between the pressures of the two sides. This sharp change in shape was a result of the randomness of turbulence. Air-bubble entrainment occurred as a result of the closure of the free surface on the two sides of the depression during the instability process under the turbulent action. This process can be summarized as follows: limit turbulent depressed deformation → unstable and irregular deformation → closure of the free surface on the two sides.

Through the analysis of the air-bubble entrainment observed in the experiments, the relationship between the size (represented by d_{ab}) of the air bubbles entrained in the water and the actual curvature radius r of the turbulent free-surface depression before becoming unstable was determined (Fig. 4.16). As demonstrated in Fig. 4.16, the r values corresponding to small ($d_{ab} < 5$ mm) air bubbles are distributed in a notably wider range than those corresponding to large ($d_{ab} > 5$ mm) air bubbles. The d_{ab}–r relationship is analyzed as follows. The r at the apex of the Gaussian curve is defined as $L^2/(8y)$, which consists of two components, namely, the shape scale L and the shape feature L/y. L represents the overall scale of a local free-surface depression. The greater L is, the larger the depression is. L/y represents the overall shape of a local free-surface depression. The greater L/y is, the more notable the "wide–shallow" shape of the depressed deformation. The smaller L/y is, the more notable the "narrow–deep" shape of the depressed deformation. The difference between the sizes of the entrained air bubbles can be explained from these two aspects.

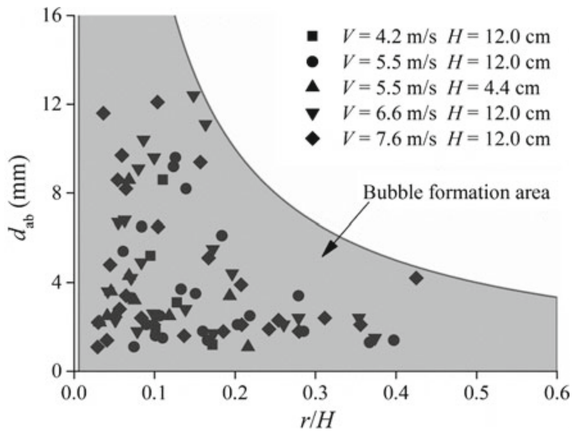


Fig. 4.16 Relationship between the curvature radius of depression shape, r, and the size of the entrained air bubble, d_{ab}

1. The d_{ab} of an entrained air bubble is mostly directly related to the L of the free-surface depression. The smaller L is, the smaller the d_{ab} of the air bubble is. The greater L is, the easier it is for a relatively large air bubble to form.
2. When L remains unchanged, the r of a "wide–shallow" depression is greater than that of a "narrow–deep" depression. This suggests that a "narrow–deep" depression is more concave and more prone to closure as its shape becomes unstable, which leads to the entrainment and formation of an air bubble. Two conditions need to be taken into consideration.

(1) The entrainment of large air bubbles requires the flow to have sufficient air-carrying capacity near the free surface. This in turn requires relatively strong local turbulence, which leads to more significant deformation, i.e. a relatively small r.

(2) There is uncertainty in the location of closure after a depression becomes unstable. Turbulent motion is intrinsically random. As a result, a free-surface depression exhibits a loose shape after becoming unstable. Here, an analysis is performed from two aspects, namely, the depression shape and fluctuation velocity. The free-surface regions on the two sides of the bottom of a depression are relatively close to one another. As a result, there is a relatively high probability for closure to occur between these free-surface regions. This factor is more pronounced for a "narrow–deep" depression. The free-surface regions on the two sides of the top of a depression are relatively far from one another. As a result, it is relatively difficult for closure to occur between these free-surface regions.

Thus, it can also be inferred that the aeration caused by the instability of a free-surface depression is more likely to result in the formation of a small air bubble than a large air bubble. This is in line with previous findings on the d_{ab} probability distribution in aerated flows (Chanson 1997).

The above analysis shows that free-surface aeration in an open-channel flow is notably related to its shape evolution. Under turbulent action, the evolution of free-surface deformation is closely related to the turbulence properties. Turbulent motion is composed of numerous interrelated vortices of varying size and intensity. Each parameter of turbulent motion changes in an irregular manner with time and appears to be disorderly and to change rapidly. In addition, each of these parameters exhibits non-permanence of varying frequencies, periods, and scales. Consequently, a free-surface depression exhibits a loose shape after becoming unstable. An air bubble can be entrained into the water only when the surfaces in disorderly motion on the two sides of a depression close. During this process, if the free surfaces on the two sides of the depression do not close, then no air bubble will be entrained in the water. Thus, the process in which a surface depression in a turbulent flow becomes unstable and entrains an air bubble is also affected by the intrinsic properties of the turbulent flow.

4.3.3 Comparison of Calculated and Experimental Results

First, the free-surface shape evolution corresponding to air entrainment and aeration is comparatively analyzed. In a high-velocity, highly turbulent open-channel flow, the shape of a local depression formed as a result of the turbulent action of the free surface is unavoidably affected by the shape of the surrounding free surface as well as the turbulent conditions. Thus, due to the constraint exerted by the surrounding environment, the actual shape of a free-surface depression is unable to reflect the theoretical shape of the Gaussian curve at the corresponding fluctuation velocity. The actual values of the width L and depth y are often lower than their respective corresponding theoretical values (L^* and y^*), i.e. $L \leq L^*$ and $y \leq y^*$. In Fig. 4.17, a fitted Gaussian distribution curve is used as the ideal depression shape. The Gaussian curve parameters corresponding to this ideal shape are used to analyze the shape evolution of the free surface. The following shows the basic form of the Gaussian function used to depict the depression:

$$y_L = \frac{-1}{\sqrt{2\pi}\sigma} \exp\left[-\frac{L_y^2}{2\sigma^2}\right] \tag{4.26}$$

The location of the lowest endpoint on the axis of symmetry is used to represent y^*. L^* is determined using the "3σ principle" of the Gaussian function, i.e., the curve range excluding the two sides of the "low-probability" range is used as the curve width L^* ($L^* = 2 \times 3\sigma$). Then, the curvature radius r corresponding to the shape of the local free-surface depression under this condition is calculated based on y^* and L^*.

Figure 4.18 shows the patterns of change in r during air entrainment caused by eight local free-surface depressions in the corresponding time periods. This process involved both relatively small ($d_{\text{ab}} = 1.7$ mm) and large ($d_{\text{ab}} = 8.6$ mm) air bubbles. The following depression-induced air-entrainment and aeration characteristics can be observed in this process:

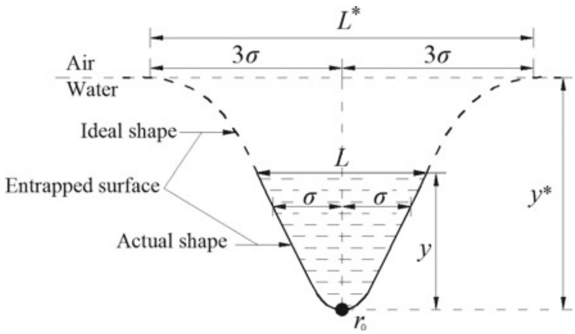


Fig. 4.17 Actual and ideal shapes of a free-surface depression

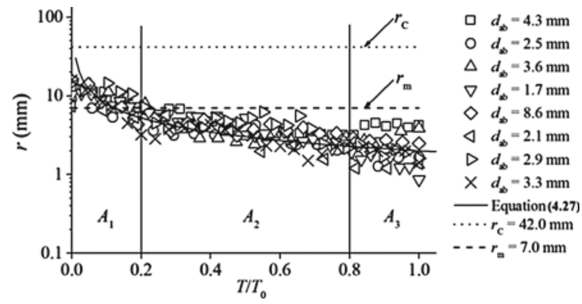


Fig. 4.18 Patterns of change in the curvature radius r as a free surface underwent depressed deformation and became unstable

1. During the inception and initial formation stages of a free-surface depression, r was relatively large, and the free surface was relatively insignificantly deformed. In addition, within a relatively short period of time ($A_1 \approx T/T_0 < 0.2$, approximately corresponding to a time scale of 10^{-3} s), there was a rapid decrease in r and a sharp increase in the extent of deformation. The following was found through statistical analysis of the experimental observations. On the one hand, r was basically smaller than r_C under the corresponding flow conditions. This suggests that the depression was significant enough to destabilize the free surface and equip it with the capacity to form closures and entrain air bubbles. On the other hand, r was basically greater than r_m under the corresponding flow conditions. The free surface did not reach the theoretical maximum deformation.
2. During the formation and development stages of a free-surface depression, there was a gentle change in r, and $A_2 \approx 0.2 < T/T_0 < 0.8$. In addition, the extent of deformation gradually stabilized. During this process, $r < r_m$. This suggests that in the actual flow, the turbulent depressed deformation of the free surface during the air-entrainment and aeration process was more significant than the theoretical deformation as a result of the turbulence and the shape deformation of the free surface in the adjacent regions. During the last phase of development when an air bubble was about to form, similar extents of free-surface deformation were observed in the air-entrainment processes corresponding to air bubbles of varying sizes, i.e. $r = 2$ to 3 mm.
3. After the depressed deformation of the free surface became unstable during the last phase of development, r remained basically unchanged as time passed. In addition, the extent of deformation of the free surface was relatively small, whereas the extent of dispersion of the free surface increased somewhat. This is primarily due to two factors. According to the previous analysis, the instability process primarily involved the shape evolution of the deformation, e.g. the loosening and fluctuation of the free surface on the two sides of the depression. Moreover, each characteristic of the turbulence changed in an irregular manner with time and appeared to be disorderly and to change rapidly. In addition, each of these characteristics exhibited non-permanence of varying frequencies, periods, and scales. Consequently, the air entrainment and aeration varied to a certain extent during the instability process.

4. During the air-entrainment process induced by a local free-surface depression, the changes in r with time followed the power function distribution given in the equation below:

$$r \sim a_0 \cdot \left(\frac{T}{T_0}\right)^{-b_0} \tag{4.27}$$

where the coefficients a_0 and b_0 are greater than zero. When $T \to 0$, $r_0 \to \infty$ (r_0 is the initial state of entrapped surface). This suggests that the free surface is assumed to be relatively flat and move along the mean flow velocity direction before a local depression is formed and that when the free-surface depression is close to becoming unstable (i.e. $T/T_0 \to 1$), r_0 tends to be a stable constant, which is the deformation condition required for air entrainment and aeration under the corresponding flow conditions.

The shape evolution of the free surface of a high-velocity flow under turbulence in a local region is the direct cause of air entrainment and aeration. The turbulence intensity and the shape of the free surface in a local region both directly affect the size of the air bubble entrained into the water. An increase in the local turbulence intensity increases the overall intensity of the deformation of the free surface. On the one hand, an increase in the local turbulence intensity results in a relatively large critical extent of deformation for the free surface, which in turn renders the formation of a relatively large air bubble possible. On the other hand, strong turbulence renders a local depression more prone to closure at its bottom. This will increase the probability for a small air bubble to form. Figure 4.19 shows the statistical relationships between d_{ab} and the intensity and scale of deformation within a test range (Wei and Xu et al. 2019). As demonstrated in Fig. 4.19, d_{ab} gradually increased with the turbulence intensity and critical deformation intensity. The maximum d_{ab} was on par with the scale of the free-surface depression. In addition, small air bubbles accounted for

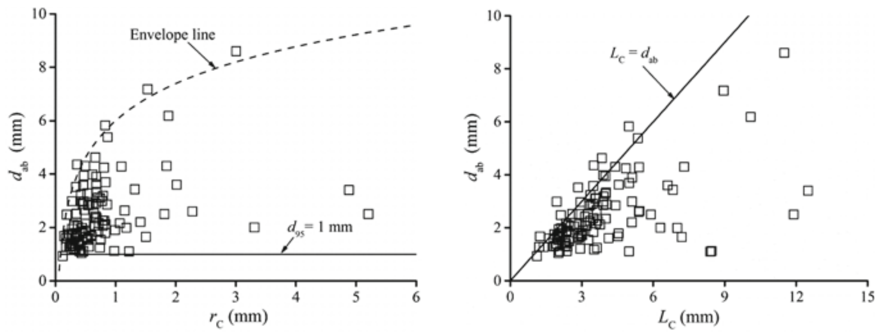


Fig. 4.19 Patterns of change in the curvature radius r as a free surface underwent depressed deformation and became unstable

a relatively large proportion of all the air bubbles. The smallest air bubbles were basically larger than those of the critical d_{ab} that could be formed by shear flow.

Furthermore, a comparative analysis of the critical entrainment velocity V_C in high-velocity open-channel flows was performed. To date, numerous researchers have studied free-surface aeration conditions for open-channel flows and proposed a variety of methods to determine whether free-surface aeration will occur in a flow. Ehrenburger (1927) was the first to propose a method that uses the cross-section-averaged V_C as the critical condition and noted that free-surface aeration begins to occur in a flow at a mean flow velocity V of 3.5–4.5 m/s. Subsequently, continuous research has been conducted to examine the V_C in high-velocity open-channel flows. Through laboratory model tests and prototype observations, V_C has been found to generally range from 3 to 6 m/s in a flow. However, a range of 7–8 m/s has often been found from theoretical analysis under interfacial wave-breaking conditions. Evidently, it is necessary to determine the V_C in a flow based on its intrinsic aeration conditions, i.e. the response of the turbulent development of its free surface to V at flow depth H. Table 4.1 compares the V_C values of flows obtained from theoretical analysis and the real-world V values under various H and slope α conditions obtained in various studies. When the real-world V is greater than V_C, free-surface aeration is considered to have occurred. In addition, this conclusion is compared with the real-world situation. As demonstrated in Table 4.1, all the methods that determine V_C in a flow based on the shape evolution of its free surface are able to relatively satisfactorily predict the aeration in real-world open-channel flows in hydraulic engineering practice.

4.4 Calculation of Concentration Distribution for Surface Aeration of High-Velocity Flows

4.4.1 Regional Characteristics of Surface Aeration in High-Velocity Flows

In the cross-sectional air-water mixture region of an aerated flow, the distribution gradient of the entrained air concentration C_a is relatively significantly affected by the extent of aeration. As demonstrated in Fig. 4.20, at a relatively low slope α ($< 45°$), the extent of the surface self-aeration is relatively small (Anderson 1955; Chanson 1995; Wei 2015), and there is often a clear-water region in the water–air cross-section. With regard to the C_a distribution gradient, there is a symmetrical distribution of C_a around a value of 0.5 in the cross-section. As α increases, there is an increase in the extent of aeration, and the cross-sectional clear-water region disappears. Under this condition, the C_a distribution gradient deviates from the original symmetrical distribution pattern below the value of 0.5 in the cross-section and gradually decreases. In contrast, the C_a distribution gradient remains basically unchanged above the value of 0.5 in the cross-section (i.e. in the aerated region close to the upper free surface).

Table 4.1 Comparison of the critical entrainment velocities for free-surface aeration in open-channel flows

Data source	Slope α, °	Flow depth H, m	Real-world flow velocity V, m/s	Critical entrainment velocity V_C, m/s	Real-world situation	Prediction
Wu	8.5	0.063	4.75	4.15	Aerated	Aerated
	8.5	0.089	5.67	4.28	Aerated	Aerated
	8.5	0.048	2.75	4.04	Non-aerated	Non-aerated
	8.5	0.119	3.22	4.39	Non-aerated	Non-aerated
	8.5	0.129	3.27	4.42	Non-aerated	Non-aerated
Rao	9.13	0.030	4.15	3.87	Aerated	Aerated
	14.33	0.026	4.77	3.81	Aerated	Aerated
	14.33	0.031	5.34	3.88	Aerated	Aerated
	25.15	0.022	5.65	3.75	Aerated	Aerated
Big Hill Chute	4.16	0.152	4.87	4.48	Aerated	Aerated
	4.16	0.163	5.04	4.5	Aerated	Aerated
No. 1 tunnel spillway of the Sanmenxia Dam	0.62	9.471	13.73	6.03	Aerated	Aerated
	0.62	9.338	13.68	6.03	Aerated	Aerated
Halbronn	1.83	0.049	2.45	4.05	Non-aerated	Non-aerated
	14	0.026	4.63	3.81	Aerated	Aerated
Kittitas	33.16	0.178	12.58	4.54	Aerated	Aerated
	33.16	0.524	22.27	4.94	Aerated	Aerated
Ai	4.16	0.197	6.10	4.58	Aerated	Aerated
Straub	7.5	0.073	5.42	4.2	Aerated	Aerated
	15	0.058	6.78	4.12	Aerated	Aerated
	15	0.093	8.55	4.29	Aerated	Aerated
Cain	45	1.520	16.00	5.34	Aerated	Aerated
	45	1.940	18.2	5.43	Aerated	Aerated
Spring Gully chute	5.28	0.099	5.08	4.32	Aerated	Aerated
	5.28	0.113	5.45	4.37	Aerated	Aerated
Werribee Weir	8.97	0.034	4.15	3.91	Aerated	Aerated
	45	0.042	5.00	3.99	Aerated	Aerated

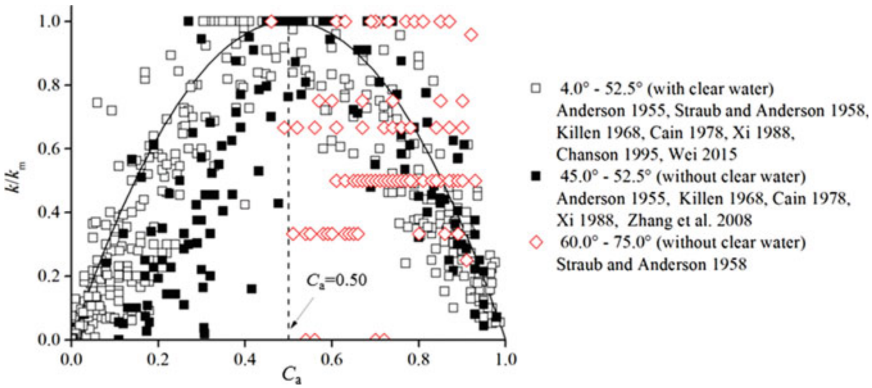


Fig. 4.20 Cross-sectional C_a gradient distribution patterns

A further increase in α results in a very large extent of aeration. Under this condition, C_a can often reach close to 0.5 at the bottom (Straub and Anderson 1958), and its distribution gradient is similar to the original pattern near the free surface. Thus, the use of the location of the C_a value of 0.5 in the cross-section (i.e. y_{50}) as a characteristic location or characteristic flow depth to analyze the surface self-aeration in a high-velocity flow is very significant.

Based on the above analysis, the location at $C_a = 0.50$ (i.e., y_{50}) is used to divide the cross-sectional water–air structure of an aerated flow. Above y_{50} (i.e. $y > y_{50}$) is a high-C_a region. In this region, C_a is composed primarily of the air within the depression between the regions of the free surface of the flow. Due to the relatively low water content, a process in which the flow in this region diffuses towards the air in the transverse direction under turbulent action can be considered to occur roughly in this region, i.e. the turbulent diffusion of "water in air". Below y_{50} (i.e. $y < y_{50}$) is a low-C_a region. In this region, C_a is composed primarily of the granular air bubbles entrained in the water. Due to the relatively low C_a, a process in which the air bubbles diffuse towards the water in the transverse direction under turbulent action can be considered to occur roughly in this region, i.e., the turbulent diffusion of "air in water". On this basis, the cross-sectional C_a in a self-aerated flow is calculated in this study. Specifically, calculations are performed separately for the regions separated by y_{50} in the cross-section of the aerated flow.

For a 2D self-aerated open-channel flow, the cross-sectional water–air structure can be divided into an upper part and a lower part. In the upper structure, the water droplets formed by the free surface under turbulent action as well as the coarse surface undergo turbulent diffusion in the air. In the lower structure, the air bubbles entrained in the water undergo turbulent diffusion in the water. The boundary between the upper and lower regions is determined based on the proportions of the water and air phases. In the upper region, the air-phase concentration is higher than the water-phase concentration in the flow. In the lower structure, the water-phase concentration is higher than the air-phase concentration in the flow. Thus, the location of $C_a = 0.5$

(i.e. y_{50}) is defined as the boundary between the upper and lower structures ($y > y_{50}$ and $y < y_{50}$ for the upper and lower structures, respectively). In addition, a calculation model is established based on the following assumptions:

(1) Calculations are performed based on the self-aeration development region and a steady uniform flow (i.e. the hydraulic properties (C_a and velocity) of the flow remain constant along the course).
(2) The water- and air-phase velocities are the same in the aerated flow. There is no slip velocity between the water and air phases.
(3) The air bubble has not yet diffused to the bottom of the channel.

The lower air-phase C_{mean} ($(C_{mean})_L$) and the upper water-phase C_{mean} ($(C_{mean})_w$) are defined respectively as follows:

$$(C_{mean})_L = \int_0^1 C_a d\frac{y}{y_{50}} \tag{4.28}$$

$$(C_{mean})_w = 1 - (C_{mean})_u = \int_1^{y_{90}/y_{50}} C_w d\frac{y}{y_{50}} \tag{4.29}$$

where $(C_{mean})_u$ is the upper air-phase C_{mean} and C_w is the water concentration at a certain location. C_a and C_w satisfy the following equation:

$$C_a + C_w = 1 \tag{4.30}$$

First, the theoretical method for calculating the cross-sectional C_a distribution in an infinite domain is discussed as follows:

(1) Lower cross-section ($y < y_{50}$)

The governing equation for a 2D uniform aerated flow is an air-phase continuity equation, which is written in the Cartesian coordinate system as follows:

$$\begin{aligned}
&\frac{\partial C_a}{\partial t} + \frac{\partial}{\partial x}(V_x C_a) + \frac{\partial}{\partial y}(V_y C_a) \\
&= \frac{\partial}{\partial x}\left[(D_{tx})_a \frac{\partial C_a}{\partial x}\right] + \frac{\partial}{\partial y}\left[(D_{ty})_a \frac{\partial C_a}{\partial y}\right] \\
&- \sin\alpha \frac{\partial}{\partial x}(-u_r C_a) - \cos\alpha \frac{\partial}{\partial y}(u_r C_a)
\end{aligned} \tag{4.31}$$

where C_a is the air-phase concentration (i.e. entrained air concentration), V_x and V_y are the time-averaged velocities along (x-direction) and perpendicular (y-direction) to the flow direction, respectively, $(D_{tx})_a$ and $(D_{ty})_a$ are the air-phase turbulent diffusion

coefficients for the x- and y-directions, respectively, u_r is the rising velocity of the air bubble under buoyancy in the y-direction, α is the slope of the channel, and t is the motion duration. In addition, this equation is based on the assumption that an aerated flow is incompressible.

Based on the steady, uniform flow condition, $\partial/\partial x = 0$, and $V_y = 0$. Thus, Eq. (4.31) can be simplified as follows:

$$\frac{\partial}{\partial y}\left[(D_{ty})_a \frac{\partial C_a}{\partial y}\right] - \cos\alpha \frac{\partial}{\partial y}(C_a u_r) = 0 \tag{4.32}$$

According to Chanson's (1995) study, when the air-bubble mass is not taken into account, the square of the u_r of a single air bubble in still water is directly proportional to the pressure gradient, i.e.,

$$(u_r)_H^2 \sim \frac{dp}{dy} \tag{4.33}$$

where $(u_r)_H$ is the rising velocity of a single air bubble in still water and p is the pressure. For an air-water two-phase flow, the cross-sectional pressure gradient distribution satisfies the following equation:

$$\frac{dp}{dy} = \rho(1 - C_a) g \cos\alpha \tag{4.34}$$

where ρ is the density of water and g is gravitational acceleration. Let us assume that the u_r in an aerated flow is as follows:

$$u_r^2 = \left[(u_r^2)_H\right]^2 (1 - C_a) \tag{4.35}$$

By substituting the above equation into Eq. (4.32), we have

$$\frac{\partial}{\partial y}\left[(D_{ty})_a \frac{\partial C_a}{\partial y}\right] = (u_r)_H \cos\alpha \frac{\partial}{\partial y}\left(C_a\sqrt{1 - C_a}\right) \tag{4.36}$$

Here, a dimensionless water depth y' and an air-phase turbulent diffusion coefficient D_a are introduced as follows:

$$y' = \frac{y}{y_{50}} \tag{4.37}$$

$$D_a = \frac{(D_{ty})_a}{(u_r)_H \cos\alpha\, y_{50}} \tag{4.38}$$

By substituting the above equations into Eq. (4.36), we have

$$\frac{\partial}{\partial y'}\left[D_{\mathrm{a}}\frac{\partial C_{\mathrm{a}}}{\partial y'}\right] = \frac{\partial}{\partial y'}(C\sqrt{1-C_{\mathrm{a}}}) \tag{4.39}$$

By integrating and rearranging the above equation, we obtain the following equation for calculating the cross-sectional C_{a} in a flow:

$$C_{\mathrm{a}} = 1 - \tanh^2\left(K_{\mathrm{a}} - \frac{y'}{2D_{\mathrm{a}}}\right) \tag{4.40}$$

where K_{a} is a dimensionless coefficient. Based on the boundary condition ($C_{\mathrm{a}} = 0.5$ when $y' = 1$), we have

$$K_{\mathrm{a}} = \tanh^{-1}(\sqrt{0.5}) + \frac{1}{2D_{\mathrm{a}}} \tag{4.41}$$

Thus, the equation for calculating the C_{a} distribution in the lower cross-section of a self-aerated flow is obtained as follows:

$$C_{\mathrm{a}} = 1 - \tanh^2\left(\tanh^{-1}(\sqrt{0.5}) + \frac{1-y'}{2D_{\mathrm{a}}}\right) \tag{4.42}$$

For D_{a}, based on the mean C_{a} ($(C_{\mathrm{mean}})_{\mathrm{L}}$) in the lower cross-section of a flow ($(C)_{0.5}$), we have

$$(C_{\mathrm{mean}})_{\mathrm{L}} = \int_0^1 C_{\mathrm{a}}\mathrm{d}y' = 2D_{\mathrm{a}}\left[\tanh\left(\tanh^{-1}\sqrt{0.5} + \frac{1}{2D_{\mathrm{a}}}\right) - \tanh\left(\tanh^{-1}\sqrt{0.5}\right)\right] \tag{4.43}$$

When $(C_{\mathrm{mean}})_{\mathrm{L}} \leq 0.3$, $(C_{\mathrm{mean}})_{\mathrm{L}}$ and the corresponding D_{a} approximately satisfy the following equation:

$$D_{\mathrm{a}} = 1.8012(C_{\mathrm{mean}})_{\mathrm{L}}^{1.02} \tag{4.44}$$

(2) Upper cross-section ($y > y_{50}$)

The governing equation for a 2D uniform aerated flow is a water-phase continuity equation, which is written in the Cartesian coordinate system as follows:

$$\begin{aligned}\frac{\partial C_{\mathrm{w}}}{\partial t} + \frac{\partial}{\partial x}(V_x C_{\mathrm{w}}) + \frac{\partial}{\partial y}(V_y C_{\mathrm{w}}) &= \frac{\partial}{\partial x}\left[(D_{tx})_{\mathrm{w}}\frac{\partial C_{\mathrm{w}}}{\partial x}\right] \\ &+ \frac{\partial}{\partial y}\left[(D_{ty})_{\mathrm{w}}\frac{\partial C_{\mathrm{w}}}{\partial y}\right] - \sin\alpha\frac{\partial}{\partial x}(u_{\mathrm{f}}C_{\mathrm{w}}) + \cos\alpha\frac{\partial}{\partial y}(C_{\mathrm{w}}u_{\mathrm{f}})\end{aligned} \tag{4.45}$$

where C_{w} is the water-phase concentration (i.e. water concentration in air), $(D_{tx})_{\mathrm{w}}$ and $(D_{ty})_{\mathrm{w}}$ are the water-phase turbulent diffusion coefficients for the x- and y-directions, respectively, and u_{f} is the falling velocity of the water phase under gravity in the negative y direction. In addition, the above equation is based on the assumption that an aerated flow is incompressible.

Similar to the analysis of the lower cross-section, under the steady, uniform flow conditions, $\partial/\partial x = 0$, and $V_y = 0$. Thus, the above equation can be simplified as follows:

$$\frac{\partial}{\partial y}\left[(D_{ty})_{\mathrm{w}}\frac{\partial C_{\mathrm{w}}}{\partial y}\right] - \cos\alpha\frac{\partial}{\partial y}\ominus - u_{\mathrm{f}}C_{\mathrm{w}}\ominus = 0 \tag{4.46}$$

According to Wood's (1985) study on the u_{f} of water droplets in aerated flows, the u_{f} of water droplets at a certain site is affected by the relative location of the site in the cross-section and the corresponding C_{a}. Let us assume that u_{f} satisfies the following equation:

$$u_{\mathrm{f}} = (u_{\mathrm{f}})_C(1 - C_{\mathrm{w}})\frac{y}{y_{50}} \tag{4.47}$$

where $(u_{\mathrm{f}})_C$ is the assumed falling velocity of a water droplet that jumped from the surface under turbulence before the flow is aerated. As the self-aeration condition is only related to the intrinsic turbulent conditions of a flow, $(u_{\mathrm{f}})_{\mathrm{C}}$ can be considered a constant under the critical aeration condition required for a water droplet to jump out of the surface:

$$\frac{\partial}{\partial y}\left[(D_t)_y\frac{\partial C_{\mathrm{w}}}{\partial y}\right] + (u_{\mathrm{f}})_{\mathrm{C}}\cos\alpha\frac{\partial}{\partial y}\left[(1 - C_{\mathrm{w}})C_{\mathrm{w}}\frac{y}{y_{50}}\right] = 0 \tag{4.48}$$

Here, y' and the water-phase turbulent diffusion coefficient D_{w} are introduced as follows:

$$y' = \frac{y}{y_{50}} \tag{4.49}$$

$$D_{\mathrm{w}} = \frac{(D_{\mathrm{ty}})_{\mathrm{w}}}{(u_{\mathrm{f}})_{\mathrm{C}}\cos\alpha\, y_{50}} \tag{4.50}$$

Through integration and rearrangement, we have

$$\ln\frac{C_{\mathrm{w}}}{1 - C_{\mathrm{w}}} + K_{\mathrm{w}} = -\frac{(y')^2}{2D_{\mathrm{w}}} \tag{4.51}$$

where K_{w} is a dimensionless coefficient. Based on the boundary condition ($C_{\mathrm{a}} = 0.5$ when $y' = 1$), we have

$$K_{\mathrm{w}} = -\frac{1}{2D_{\mathrm{w}}} \tag{4.52}$$

Thus, the equation for calculating the C_{w} distribution in the upper cross-section of a self-aerated flow is obtained as follows:

$$C_{\mathrm{w}} = \frac{1}{1+\exp\left[\frac{(y')^2-1}{2D_{\mathrm{w}}}\right]} \tag{4.53}$$

For D_{w}, based on the mean $(C_{\mathrm{mean}})_{\mathrm{w}}$ in the upper cross-section of a flow $((C_{\mathrm{w}})_{0.5})$, we have

$$(C_{\mathrm{mean}})_{\mathrm{w}} = \int_1^{+\infty} C_{\mathrm{w}}\mathrm{d}y' = \int_1^{+\infty} \frac{1}{1+\exp\left[\frac{(y')^2-1}{2D_{\mathrm{w}}}\right]}\mathrm{d}y' \tag{4.54}$$

When $(C_{\mathrm{w}})_{0.5} \leq 0.4$, $(C_{\mathrm{mean}})_{\mathrm{w}}$ and the corresponding D_{w} approximately satisfy the following equation:

$$D_{\mathrm{w}}{=}0.4725 \cdot (C_{\mathrm{mean}})_{\mathrm{w}}^{1.23} \tag{4.55}$$

The correlation coefficient between $(C_{\mathrm{mean}})_{\mathrm{w}}$ and D_{w} is 0.9965. Thus, based on the relationship between C_{a} and C_{w}, the equation for calculating the C_{a} distribution in the upper cross-section of a self-aerated flow is obtained as follows:

$$C_{\mathrm{a}} = 1 - C_{\mathrm{w}} = \frac{\exp\left[\frac{(y')^2-1}{2D_{\mathrm{w}}}\right]}{1+\exp\left[\frac{(y')^2-1}{2D_{\mathrm{w}}}\right]} \tag{4.56}$$

Second, the theoretical method used to calculate the cross-sectional C_{a} distribution in a finite domain is discussed.

In a self-aerated open-channel flow, as the extent of aeration increases, the air bubbles that have sufficiently diffused to the bottom of the channel will be reflected by the solid boundary in this region as the solid boundary does not absorb air bubbles. As a result of the buoyancy and the difference in concentration, these air bubbles will overcome the action of downward turbulent diffusion and move upwards. Thus, the C_{a} within the affected region along the course should be the sum of the concentration of air bubbles that diffuse downwards and that of the air bubbles that are reflected by the wall and move upwards. This is the characteristic of the concentration distribution of entrained air that diffuses in a finite domain.

The concept of "imaginary diffusion" is introduced to analyze the reflection and diffusion of wall-constrained air bubbles. As C_{a} is distributed continuously along the flow depth direction in the cross-section, when the location of the constraint at

the bottom is not taken into consideration, a continuous distribution range of cross-sectional C_a from 0 to 1 can always be determined, as shown in Fig. 4.21. Thus, when the cross-sectional q_a (i.e. C_{mean}) is known, the corresponding distribution location can be derived from C_{mean} using the direct method for calculating the C_a distribution. Through comparison with the result of the initial direct calculation, the range of the imaginary diffusion can then be determined, as shown in Fig. 4.22. As demonstrated in Fig. 4.22, as C_{mean} increases, there is an increase in the extent of aeration. Specifically, the following can be observed:

(1) When $0 < C_{mean} < 0.2–0.3$, the cross-sectional C_a distribution pattern is primarily a clear-water region-containing distribution pattern and is in line with the distribution pattern in an infinite domain, i.e. when $C_a = 0$, $y/y_{90} \neq 0$.
(2) When $C_{mean} > 0.2–0.3$, the cross-sectional C_a has diffused to the wall, i.e. when $y/y_{90} = 0$, $C_a \neq 0$. At this time point, there exists a relatively pronounced

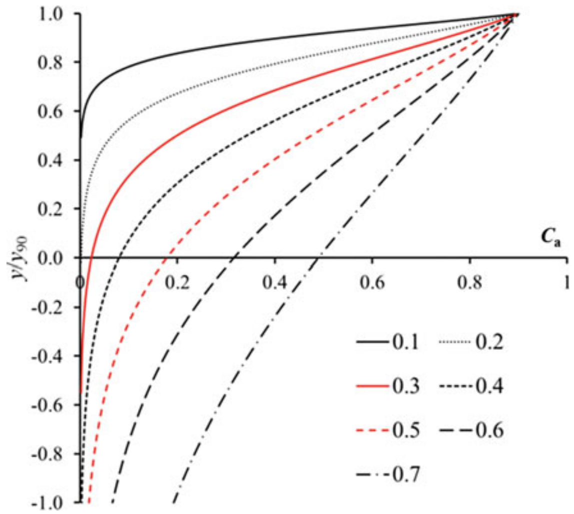


Fig. 4.21 Theoretical cross-sectional C_a distribution patterns at various C_{mean} values (including the effects of imaginary diffusion)

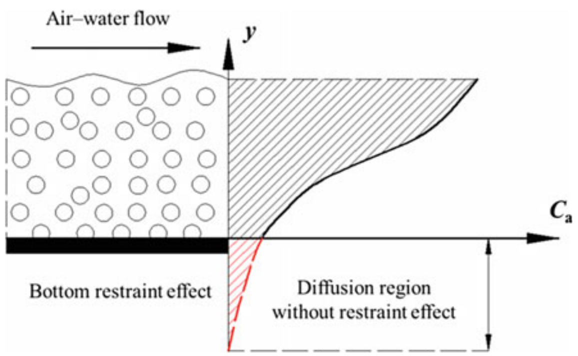


Fig. 4.22 Schematic diagram depicting the effects of imaginary diffusion in the cross-sectional C_a distribution

imaginary diffusion region. The effects of imaginary diffusion must be taken into consideration when calculating the C_a distribution.

For the C_a distribution in a finite domain when full cross-sectional aeration occurs, the initial C_a distribution is first calculated based on C_{mean} to determine the range of imaginary diffusion. The C_a within the range of the imaginary diffusion is added in a "symmetrical" fashion to the calculated value of the initial C_a at the corresponding symmetrical location for correction purposes, as shown in Fig. 4.23. Thus, the actual cross-sectional C_a distribution is obtained.

There are two scenarios when "symmetrically" correcting the C_a in the imaginary diffusion region.

(1) When the region affected by imaginary diffusion is smaller than the cross-section of the aerated flow (0.2 to 0.3 < C_{mean} < 0.5), as a result of being constrained and reflected by the wall, air bubbles move upwards but are unable to reach the initial free surface of the flow, as shown in Fig. 4.24. In this scenario, the reflected air bubbles can be considered to be able to completely remain in the original aerated flow under turbulence. In the calculation process, the C_a in the imaginary diffusion region is directly added in a "symmetrical" fashion to the

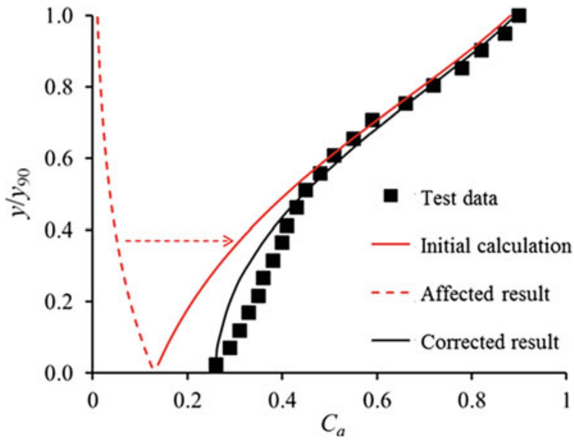


Fig. 4.23 Schematic diagram depicting the calculation of the cross-sectional C_a distribution

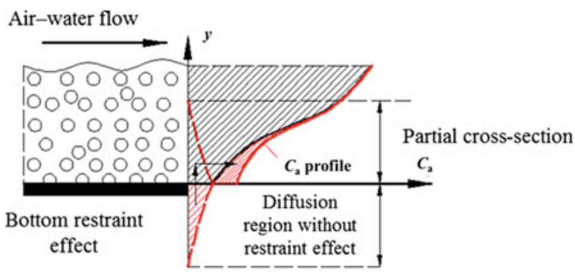


Fig. 4.24 Schematic diagram depicting the effects of imaginary diffusion on the partial cross-section

calculated value of the initial C_a at the corresponding location in the cross-section of the original aerated flow to determine the actual cross-sectional C_a distribution.

(2) When the region affected by imaginary diffusion is larger than the cross-section of the aerated flow ($C_{mean} > 0.5$), as a result of being constrained and reflected by the wall, air bubbles move upwards and are able to reach the initial free surface of the flow, as shown in Fig. 4.25. In this scenario, the effects of the diffusion and motion pattern of air bubbles on the C_a distribution are primarily reflected by its effects on the diffusion intensity. If C_{mean} is assumed to remain constant and air bubbles are assumed to not escape from the free surface, then the air bubbles will, to a certain extent, "uplift" the free surface under buoyancy, i.e., the location of the free surface rises to a certain extent compared to its initial location. Based on the method for calculating D_a in the turbulent diffusion equation, as the location of the free surface (y_{90}) rises, D_a decreases; i.e. the diffusion intensity of the air bubbles decreases. Therefore, when the cross-sectional C_a distribution is calculated while taking into account the effects of imaginary diffusion, it is necessary to reduce the D_a used to calculate the initial C_a, i.e.,

$$D_a^* = \zeta D_a \tag{4.57}$$

where ζ is the correction coefficient for the effects of the imaginary diffusion at the bottom of the channel on the free surface ($\zeta < 1.0$). Based on the data obtained from experiments and the prototype processes, ζ is set to 0.70. In the calculation process, the C_a within the imaginary diffusion region is added in a symmetrical fashion to the initial calculated value of C_a at the corresponding location in the initial cross-section of the aerated flow. Thus, the actual cross-sectional C_a distribution is determined.

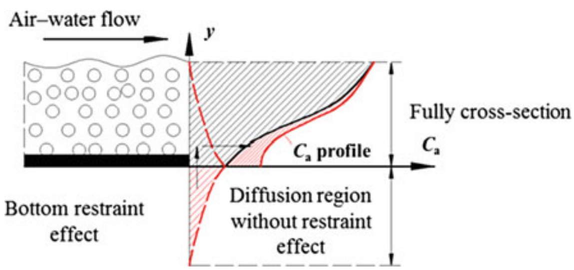


Fig. 4.25 Schematic diagram depicting the effects of imaginary diffusion on the full cross-section

4.4.2 Comparison of the Calculated and Measured Values of the C_a Distribution in High-Velocity Aerated Flows

Figure 4.26 compares the theoretical values of the cross-sectional C_{a} distribution in self-aerated open-channel flows determined using the equations with the corresponding measurements. The values of D_{a} and D_{w} required for the calculations using the equations were derived from the measurements. The comparison finds that in the self-aeration development region, the values of the cross-sectional C_{a} distribution calculated under the assumption that a self-aerated flow is steady and uniform as well as at various extents of cross-sectional aeration along the course are in good agreement with the measurements and are in line with the aeration development and diffusion process.

The above comparison demonstrates the reasonableness of the previous analysis of the air-water structure of a self-aerated flow. For a self-aerated flow, it is necessary to consider two states of aeration, namely, free-surface deformation and granular air bubbles. Even when the self-aeration has evolved to a uniform state, there remains a need to consider the effects of air entrapment resulting from the turbulent deformation

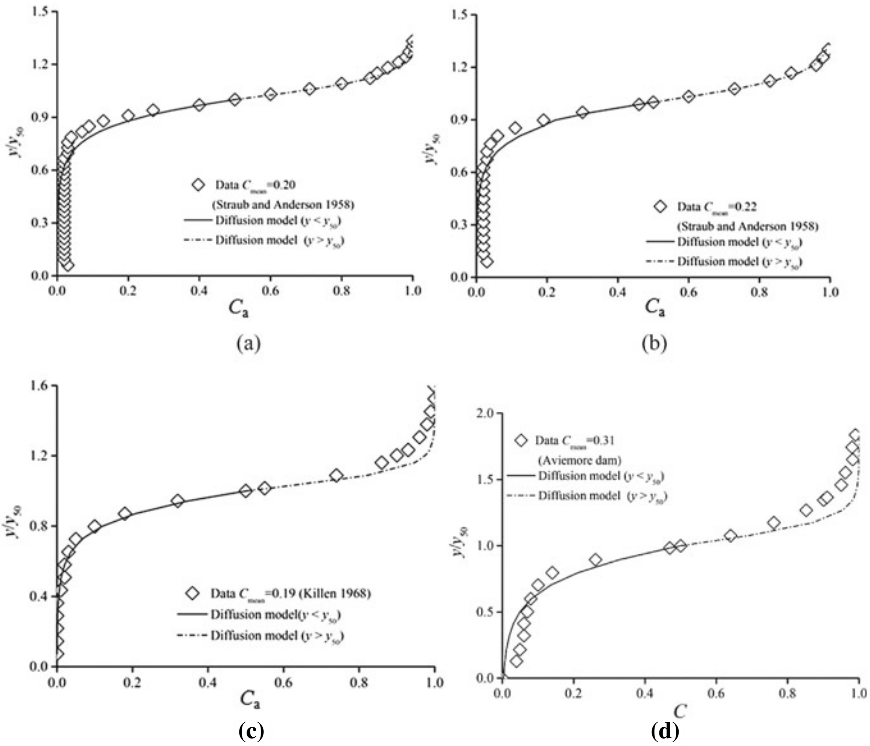


Fig. 4.26 Comparison of the calculated and measured values of the C_{a} distribution

of the free surface on water- and air-phase turbulent diffusion. This is fundamentally different from the calculation of the cross-sectional C_a distribution based on the turbulent diffusion of granular air bubbles or water droplets alone in previous studies.

Note that the two air-water structures of a self-aerated flow are not completely independent of one another. For example, instability will occur when the free-surface deformation reaches a certain extent. During this process, the adjacent free-surface regions will close, which results in the entrainment of an air bubble in the water. Thus, the "entrapped air" evolves into a granular air bubble, as mentioned in the analysis of the air-bubble entrainment mechanism of free surfaces in the previous chapter. Hence, future research on flow self-aeration should be focused on the relationship between the two air-water structures. Figure 4.27 compares the values of the cross-sectional C_a distribution in a finite domain calculated using the abovementioned method with the corresponding measurements. As demonstrated in Fig. 4.27, for full cross-sectional self-aeration, the calculated values of the cross-sectional C_a distribution are in good agreement with the measured values in terms of the trend and numerical magnitude

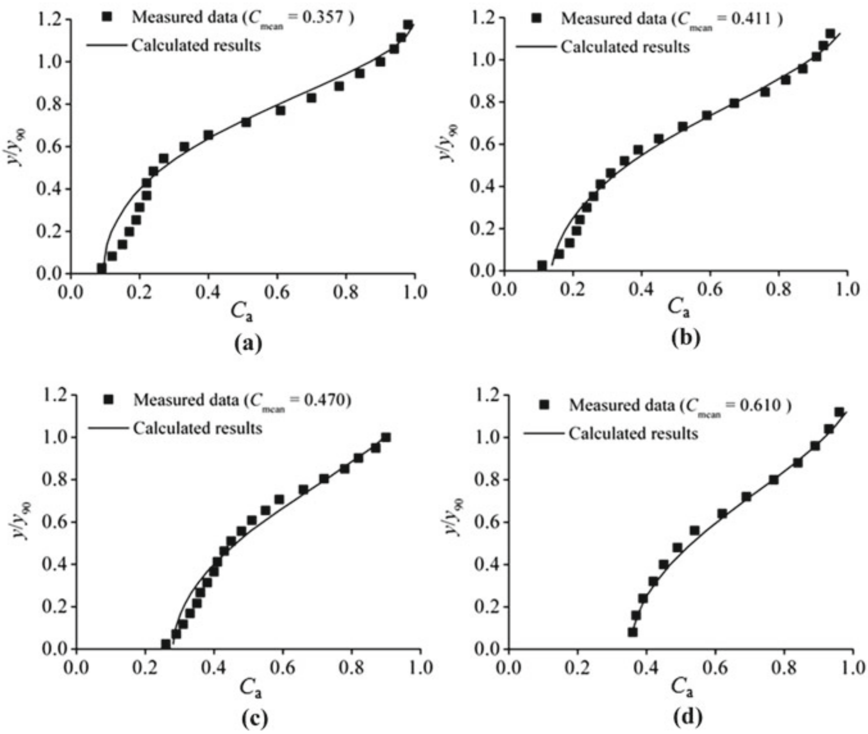


Fig. 4.27 Comparison of the calculated and measured values of the cross-sectional C_a distribution: **a** $(C_{mean})_{calculated\ value} = 0.357$ (Cain, prototype observations, $q_w = 2.23$ m^2/s); **b** $(C_{mean})_{calculated\ value} = 0.411$ (Cain, prototype observations, $q_w = 2.23$ m^2/s); **c** $(C_{mean})_{calculated\ value} = 0.470$ (Cain, prototype observations, $q_w = 2.23$ m^2/s); **d** $(C_{mean})_{calculated\ value} = 0.610$ (Killen, experimental measurements, $q_w = 0.40$ m^2/s)

along the flow depth direction. This suggests that for a self-aeration scenario involving full cross-sectional diffusion of air bubbles, the “imaginary diffusion” approach is reasonable and feasible for the analysis of the effects of the bottom wall of an open channel on the finite-domain diffusion of air bubbles.

4.4.3 Diffusion Pattern of C_a Along the Course

For a self-aerated open-channel flow, the air-bubble diffusion pattern is established under the assumptions of material and turbulent diffusion. As a result, there are two main factors that affect the diffusion of entrained air, namely, the diffusate (air) concentration in the diffuser (water) and the turbulence intensity of the diffuser (water). The effects of the flow velocity and depth on the diffusion of entrained air are mainly reflected by the turbulence intensity of the flow As the flow velocity and depth increase, the bottom edge (i.e. location y_2 in the cross-section where $C_a = 0.02$) of the aerated region extends at an increasing rate towards the bottom plate of the open channel, as shown in Fig. 4.28. With regard to the effects of the extent of the flow aeration on the air-bubble diffusion, as the C_{mean} in the flow increases, there is a notable increase in the rate of change at the bottom edge of the aerated region.

The above analysis shows that the self-aeration development in a flow is affected by three factors, namely, the inflow velocity V_0, flow depth d_0, and C_{mean}. Increasing each of these three factors can enhance the diffusion of air bubbles in the flow and allow the bottom edge of the aerated region to move towards the inner region of the flow, i.e.

$$\frac{y_2}{d_0} \sim f\left(\frac{x}{d_0}, V_0, d_0, C_{mean}, \alpha\right) \tag{4.58}$$

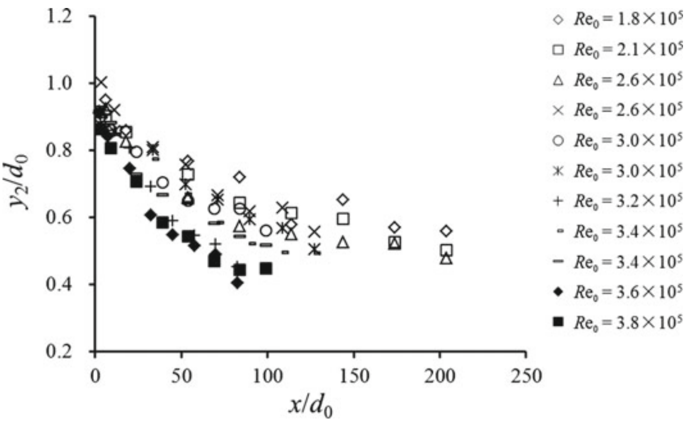


Fig. 4.28 Development of entrained-air diffusion in a free-surface flow along the course

As both V_0 and d_0 affect air-bubble diffusion by affecting the turbulence intensity of a flow, the Reynolds number Re_0, which represents the turbulence intensity of a flow, is used as a characteristic parameter for the development of the bottom edge of the aerated region, i.e.

$$Re_0 = \frac{V_0 D_0}{\nu} \tag{4.59}$$

where ν is the coefficient of the kinematic viscosity of the flow and D_0 is the hydraulic radius of the flow at the initial location of the open channel. Thus, the relationship between the location of the bottom edge of the self-aerated region along the course and hydraulic conditions can be represented by the following equation:

$$\frac{y_2}{d_0} \sim f(\frac{x}{d_0}, Re_0, C_{\text{mean}}, \alpha) \tag{4.60}$$

As self-aeration develops along the course of an open channel, the bottom edge of the aerated region continuously moves towards the inner region of the flow, and air bubbles continuously diffuse towards the inner region of the flow. As the initial turbulence intensity of the flow increases, there is an increase in the capacity of the air bubbles in the flow to overcome the buoyancy under turbulence. This can help increase the diffusion range of the entrained air.

In the cross-section of a self-aerated flow in the aeration development region, the entrained air has yet to reach the bottom of the channel. The cross-section of the flow can be divided into three regions, namely, a water-droplet leaping region, an air-bubble suspension region, and a clear-water region. In the water-droplet leaping region, under turbulence, the water near the free surface has sufficient kinetic energy, which is generated by its transverse fluctuation velocity, to overcome the surface tension and gravity. As a result, the water escapes from the surface and leaps into air in the form of droplets or masses. In the air-bubble suspension region, the air bubbles that have entered the water are suspended while overcoming the buoyancy under turbulence and move with the flow. The C_a in a self-aerated flow is most directly affected by the turbulence intensity. The C_{mean} at each site depends primarily on the turbulence and mixing in the flow. The distribution of the air bubbles and water droplets is similar to the suspension phenomena observed in a sediment-laden flow.

According to the previous analysis of the effects of the flow velocity V_0 and depth d_0 on the development of the aerated region, there is an increase in the size of the aerated region as V_0 and d_0 increase. At a relatively small slope α (< 30°), the water-droplet region of an open-channel flow is relatively small, whereas the air-bubble suspension region is relatively large. This trend becomes more pronounced as the volume flow of water q_w increases. This is in line with the findings of this study. Hence, this demonstrates that C_a is more directly and closely related to the turbulence intensity of a flow under these conditions and that the Re_0 for a flow is directly related to C_{mean}. Thus, the overall relationship between the location of the bottom edge of the aerated region of a flow along the course and its turbulent conditions is established as follows:

$$\frac{y_2}{d_0} \sim f(\frac{x}{d_0}, Re_0, \alpha) \tag{4.61}$$

Based on the experimental measurements taken in this study, the relationship between the location of the bottom edge of the aerated region of an open-channel flow along the course and its initial turbulence conditions is established as follows:

$$\frac{y_2}{d_0} = 1 - m \cdot (\frac{x}{d_0})^{0.5} \cdot Re_0^{0.1} \tag{4.62}$$

where m is an empirical coefficient. Within the experimental range of this study, the m and the initial Re_0 for the flow approximately satisfy the following equation:

$$m = \xi \cdot \exp\left[0.21 \cdot \frac{Re_0^{0.2}}{(\cos\alpha)^{0.5}}\right] \tag{4.63}$$

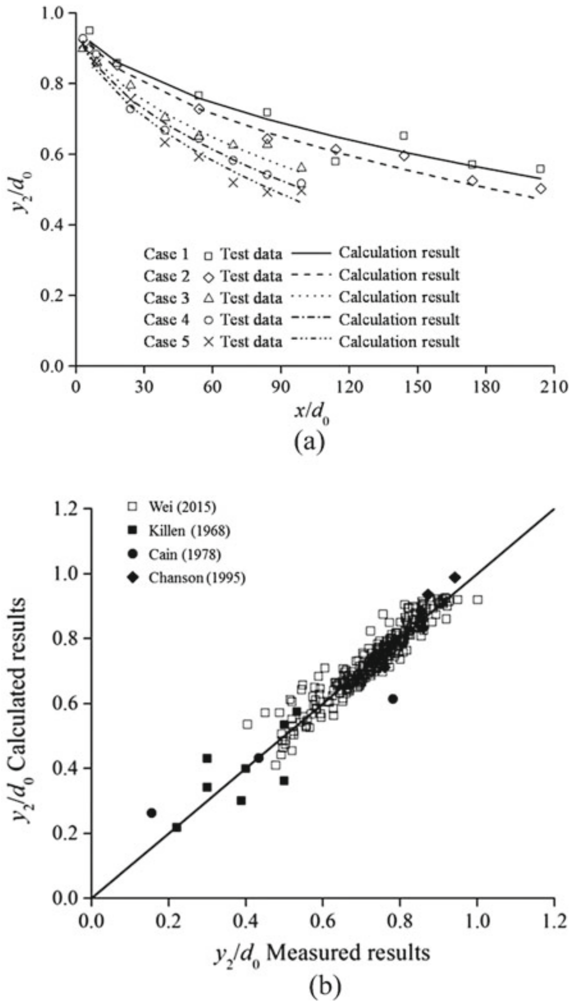
where ξ is an empirical coefficient. According to previous experimental results for changes in the C_a distribution in the aeration development region in self-aerated flows, the value of ξ varies slightly between experimental conditions ($\xi = 0.0008$–0.0012). Figure 4.29 compares the results calculated using the equations and the experimental measurements. As demonstrated in Fig. 4.29, the calculated values can reflect the pattern of change in the location of the bottom edge of the self-aerated region and are in good agreement with the measured values. Calculations can predict the development of the self-aerated region within the experimental range.

4.5 Analysis of Depth and Concentration of Aerated Flows in Engineering Practice

4.5.1 Analysis of Self-Aerated Open-Channel Flows in Terms of H_m

For a high-velocity aerated open-channel flow, the aerated flow depth h_m is an important parameter that affects the flood discharge structure design. Flow aeration results in water expansion. Compared to a non-aerated flow of the same q_w, an air-water mixture has significantly larger flow depth. This increases the engineering design requirements. h_m needs to be determined for a flood discharge structure (e.g., open spillway). An insufficient sidewall-height design will cause the flow to spill over the sidewalls and, thereby, affect the operational safety of the flood discharge structure. For a free-flow tunnel, an insufficient clearance (margin) at the top of the tunnel due to underestimation of the effects of h_m may lead to alternation of pressure and free-surface flow during the discharge process. As a result, the flow will continuously scour the tunnel walls and, thereby, threaten the safety of the tunnel.

Fig. 4.29 Comparison of the predicted and measured results at the bottom edge of the aerated region



The C_{mean} in a self-aerated flow along the course can be calculated based on its initial aeration conditions, i.e. the total unit-width discharge rate q_0 of an air-water two-phase flow along the course can be quantified as:

$$q_0 = q_{\text{w}} + q_{\text{a}} = \frac{q_{\text{w}}}{1 - C_{\text{mean}}} \tag{4.64}$$

If an air-water two-phase flow is treated as a uniform flow, then the corresponding critical flow depth $(h_{\text{k}})_0$ can be determined based on the principle that the cross-sectional unit energy of an equal-width channel flow is the lowest:

Table 4.2 Values of influence factor K_h obtained under various experimental and measurement conditions

No.	α (°)	K_h	Note
1	4	0.24	Model test (Chanson 1997)
2	7.5	0.3	Model test (Straub and Anderson 1958)
3	15	0.255	
4	22.5	0.235	
5	28	0.19	Model test (Wei 2015)
6	30	0.215	Model test (Straub and Anderson 1958)
7	45	0.205	Prototype observations (Cain 1978)
8	45	0.19	Model test (Straub and Anderson 1958)
9	52.5	0.16	Model test (Xi 1988)
10	52.5	0.16	Model test (Killen 1969)
11	60	0.16	Model test (Straub and Anderson 1958)
12	75	0.15	

$$(h_K)_0 = \sqrt[3]{\frac{(q_0)^2}{g}} \tag{4.65}$$

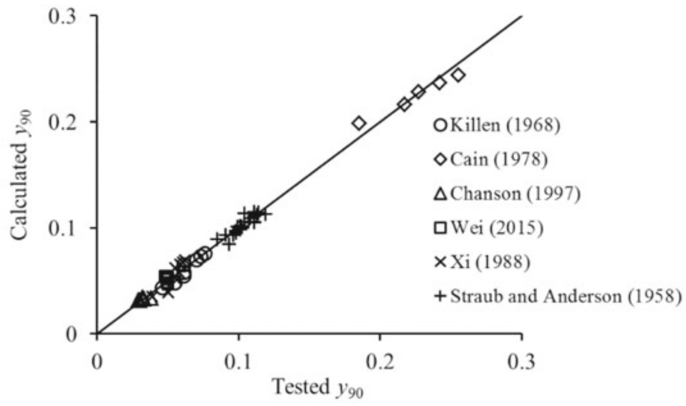
The location y_{90} in the cross-section where $C_a = 0.9$ along the flow depth direction is selected as h_m. Based on experimental measurements and prototype observations in various studies, a linear relationship between $(h_k)_0$ and y_{90} is established as follows:

$$y_{90} = K_h(h_K)_0 = K_h\sqrt[3]{\frac{(q_0)^2}{g}} \tag{4.66}$$

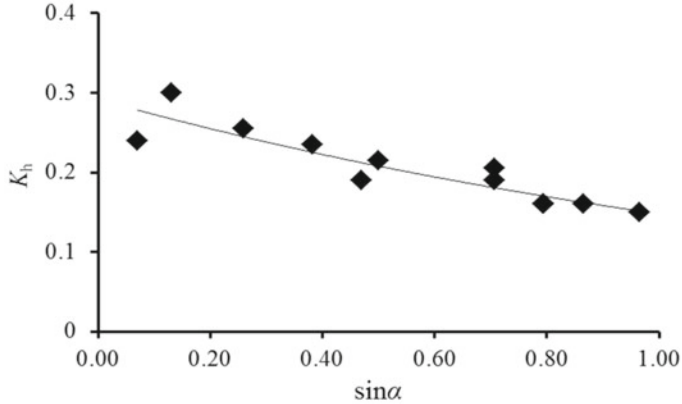
where K_h is the influence factor. Table 4.2 summarizes the K_h values obtained by various researchers under various measurement conditions.

As demonstrated in Table 4.2, as the slope α increases, there is a gradual decrease in K_h. K_h falls in the range of 0.15–0.30 when α varies between 4 and 75°. Due to the differences in the model fabrication and experimental measurement techniques, the obtained K_h values vary but, overall, exhibit a consistent trend. Figure 4.30 compares the calculated and measured values of y_{90} for self-aerated open-channel flows. As demonstrated in Fig. 4.30, Eq. (4.66) is capable of predicting y_{90} and its changes along the course with satisfactory accuracy.

The conventional methods used to predict y_{90} differ relatively considerably in the involved hydraulic parameters (including q_w, the Froude number, channel size, roughness, and empirical coefficients introduced based on measurement conditions) and are difficult to unify. In this section, based on the flow conditions and the variation range of channels in engineering practice, a prediction method for the self-aeration development in flows is first formulated. Then, this method is employed with three



(a) Comparison of the calculated and measured values of y_{90}



(b) Relationship between the influence factor K_h and open-channel slope α

Fig. 4.30 Prediction of y_{90} for self-aerated open-channel flows

parameters, namely, q_w, α, and C_{mean}, to predict y_{90}. The unit-width q_w, α, and C_{mean} are set to 20 to 400 m^2/s, 2–75°, and 2–70%, respectively. An increase in C_a can be treated as aeration development along the course. The calculated absolute values of y_{90} are analyzed. When $\alpha = 45°$ and $q_w = 300$ m^2/s, y_{90} ranges from 3.87 to 8.52 m as the extent of aeration increases. These results are in line with real-world engineering conditions. For a high-C_a, low-α channel, h_m can reach close to 15 m. This is also within the h_m design range for channels. Clearly, the theoretical analysis and calculation method is basically reasonable.

Figures 4.31 and 4.32 show the variation in h_m with aeration development. As demonstrated in Figs. 4.31 and 4.32, h_m changes nonlinearly. There is a sudden increase in the h_m gradient when $C_{mean} > 0.30$ to 0.50 compared to that when C_{mean}

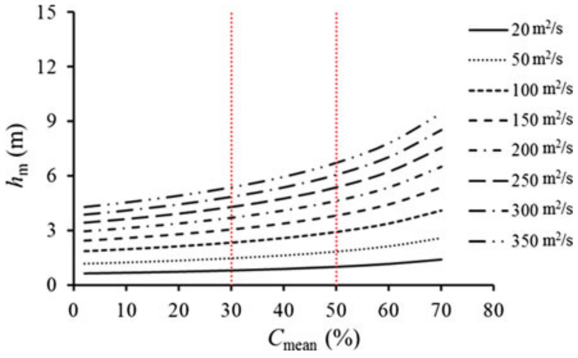


Fig. 4.31 Variation in h_m with the extent of aeration at various unit-width q_w values ($\alpha = 45°$)

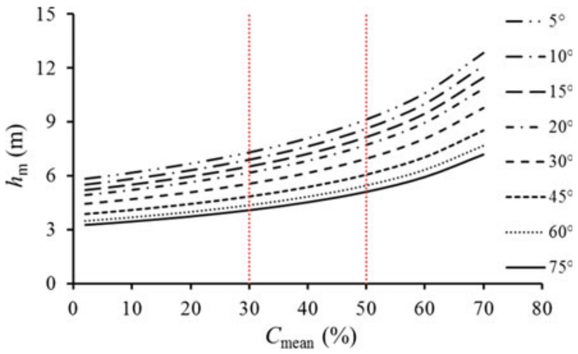


Fig. 4.32 Variation in h_m with the extent of aeration at various α values ($q_w =$ 300 m^2/s)

< 0.30. This is, to a certain extent, consistent with the analysis of the C_a distribution in the previous chapter. When $C_{mean} > 0.30$–0.50, the air-bubble diffusion is constrained by the bottom plate of the channel (specifically, the air bubbles are reflected by the bottom plate of the channel). Under this condition, the surface-bound air-bubble diffusion will affect the free surface of the air-water two-phase flow, i.e. h_m. Thus, the increase in h_m is more pronounced when the flow is highly aerated.

Figures 4.33 and 4.34 show the results for self-aeration development calculated at various q_w and α values. C_{mean} gradually increases along the course, starting from the inception point of self-aeration. As the extent of aeration increases, the ascent gradient of C_{mean} gradually decreases and reaches a certain relatively stable value. This suggests that the aeration evolves to an approximately uniform state.

At a certain α, the C_{mean} corresponding to the uniform state of aeration remains basically the same as q_w changes. However, the aeration development process varies with q_w. The aeration develops over a relatively short distance at a small q_w and over a relatively long distance at a large q_w. The C_{mean} corresponding to the uniform state of aeration increases as α increases. This suggests that increasing α can increase the carrying capacity of a flow.

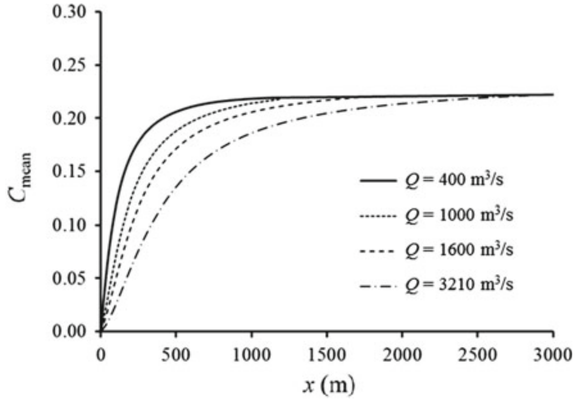


Fig. 4.33 Changes in C_{mean} at various q_w values ($\alpha = 24.5°$)

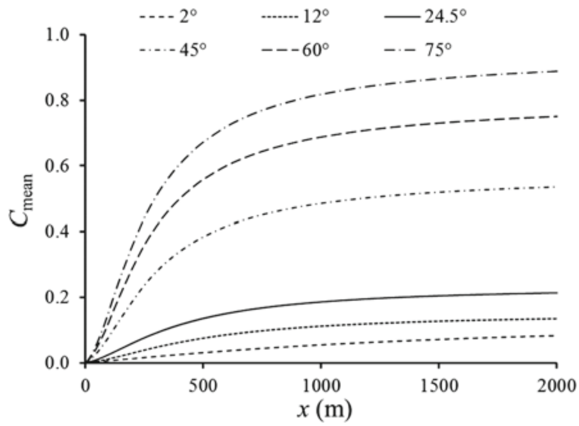


Fig. 4.34 Changes in C_{mean} at various α values ($q_w = 3{,}210\ m^3/s$)

Based on the above analysis, for a self-aerated open-channel flow, α dictates the ultimate extent of aeration, which is unrelated to the flow conditions. The flow conditions dictate the aeration development process. The length of the self-aeration development region varies significantly with q_w. α and the flow conditions jointly dictate the air demand of a self-aerated flow.

4.5.2 Analysis of the Aerated Flow in the Spillway of the Jinping-I Hydropower Station

The applicability of the method proposed in the previous section to calculate h_m is analyzed based on prototype observations and model test results for the shoreside spillway of the Jinping-I Hydropower Station. The spillway has a "tail down" section. The steep section of the spillway has a slope of 24.5°. At a water level of 1,880 m,

the dam has a flood discharge capacity of 3,210 m^3/s. The flow depth and pressure measurements taken along the spillway show that the maximum depth sites in the free-flow section were all located near the exit of the arc-shaped service gate and that the flow depth at each maximum depth site was basically the same as the height (10.5 m) of the pressure exit. The flow depth gradually decreased along the course. Specifically, the flow depth decreased from 10.5 m at the exit of the service gate to 8.48 m before the first-level aerator (pile no. 1009.78). The flat upper section had a relatively small α and a relatively large depth. In addition, aeration developed relatively slowly in this section. In view of this, the flat upper section was selected as the incipient location for the aeration calculations. Figures 4.35 and 4.36 show the calculated results, which are analyzed below:

(1) In the steep channel section of the spillway of the Jinping-I Hydropower Station, if the effects of aerators are not considered, the C_{mean} at the free-surface flow exit of the spillway can only reach approximately 0.10 when self-aeration develops

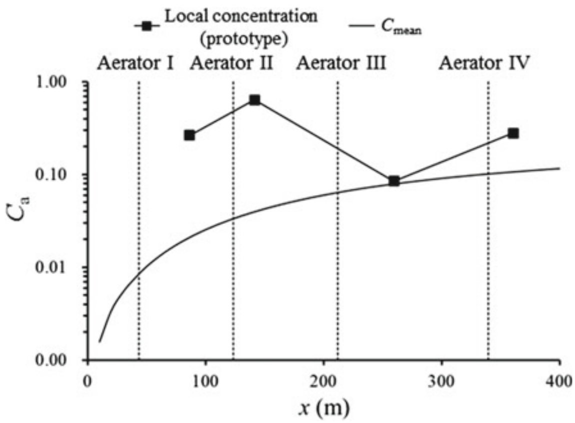


Fig. 4.35 Engineering evaluation of C_a based on the prediction method for aerated flows

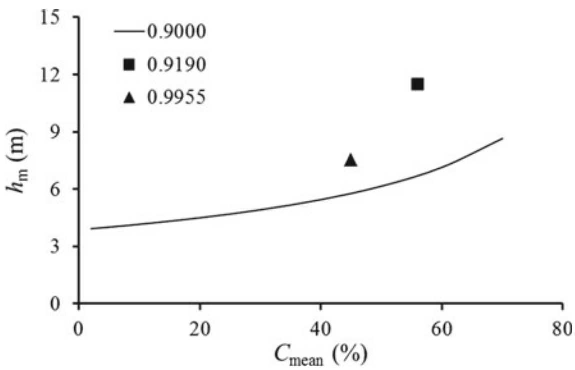


Fig. 4.36 Engineering evaluation of h_m based on the prediction method for aerated flows

at a q_w of 3,210 m^3/s. Based on the calculation method for the C_a distribution, under this condition, free-surface aeration cannot develop to the bottom of the channel. As a result, the aeration and erosion reduction requirements will not be met. Therefore, it is necessary to add a wall with aerators in the steep channel section to facilitate aeration and erosion reduction.

(2) The prototype measurements of the C_a at the bottom plate after the aerators show that overall, there is a gradual decrease in C_a along the course. The predictions for the self-aeration show that if the spillway is long enough to allow the aeration to reach a uniform state, the maximum C_{mean} in the flow will reach approximately 0.22. In addition, theoretical calculations show that the C_a near the bottom plate of the channel is approximately 0.04. This suggests that full cross-sectional aeration can occur. However, the q_a under these conditions is still lower than the prototype measurement of the minimum q_a at the bottom plate formed by forced aeration (0.0852). This suggests that the air-carrying capacity of the flow is insufficient relative to the volumes of aeration at the aerators. This is in agreement with the predictions for self-aeration.

(3) The h_m values after the flow passes the aerators are greater than the predicted values because of two reasons. (1) The C_a values at the prototype observation sites are 0.9190 and 0.9955, higher than the predicted value of 0.90. (2) The free surface undergoes violent fluctuations when the water jets that are formed after the flow passes the aerators become attached to the wall. The prototype observation sites are located after the first and fourth aerators. As a result, the prototype measurements are higher than the predicted values. However, from the perspectives of the trend and its relationship with C_{mean}, the method proposed in this study to predict h_m can provide a certain theoretical reference for predicting h_m in engineering practice.

Based on a comparison of the predictions for a self-aerated open-channel flow modeled on the aerated flow in a real-world high-velocity, high-q_w spillway and the measurements of the aerated flow in the prototype spillway, it is found that the method established based on the mesoscale free-surface aeration mechanism to predict high-velocity self-aerated open-channel flows has a reasonable scientific and theoretical basis. This method can be used to scientifically evaluate the occurrence of, development of, and variation in the aeration in aerated flows in engineering practice, predict flows in terms of the air-carrying capacity and C_a distribution with relatively satisfactory accuracy, and evaluate the reasonableness of aeration and erosion reduction facility designs for flood discharge structures. In addition, this method can reflect h_m and, thereby, provide a reference for designing engineering structures for flood discharge. Moreover, this method provides a new approach for further studying and predicting the mesoscale water–air structure of aerated flows.

4.6 Conclusions

The following major conclusions are drawn from the analysis in this chapter:

(1) The self-aeration in a high-velocity flow is caused by the inner region-bound turbulent diffusion of air entrapped as a result of the intense fluctuations and depressions of its free surface under strong turbulence.
(2) The methods formulated based on the above self-aeration mechanism of high-velocity flows to calculate the critical self-aeration conditions, distribution of the entrained air concentration, and aerated flow depth are capable of producing results that are consistent with measurements.

References

Anderson, A.G. (1955). The Distribution of Air in Self-Aerated Flow in a Smooth Open Channel.

Brocchini, M., & Peregrine D.H. (2001). The dynamics of strong turbulence at free surfaces. Part 1. Description. *Journal of Fluid Mechanics*, *449*, 225.

Cain, P. (1978). Measurements within self-aerated flow on a large spillway.

Chanson, H. (1995). Air bubble entrainment in free-surface turbulent flows: Experimental investigations.

Chanson, H. (1997). Air bubble entrainment in open channels. Flow structure and bubble size distributions. *International Journal of Multiphase Flow, 23*(1), 193–203.

Davies, J.T. (1972). Turbulence phenomena. Turbulence Phenomena.

Ehrenberger, R. (1927). Flow in steep chutes with special reference to self-aeration, US Department of the Interior, Bureau of Reclamation.

Ervine, D., & Falvey, H. (1987). Behaviour of turbulent water jets in the atmosphere and in plunge pools. *Proceedings of the Institution of Civil Engineers, 83*(1), 295–314.

Falvey, H.T. (1980). Air-water flow in hydraulic structures: Engineering monograph No. 41. USBR. December.

Geist, D. R., Linley, T. J., Cullinan, V., & Deng, Z. (2013). The effects of total dissolved gas on chum salmon fry survival, growth, gas bubble disease, and seawater tolerance. *North American Journal of Fisheries Management, 33*(1), 200–215.

Killen, J. M. (1969). The surface characteristics of self-aerated flow in steep channels, Ph. D. Thesis, University of Minnesota, USA.

Lane, E. (1939). Entrainment of air in swiftly flowing water. *Civil Engineering, 9*(2), 88–91.

Medwin, H., Kurgan, A., & Nystuen, J. A. (1990). Impact and bubble sound from raindrops at normal and oblique incidence. *Journal of the Acoustical Society of America, 88*(1), 413–418.

Mendelson, H. D. (1967). The prediction of bubble terminal velocities from wave theory. *AIChE Journal, 13*(2), 250–253.

Pfister, M., & Hager, W. H. (2011). Self-entrainment of air on stepped spillways. *International Journal of Multiphase Flow, 37*(2), 99–107.

Rein, M. (1998). Turbulent open-channel flows: Drop-generation and self-aeration. *Journal of Hydraulic Engineering, 125*(1), 98–102.

Russell, S., & Sheehan, G. (1974). Effect of entrained air on cavitation damage. *Canadian Journal of Civil Engineering, 1*(1), 97–107.

Straub, L. G., & Anderson, A. G. (1958). Experiments on self-aerated flow in open channels. *Journal of the Hydraulics Division, 84*(7), 1–35.

Volkart, P. (1980). The mechanism of air bubble entrainment in self-aerated flow. *International Journal of Multiphase Flow, 6*(5), 411–423.

Wei, W.R. (2015). Research on self-aeration characteristics in developing region of open channel flows, Ph. D. Thesis, Sichuan University, China. (in Chinese).

Wei, W., Deng, J., & Zhang, F. (2016). Development of self-aeration process for supercritical chute flows. *International Journal of Multiphase Flow, 79,* 172–180.

Wei, W., Xu, W., Deng, J., Tian, Z., & Zhang, F. (2017). Free-surface air entrainment in open-channel flows. *Science China Technological Sciences, 60*(6), 893–901.

Wei, W., Xu, W., Deng, J., Tian, Z., & Zhang, F. (2019). Bubble formation and scale dependence in free-surface air entrainment. *Scientific Reports, 9*(1), 1–8.

Weitkamp, D. E., & Katz, M. (1980). A review of dissolved gas supersaturation literature. *Transactions of the American Fisheries Society, 109*(6), 659–702.

Wilhelms, S. C., & Gulliver, J. S. (2005). Bubbles and waves description of self-aerated spillway flow. *Journal of Hydraulic Research, 43*(5), 522–531.

Wood, I. (1985). Air water flows. Proc. 21st IAHR Congress.

Wu, C. (1988). A study on self-aerated open-channel flows. *Journal of Hydroelectric Engineering., 23*(4), 23–32. (in Chinese).

Xi, R. (1988). Characteristics of self-aerated flow on steep chutes. Proc. Intl Symp. on Hydraulics for High Dams.

Chapter 5
Mesoscale Analysis of Flood Discharge and Energy Dissipation

5.1 Background

In a high-head dam project, due to the limitation of the storage capacity of the reservoir, it is necessary to discharge excess water downstream, which is the so-called "flood discharge." Some of today's mega-projects can have dam heights in excess of 300 m, maximum flood discharge flow rates exceeding 50,000 m^3/s, flood discharge flow velocities over 50 m/s, and total flood discharge powers reaching 100,000 MW (Jia 2016). This large amount of kinetic energy can easily cause severe damage to the riverbed and structures behind the dam and even threaten the safety of the dam. Therefore, it is necessary to take appropriate measures so that the energy of the high-velocity flow is dissipated substantially in the discharge process, which is called "energy dissipation". In hydraulic and hydropower projects, the major forms of flood discharge and energy dissipation include ski-jump energy dissipation, underflow energy dissipation, and energy dissipation in a tunnel. From the perspective of energy dissipation, regardless of the form of flood discharge and energy dissipation, energy dissipation mainly results from the strong shear of water flow. The turbulent flow contains many vortex blobs of various sizes. Among them, the large vortex blobs obtain energy from the turbulent flow and transfer it by motion to small vortex blobs to drive the movement of the latter, which in turn further transfer the energy to smaller vortex blobs. This energy transfer continues until the very small vortex blobs dissipate the energy as heat in the process of overcoming the viscosity of water. This is known as the cascade mode of turbulent energy dissipation. Therefore, just like cavitation erosion, which is essentially a mesoscopic phenomenon, energy dissipation occurs on the mesoscale.

Traditionally, the main indicator for evaluating energy dissipation measures in an engineering project is the energy dissipation ratio, which is the ratio of the dissipated energy to the total energy before energy dissipation. An effective energy dissipation method must first have a high energy dissipation ratio. However, it is not sufficient to analyze and evaluate flood discharge and energy dissipation solely by macroscopic parameters such as the energy dissipation ratio (Wei-lin et al. 1996;

W. Xu, *Mesoscale Analysis of Hydraulics*,
https://doi.org/10.1007/978-981-15-9785-5_5

Ohtsu et al. 1999). First, there are very large differences in the amounts of energy dissipated at different locations by water discharged at a high velocity from a reservoir. Hence, it is difficult to analyze this difference using macroscopic parameters, making it difficult to reasonably evaluate the effectiveness of energy dissipation measures. Second, energy dissipation and cavitation erosion prevention are conflicting objectives, as the former requires a change in the original flow state of the water, while the latter requires the minimization of the interference with the flow movement. In this context, we hope to determine not only the energy dissipation effect but also the risk of localized cavitation erosion damage.

A typical example in this regard is the Xiangjiaba Hydropower Station on the Jinsha River. A new form of energy dissipation called a "submerged jet", which is neither a ski-jump nor an underflow, is adopted for the dam of the station. The high-velocity water flow discharged from the surface and intermediate outlets of the dam body jets horizontally into the stilling basin in the middle of the water body between the water surface and the floor (Chen et al. 2010). To prevent the jets entering the stilling basin from rising to the surface of the water, leading to reduced energy dissipation performance, or diving to the bottom of the water, causing damage to the floor from the high-velocity water flow, the jets entering the stilling basin are divided into multiple jets at different heights that are independent of each other (Deng et al. 2008; Chen et al. 2014). This arrangement effectively guarantees the shear effect of the jets, but at the same time it forms transverse vortices between the jets and the floor, especially vertical vortices between different jet flows. If the vertical vortices penetrate the floor, it is possible for low pressure to be created at the floor but not cavitation erosion damage.

Clearly, only in-depth analysis of the small-scale vertical vortex structure under the horizontal jet condition can answer the question of whether cavitation erosion damage will occur. Moreover, for jet shear energy dissipation (including the vertical jet in the ski-jump energy dissipation method and the horizontal jet in the underflow energy dissipation method), it is necessary to understand the motion of vortex blobs in the shear zone and their energy dissipation effect to guide the development of engineering design solutions and operating methods. Pressure propagation in fissures also plays a decisive role even in the process of scouring and the failure of rock blocks or concrete floor blocks caused by high-head dam flood discharge. All of these flood discharge energy dissipation problems need to be analyzed on the mesoscale, such as the use of vortex blobs.

5.2 Vortex Structure of a Single Jet

Both main forms of flood discharge and energy dissipation, namely, the ski-jump and underflow energy dissipations, in high-head dam projects are classified as jet motion from the perspective of fluid motion (Fiorotto and Rinaldo 1992; Manso et al. 2007). The energy dissipation of the jet is first caused by the strong shear of the flow, then by the streamline curvature due to the collision with the solid boundary, and finally

by the turbulent mixing of the flow (Ervine and Falvey 1987; Bollaert and Schleiss 2003). Among them, strong shear is the main cause of energy dissipation. Therefore, the study of the vortex structure during the jet shearing process is obviously very important.

5.2.1 Velocity Field Characteristics of a Single Jet

Figure 5.1 shows a schematic diagram of a single jet. Figure 5.2 shows the high-speed photographic visualization of jet flow patterns at different times. The cross section

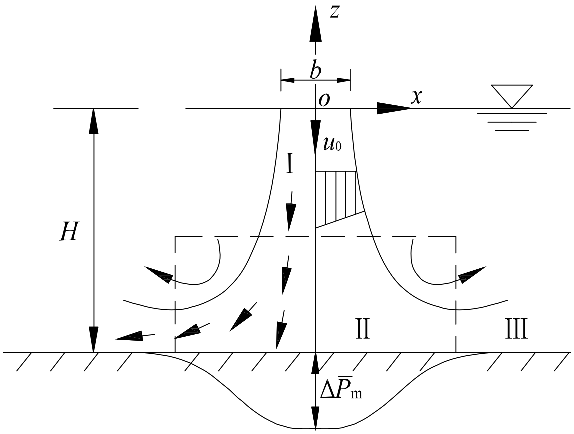


Fig. 5.1 Schematic diagram of a single jet

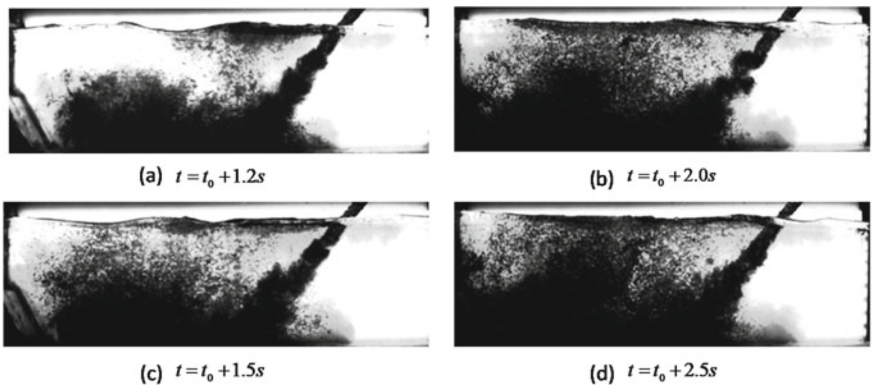


Fig. 5.2 Flow patterns of a single jet

of the jet exit is 2.0 cm × 2.5 cm, the exit velocity is 3.85 m/s, the exit angle is $\beta = 50°$, and the downstream water depth is 20 cm.

As seen, after the jet enters the downstream water, it shears the surrounding water and then impacts the floor. Finally, the jet moves along the floor and leaps. The movement of the jet in the downstream water can be divided into the shearing zone, impinging zone, and mixing zone.

The details of the jet movement can be clearly observed based on the particle image velocimetry (PIV) of the jet (Fig. 5.3) (Liu et al. 2015).

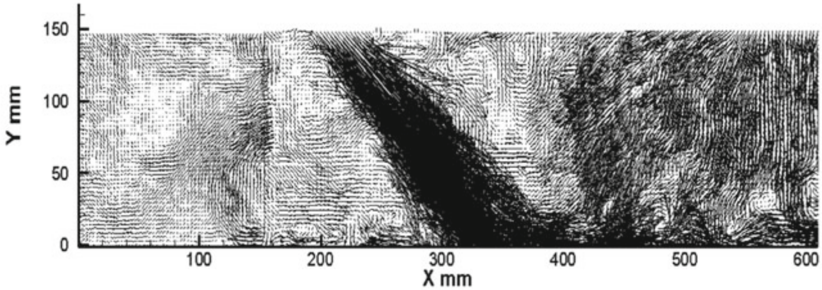
In the shearing zone, the incident flow shears with the surrounding water and drives it downward, resulting in instantaneous shear vortices of different sizes. The jet oscillates to some extent under the influence of the shear vortex motion. In the impinging zone, the jet impinges on the floor, which causes the streamline to bend sharply, resulting in a high impingement pressure. In the mixing zone, strong turbulent diffusion of the jet is present with numerous random vortices of different sizes.

5.2.2 *Vorticity Field Characteristics of a Single Jet*

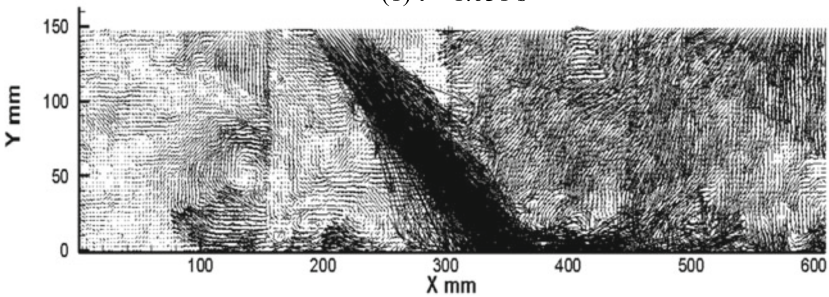
According to turbulence theory, in addition to strong velocity pulsation, vortex motion exists in turbulence. That is, turbulence is composed of instantaneous vortices of different sizes, of which large vortices transfer energy while small vortices dissipate energy through shear and friction. At the places where violent vortex movement is present, intense energy transfer and dissipation is also present. The vortex strength of a turbulent flow is expressed by the vorticity. Figure 5.4 shows the time-averaged vorticity field of a jet. The jet edge in the shearing zone continuously entrains the surrounding water, and the vorticity field is characterized by a high strength and a concentrated range, while the vorticity field in the mixing zone has the characteristics of a weak strength but a large range.

The vortices formed by the shearing between the jet and the surrounding water are clockwise upstream of the jet and counterclockwise downstream. The size and position of the vorticity change constantly along the course, with remarkable instantaneous and random characteristics.

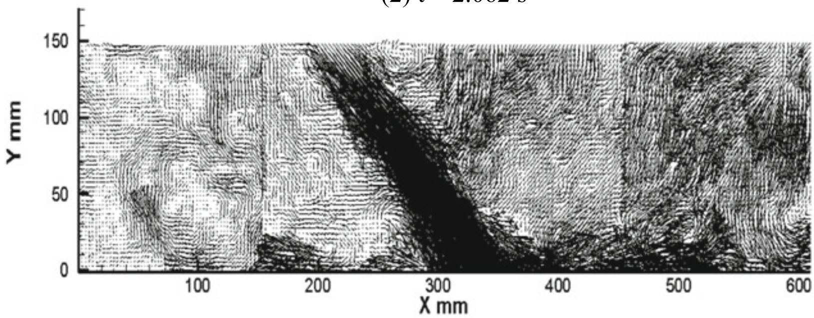
On the jet axis, the absolute value of the vorticity is approximately 0, while from the jet axis to the boundary on both sides of the jet, the absolute value of the vorticity first increases and then decreases. This indicates that the relatively large velocity gradient between the jet and the surrounding water causes the turbulent vortices to rotate at a high velocity, generating a relatively high vorticity. The greater the velocity gradient between the jet and the surrounding fluid, the greater the ability of the jet to drive the motion of the surrounding fluid is, and the larger the vorticity value is. Along the jet flow, due to the constant motion of the vortices, the jet flow velocity keeps decreasing, and the velocity gradient between the jet and the surrounding fluid decreases, so the vorticity value keeps decreasing. In the mixing zone far away from the jet, the vorticity value decreases significantly and is evenly distributed. Therefore, shear is the main cause of jet energy dissipation unless the water is very shallow.



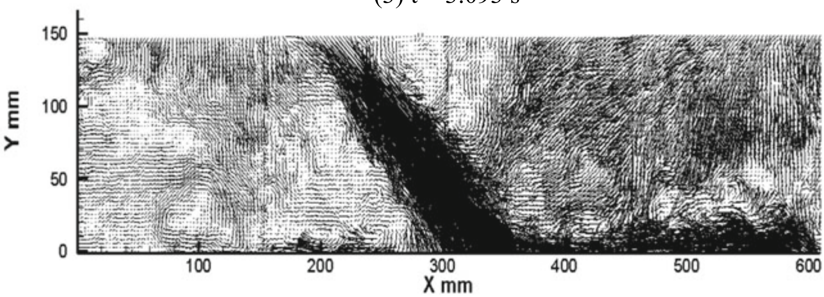
(1) t = 1.031 s



(2) t = 2.062 s



(3) t = 3.093 s



(4) t = 4.124 s

Fig. 5.3 Instantaneous vector diagrams of the oblique jet incident to an axial streamwise section

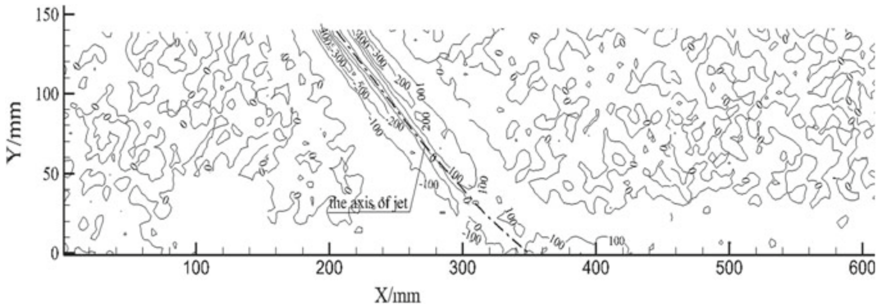


Fig. 5.4 Average vorticity field of a jet

The large-eddy simulation (LES) technique was used to numerically simulate vortices of all scales in the turbulent flow. Figure 5.5 shows the map of the vorticity evolution in the shearing zone (Guo et al. 2017). To help determine the relationship between the pressure and vorticity, the pressure contour map is superimposed on the original vorticity map. The red "+" and the black "−" marks denote high pressure and low pressure at the centers of the circular regions, respectively.

When the jet first enters the water, the shear motion on both sides of the jet is the strongest, and the vorticity reaches its maximum. The velocity gradient first increases and then decreases from the jet axis to the outer edge of the jet. Therefore, the vorticity first increases and then decreases from the jet axis to each side of the jet. In the shearing zone, both vorticity beams are relatively regular, being large in the middle and small at both ends and exhibiting a lotus-root-shaped distribution. After entering the impinging zone, the jet diverts under the influence of the wall surface, causing the velocity gradient to change significantly, so the vorticity beams begin to differentiate.

With the continuous transport of the jet kinetic energy, the vortices generated by the shearing between the jet and the surrounding water move downstream along with the jet, corresponding to the high-vorticity region moving downstream in the figure. As seen in the figure, the two vorticity beams simultaneously oscillate to the right at time t and, after 0.02 s, simultaneously oscillate to the left and then return to their original positions. As the jet continues, the two vorticity beams oscillate in opposite directions and then gradually return to their original positions, ready for the next round of oscillation. The oscillation of the vorticity beams is consistent with the random oscillation of the jet observed in the experiment, indicating that the random oscillation of the jet mainly results from vortex oscillation.

A comparison of the vorticity and pressure distributions shows that high-vorticity regions are usually of oblate shape, corresponding to low pressures at the centers of the circular regions, and the low-vorticity regions at the two ends of the oblate regions correspond to high pressure at the centers of the circular regions, indicating that the presence of high vortices results in low pressure at the centers of the circular regions. Taking the lower side of the jet as an example, the shearing between the jet and the downstream water continuously produces counterclockwise vortices. As

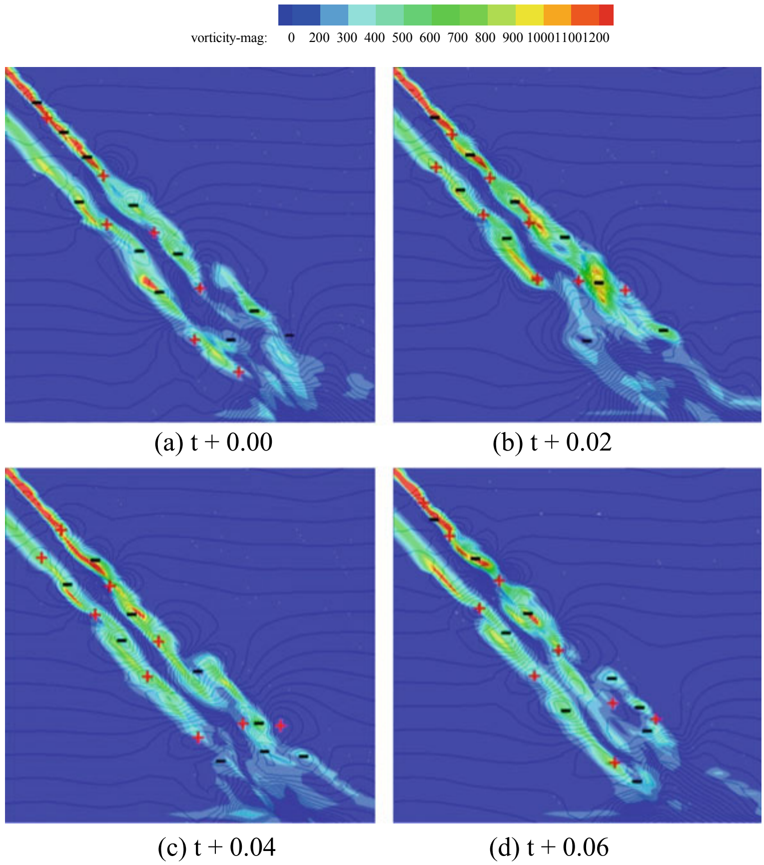


Fig. 5.5 Vorticity distribution and evolution (unit: s^{-1})

the vortices move downstream along with the jet, low pressure is generated at the centers of the circular regions where vortices exist, and high pressure at is generated the centers of the circular regions due to the squeezing of the fluid by the two vortices in front of and behind it. This explains the alternating distribution of low pressure and high pressure at the centers of the circular regions.

5.3 Vortex Structure with Multijets

Multijets usually appear in high-head dam projects (Saripalli 1987; Barata et al. 1991). From the perspective of the vortex structure, the relatively complex multijets, the so-called multihorizontal submerged jets, enter the downstream water from the horizontal direction at a certain height between the water surface and the floor.

The complexity of the multihorizontal submerged jets is mainly reflected by the simultaneous existence and mutual interference of transverse vortices and transverse vortices (Chen et al. 2013). In particular, if the vertical vortices penetrate the floor, they may generate low pressure at the floor and induce cavitation erosion.

5.3.1 Transverse Vortices

Figure 5.6 shows the layout of the test model, for which particle image velocimetry (PIV) was used to measure the flow field. In the model, the water flows through the surface and intermediate outlets of the dam and enters the stilling basin at two levels in the form of multijets.

Figure 5.7 is the streamline diagram of the transverse vortices in the streamwise section near the sidewall of the stilling basin for the multilevel multihorizontal submerged jets. The merging and breakdown of the transverse vortices can be clearly seen in the figure. At time $T = (t_0 + 0)$ s, a vortex with a size of approximately 16 m $\times$ 10 m appeared in the turbulent shear layer near the sidewall of the stilling basin. This vortex disappeared at $T = (t_0 + 1)$ s. At $T = (t_0 + 2.5)$ s, two vortices of different sizes occurred in the turbulent shear layer. At $T = (t_0 + 3)$ s, the two vortices merged into one. The vortices continued to form and disappear with increasing time. Due to the complex boundary conditions and violent turbulent flow in the stilling basin, the interaction between the vortices was very strong, and the vortex structure was very irregular. When large-size vortices occurred in the turbulent shear layer, they soon broke down to form smaller vortex structures. The vortices in the turbulent shear layer experienced a continuous process of formation-merging-breakdown-disappearance. The position of a transverse vortex was not fixed at a certain location but constantly changed within a range of 0–50 m from the step-down floor. Additionally, the distance from the center of the vortex to the floor of the stilling basin changed constantly.



Fig. 5.6 Layout of the test model

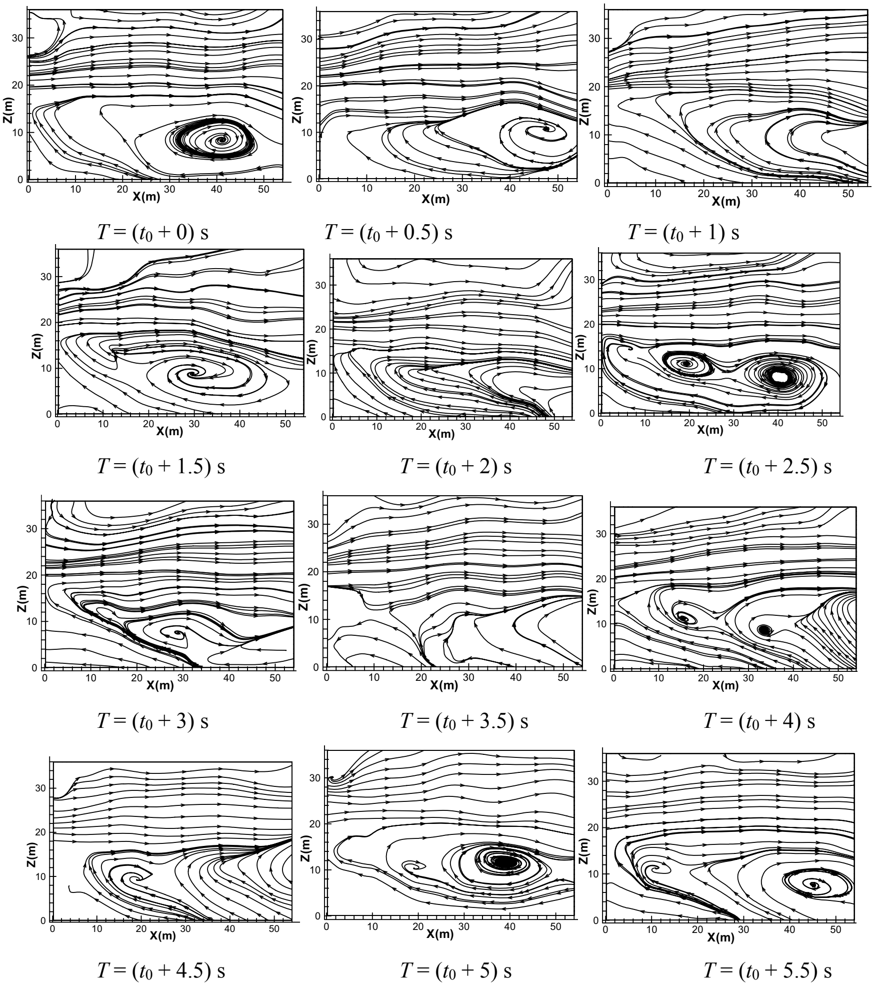
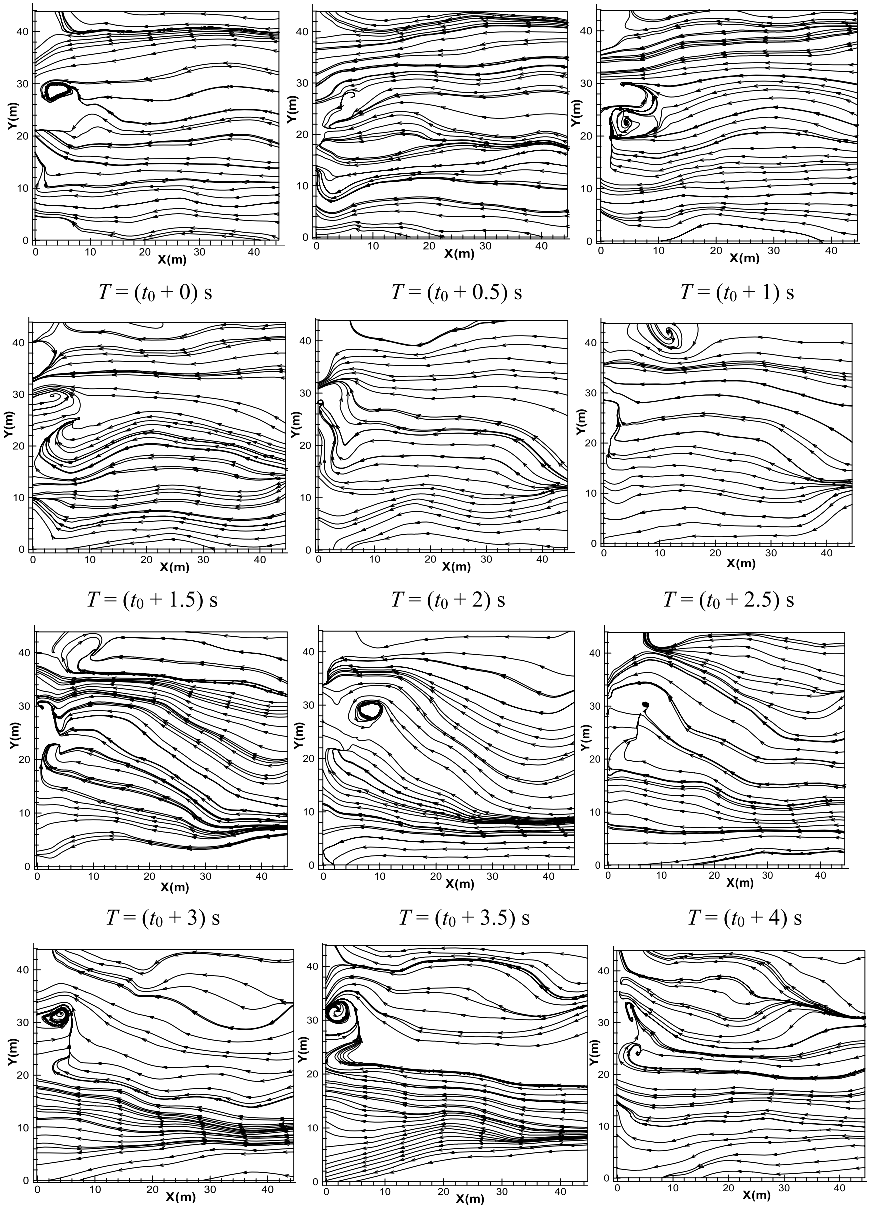


Fig. 5.7 Streamline diagram of transverse vortex motion (streamwise section near sidewall)

5.3.2 Vertical Vortices

Figure 5.8 shows the distribution and streamline diagram of the vertical vortices in the horizontal section 1 cm away from the floor. As seen from the figure, there was an obvious vortex blob structure in the flow field most of the time near the floor of the stilling basin, indicating that the vertical vortices generated in the stilling basin were intermittent underflow. The range of the vertical vortices near the floor of the stilling basin was smaller than 4 cm × 4 cm, and the position of a vertical vortex was not fixed at a certain location but changed constantly. As seen from the streamline distribution diagram at different moments in time, the vertical vortices near the step-down floor



$T = (t_0 + 0)$ s
$T = (t_0 + 0.5)$ s
$T = (t_0 + 1)$ s
$T = (t_0 + 1.5)$ s
$T = (t_0 + 2)$ s
$T = (t_0 + 2.5)$ s
$T = (t_0 + 3)$ s
$T = (t_0 + 3.5)$ s
$T = (t_0 + 4)$ s
$T = (t_0 + 4.5)$ s
$T = (t_0 + 5)$ s
$T = (t_0 + 5.5)$ s

Fig. 5.8 Streamline diagram of the vertical vortex motion (horizontal section near floor)

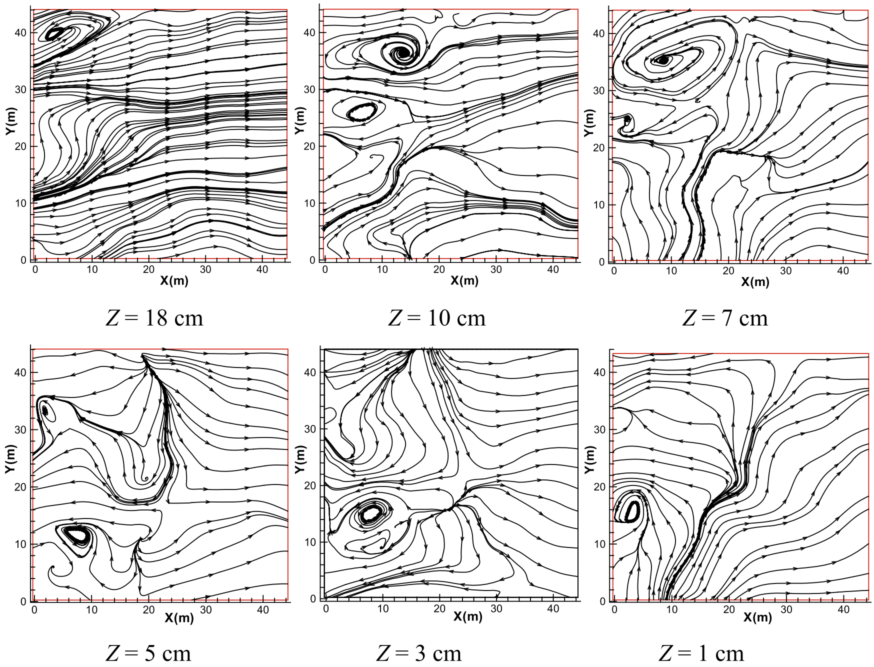


Fig. 5.9 Vertical transfer of vertical vortices

constantly formed and disappeared, and vertical vortices continued to appear, some disappearing immediately after generation and others lasting for a short time. Thus, the vertical vortices occurred intermittently near the floor of the stilling basin, and the vertical vortices did not appear at a fixed position on the floor of the stilling basin. The transverse vortices played a role in enhancing the randomness of the vertical vortices.

Figure 5.9 shows the formation and vertical transfer of the vertical vortices in the stilling basin, where Z is the distance from the test plane to the floor of the stilling basin. As shown in the figure, there was violent turbulence in the flow in the stilling basin, and vertical vortices constantly formed and disappeared in the vertical direction. The vertical vortex formed between the high-velocity jets was transferred toward the floor of the stilling basin, and the vortex area first increased and then gradually decreased and finally disappeared in the water of the stilling basin. The vertical vortex formed in the water below the high-velocity mainstream continuously developed downward and ultimately reached the floor of the stilling basin with a vortex area of approximately 4 cm $\times$ 4 cm.

The above analysis shows that under the interference of the turbulence of the jets themselves and the transverse vortices, although the vertical vortex formed by the multihorizontal jets could intermittently reach the floor of the stilling basin, there was no continuously penetrating vertical vortex, so the floor of the stilling basin was not damaged by cavitation erosion.

5.4 Vortex Structure of a Pressure Flow with a Sudden Contraction

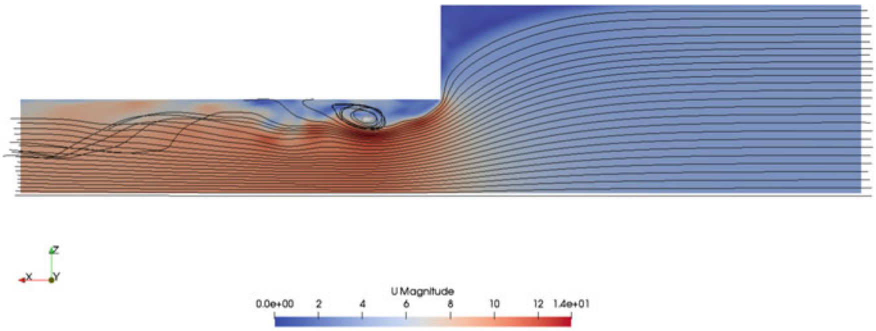
In high-head dam projects, in addition to the traditionally used ski-jump and underflow energy dissipation methods, the so-called internal flow energy dissipation method, with which energy is dissipated in spillway tunnels, has been increasingly adopted in engineering projects over the past two decades (Chen et al. 2007; Zhong et al. 2009; Wu and Ai 2010). Sudden contraction is a typical internal flow energy dissipation method for the pressure flow in spillway tunnel. In this section, the LES method is used to analyze the vortex structure of a pressure flow with a sudden contraction.

5.4.1 Flow Field Characteristics of a Pressure Flow with a Sudden Contraction

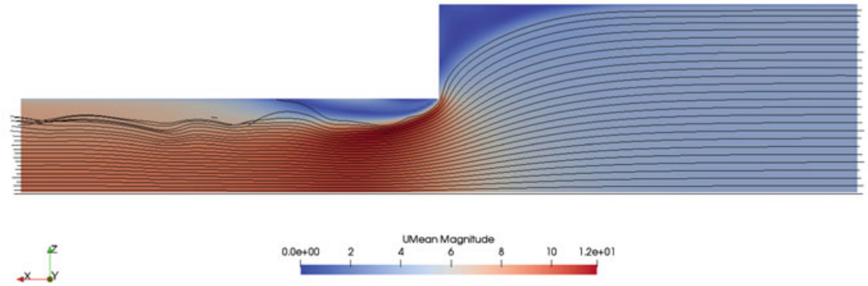
Figure 5.10a shows the instantaneous velocity contour plot and streamlines of a pressure flow with a sudden contraction. The fluid boundary layer is separated at the front edge of the sudden contraction, forming a recirculation zone near the wall (Durrett et al. 1988; Tamura and Matsumoto 2009; Roul and Dash 2011). There is a mixed layer at the junction of the recirculation zone and the mainstream that has properties similar to those of the boundary layer, with relatively large shear stress and strong turbulence. Under the shear of the mixed layer, vortex blobs were formed in the recirculation zone, and the pressure at the center of the vortex blob decreased, making cavitation possible. In the figure, the streamlines are actually three-dimensional, and the intersecting of the streamlines is an optical illusion due to the viewing angles. Figure 5.10b, c shows the contour plots of the corresponding time-average and root-mean-square (RMS) values of the flow velocity, respectively.

5.4.2 Vortex Blob Characteristics of a Pressure Flow with a Sudden Contraction

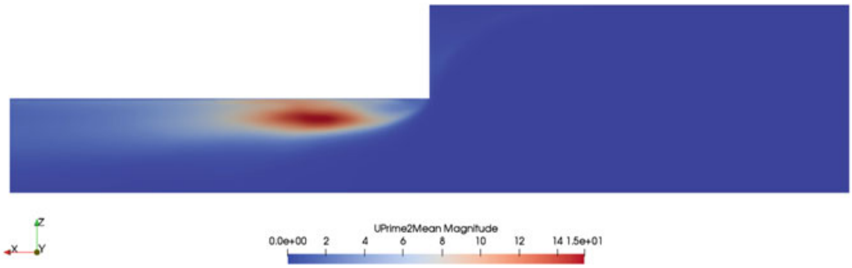
According to turbulence theory, large vortices draw energy from the mainstream and transfer it in layers to small vortices, which eventually convert the kinetic energy into heat through viscous dissipation. The form of the large vortices mainly depends on the shape of the boundary. In a pressure flow with a sudden contraction, the boundary layer at the front edge of the sudden contraction is separated, and a large number of vortex blobs are generated in the low-pressure region formed by the separation, playing a decisive role in the cavitation inception. Next, the form and distribution of these vortex blobs are investigated.



a) Contour plot and streamlines of the instantaneous flow velocity



b) Contour plot and streamlines of the time-averaged flow velocity



c) Contour plot of the RMS of the flow velocity

Fig. 5.10 Contour plots of the instantaneous, time-averaged, RMS flow velocities

The Q criterion and λ_2 criterion are common indicators for identifying vortex blobs. The core idea of the Q criterion is to define the region where the vorticity is greater than the strain rate as a vortex. λ_2 is the second characteristic value of the sum of the squares of the strain rate tensor and the vorticity tensor. They are calculated as follows:

The gradient tensor of the flow velocity field is defined as

$$\mathrm{J} = \nabla \mathbf{u} = \begin{bmatrix} \frac{\partial u_1}{\partial x} & \frac{\partial u_2}{\partial x} & \frac{\partial u_3}{\partial x} \\ \frac{\partial u_1}{\partial y} & \frac{\partial u_2}{\partial y} & \frac{\partial u_3}{\partial y} \\ \frac{\partial u_1}{\partial z} & \frac{\partial u_2}{\partial z} & \frac{\partial u_3}{\partial z} \end{bmatrix} \tag{5.1}$$

Then, its symmetric component is the strain rate tensor

$$\mathrm{S} = \frac{\mathrm{J} + \mathrm{J}^{\mathrm{T}}}{2} \tag{5.2}$$

and its antisymmetric component is the vorticity tensor

$$\Omega = \frac{\mathrm{J} - \mathrm{J}^{\mathrm{T}}}{2} \tag{5.3}$$

The Q value is defined as

$$\mathrm{Q} = \frac{1}{2}\left(\left\|\Omega^2\right\| - \left\|S^2\right\|\right) \tag{5.4}$$

The position where Q is greater than zero is a vortex. In practice, this criterion is too weak, and hence, too many vortices would be obtained, adversely affecting the analysis. Therefore, the Q value is generally set to be greater than simply a positive number.

The λ_2 criterion requires the determination of the three eigenvalues (λ_1, λ_2, and λ_3) of $\mathrm{S}^2 + \Omega^2$. For a point in the flow field to be the center of a vortex, two of the three eigenvalues must be less than 0. We know that $\lambda_1 > \lambda_2 > \lambda_3$; thus, $\lambda_2 < 0$ is a necessary condition. In practical applications, this criterion is weak and would lead to a large number of vortices. Therefore, λ_2 is generally set to be less than simply a negative number to obtain the vortex structure. The disadvantage of this method is that it is difficult to distinguish several vortex blobs at relatively close distances. Note that the value calculated for Lambda2 in OpenFOAM is the opposite of the aforementioned λ_2, and the original definition of λ_2 is adopted here.

Figure 5.11 shows that the identification results with the two criteria are almost the same. In principle, the λ_2 criterion is better and thus is used in the following analysis.

To illustrate the motion of the vortex blob at different flow velocities, the vortex blob downstream of the sudden contraction as the inlet flow velocity increased from 2 to 8 m/s is shown in Fig. 5.12. The higher the flow velocity was, the more and larger the vortices were in the flow field.

According to the mesoscopic analysis of the vortex blob structure of a pressure flow with a sudden contraction, there was a high risk of cavitation in the vortex zone after the sudden contraction (Arndt et al. 1995; Chen et al. 2009). Therefore, a decompression model test is necessary to evaluate the risk of cavitation when designing



(a) Contour surface $Q = 100000$



(b) Contour surface $\lambda_2 = -50000$

Fig. 5.11 Comparison of the identification results by criteria Q and λ_2

energy dissipation facilities with a sudden contraction in engineering projects. Unlike orifice plate structures, structures with sudden contractions make it difficult to ensure that the cavitation bubbles do not collapse near the sidewall after their formation. In addition, unlike in nonpressure flow, it is impossible to use a bucket-chute in a pressure flow to achieve forced aeration for cavitation reduction because a large amount of air would accumulate in the tunnel and form high-pressure air pockets, which would adversely affect the structural safety. Therefore, when cavitation occurs, air vents, as shown in Fig. 5.13, can be used to reduce the cavitation erosion damage. Figure 5.14 shows the distribution of the air concentration formed by aeration with an air vent. Even if the air vent is not close to the front edge of the sudden contraction and there is only one air vent in the contraction section, the entrained air bubbles can still counterdiffuse in the flow direction to reach the front edge of the contraction and spread across the entire width in the transverse direction. This occurs because these are all low-pressure regions, which attract the air bubbles moving toward them (Li et al. 2019).

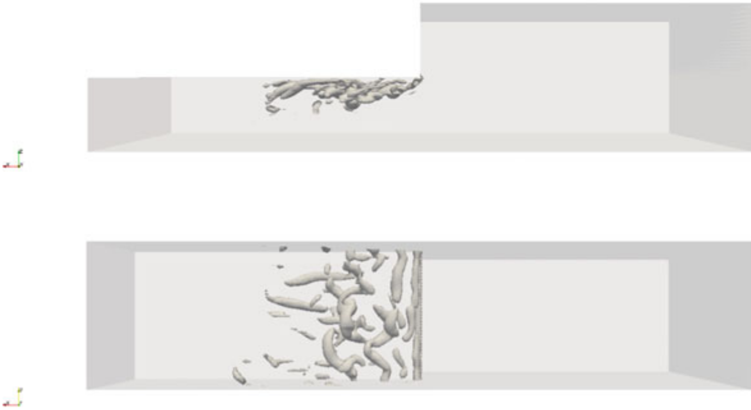
5.5 Application of Multihorizontal Submerged Jets in Engineering Project

5.5.1 Overview of the Project

The Xiangjiaba Hydropower Station is the last in the cascade development of the lower reaches of the Jinsha River. The dam is located on the lower reaches of the



(a) Inlet flow velocity = 2 m/s



(b) Inlet flow velocity = 3 m/s

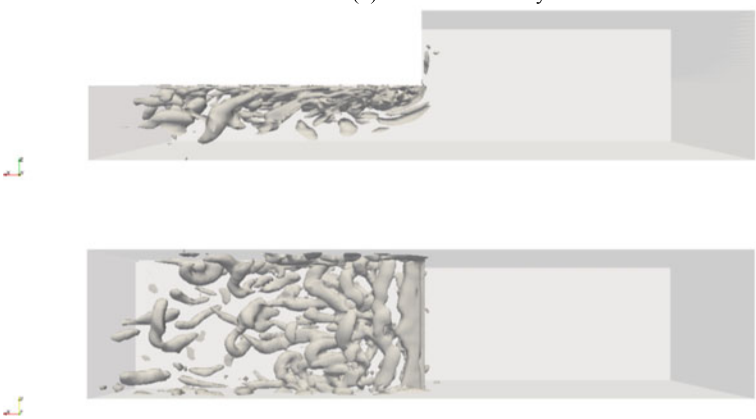


(c) Inlet flow velocity = 4 m/s

Fig. 5.12 Vortex blob at different flow velocities (contour surface $\lambda_2 = -50000$)



(d) Inlet flow velocity = 6 m/s



(e) Inlet flow velocity = 8 m/s

Fig. 5.12 (continued)

Jinsha River at the junction of Shuifu County in Yunnan Province (right bank) and Yibin County in Sichuan Province (left bank). Xiangjiaba is 157 km upstream away from the Xiluodu Hydropower Station, 1.5 km downstream away from the downtown Shuifu and 33 km upstream away from downtown Yibin. Xiangjiaba is a gravity dam with a crest elevation of 383 m, a maximum height of 161 m, and a crest length of 909.3 m. It has a normal storage water level of 380 m, check flood level of 381.86 m, dead water level (drawdown water level when power is not generated during the water supply period) and flood control water level during flood season of 370 m, upstream highest navigable water level of 380 m, downstream highest navigable water level of 278 m, maximum navigable flow rate of 12,000 m^3/s, and minimum navigable flow rate of 1200 m^3/s. The reservoir covers an area of 95.6 km^2 and is of a canyon type. The reservoir has a control drainage area of 458,800 km^2, a total capacity of 5.163 billion m^3, and a backwater length of 156.6 km. With an installed capacity

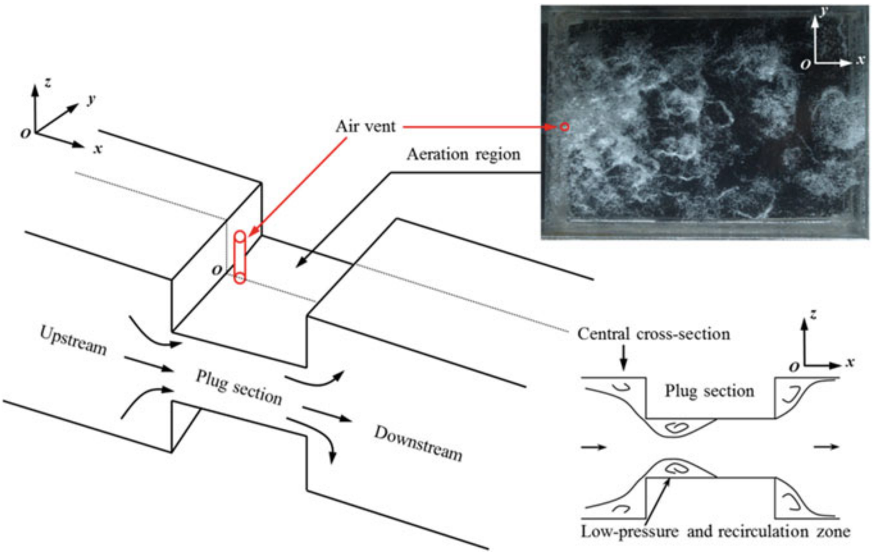
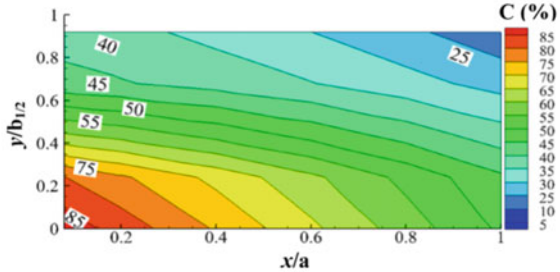
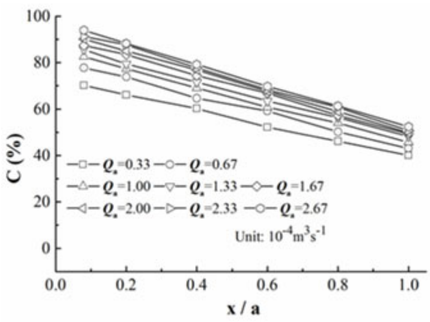


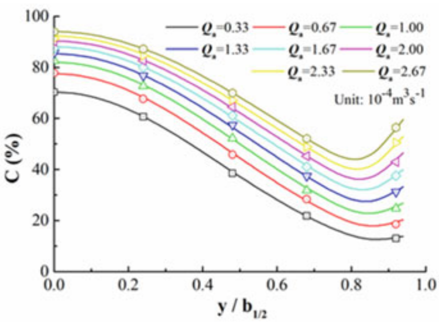
Fig. 5.13 Aeration for erosion reduction by air vents in pressure flow with sudden contraction



(a) Air replenishment $Q_{\text{a}} = 1.67\ \text{m}^3/\text{s}$



(b) $y/b_{1/2} = 0$



(c) $x/a = 0.08$

Fig. 5.14 Distribution of the air concentration by aeration with an air vent (flow velocity: 1.19 m/s)

of 6.4 million KW and a normal water level of 380 m, Xiangjiaba has a guaranteed power output of 2.009 million KW, a mean annual energy production of 307.447 billion KW · H, and 5125 annual installed utilization hours.

The key structures include the dam, the powerhouse at the dam toe on the left bank, the ship lift on the left bank, the flood discharge dam section, the underground powerhouse on right bank, powerhouses at the dam toe on both banks, and irrigation water intake on both banks. The structures for flood discharge and energy dissipation of Xiangjiaba are adjacent to Shuifu County and the Yunnan Natural Gas Chemical Plant, a large enterprise. Because the dam site has special environmental requirements, ski-jump energy dissipation, which has a relatively severe atomization impact, cannot be used. For this reason, underflow energy dissipation was adopted in the preliminary design. However, due to the high hydraulic head and large flow rate per unit width, the near-bottom flow velocity of the stilling basin reached more than 40 m/s, severely threatening the safety of the flood discharge. Considering both the technical characteristics of the project and the requirements of flood discharge and energy dissipation, the State Key Laboratory of Hydraulics and Mountain River Engineering, Sichuan University, proposed a new form of energy dissipation using multilevel multihorizontal submerged jets. The flood discharge structure adopts six surface outlets and five intermediate outlets. For the surface outlets, an open overflow weir is adopted with a crest elevation of 354.0 m, the discharge chute is 8 m wide and is connected to the horizontal section after the ogee section, and the floor of the exit has an elevation of 261.0 m. For the intermediate outlets, the discharge chute has a width of 6 m, the floor of the entrance has an elevation of 305.0 m, the outlet has a size of 6.0 × 9.6 m (width × height), the outlet section is still horizontal (no depression angle), and the floor of the exit has an elevation of 253.0 m. The flood discharge section of the dam has a length of 132 m, the stilling basin has a width of 108 m, a length of 228 m, a basin floor elevation of 245.0 m, a tail bucket elevation of 270 m, and sidewall crest elevation of 296.0 m on both sides.

5.5.2 Characteristics of the Flood Discharge and Energy Dissipation

In the stilling basin with multilevel multihorizontal submerged jets, energy is dissipated by generating swirling and strong turbulence through the hydraulic jump (Fig. 5.15). In addition, because the high-velocity mainstream is always far from the floor, the near-bottom flow velocity of the stilling basin can be significantly reduced. Tests showed that the near-bottom flow velocity of the stilling basin had a maximum positive value in the range of 15.84–17.81 m/s and a maximum negative value in the range of −10.48 to −13.02 m/s, much lower than the near-bottom flow velocity of conventional underflow, which is greater than 40 m/s, so erosion damage to the floor of the stilling basin can be avoided. The maximum positive flow velocity occurred on the floor of the stilling basin with a maximum distance



Fig. 5.15 Water flow regime in the stilling basin with multihorizontal submerged jets

of 64 m and a minimum distance of 52 m from the step-down floor of the stilling basin. The maximum negative flow velocity occurred on the floor of the stilling basin with a maximum distance of 20 m and a minimum distance of 12 m from the step-down floor of the stilling basin. The jet flow velocity attenuated rapidly in the range of 0–100 m from the step-down floor, beyond which the velocity diffused uniformly in the water depth direction. When the surface and intermediate outlets were combined for flood discharge, the length of the recirculation zone under the jets increased, and the corresponding flow velocity increased slightly. The range of the downstream swirling varies with different types of step-down floors, the position of the mainstream reaching the floor of the stilling basin moves between the upstream and downstream, and the near-bottom flow velocity at the fixed measuring point near the impinging zone varies between positive and negative.

In engineering design, the vertical vortex problem has received much attention. However, as discussed in Sect. 5.3 of this chapter, under the turbulence of the jet itself and the interference of transverse vortices, although the vertical vortices formed by multihorizontal jets could intermittently reach the floor of the stilling basin, there was no continuous penetration of vertical vortices and hence no cavitation erosion damage to the floor of the stilling basin. Thus, the stilling basin has been operated safely since the project was completed.

5.6 Conclusions

The following main conclusions can be drawn based on the analysis in this chapter:

(1) Strong shear is the main form of jet energy dissipation. Therefore, the range of the zone of energy dissipation by shear should be maximized in the ski-jump energy dissipation of high-head dam projects to reduce the impingement intensity of the impact energy dissipation zone.
(2) Under the turbulence of the jets themselves and the interference of the transverse vortices, although the vertical vortices formed by multihorizontal jets can

intermittently reach the floor of the stilling basin, there is no continuous penetration of vertical vortices and thus no cavitation erosion damage to the floor of the stilling basin.

(3) There is a high risk of cavitation in the vortex area of the pressure flow after the sudden contraction of the flow area. Decompression model tests are needed in engineering design to assess the risk of cavitation. When cavitation is unavoidable, one can consider the use of vent aeration to reduce or eliminate cavitation erosion damage.

References

Arndt, R. E., Ellis, C., & Paul, S. (1995). Preliminary investigation of the use of air injection to mitigate cavitation erosion.

Barata, J. M., Durao, D., Heitor, M., & McGuirk, J. (1991). Impingement of single and twin turbulent jets through a crossflow. *AIAA Journal, 29*(4), 595–602.

Bollaert, E., & Schleiss, A. (2003). Scour of rock due to the impact of plunging high velocity jets Part I: A state-of-the-art review. *Journal of Hydraulic Research, 41*(5), 451–464.

Chen, I. Y., Liu, C. C., Chien, K. H., & Wang, C. C. (2007). Two-phase flow characteristics across sudden expansion in small rectangular channels. *Experimental Thermal & Fluid Science, 32*(2), 696–706.

Chen, J.-G., Zhang, J.-M., Xu, W.-L., Li, S., & He, X.-L. (2013). Particle image velocimetry measurements of vortex structures in stilling basin of multi-horizontal submerged jets. *Journal of Hydrodynamics, 25*(4), 556–563.

Chen, J.-G., Zhang, J.-M., Xu, W.-L., & Wang, Y.-R. (2010). Numerical simulation of the energy dissipation characteristics in stilling basin of multi-horizontal submerged jets. *Journal of Hydrodynamics, 22*(5), 732–741.

Chen, J. G., Zhang, J. M., Xu, W. L., & Peng, Y. (2014). Characteristics of the velocity distribution in a hydraulic jump stilling basin with five parallel offset jets in a twin-layer configuration. *Journal of Hydraulic Engineering, 140*(2), 208–217.

Chen, Y., Tseng, C.-Y., Lin, Y.-T., & Wang, C.-C. (2009). Two-phase flow pressure change subject to sudden contraction in small rectangular channels. *International Journal of Multiphase Flow, 35*(3), 297–306.

Deng, J., Xu, W. L., Zhang, J. M., Qu, J. X., & Yang, Y. Q. (2008). A new type of plunge pool—Multi-horizontal submerged jets. *Science in China, 51*(12), 2128–2141.

Durrett, R., Stevenson, W., & Thompson, H. (1988). Radial and axial turbulent flow measurements with an LDV in an axisymmetric sudden expansion air flow.

Ervine, D., & Falvey, H. (1987). Behaviour of turbulent water jets in the atmosphere and in plunge pools. *Proceedings of the Institution of Civil Engineers, 83*(1), 295–314.

Fiorotto, V., & Rinaldo, A. (1992). Fluctuating uplift and lining design in spillway stilling basins. *Journal of Hydraulic Engineering, 118*(4), 578–596.

Guo, W. S., Li, L. G., Liu, C., & Li, N. W. (2017). Study on the flow field of a submerged jet. *Advanced Engineering Sciences, 49*(S1), 35–43.

Jia, J. (2016). A technical review of hydro-project development in China. *Engineering, 3,* 302–312.

Li, R., Xu, W.-L., Luo, J., Yuan, H., & Zhao, W.-Y. (2019). A study on aeration to alleviate cavitation erosion in the contraction section of pressure flow. *Journal of Fluids Engineering, 141*(9).

Liu, C., Li, L. G., & Li, N. W. (2015). Research on instantaneous flow characteristics of the falling submerged jet in a pool based on PIV technique. *South to North Water Transfers and Water Science & Technology, 13*(3), 471–475.

Manso, P., Bollaert, E., & Schleiss, A. (2007). Impact pressures of turbulent high-velocity jets plunging in pools with flat bottom. *Experiments in Fluids, 42*(1), 49–60.

Ohtsu, I., Yasuda, Y., & Ishikawa, M. (1999). Submerged hydraulic jumps below abrupt expansions. *Journal of Hydraulic Engineering, 125*(5), 492–499.

Roul, M. K., & Dash, S. K. (2011). Two-phase pressure drop caused by sudden flow area contraction/expansion in small circular pipes. *International Journal for Numerical Methods in Fluids, 66*(11), 1420–1446.

Saripalli, K. (1987). Laser doppler velocimeter measurements in 3-D impinging twin-jet fountain flows. In *Turbulent shear flows 5* (pp. 146–168). Berlin: Springer.

Tamura, Y., & Matsumoto, Y. (2009). Improvement of bubble model for cavitating flow simulations. *Journal of Hydrodynamics, 21*(1), 41–46.

Wei-lin, X., Hua-sheng, L., Yong-quan, Y., & Chi-gong, W. (1996). Numerical simulation of 3-D turbulent flows of plunge pool and energy dissipation analysis. *Journal of Hydrodynamics, 5*.

Wu, J. H., & AI, W. Z. (2010). Flows trough energy dissipaters with sudden reduction and sudden enlargement forms. *Journal of Hydrodynamics, 3*, 70–75.

Zhong, T., Xu, W.-L., Wang, W., & Liu, S. J. (2009). Hydraulic characteristics of plug energy dissipater in flood discharge tunnel. *Journal of Hydrodynamics, 6*, 73–80.

Chapter 6
Mesoscale Analysis of Flood Discharge Atomization

6.1 Background

Flood discharge atomization (FDA) refers to a phenomenon in which a flow discharged at a high velocity first spalls in air and entrains a large amount of air and subsequently falls into and splashes the downstream water as a result of an intense impact, resulting in local precipitation in the immediate region and a drift of mist over the far region. FDA is one of the issues that require attention in high-head dam projects. FDA has serious consequences if not treated properly. For example, FDA can damage power plants and trigger riverbank landslides in heavy-precipitation regions. Currently, there are three main approaches for studying FDA: (1) predicting FDA through mechanical analysis and modeling of the motion of water droplets (Hoyt and Taylor 1977; Liang 1992; Sun and Liu 2008); (2) simulating real-world FDA through large-scale model tests (Liu et al. 2005; Wang et al. 2013); and (3) estimating the FDA conditions of planned structures through comparison with the FDA conditions of built structures based on prototype observations (Lian et al. 2014). Apart from the flow conditions (e.g., the flow velocity, flow rate, mode of entry into water, and form in air), FDA is affected by the surrounding terrain, meteorological conditions, and even valley winds. As a result, it is extremely difficult to predict FDA. A combination of various prediction methods is often required to give an approximate prediction of the range and intensity of FDA.

While it is difficult to accurately predict FDA, one thing is certain—the in-depth determination of its intrinsic mechanical mechanism is imperative. Evidently, based on its formation process, FDA is, in essence, a macroscopic assembly of mesoscale phenomena, similar to cavitation erosion and aerated flows, which have been discussed in the previous chapters. Hence, the intrinsic pattern of FDA can be truly understood only by mesoscale analysis.

The FDA problems associated with a group of arch dams over 200 m in height in China are highly representative (Sun 2009). These dams are characterized by large heights, high flow rates, and narrow river valleys. As a result, intense FDA directly affects the slope stability of the banks behind these dams. The Ertan hydropower

W. Xu, *Mesoscale Analysis of Hydraulics*,
https://doi.org/10.1007/978-981-15-9785-5_6

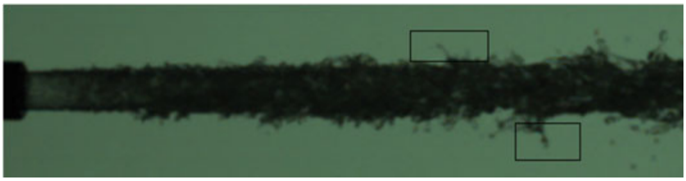
station on the Yalong River discharges floods through the simultaneous use of two rows of dam outlets and collision of flows in air, pioneering flood discharge at a high flow rate by high arch dams. In addition, owing to its large height, high flow rate, and pronounced FDA problem, the Ertan hydropower station is a milestone in FDA research. A series of high arch dams subsequently constructed, including the Xiaowan hydropower station on the Lancang River, the Xiluodu hydropower station on the Jinsha River, and the Baihetan hydropower station, all drew lessons from the way the Ertan hydropower station discharges floods. However, when the Jinping-I hydropower station on the Yalong River was later designed, the necessity and feasibility of the simultaneous use of two rows of dam outlets without collisions of flows in air garnered attention due to the geological conditions of the downstream slopes. Thus, it is necessary to determine the increase in the extent of FDA resulting from collisions of flows in air, which requires an understanding of the mesoscale mechanism of FDA caused by collisions of flows in air.

In fact, not only is research on the mesoscale mechanism of FDA caused by collisions of flows in air insufficient, but mesoscale research on the splashing of water caused by impacting flows as well as spallation of flows in air is also deficient. These issues are discussed in this chapter.

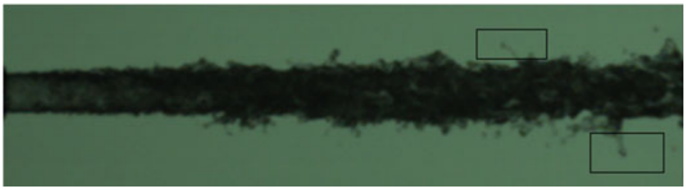
6.2 Jet Spallation in Air

There are three main causes of FDA, namely, jet spallation in air, jet collision, and water splash by plunging jets (Reitz and Bracco 1982; Lian et al. 2006; Choo and Kang 2007). Figure 6.1 shows the spallation of a jet in air. After leaving the exit of the nozzle, the jet was able to remain relatively stable within a short distance. After traveling a certain distance, the jet began to become unstable. As the distance increased, the jet became increasingly unstable, and water droplets and water-droplet masses began to break away from the surface of the flow.

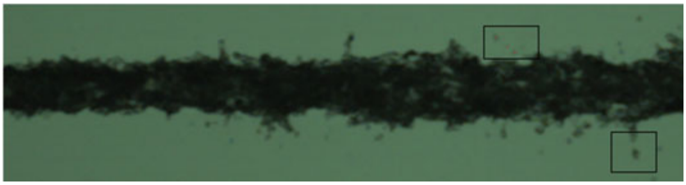
Figure 6.2 shows generalized diagrams of several main modes of the formation of water droplets during the spallation process. Overall, there are three scenarios for the formation of water droplets. (1) A low-velocity jet has a turbulent surface, and consequently, a small finger-shaped water column is formed on its surface. The difference between the velocities of the water column and the mainstream of the jet becomes increasingly significant under the action of air. After reaching a certain length, the water column contracts to form a nearly spherical water droplet as a result of its surface tension. However, the water droplet is still linked to the jet via a “ligament”. Ultimately, the finger-shaped water column breaks up into several water droplets that are directly separated from the mainstream of the jet. Due to air drag, the water droplets continue to deform and vibrate. At this time point, the water droplets are relatively large and vary relatively insignificantly in diameter. The spallation angle of each water droplet is relatively small (Fig. 6.3). (2) The mainstream of a high-velocity jet is extremely unstable. As a result, the jet breaks up into sheet- and thin membrane-like water structures. Due to the high velocity, the water structures



(a) $t = 0$ ms



(b) $t = 0.8$ ms



(c) $t = 2.3$ ms

Fig. 6.1 Separation of the water droplets from a jet (nozzle diameter $D = 5.5$ mm, pressure $P = 0.3$ MPa, flow velocity $v = 16.32$ m/s, Reynolds number $Re = 89{,}815$, and Weber number $We = 20{,}953$)

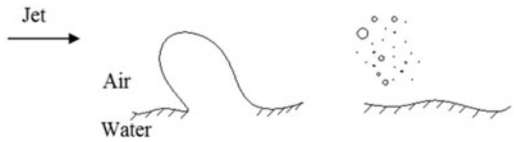
formed from the breaking up of the jet further break up into water droplets of varying sizes as well as fine mist droplets. These droplets have large spallation angles and affect a relatively large space. (3) A water droplet formed from the spallation of a jet is relatively large in size and moves at a relatively high velocity. As a result, its surface tension is insufficient for maintaining its form in the air. Consequently, the water droplet breaks up into finer water and mist droplets (Fig. 6.4). Moreover, water droplets are formed from collisions between the water droplets formed from the spallation of a jet, i.e., collisions between high-velocity water droplets lead to the formation of water and mist droplets of smaller sizes. However, this is not a main cause of the formation of water droplets based on the captured images.

6.2.1 Velocity Distribution of Jet-Spalled Water Droplets

To quantitatively study the jet spallation characteristics, the motion characteristics of a large number of water droplets spalled from jet mainstreams were statistically



(a) Main mode of the formation of water droplets from a low-velocity jet



(b) Main mode of the formation of water droplets from a high-velocity jet

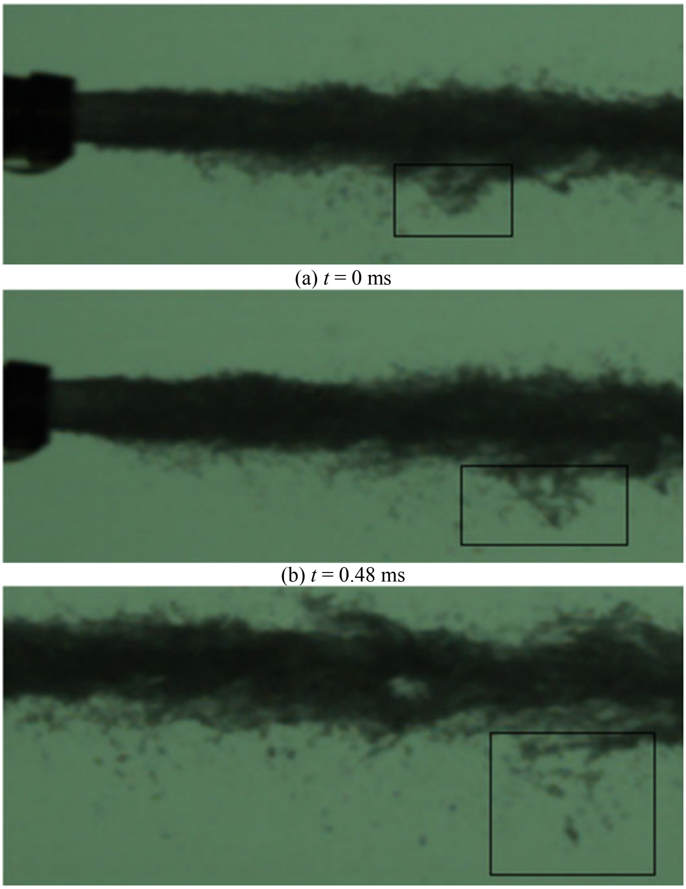


(c) Breaking up of a water droplet

Fig. 6.2 Generalized diagrams depicting several main modes of formation of water droplets

analyzed. Because the axial velocity v_X of a water droplet was significantly higher than its vertical velocity v_Y, the resultant velocity v_r calculated using an equation differed insignificantly from v_X. In addition, the statistical probability distribution of v_r was highly similar to that of v_X, as shown in Fig. 6.5. In each histogram in Fig. 6.5, the bar width represents a velocity range of 0.25 m/s. In addition, each velocity v' on the x-axis represents a velocity range from ($v' - 0.25$) to v' m/s, and the bar height represents the velocity value within this velocity range. The probability distributions of the v_X and v_r of the water droplets spalled from a low-velocity jet each approximately exhibited a bell-shaped pattern, i.e., a relatively small number of values were distributed at the two ends, while a relatively large number of values were distributed in the center. However, as the cross-sectional mean velocity of the jet increased to a relatively large value, each distribution gradually changed from a notable bell-shaped pattern to a flat pattern. The x-axis shows that the velocity distribution range gradually increased as the cross-sectional mean velocity of the jet increased. This suggests that as the cross-sectional mean velocity of jet increased, there was an increase in the distribution ranges of v_X and v_r and a decrease in the probability of each single velocity. This indicates that the water-droplet spallation velocity distribution is more uniform at a high flow velocity.

To more accurately describe the statistical probability distributions of the droplet velocity and to test the overall normality, the p-value of the normality test for the data was calculated using the W-test method. The following criterion was used: If the p-value is greater than 0.05, the hypothesis that the data are normally distributed is not rejected. The closer the p-value is to 1, the more the data conform to a normal



(a) $t = 0$ ms

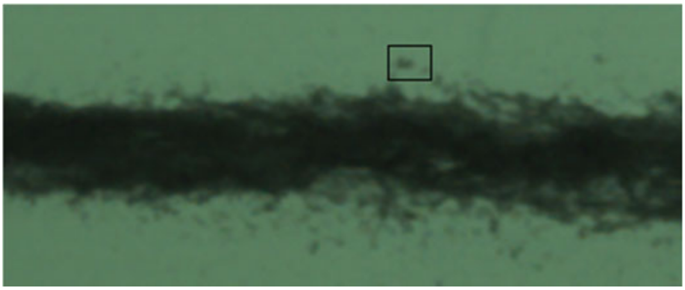
(b) $t = 0.48$ ms

(c) $t = 1.95$ ms

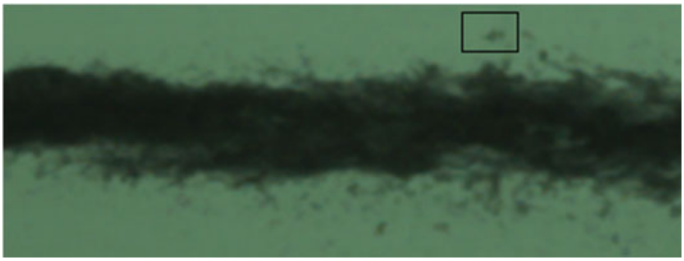
Fig. 6.3 Spallation of a high-velocity jet ($D = 4.5$ mm, $P = 0.5$ MPa, and $v_0 = 21.49$ m/s)

distribution. Table 6.1 summarizes the calculation results. The kurtosis κ is primarily used to measure the thickness of the tails of a distribution graph and can reflect the leptokurtosis of the top of a distribution graph and the thickness of the tails at its two ends. However, κ is unrelated to the value of the top of a distribution graph. The κ of each univariate normal distribution is 3 and is unrelated to its mean and standard deviation. κ is calculated using Eq. (6.1). A $\kappa > 3$ suggests that the peak of the distribution graph is relatively steep. A $\kappa < 3$ suggests that the peak of the distribution graph is relatively flat.

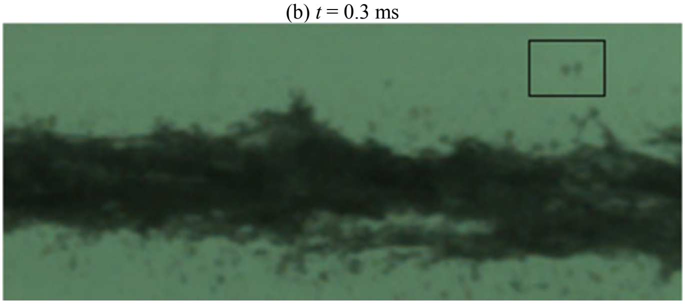
$$\kappa = \frac{E(X - \mu)^4}{\sigma^4} \tag{6.1}$$



(a) $t = 0$ ms



(b) $t = 0.3$ ms



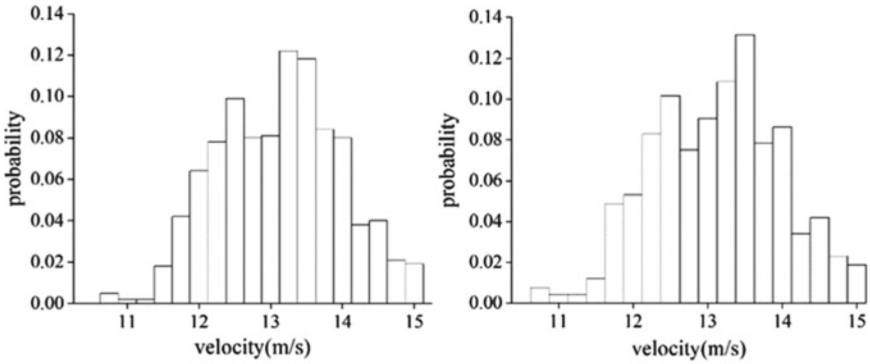
(c) $t = 2.1$ ms

Fig. 6.4 Spallation of a high-velocity jet ($D = 4.5$ mm, $P = 0.6$ MPa, and $v_0 = 22.74$ m/s)

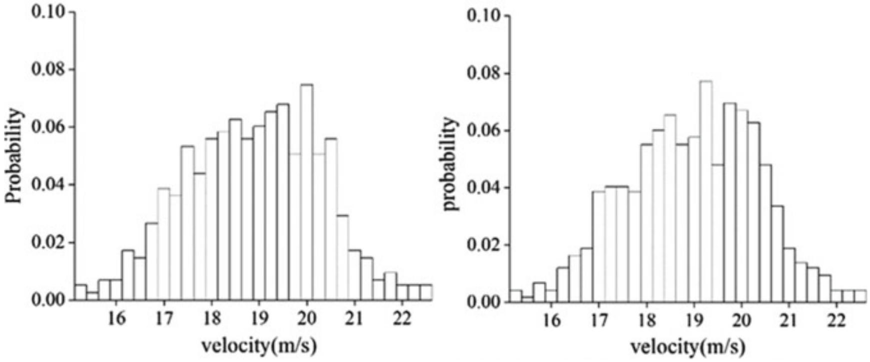
The skewness s reflects the symmetry of a distribution graph and is calculated using the following equation:

$$s = \frac{E(X - \mu)^3}{\sigma^3} \tag{6.2}$$

where σ and μ are the standard deviation and mean of the samples. The variations in the μ and σ of the resultant velocity v_r values show the variation in the shape of the normal distribution corresponding to μ and σ. Then, based on s and κ, the difference from a normal distribution can be determined. As demonstrated in Table 6.1, as σ increased, there was a gradual decrease in the peak extreme value $\left(\sqrt{2\pi}\sigma\right)^{-1}$, a gradual increase in the flatness of the shape of the normal distribution, and an



(a) $P = 0.2$ MPa, $v_0 = 13.57$ m/s



(b) $P = 0.6$ MPa, $v_0 = 22.77$ m/s

Fig. 6.5 Probability distributions of the axial velocity v_X (left) and resultant velocity v_r (right) at various jet velocities v_0 with a nozzle diameter D of 5.5 mm

increase in the degree of dispersion. In addition, an increase in μ caused the normal distribution to gradually shift to the right. However, as μ increased beyond a certain value, the normal distribution began to shift at a decreasing rate. At a low flow velocity, σ was smaller and the data were more concentrated for the jet discharged from the nozzle with a diameter D of 4.5 mm (hereinafter the 4.5-mm jet) than the jet discharged from the nozzle of $D = 5.5$ mm (hereinafter the 5.5-mm jet). As the pressure P increased to 0.5 MPa, the 4.5-mm jet dispersed to a much more significant extent than the 5.5-mm jet. In addition, the normally distributed data for the 4.5-mm jet were much more dispersed and the shape of their normal distribution was flatter than those of the 5.5-mm jet.

Next, the effects of κ and s on the shape of the distribution graph were taken into consideration. When $P = 0.2$ MPa, κ was positive for the 4.5-mm jet and negative for the 5.5-mm jet. This suggests that the peak of the graph for the 4.5-mm jet was steeper than that for the 5.5-mm jet. In addition, s was negative for the 4.5-mm jet and positive for the 5.5-mm jet (the difference was insignificant). This indicates that the data for the 5.5-mm jet were basically symmetrical, whereas the data for the

Table 6.1 Distribution characteristics of the axial velocity v_X and resultant velocity v_r

Working conditions	D (mm)	v_X					v_r				
		s	κ	σ	μ	p-value	s	κ	σ	μ	p-value
1	4.5	–	–	–	–	–	–	–	–	–	–
2		−0.753	0.674	0.776	13.38	0	−0.758	0.703	0.774	13.38	0
3		−0.144	0.254	0.735	16.02	0.294	−0.143	0.219	0.732	16.03	0.344
4		−0.195	0.536	1.399	18.31	0.019	−0.176	0.575	1.365	18.35	0.024
5		−0.694	0.473	2.576	18.3	0	−0.687	0.488	2.553	18.39	0
6		−0.423	−0.466	3.081	18.51	0	−0.432	−0.458	3.052	18.64	0
7	5.5	–	–	–	–	–	–	–	–	–	–
8		−0.062	−0.368	0.860	12.99	0.215	0.061	−0.369	0.856	13.00	0.244
9		−0.264	0.225	0.990	14.77	0.137	−0.262	0.223	0.987	14.79	0.152
10		−0.181	−0.130	1.108	15.82	0.322	−0.186	−0.114	1.101	15.85	0.351
11		−0.171	−0.339	1.282	16.87	0.143	−0.171	−0.317	1.275	16.92	0.179
12		−0.076	−0.399	1.972	18.76	0.170	−0.093	−0.374	1.950	18.83	0.171

4.5-mm jet were left-skewed and their distribution had a long tail pointing to the left. This is consistent with the distribution graph. When $P = 0.3$ MPa, similar graphs were observed, but the graph for the 4.5-mm jet had a higher peak and thicker tails than those for the 5.5-mm jet. The s values of the graphs differed insignificantly and were both very small. When $P = 0.6$ MPa, the σ of the 4.5-mm jet was much larger. However, the κ values of both graphs were negative and differed insignificantly. This suggests that the distribution of the v data for the 4.5-mm jet was much more dispersed but slightly left-skewed.

When $D = 5.5$ mm, κ was lower than that of the normal distribution corresponding to the μ and σ in most cases, though the difference was insignificant. This suggests a slightly flatter peak (i.e., thinner tails) than a normal distribution and a relatively low probability of extreme values. The graphs were left-skewed, albeit insignificantly, as shown in the figure. The data for the 4.5-mm jets were similar to those for the 5.5-mm jets in terms of the distribution shape. The distribution graphs for the 4.5-mm jets were all left-skewed, albeit insignificantly. In addition, the peaks of the distributions for the 4.5-mm jets were steeper, albeit insignificantly, than that of a normal distribution.

The normality test results for the v data show the following. When $D = 5.5$ mm, the significance was greater than 0.05, and the distribution of v_X conformed to the normality assumption. The normality test results for the 4.5-mm jets show that the data for the 4.5-mm jet with a flow velocity of 16.32 m/s conformed to a normal distribution. However, the resultant velocity data for the 4.5-mm jets did not conform to a normal distribution, except for those for the 4.5-mm jet with a velocity of 19.27 m/s, which were relatively weakly normally distributed. When $D = 4.5$ mm, water droplets began to be spalled at a velocity of 13.41 m/s but at a very small quantity. The limited statistical data samples failed the normality test. Intense spallation began as the velocity increased to 19.27 m/s. However, the statistical data samples for mist droplets at this high velocity also failed the normality test. The spallation intensity of the 5.5-mm jets under the conditions selected for statistical analysis was between that of the 4.5-mm jet with the minimum velocity and that of the 4.5-mm jet with the maximum velocity. Thus, the normality of the droplet velocity was related to the spallation intensity.

Based on the distribution graph parameters and normality test results for the 4.5- and 5.5-mm jets, the resultant velocity data for low jet flow velocity ($P = 0.2$ and 0.3 MPa) 4.5-mm jets were distributed in a more concentrated pattern than those for the 5.5-mm jets. At high jet flow velocity ($P = 0.5$ and 0.6 MPa), the data for the 4.5-mm jets were more dispersed and distributed in a more scattered pattern. All the graphs were left-skewed, albeit insignificantly, and were basically symmetrical. At a constant D, as the jet flow velocity increased, there was a gradual increase in the extent of the dispersion of the droplet velocity. Thus, the variation in the distribution curve of the droplet velocity with the jet flow velocity can be summarized as follows: as the jet flow velocity increased, the bell-shaped curve shifted to the right (as the jet flow velocity increased beyond a certain value, there was a decrease in the rate of the shift of the mean value) and gradually became flat. The experimental results obtained

in this study show that the normality of the distribution of the droplet velocity was related to the spallation intensity.

Figures 6.6 and 6.7 show the cumulative probability curves of v_r when $D = 5.5$ and 4.5 mm, respectively. An "S" shape can be observed in each distribution curve. Thus, examining the cumulative probability distribution can more directly help determine the rate and range of change in v_r. A rightward shift can be observed in the distribution of v_r with an increasing jet flow velocity when $D = 5.5$ mm. In addition, a decrease in the slope of the curve can be observed due to an increase in the range of v_r. A similar pattern can be observed in the distribution of v_r when $D = 4.5$ mm—a gradual rightward shift in the distribution curve and a decrease in its slope with an increasing jet flow velocity. Moreover, the v_r curves for the 4.5-mm jet with a high flow velocity intersect at the v_r value of 18 m/s and near the probability of 0.375. This suggests the same probability of water droplets at v_r below 18 m/s.

Table 6.2 summarizes the characteristic droplet velocities of statistical samples at various jet flow velocities. The measured cross-sectional mean flow velocity of

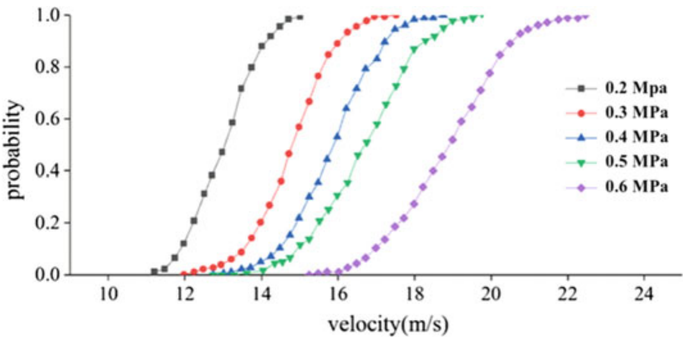


Fig. 6.6 Cumulative probability curves of resultant velocity of water droplets spalled from 5.5-mm jets

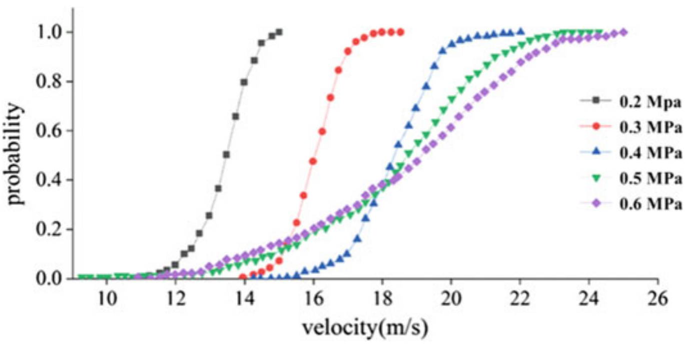


Fig. 6.7 Cumulative probability curves of the v_r of water droplets spalled from 4.5-mm jets

Table 6.2 Characteristic values of the axial velocity v_X and resultant velocity v_r of the water droplets determined from the statistical samples

Jet flow velocity v_0 ($D = 4.5$ mm) (m/s)	v_X (m/s)			v_r (m/s)		
	Max	Min	Average	Max	Min	Average
13.41	14.94	10.71	13.38	14.95	10.71	13.38
16.30	18.42	13.92	16.02	18.43	13.92	16.03
19.05	21.94	14.02	18.31	21.96	14.03	18.35
20.60	23.97	8.93	18.3	24.08	9.13	18.39
22.74	24.91	10.81	18.51	24.97	10.95	18.64
v_0 ($D = 5.5$ mm) (m/s)	v_X (m/s)			v_r (m/s)		
	Max	Min	Average	Max	Min	Average
13.57	14.92	10.53	12.99	14.93	10.54	13
16.32	17.47	11.57	14.77	17.5	11.6	14.79
19.27	18.71	12.66	15.82	18.72	12.67	15.85
21.49	19.469	12.79	16.87	20	12.83	16.92
22.77	22.42	15.05	18.76	22.45	15.08	18.83

each jet was higher than the mean droplet velocity. The turbulence intensity of high-velocity jets was as high as 0.25. A scenario where the cross-sectional mean flow velocity of the jet was lower than the maximum velocity of water droplets was observed in the statistical samples. Figure 6.8 shows the statistical variations in v_X and v_r with the jet flow velocity when $D = 5.5$ mm. As demonstrated in Fig. 6.8, as jet flow velocity increased, both v_X and v_r increased, though nonlinearly.

Figure 6.9 compares the mean v_r values of all the atomized water droplets at various jet flow velocities when $D = 4.5$ and 5.5 mm. As demonstrated in Fig. 6.9, there was an insignificant difference in the mean v_X and v_r of the atomized water

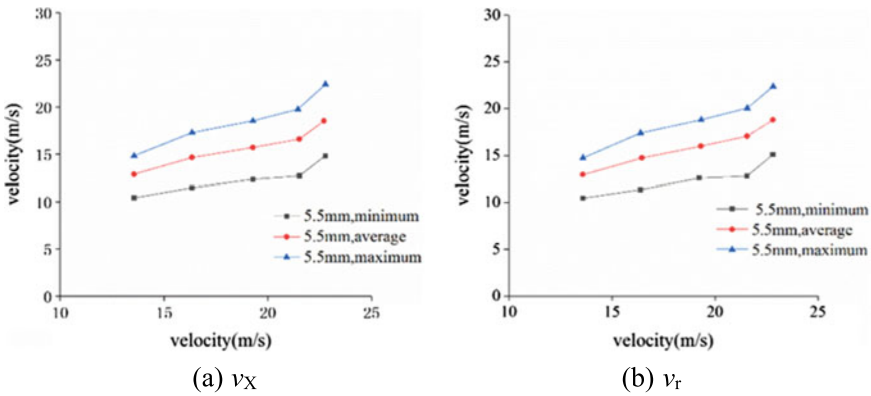


Fig. 6.8 Variations in the characteristic values of the motion parameters of the spalled water droplets with the cross-sectional mean jet flow velocity v_0 when $D = 5.5$ mm

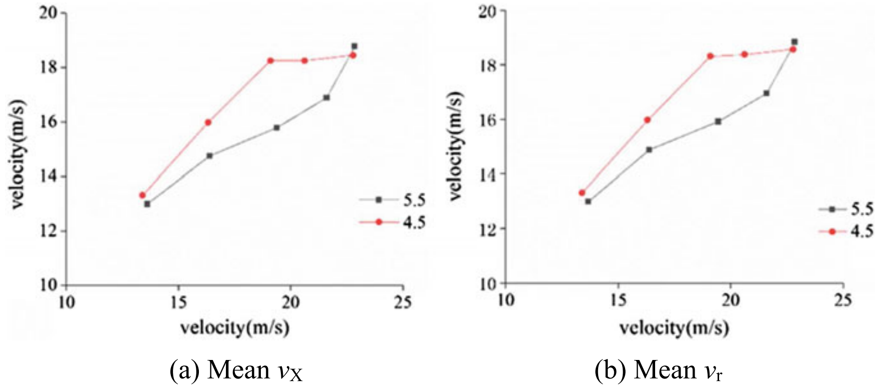
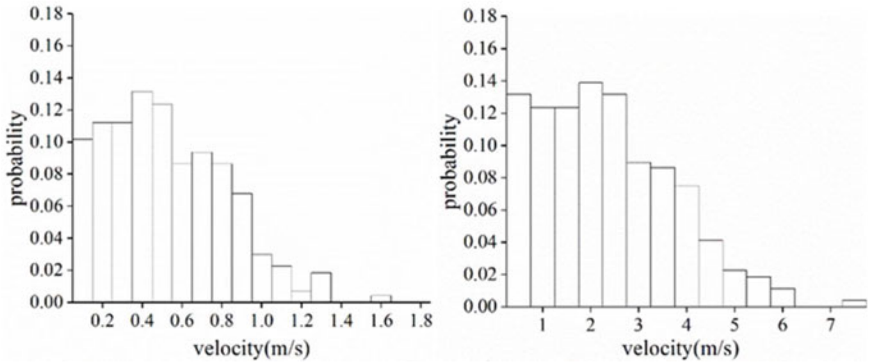


Fig. 6.9 Comparison of the mean values of the motion parameters of the spalled water droplets at various *D* values and jet flow velocities

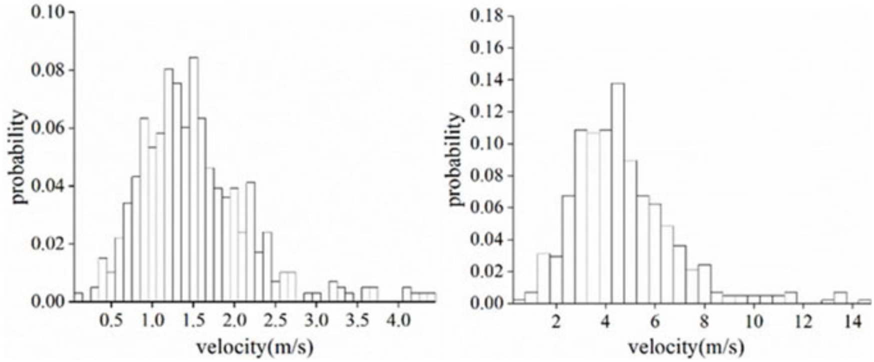
droplets between the 4.5- and 5.5-mm jets at a low jet flow velocity ($P = 0.2$ MPa). As jet flow velocity increased, there was an increase in the differences in the mean v_X and v_r between the two jet sizes. The difference reached the maximum when $P = 0.4$ MPa and gradually decreased as P increased beyond 0.4 MPa. When $P = 0.6$ MPa, the mean v_X and v_r of the water droplets atomized from the 5.5-mm jet were almost the same as those of the water droplets atomized from the 4.5-mm jet.

6.2.2 Distribution of the Moving Directions of the Water Droplets Formed by Jet Spallation

In this section, the distributions of the vertical velocity v_Y and spallation angle α_s are examined. The v_Y of the water droplets spalled from a low-velocity jet was very low, and they moved almost in parallel to the mainstream of the jet. As a result, most of the water droplets moved at a low v_Y (Fig. 6.10). As v_Y increased, there was a gradual decrease in the number of water droplets. A descending sloped shape at a certain angle can be observed in the probability distribution of v_Y. As the jet flow velocity increased, there was a gradual increase in the number of water droplets formed from jet spallation. Under this condition, v_Y was distributed in an asymmetrical bell-shaped pattern. As the jet flow velocity increased, there was a corresponding increase in the maximum v_Y and the maximum α_s. In addition, a gradual rightward shift in the v_Y and α_s corresponding to the respective highest probabilities as well as a gradual decrease in the extreme values of v_Y and α_s corresponding to the respective highest probabilities can be observed in the distribution graphs with increasing jet flow velocity. This suggests that as the mean α_s of the water droplets increased, the distribution of the numbers of water droplets of various α_s values became increasingly uniform.



(a) $P = 0.2$ MPa, $v_0 = 13.57$ m/s



(b) $P = 0.6$ MPa, $v_0 = 22.77$ m/s

Fig. 6.10 Probability distributions of the vertical velocity v_Y and spallation angle α_s of the water droplets spalled from 5.5-mm jets at various flow velocities v_0 (the bar width represents a range of 0.1 m/s in the v_Y distribution graphs and a range of 0.5° in the α_s distribution graphs)

Table 6.3 summarizes the shape characteristics of the probability distribution of the α_s of water droplets. When D remained unchanged ($D = 4.5$ and 5.5 mm), as the jet flow velocity gradually increased, there was a gradual increase in the σ and μ of the α_s values. This suggests that the normal distribution corresponding to σ and μ became gentler, the data became more dispersed, and the axis of symmetry moved to the right as the jet flow velocity increased. At a low jet flow velocity, the normally distributed data corresponding to $D = 4.5$ mm were more concentrated. At a relatively high jet flow velocity, the normally distributed data corresponding to $D = 4.5$ were more dispersed. Next, the kurtosis κ and skewness s of the samples were considered, and the differences between the actual distribution graphs and a normal distribution were analyzed. At a constant D, the s of the distribution of α_s values was positive, regardless of the jet flow velocity. This suggests that the distribution of the α_s values at each jet flow

Table 6.3 Distribution shape characteristics of the vertical velocity v_Y and spallation angle α_s

Jet flow velocity v_0 (m/s)	D (mm)	v_Y					α_s				
		s	κ	σ	μ	p-value	s	κ	σ	μ	p-value
13.41	4.5	1.122	1.430	0.262	0.35	0	1.208	1.705	1.168	1.50	0
16.30		1.120	2.042	0.318	0.45	0	1.209	2.443	1.145	1.61	0
19.05		0.747	0.263	0.607	1.06	0	0.917	0.842	2.007	3.37	0
20.60		0.442	0.239	0.868	1.60	0	0.449	0.027	2.948	5.19	0
22.74		1.110	3.288	1.067	1.80	0	0.645	0.862	3.517	5.82	0
13.57	5.5	0.601	0.034	0.302	0.47	0	0.643	0.075	1.390	2.10	0
16.32		0.821	0.996	0.357	0.72	0	0.808	0.906	1.424	2.82	0
19.27		0.811	0.294	0.446	0.89	0	0.881	0.571	1.685	3.24	0
21.49		1.121	2.520	0.573	1.23	0	1.133	2.263	2.009	4.21	0
22.77		1.246	2.693	0.679	1.46	0	1.403	3.378	2.135	4.47	0

velocity was skewed right, that most of the data were to the left of the mean value, and that the left end of the distribution was relatively thick. The right end of the distribution of the α_s values at each jet flow velocity had a long tail and a positive κ value. This suggests that the peak of the distribution was steeper than that of a normal distribution. At a low jet flow velocity, a higher κ and a smaller σ were found when $D = 4.5$ mm. This suggests that the top of the distribution of the α values was steeper and the data near the top of the distribution were more concentrated when $D = 4.5$ mm. At a relatively high jet flow velocity, a lower κ and a larger σ were found when $D = 4.5$ mm. This suggests that the top of the graph was gentler and the data were more dispersed when $D = 4.5$ mm than when $D = 5.5$ mm. In addition, as demonstrated in Table 6.3, the α_s values at each jet flow velocity exhibited a positive s and were concentrated on the left side (i.e., the low-value side) of the distribution, which had a tail on its right side. The data were subjected to a normality test. As demonstrated in Table 6.3, the significance was 0 when $D = 4.5$ and 5.5 mm. This indicates that the distributions of the α_s values did not conform to the normality assumption.

Hence, the statistical distribution graphs of the α_s values were skewed right, and large extreme values of α_s existed at the same jet flow velocity, albeit in small quantities. As the jet flow velocity increased, the distribution graph of the statistical samples gradually became gentler, and the data became more dispersed. In regard to the distribution of the α_s values at various D values, at a low jet flow velocity, the distribution graph was steeper and the data were more concentrated at a smaller D; at a high jet flow velocity, the α_s values of the water droplets formed from the spallation of a jet discharged from a nozzle with a smaller D were more dispersed.

The distribution graphs of the α_s values observed in the experiment were notably skewed right. This suggests a very low probability of relatively large α_s values in the statistical samples. This is because a relatively large α_s often resulted from a relatively

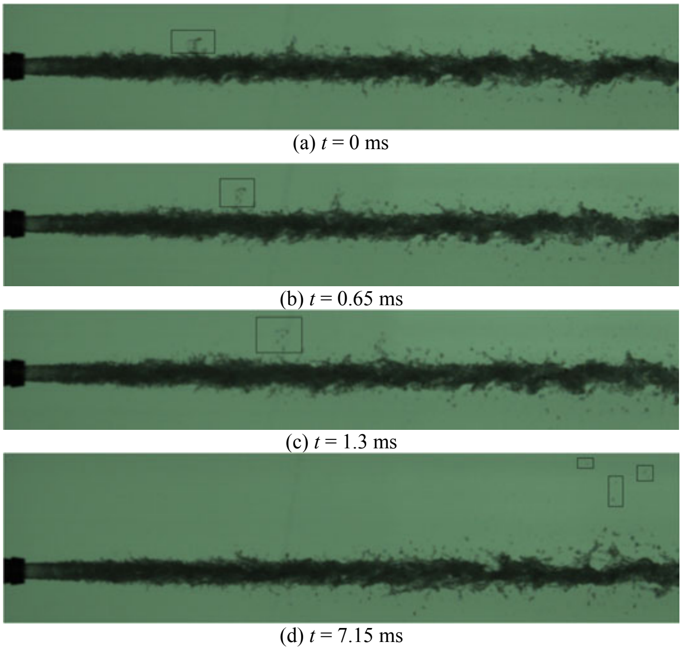


Fig. 6.11 Formation of water droplets from jet dispersion at large α_s values ($D = 5.5$ mm, $P = 0.5$ MPa, and $v_0 = 21.49$ m/s)

significant disturbance of the jet form (as shown in Fig. 6.11). Consequently, there were only a relatively small number of large α values, which exerted an insignificant impact on the formation of water droplets from jet spallation. Thus, the cumulative probability distribution of α_s in the statistical samples could cover the majority of α_s values. Figures 6.12 and 6.13 show the cumulative probability distribution patterns.

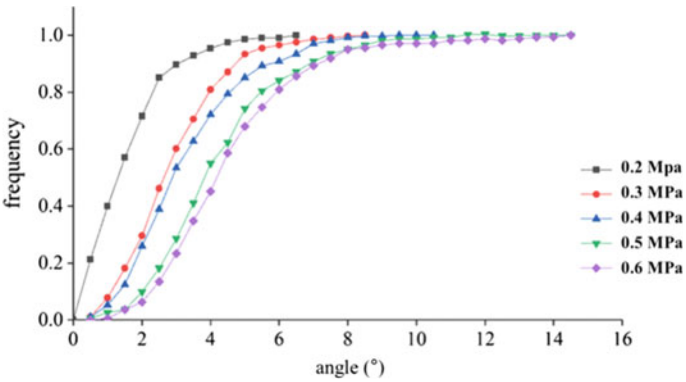


Fig. 6.12 Cumulative probability curves of the α_s of the water droplets spalled from 5.5-mm jets

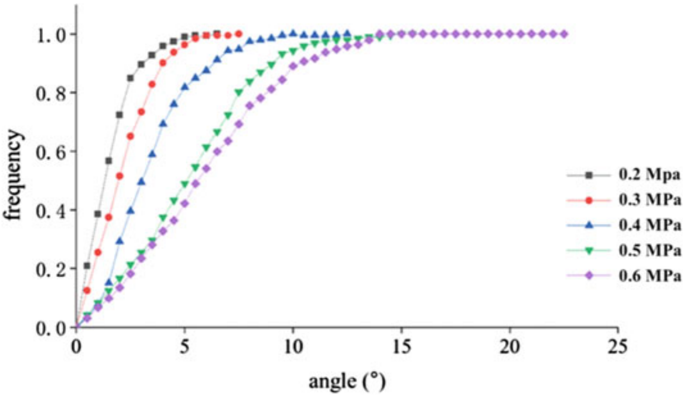


Fig. 6.13 Cumulative probability curves of the α_s of the water droplets spalled from 4.5-mm jets

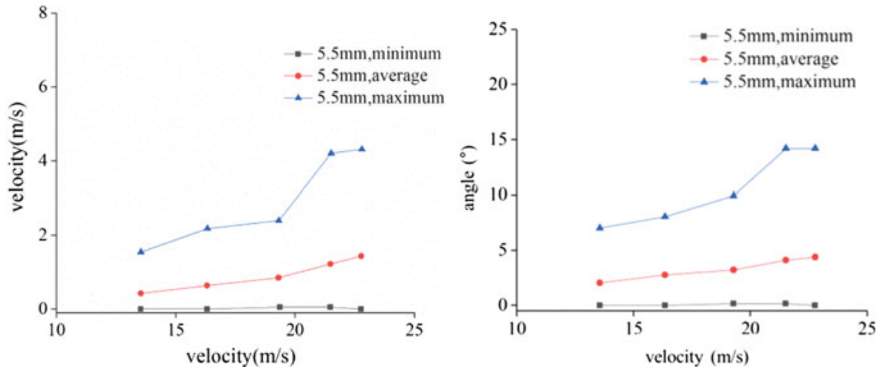
As demonstrated in Figs. 6.12 and 6.13, α_s increased as the jet flow velocity increased. As the jet flow velocity increased beyond a certain large value, the maximum α_s continued to increase but varied insignificantly. The α_s values of the majority of the water droplets formed from the spallation of 4.5- and 5.5-mm jets at various jet flow velocities were below 14°.

Table 6.4 summarizes the characteristic values of the vertical velocity v_Y and spallation angle α_s of the experimental water-droplet samples formed from jet spallation. As the jet flow velocity increased, there was an increase in the characteristic values of v_Y and α_s. At a constant D, as the jet flow velocity increased, compared to the

Table 6.4 Characteristic values of the vertical velocity v_Y and spallation angle α_s of the water-droplet samples

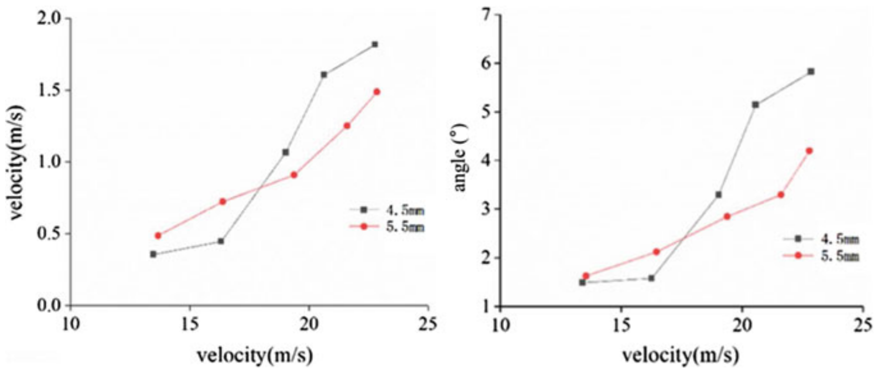
Jet flow velocity v_0 ($D = 4.5$) (m/s)	v_Y (m/s)			α_s (°)		
	Max	Min	Average	Max	Min	Average
13.41	1.39	0.01	0.35	6.18	0.04	1.5
16.3	1.94	0.01	0.45	7.4	0.03	1.61
19.05	3.36	0.02	1.06	12.21	0.04	3.37
20.6	4.75	0.04	1.6	15.33	0.12	5.19
22.74	8.04	0.01	1.8	22.33	0.02	5.82
v_0 ($D = 5.5$) (m/s)	v_Y (m/s)			α_s (°)		
	Max	Min	Average	Max	Min	Average
13.57	1.55	0.02	0.47	7.3	0.06	2.1
16.32	2.2	0.04	0.72	8.26	0.13	2.82
19.27	2.41	0.07	0.89	10.25	0.24	3.24
21.49	4.23	0.06	1.23	14.24	0.22	4.21
22.77	4.31	0.01	1.46	14.32	0.02	4.47

significant increase in the maximum v_Y and α_s, the mean v_Y and α_s increased, albeit to an insignificant extent, as shown in Figs. 6.14 and 6.15. In addition, the mean v_Y and α_s were much smaller than the maximum v_Y and α_s, respectively. This is consistent with the distribution graphs of v_Y and α_s. Compared to that of a 5.5-mm jet, the maximum α_s of the water droplets formed from the spallation of a 4.5-mm jet increased faster and reached as high as 22.33° (compared to the 14.32° for the water droplets formed from a 5.5-mm jet). The maximum α_s of the water droplets formed from the spallation of a 5.5-mm jet increased more slowly as the jet flow velocity increased than that of a 4.5-mm jet. A comparison of the mean v_Y and α_s of the water droplets formed from the spallation of jets of various sizes found that at a relatively low jet flow velocity, the mean v_Y and α_s of the water droplets decreased as the size of the jet increased.



(a) v_Y (b) α_s

Fig. 6.14 Variations in the characteristic values of the spallation angle α_s of water droplets with the cross-sectional mean flow velocity when $D = 5.5$ mm



(a) Comparison of the mean v_Y (b) Comparison of the mean α_s

Fig. 6.15 Comparison of the mean values of the motion parameters of water droplets at various nozzle diameters and flow velocities

6.3 Jet Collision in Air

Both physical model tests and theoretical analyses have demonstrated that the distributions of the intensity of the rainfall atomized from two jets when they collide in air and when they do not collide in air differ significantly and that the impingement angle and flow-rate ratio of the two jets significantly affect the distribution of the intensity of the rainfall formed from their spallation after the collision in air (Yuan et al. 2018). Studying the effects of collision on the spallation trajectories of jets as well as the distributions of the characteristic values of several parameters (size, velocity, and quantity) of water droplets during the collision and spallation processes of jets from a mesoscale perspective can facilitate an in-depth understanding of the FDA pattern when jets collide in air.

6.3.1 Characteristics of the Water Droplets Formed by a Jet Collision in Air

In this section, the modes of spallation of two jets after their collision in air are investigated. Collision in air alters the initial form and motion characteristics of jets. The spallation intensity of the nappe formed after a collision in air between two jets is higher than that of the jets. The transverse and streamwise spreading ranges of the postcollision nappe increase as the spatial distance increases (Sanjay and Das 2017a, b). In addition, large numbers of water droplets and water-droplet masses break away from the postcollision nappe at its edges. The number n of water droplets per unit time (i.e., the number frequency of water droplets) is used to measure the number of water droplets at a measuring point:

$$n = \frac{N}{T} \tag{6.3}$$

where N is the number of water droplets collected within the collection time T. Let d be the measured diameter of a water droplet. The probability of a certain diameter d at a measuring point is the ratio of the number n_d of water droplets with a diameter d to N:

$$p_d = \frac{n_d}{N} \tag{6.4}$$

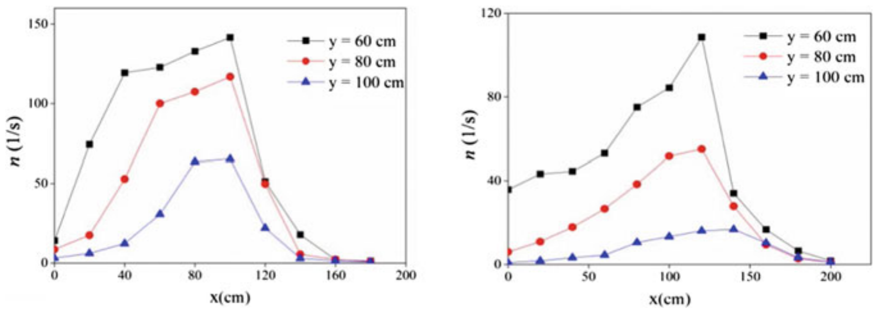
where n_d is the number of water droplets with a certain diameter d. Let v be the velocity of a water droplet. The probability of a certain v is the ratio of the number of water droplets with a velocity v (n_v) to N:

$$p_v = \frac{n_v}{N} \tag{6.5}$$

Let $\overline{v}$ and $\overline{d}$ be the mean velocity and mean diameter of the water droplets at each measuring point, respectively.

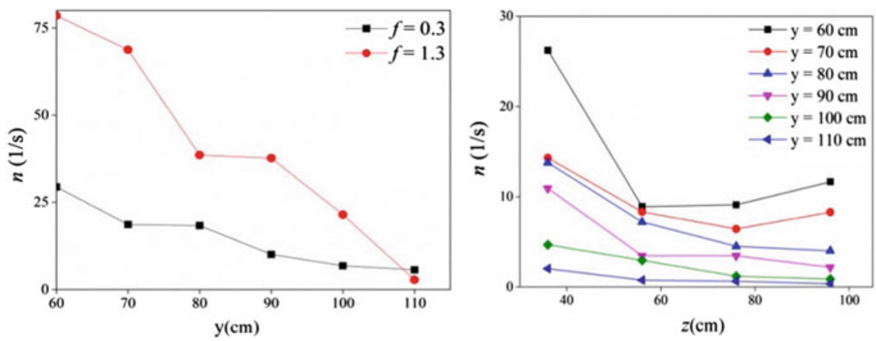
Figure 6.16 shows the distribution patterns of n in various streamwise cross-sections at various impingement angle β and flow-rate ratio f values (z is the distance between the location of a vertical cross-section from the collision point between the two jets). In each case, n first increased and then decreased along the streamwise direction and had an extreme value n_{max}. In addition, f had a more significant impact on n than β. According to the theorem of momentum, after the collision, the majority of the water droplets had a velocity component along the streamwise direction, while their vertical and transverse velocity values were random. In the transverse cross-section with the maximum rainfall intensity I_{max}, n decreased along the transverse direction and first decreased and then became stable along the vertical direction (Fig. 6.17).

In the transverse cross-section with I_{max}, $\overline{d}$ first increased and then basically remained stable along the vertical direction. However, overall, as z increased, there



(a) $\beta = 48°, f = 0.9$ (b) $\beta = 48°, f = 3.2$

Fig. 6.16 Streamwise distribution patterns of the number frequency of water droplets n



(a) $\beta = 90°$ (b) $\beta = 77°, f = 0.3$

Fig. 6.17 Transverse and vertical distribution patterns of n

was an insignificant change in $\overline{d}$ in both the transverse and streamwise cross-sections (Fig. 6.18).

In the experiment, the droplet velocity v was found to range from 0 to 15 m/s. There was a relatively high probability of v values of 0–3 m/s at the same measuring point (Fig. 6.19). $\overline{v}$ first increased and then decreased along the streamwise direction on various cross-sections and had an extreme value $\overline{v}_{max}$. There was a certain distance between the location of $\overline{v}_{max}$ and the collision point. In addition, the location of $\overline{v}_{max}$ basically coincided with that of the extreme value of $\overline{d}$ ($\overline{d}_{max}$) (Fig. 6.20). Moreover, there were similar patterns of variation in $\overline{v}$ and $\overline{d}$. The measured $\overline{d}$ of the water droplets that moved at a relatively high $\overline{v}$ was relatively large, and vice versa. This occurs because a relatively small water droplet is relatively significantly affected by drag and buoyancy and consequently moves relatively slowly. Thus, water droplets with a relatively large $\overline{d}$ moved at a relatively high $\overline{v}$, and water droplets with a

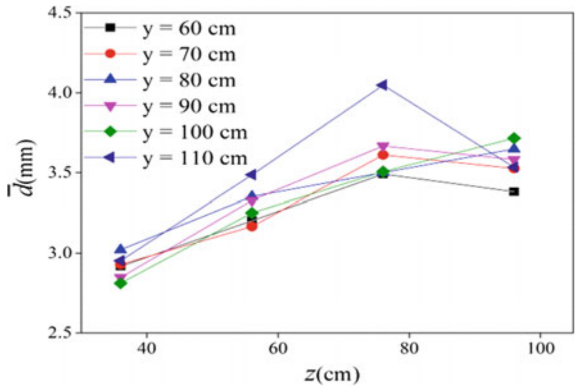
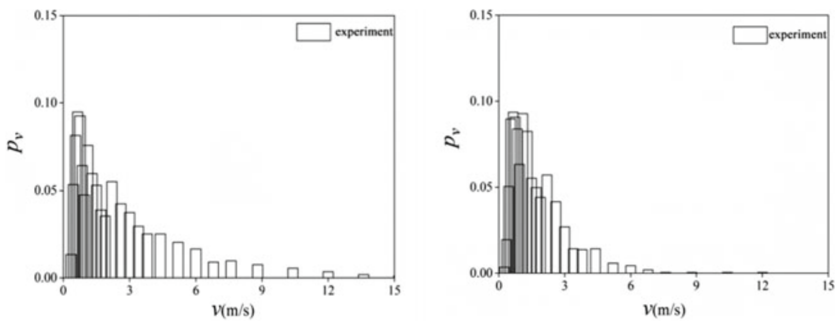


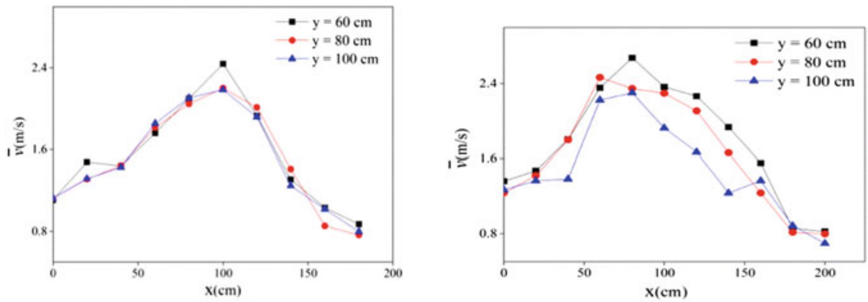
Fig. 6.18 Variations in the mean droplet diameter $\overline{d}$ in various cross-sections along the vertical direction



(a) (b)

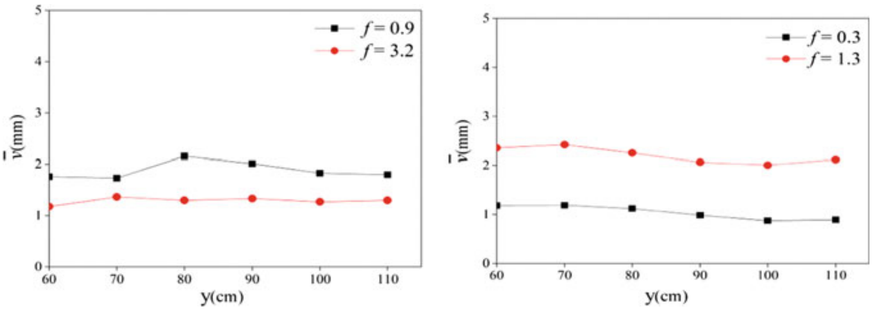
$\beta = 48°, f = 0.9$, z = 96 cm, y = 60 cm, x = 60 $\beta = 90°, f = 3.2$, z = 96 cm, y = 70 cm, x= x_{Imax}

Fig. 6.19 Probability distributions of the droplet velocity v at a given measuring point



(a) $\beta = 48°, f = 0.9$ (b) $\beta = 90°, f = 1.3$

Fig. 6.20 Streamwise distribution patterns of the mean droplet velocity $\overline{v}$



(a) $\beta = 48°$ (b) $\beta = 90°$

Fig. 6.21 Transverse distribution patterns of the mean droplet velocity $\overline{v}$

relatively small $\overline{d}$ moved at a relatively low $\overline{v}$, i.e., $\overline{v}$ was closely related to $\overline{d}$. $\overline{v}$ fluctuated to an insignificant extent along the transverse direction (Fig. 6.21). This pattern of variation was consistent with that in $\overline{d}$. This suggests that the patterns of variation in $\overline{v}$ and $\overline{d}$ were consistent in both the transverse and streamwise directions.

There were no significant changes in $\overline{v}$ along the vertical direction. As the vertical distance increased, $\overline{v}$ first increased and then decreased slightly. This was similar to the variation in $\overline{d}$ (Fig. 6.22). The similar variations in $\overline{v}$ and $\overline{d}$ suggest that the variations in $\overline{v}$ and $\overline{d}$ were similar in each spatial direction.

Figure 6.23 shows the relationship between the experimentally measured droplet diameter and velocity. In Fig. 6.23, the green curve shows the predicted values given by Clift et al. (2005), whose distribution trend is similar to that of the experimental results. However, Clift et al.'s (2005) values differ relatively significantly from the experimental values. The following droplet velocity–diameter relationship was established based on experimental measurements:

$$v = 9.5[1 - \exp(-0.4d)] \tag{6.6}$$

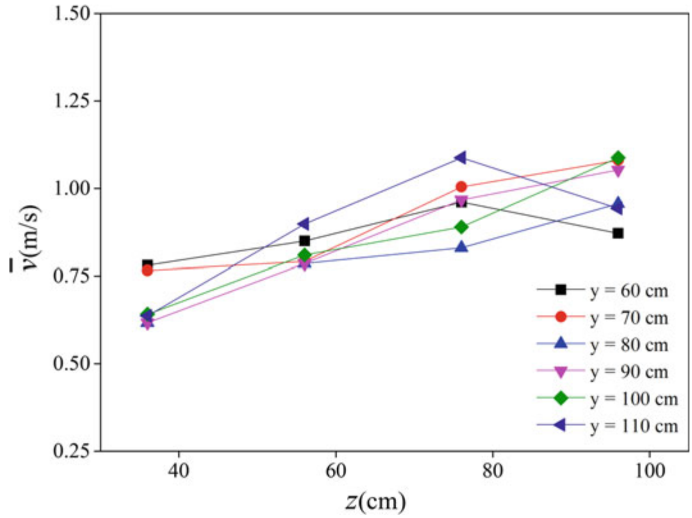


Fig. 6.22 Vertical distributions of the mean droplet velocity $\overline{v}$

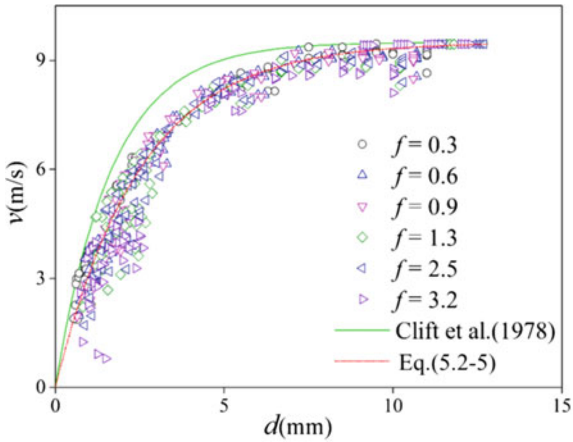


Fig. 6.23 Experimental droplet velocity–diameter relationship

6.3.2 Effects of the Flow-Rate Ratio on the Characteristics of the Water Droplets Formed by a Jet Collision

Figure 6.24 shows the spallation of water droplets due to a two-jet collision in air. The flow-rate ratio had a significant impact on the results of the collision. When the flow rate of the upper jet was significantly lower than that of the lower jet, the postcollision mainstream moved basically along the original motion trajectory of the lower jet. In addition, under these conditions, most of the water droplets were formed from the spallation of the upper jet, and the water droplets splashed over a relatively



Fig. 6.24 Water droplets formed from spallation of jets as a result of collision in air

large area. When the flow rate of the upper jet was significantly higher than that of the lower jet, the postcollision mainstream moved basically along the original motion trajectory of the upper jet. Under these conditions, most of the water droplets were formed from the spallation of the lower jet, and the water droplets splashed over a relatively small area.

Moreover, the mean diameter $\overline{d}$ and mean velocity $\overline{v}$ of the water droplets were affected by the flow-rate ratio f. Specifically, $\overline{d}$ and $\overline{v}$ first increased and then decreased as f increased. $\overline{d}$ and $\overline{v}$ reached their respective maximum values when f was approximately 1 (Fig. 6.25).

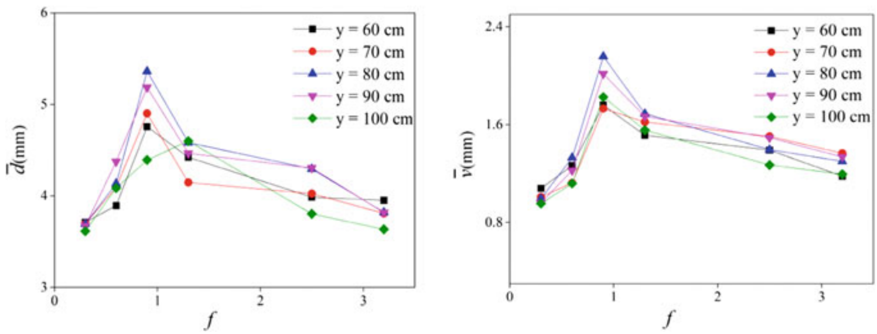


Fig. 6.25 Effects of the flow-rate ratio f on the mean diameter $\overline{d}$ and mean velocity $\overline{v}$ of water droplets (impingement angle $\beta = 48°$)

6.3.3 Spallation Area of Jets After Collision in Air

Collision in air between two jets increases the water droplet spallation area. Figure 6.26 shows the generalized characteristics of a collision in air between two jet nappes. V_1, θ_1, and q_1 are the flow velocity, angle of depression, and unit-width flow of the upper surface-outlet nappe when exiting from the bucket, respectively. V_2, θ_2, and q_2 are the flow velocity, trajectory angle, and unit-width flow of the deep-outlet nappe when exiting from the bucket, respectively. The two nappes converge at the point M. V_{1M} and β_1 are the flow velocity of the surface-outlet nappe and the angle between the surface-outlet nappe and the streamwise direction at the point M, respectively. V_{2M} and β_2 are the flow velocity of the lower deep-outlet nappe and the angle between the lower deep-outlet nappe and the streamwise direction at the point M, respectively. V_M, β_M, α_1, and α_2 are the takeoff flow velocity of the postcollision mixed nappe, the angle between the mixed nappe and the streamwise direction, the angle between the trajectory of the inner edge of the mixed nappe and the vertical direction (z-axis), and the angle between the trajectory of the outer edge of the mixed nappe and the streamwise direction (x-axis), respectively.

$$\tan \beta_M = \frac{q_1 \sin \beta_1 - q_2 \sin \beta_2}{q_1 \cos \beta_1 + q_2 \cos \beta_2} \tag{6.7}$$

$$V_M = \frac{V_{1M}(q_1 \cos \beta_1 + q_2 \cos \beta_2)}{q_M \cos \beta_M} \tag{6.8}$$

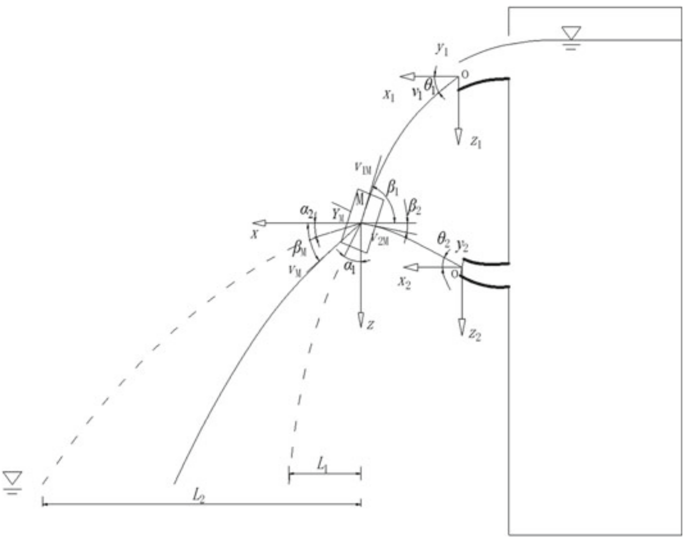


Fig. 6.26 Schematic diagram of a collision in air between deep- and surface-outlet nappes

In addition, the precollision values of V_{1M}, β_1, and β_2 must be determined. Thus, the parabolic trajectories of the surface- and deep-outlet nappes must be understood. The spatial location of the collision point M can be determined by ascertaining the trajectory of the inner edge of the surface outlet and the trajectory of the outer edge of the deep outlet. On this basis, V_{1M}, β_1, and β_2 can be calculated.

Figure 6.27 compares the measured and calculated locations of the maximum rainfall intensity I_{max}. The measured locations of I_{max} are basically on the theoretical parabolas, with an error within 5%.

Next, the postcollision trajectories of the inner and outer edges of the mixed flow are discussed. First, the trajectory of the inner edge is discussed. Projectile motion was achieved at various angles with a velocity of V_M and the location of the collision point M as the origin of the coordinates. The previous analysis demonstrated that the shape of the trajectory of the inner edge of the nappe formed after collision between two jets is similar to that of a parabola and that the postcollision velocity can be calculated. The angles between the initial velocity and the streamwise and vertical directions were derived from each parabolic trajectory with a known velocity. The errors between each parabolic trajectory and the measured locations were basically within 5%. This suggests that the trajectories of the inner edge determined through theoretical analysis combined with experimental measurements are in good agreement with the measured values (Fig. 6.28).

α_1 was relatively significantly affected by the flow-rate ratio f and impingement angle β. If f remained unchanged, an increase in β resulted in an increase in α_1; if β remained unchanged, an increase in f resulted in an increase in α_1 (Fig. 6.29).

The effects of f and β on α_1 can be represented by the following equation:

$$\alpha_1 = 16e^{(f \times \sin^2 \beta)} \tag{6.9}$$

where f ranges from 0.3 to 3.2 and β ranges from 48° to 90°.

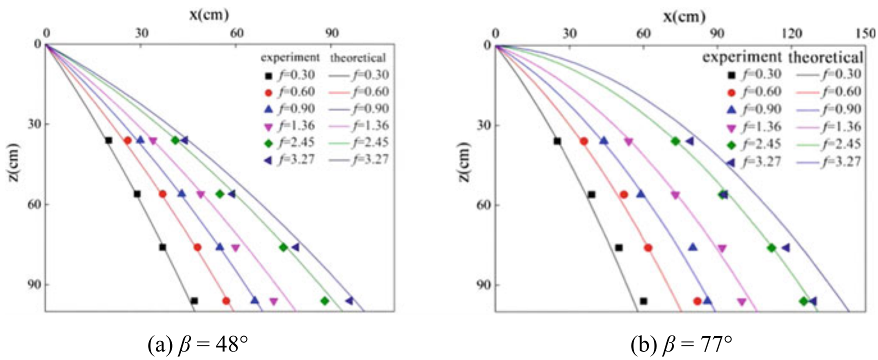
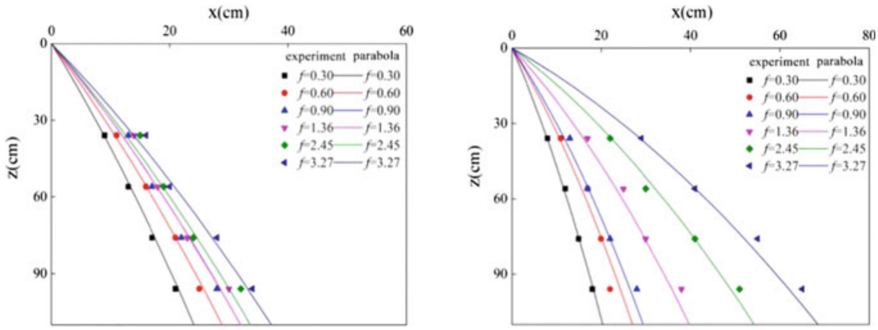
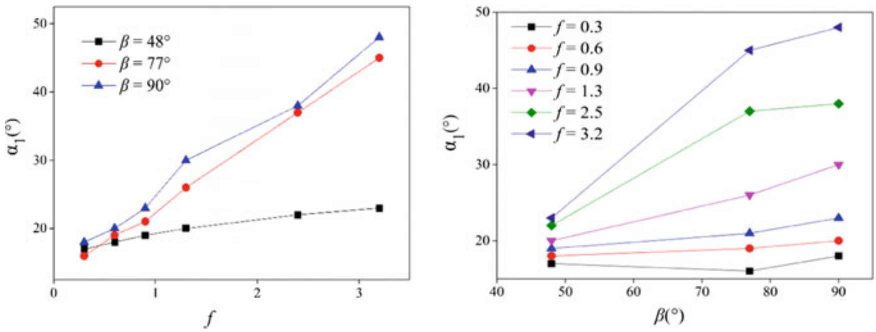


Fig. 6.27 Comparison of measured and calculated locations of maximum rainfall intensity I_{max}



(a) $\beta = 48°$ (b) $\beta = 77°$

Fig. 6.28 Comparison of the measured and calculated trajectories of the inner edge of the nappe



(a) Effects of f on α_1 (b) Effects of β on α_1

Fig. 6.29 Effects of the flow-rate ratio f and impingement angle β on α_1

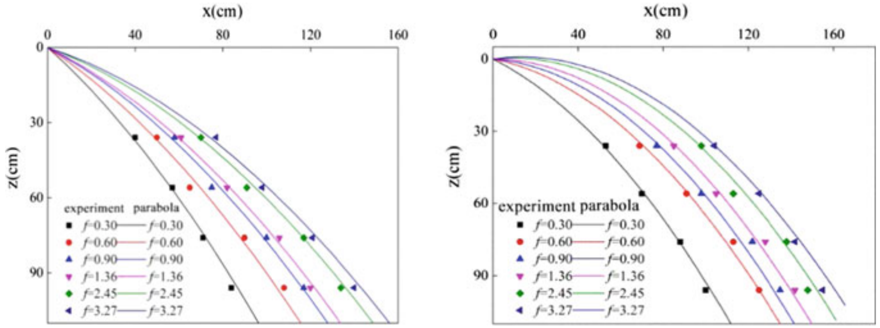
Now, the trajectory of the outer edge is discussed. Similar to the trajectory of the inner edge, α_2 can be derived. Figure 6.30 compares the calculated and measured parabolic trajectories. As demonstrated in Fig. 6.30, there is a good agreement between the calculated and measured parabolic trajectories.

The variables f, β, and α_2 satisfy the relationship below:

$$\alpha_1 = 21 \times \sin\frac{\beta}{2} \times \ln(f) + 75.5 \times \tan\frac{\beta}{2} + 28.5 \tag{6.10}$$

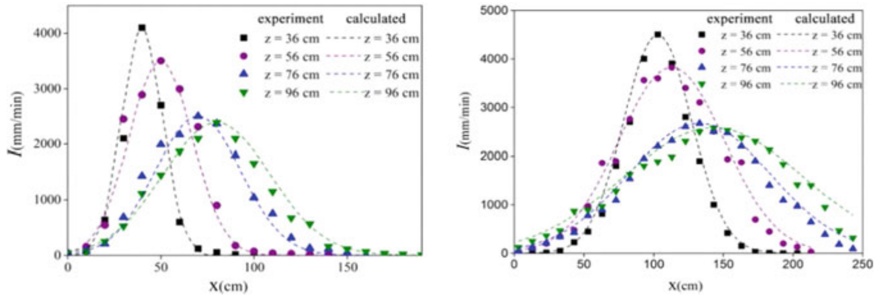
where f ranges from 0.3 to 3.2 and β ranges from 48° to 90°.

The experimental results show that rainfall intensity I followed a Gaussian distribution in the streamwise direction and that I was relatively significantly affected by f and β. The following equation for the streamwise distribution of I was derived from the experimental results:



(a) $\beta = 48°$ (b) $\beta = 77°$

Fig. 6.30 Comparison of the measured and calculated trajectories of the outer edge of the nappe



(a) $\beta = 77°, f = 0.9$ (b) $\beta = 90°, f = 3.2$

Fig. 6.31 Comparison of measured and calculated streamwise distributions of the rainfall intensity *I*

$$I = I_{max} \times e^{(-a \times (\frac{x - x_{max}}{z})^2)} \tag{6.11}$$

$$a = 10e^{(-1.8 \times f)} + 20.5 - 20 \tan \frac{\beta}{2} \tag{6.12}$$

where $I_{\max}$ is the maximum rainfall intensity measured under each set of conditions. As demonstrated in Fig. 6.31, the Gaussian distribution curves calculated using Eq. (6.11) are in good agreement with the measured values.

6.4 Water Splash by Plunging Jets

The splashing of downstream water caused by a plunging jet nappe is the largest source of atomization. Currently, when its characteristics are studied, the splashing of water caused by a plunging nappe is mainly divided into three stages of impact, splashing, and flow (Beltaos 1976; Sanjay and Das 2017a, b). In this section, the formation of water droplets from the splashing of water caused by a plunging jet as well as the movement of the water droplets after breaking away from the water are studied through mesoscale analysis of their motion characteristics. In addition, the effects of various jet parameters on splashing (the initial projection velocity v_p, splashing angle β_w, size (i.e., diameter d), and impact-point distance L_w of splashed water droplets) are investigated.

6.4.1 *Characteristics of the Water Droplets Splashed by a Jet*

The water droplets formed from the splashing of water by a plunging jet move in random directions. This section primarily analyzes several parameters of splashed water droplets, namely, β_w, d, and L.

First, β_w is analyzed. β_w under various experimental conditions was first calculated and then subjected to a gamma distribution test. Table 6.5 summarizes the results. The test results show that β_w followed a gamma distribution and that the jet-flow angle α_j of the jet was a main factor affecting β_w (Fig. 6.32).

Table 6.5 Gamma distribution test results for the splashing angle β_w

No.	Jet diameter D (cm)	Jet-flow angle α_j (°)	Jet-flow velocity U (m/s)	Calculated values of parameters			Probability (p-value)
				Alpha	Beta	Gamma	
1	0.8	30	8.37	1.76	27.94	1.89	0.915
2			11.32	1.51	26.53	2.96	0.985
3		60	8.37	5.00	15.51	17.48	0.960
4			11.97	21.06	8.47	118.52	0.985
5		90	8.64	5.83	15.73	5.19	0.960
6			11.97	25.62	9.57	147.15	0.527
7	1.6	30	4.09	1.83	33.45	11.32	0.269
8			5.40	1.53	28.40	4.54	0.684
9		60	4.40	4.48	15.20	7.72	0.997
10			6.27	4.74	12.33	−1.00	0.985
11		90	4.72	10.67	14.52	61.61	0.527
12			6.40	13.49	13.05	82.42	0.779

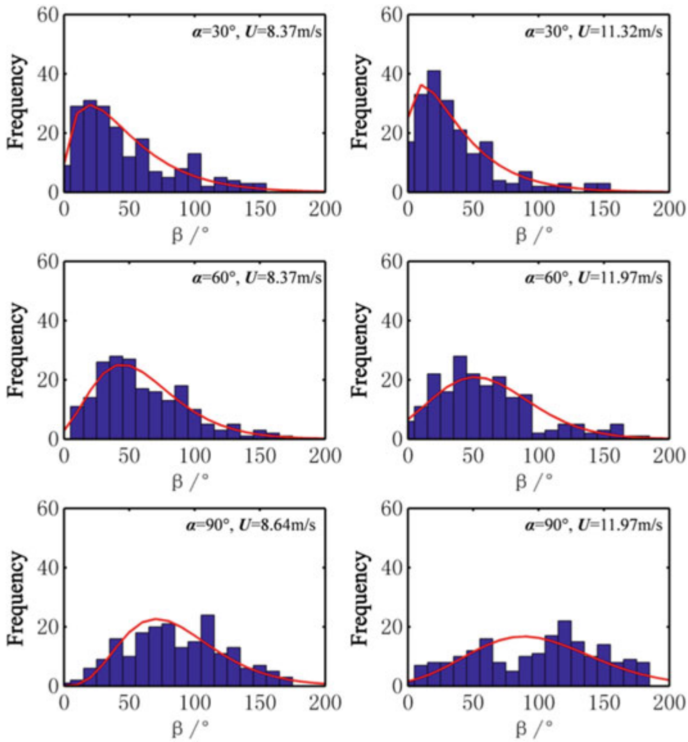


Fig. 6.32 Probability distributions of the splashing angle β_w when $D = 0.8$ cm

Second, the diameter of the splashed water droplets *d* is analyzed. *d* was statistically calculated and subjected to a gamma distribution test. Table 6.6 summarizes the results. The test results show that *d* basically followed a gamma distribution, though with a lower goodness of fit than that of β_w. This can also be observed in Fig. 6.33.

Table 6.6 Gamma distribution test results for the splashed water droplet diameter *d* under various conditions

No.	Jet diameter *D* (cm)	Jet-flow angle α_j (°)	Jet-flow velocity *U* (m/s)	Calculated values of parameters			Probability (*p*-value)
				Alpha	Beta	Gamma	
7	1.6	30	4.09	2.68	0.48	−0.54	0.081
8			5.40	3.38	0.55	−0.74	0.312
9		60	4.40	41.98	0.06	1.18	0.248
10			6.27	8.83	0.12	−0.14	0.312
11		90	4.72	13.91	0.08	0.06	0.061
12			6.40	3.05	0.20	−0.55	0.104

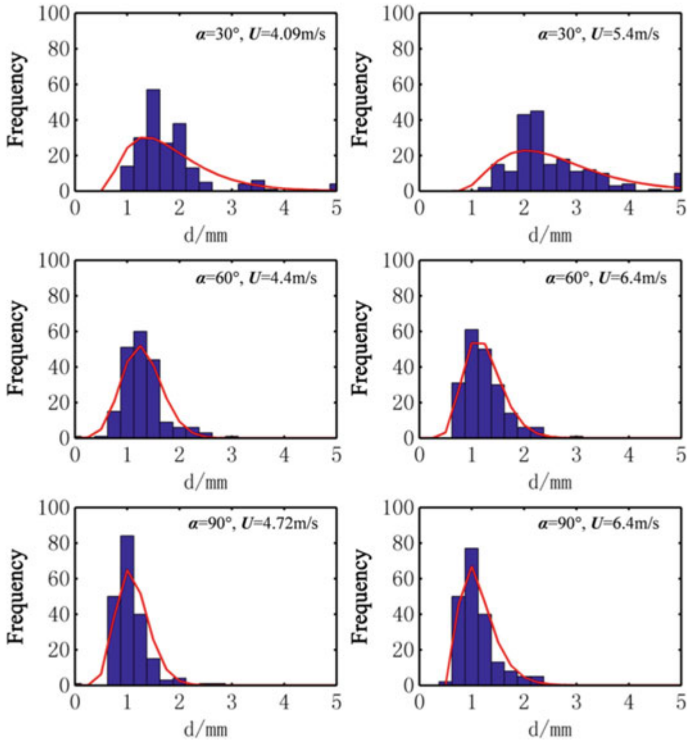


Fig. 6.33 Probability distributions of the splashed water droplet diameter d when $D = 1.6$ cm

Finally, the impact-point distance of the splashed water droplets, L, is analyzed. Table 6.7 and Fig. 6.34 both demonstrate that L similarly followed a gamma distribution.

Table 6.7 Gamma distribution test results for the impact-point distance of the splashed water droplets L_w

No.	Jet diameter D (cm)	Jet-flow angle α_j (°)	Jet-flow velocity U (m/s)	Calculated values of parameters			Probability (p-value)
				Alpha	Beta	Gamma	
7	1.6	30	4.09	19.41	0.02	0.22	0.779
8			5.40	16.78	0.01	0.12	0.997
9		60	4.40	2.61	0.02	0.02	0.985
10			6.27	2.39	0.02	0.02	0.985
11		90	4.72	3.53	0.04	0.16	0.310
12			6.40	4.00	0.04	0.15	0.449

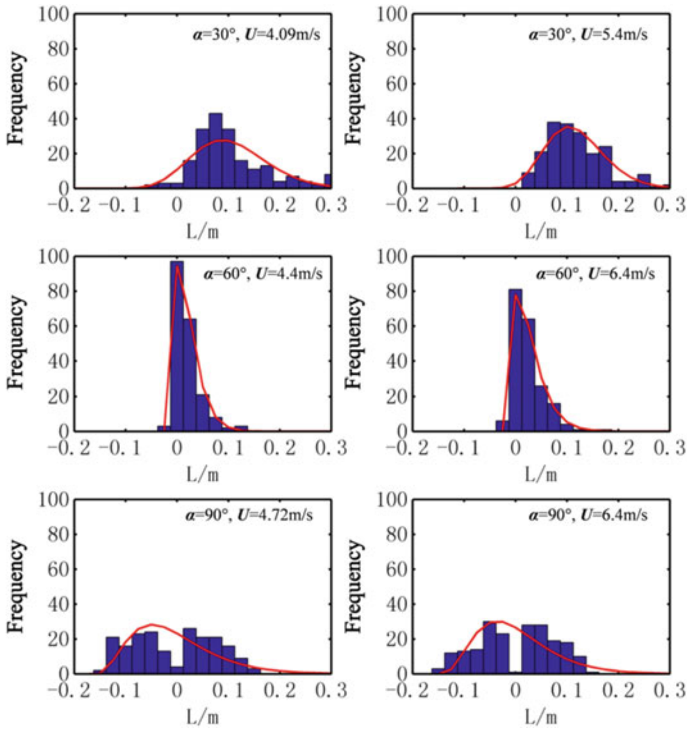


Fig. 6.34 Frequency distributions of the impact-point distance of the splashed water droplets, L, when $D = 1.6$ cm

6.4.2 Motion Pattern of the Water Droplets Formed by the Splashing of Water with a High-Velocity Plunging Jet

The initial projection velocity v_p of the water droplets formed by the splashing of water with a plunging jet plays a vital role in atomization. Table 6.8 and Fig. 6.35 show the following. At similar plunging velocities, the mean and peak values of the resultant velocity v_r of the splashed water droplets were the highest when the jet-flow angle $\alpha_j = 30°$. In addition, the mean and peak values of v_r of the splashed water droplets were significantly higher when $\alpha_j = 30°$ than when $\alpha_j = 60°$ and 90°. There was no significant difference in the mean and peak values of the v_r of the splashed water droplets between when $\alpha_j = 60°$ and when $\alpha_j = 90°$.

The velocity of the splashed water droplets can be further quantitatively analyzed. The collision between two jets satisfies the following equations:

$$J_x = m_1(u'_x - u_x) \tag{6.13}$$

Table 6.8 Distributions of the characteristic values of the initial resultant velocity v_r of the splashed water droplets

No.	Plunging jet			Initial v_r of splashed water droplets (m/s)			
	Jet diameter D (cm)	Jet-flow angle α_j (°)	Jet-flow velocity U (m/s)	Maximum	Minimum	Mean	Peak
1	0.8	30	8.37	2.86	0.08	1.05	0.89
2			11.32	3.15	0.15	1.14	0.94
3		60	8.37	2.67	0.14	0.77	0.51
4			11.97	2.03	0.11	0.73	0.61
5		90	8.64	2.28	0.14	0.89	0.77
6			11.97	2.62	0.15	0.96	0.65
7	1.6	30	4.09	3.25	0.13	1.17	0.92
8			5.40	3.5	0.13	1.29	1.13
9		60	4.40	2.41	0.17	0.74	0.46
10			6.27	2.45	0.12	0.74	0.43
11		90	4.72	2.49	0.14	0.83	0.66
12			6.40	4.32	0.23	0.83	0.71

$$J_y = m_1(u'_y - u_y) \tag{6.14}$$

$$-J_x = m_2(v'_x - v_x) \tag{6.15}$$

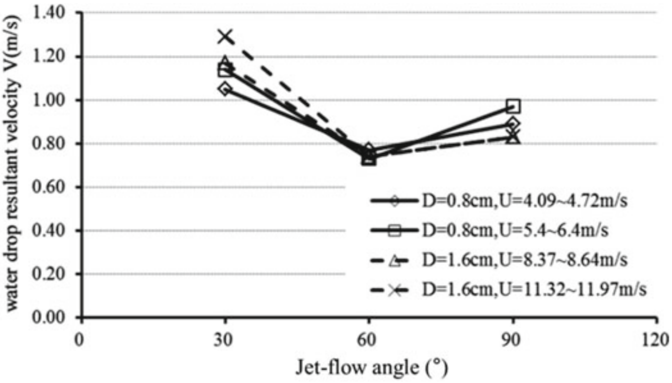
$$-J_y = m_2(v'_y - v_y) \tag{6.16}$$

where J_x and J_y are the impulse components at the collision point in the horizontal and vertical directions, respectively, m_1 is the precollision mass of the upper jet, u_x and u_y are the precollision velocity components of the upper jet in the horizontal and vertical directions, respectively, m_2 is the precollision mass of the lower jet, v_x and v_y are the precollision velocity components of the lower jet in the horizontal and vertical directions, respectively, u_x' and u_y' are the postcollision generalized velocity components of the upper jet in the two-dimensional (2D) directions, and v_x' and v_y' are the postcollision generalized velocity components of the lower jet in the 2D directions.

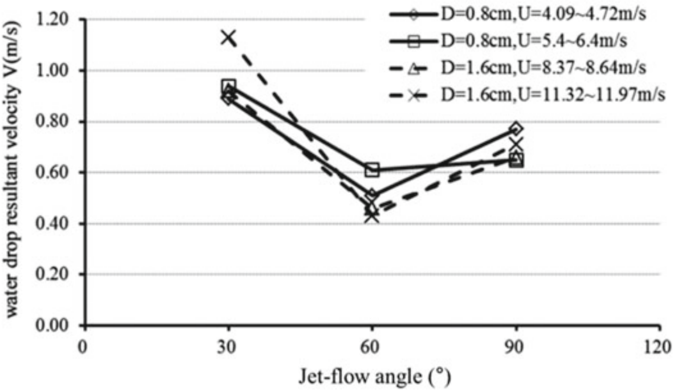
In the vertical (y) direction, the differences between the velocities before and after the collision point as well as a recovery coefficient are introduced:

$$G_y = u_y - v_y \tag{6.17}$$

$$G'_y = u'_y - v'_y \tag{6.18}$$



(a) Variation of the mean v_r of splashed water droplets



(b) Variation in the peak v_r of the splashed water droplets

Fig. 6.35 Distributions of the characteristic values of the resultant velocity v_r of the splashed water droplets

$$e = -\frac{G'_y}{G_y} \tag{6.19}$$

Thus

$$G'_y - G_y = u'_y - u_y - (v'_y - v_y) = \frac{m_1 + m_2}{m_1 m_2} J_y \tag{6.20}$$

The impulse J_y in the vertical direction is

$$J_y = -(1+e)\frac{m_1 m_2}{m_1 + m_2} G_y \tag{6.21}$$

According to Coulomb's law of friction,

$$\frac{J_x}{J_y} = c \tag{6.22}$$

The velocity components after the collision point are

$$u_x' = u_x - f(1+e)(u_y - v_y)\frac{m_2}{m_1 + m_2} \tag{6.23}$$

$$v_y' = u_y' + e(u_y - v_y) \tag{6.24}$$

For the splashing of water caused by a plunging jet, the location of the water surface is used as the collision boundary, i.e., $u_x{}' = u_y{}' = 0$, and $v_x = v_y = 0$. Thus, we have

$$e = \frac{v_y'}{u_y} \tag{6.25}$$

$$u_x' = u_x - f(1+e)\frac{m_2}{m_1 + m_2}u_y \tag{6.26}$$

The mass m_2 of the free surface can be treated as infinite relative to the mass m_1 of the impacting jet, i.e., $m_2 >> m_1$. Thus, we have

$$u_x' = u_x - c(1+e)u_y \tag{6.27}$$

The jet-flow velocity U and jet-flow angle α_{j} are the factors that affect the recovery coefficient e for a free surface impacted by a jet, as shown in Fig. 6.36. As U and α_{j} increased, there was a gradual decrease in e. This suggests that there was a moderate decrease in the vertical velocity v_{Y} of the water droplets splashed by a high-velocity, large-angle jet upon impact of a free surface (a deformable boundary) after being reflected by the free surface. Sufficiently deep water is capable of absorbing more impact energy from a jet. Let d_{m} be the mean diameter d of the water droplets formed from the splashing of water by a plunging jet. Equation (6.28) shows the approximate relationship between α_{j} and ed_{m}/D. Figure 6.37 shows the relationships of e with U and α_{j}.

$$e(d_{\mathrm{wm}}/D) = 0.035 - 0.025 \sin \alpha_{\mathrm{j}} \tag{6.28}$$

Figure 6.38 shows the relationship between the resistance coefficient c and the flow conditions during the splashing of water caused by a plunging jet. The experimental results show that c was affected primarily by α_{j}. As α_{j} increased, there was a significant decrease in c.

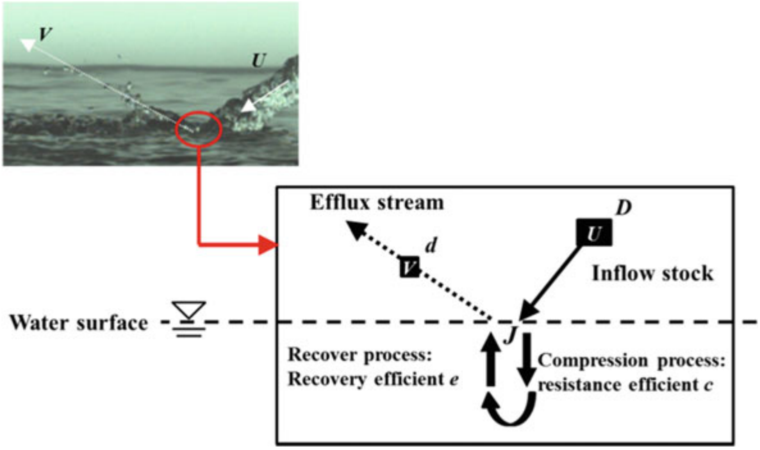
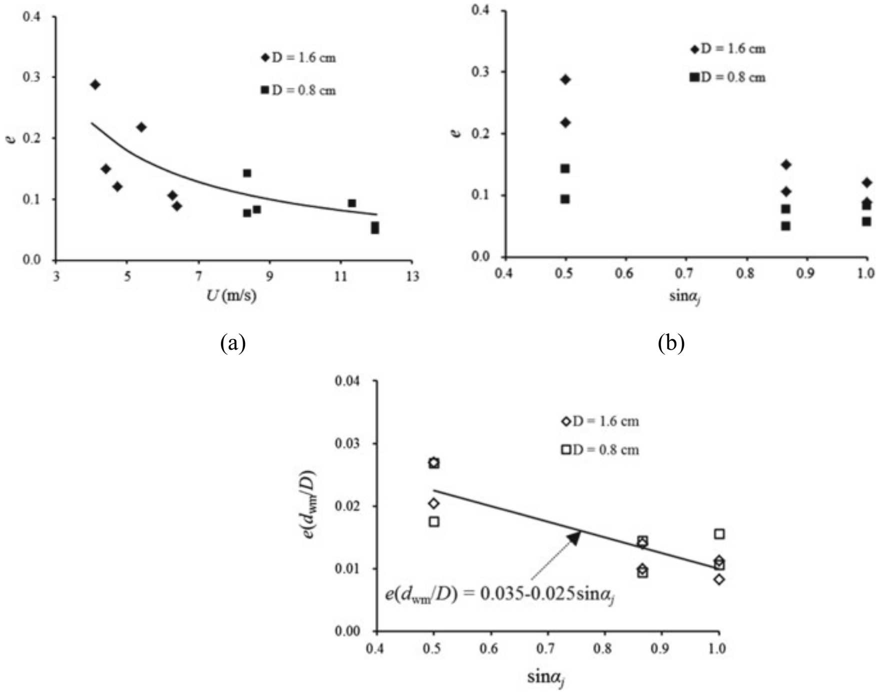


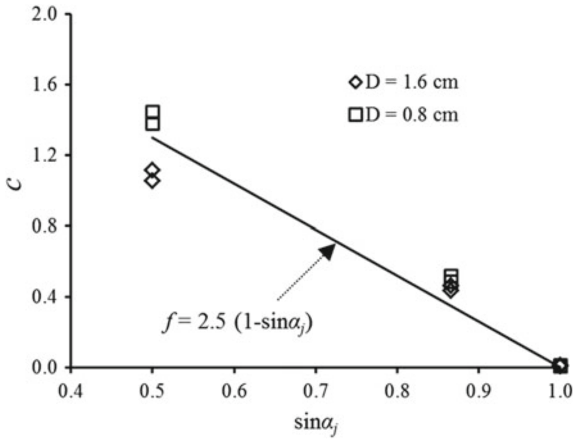
Fig. 6.36 Generalized diagram of the splashing of water droplets by a jet upon impact of a free surface



(c)

Fig. 6.37 Relationships of the recovery coefficient e with the jet-flow velocity U and jet-flow angle α_{j}

Fig. 6.38 Variation in the resistance coefficient *c*



6.5 Discussion of the Scale Effect in Flood Discharge Atomization Model Tests for High-Head Dams

Model tests are one of the main approaches to predict FDA for dams. However, model test results often differ relatively significantly from prototype measurements. Thus, the scale effect is a prominent problem faced in FDA model tests.

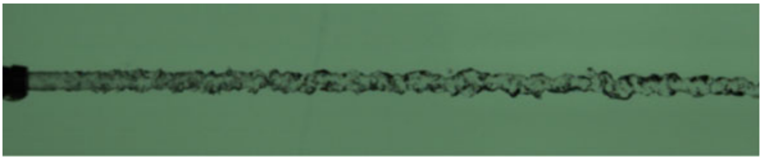
6.5.1 *Similarity Criterion for FDA Model Tests*

An FDA model is designed based on the gravity similarity criterion. The variables of a prototype structure and its model satisfy the following relationship:

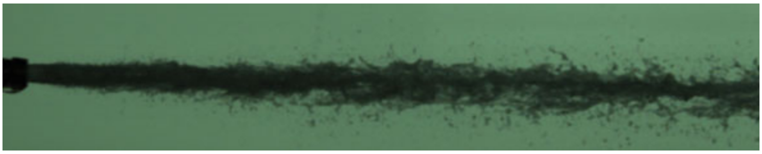
$$\frac{v_P^2}{g_{\mathrm{P}} L_P} = \frac{v_M^2}{g_{\mathrm{M}} L_M} \tag{6.29}$$

where v_P and v_M are the velocities of the prototype structure and the model, respectively, L_P and L_M are the lengths of the prototype structure and the model, respectively, and g is the gravitational acceleration.

The gravity similarity criterion treats gravity as the main acting force in the flow of a liquid. However, the surface tension of a liquid also has a relatively significant impact during the atomization of its flow. Thus, a relatively high flow velocity (e.g., >6 m/s) and a relatively large Weber number *We* (e.g., >500) are required for an FDA model test (Wu et al. 2011). However, except for a 1:1 scale, it is difficult to meet the gravity similarity criterion while also meeting the *We* similarity criterion in a model. In other words, the following equation cannot be satisfied:



(a) $v_0 = 9.46$ m/s, $Re = 41{,}212$, $We = 5{,}413$



(b) $v_0 = 22.74$ m/s, $Re = 99{,}065$, and $We = 31{,}275$

Fig. 6.39 Comparison of the spallation forms of 4.5-mm jets at low- and high-velocities (v_0), respectively

$$\frac{\rho_P l_P V_P^2}{\sigma_\mathrm{p}} = \frac{\rho_M l_M V_M^2}{\sigma_\mathrm{M}} \tag{6.30}$$

where ρ is the density, l is the characteristic length of the flow, V is the velocity of the flow, and σ is the surface tension coefficient. Thus, an FDA model test does not strictly follow the similarity laws.

6.5.2 Scale Effect in FDA Model Tests

Figure 6.39 shows the spallation of jets at flow velocities of approximately 10 and 20 m/s, respectively. Almost no water droplets were spalled from the jet at a relatively low flow velocity within the limited window. In comparison, the jet at a relatively high flow velocity spalled significantly, resulting in the formation of a large number of splashed water droplets. In a model test, even one with a large-scale model, the jet flow velocity is generally lower than 10 m/s. Thus, it is difficult to simulate the spallation of a flow.

In regard to the selection of a scale for an FDA model test, a jet flow velocity higher than 6 m/s and a *We* greater than 500 are generally required. However, the experimental observations were as follows. The set of experimental conditions consisting of a *D* of 4.5 mm, a *We* of 5413 and a jet flow velocity of 9.46 m/s as well as that consisting of a *D* of 5.5 mm, a *We* of 7440 and a jet flow velocity of 9.92 m/s completely meet the requirements that the *We* value be greater than 500 and the jet flow velocity be higher than 6 m/s. Nevertheless, almost no water droplets were spalled from the 4.5-mm jet within the window. While an extremely small number of water droplets were present within the window for the 5.5-mm jet, this jet was far from significantly spalled.

In fact, the experimental observations found the following. (1) When D remained unchanged, as the jet flow velocity increased, there was a gradual increase in the extent of spallation of the jet, a gradual decrease in the length of the stable section of the jet after discharge from the outlet, and a continuous increase in the α_s of the water droplets. In addition, the smallest water droplets spalled from a high-velocity jet were even smaller than those spalled from a low-velocity jet in terms of d. (2) At a relatively low jet flow velocity, the 4.5-mm jet spalled to a lesser extent than the 5.5-mm jet and remained relatively highly stable. In addition, at a relatively low jet flow velocity, the 4.5-mm jet did not significantly disperse into water droplets. At a relatively high jet flow velocity, the mainstream of the 4.5-mm jet broke up violently, resulting in the formation of a large number of water droplets of varying d values and high α_s values. At a relatively high jet flow velocity, the 4.5-mm jet spalled to a notably greater extent than the 5.5-mm jet. (3) At a relatively low jet flow velocity, water droplets were mainly formed as a result of the surface turbulence of a jet. At a relatively high jet flow velocity, apart from the water droplets formed as a result of turbulence, large water masses broke away from a jet. These water masses further broke up into small water droplets as a result of air drag (Fig. 6.2). Thus, the spallation of a high-velocity jet into water droplets differs from that of a low-velocity jet.

It is difficult to use a reduced-scale model to reasonably simulate the spallation of a jet. However, Sect. 6.4 of this chapter shows that a reduced-scale model is capable of more reasonably and accurately simulating the splashing of water caused by an impacting jet. In addition, the drift of mist in air is not primarily controlled by gravity. Thus, an FDA model test is capable of relatively satisfactorily simulating the splashing of water caused by an impacting jet but incapable of effectively simulating the spallation of a jet in air and the drift of mist.

6.6 Conclusions

The following summarizes the main conclusions derived from the analysis in this chapter:

1. The extent of the spallation of a high-velocity jet increases as the jet flow velocity increases. In addition, the spallation patterns of high- and low-velocity jets are different.
2. The splashing angle β_w and diameter d of the water droplets formed from the splashing of water caused by a high-velocity plunging flow both follow a gamma distribution.
3. Two-jet collision in air significantly increases the FDA intensity and is significantly affected by the flow-rate ratio f and impingement angle β.
4. An FDA model test is capable of relatively satisfactorily simulating the splashing of water caused by a plunging jet but incapable of effectively simulating the spallation of a jet in air and the drift of mist.

References

Beltaos, S. (1976). Oblique impingement of plane turbulent jets. *Journal of the Hydraulics Division, 102*(9), 1177–1192.

Choo, Y., & Kang, B. (2007). The effect of jet velocity profile on the characteristics of thickness and velocity of the liquid sheet formed by two impinging jets. *Physics of Fluids, 19*(11), 112101.

Clift, R., Grace, J. R., & Weber, M. E. (2005). *Bubbles, drops, and particles*. Courier Corporation.

Hoyt, J. W., & Taylor, J. (1977). Waves on water jets. *Journal of Fluid Mechanics, 83*(1), 119–127.

Lian, J., Liu, F., & Zhang, H. (2006). Numerical simulation of atomization due to flood discharges of hydropower stations.

Lian, J., Li, C., Liu, F., & Wu, S. (2014). A prediction method of flood discharge atomization for high dams. *Journal of Hydraulic Research, 52*(2), 274–282.

Liang, Z. (1992). A computation model for atomization flow. *Journal of Hydrodynamics, 3*.

Liu, H., Sun, S., Liu, Z., & Wang, X.-S. (2005). Atomization prediction based on artificial neural networks for flood releasing of high dams. *Journal of Hydraulic Engineering Division of the American Society of Civil Engineers, 36,* 1241–1245.

Reitz, R., & Bracco, F. (1982). Mechanism of atomization of a liquid jet. *The Physics of Fluids, 25*(10), 1730–1742.

Sanjay, V., & Das, A. K. (2017a). Formation of liquid chain by collision of two laminar jets. *Physics of Fluids, 29*(11), 112101.

Sanjay, V., & Das, A. K. (2017b). On air entrainment in a water pool by impingement of a jet. *AIChE Journal, 63*(11), 5169–5181.

Sun, S. (2009). Summary of research on flood discharge and energy dissipation of high dams in China. *Journal of China Institute of Water Resources and Hydropower Research, 2*.

Sun, X.-F., & Liu, S.-H. (2008). Investigation on the motion of splash droplets in atomized flow. *Journal of Hydrodynamics (Ser. A), 1*.

Wang, S.-Y., Chen, D., & Hou, D.-M. (2013). Experimental research on the rainfall intensity in the source area of flood discharge atomization. *Journal of Yangtze River Scientific Research Institute, 8,* 19.

Wu, S., Wu, X., Zhou, H., Chen, H., Sha, H., & Zhou, J. (2011). Analysis and application of the scale effect of flood discharge atomization model. *Science China Technological Sciences, 54*(1), 64–71.

Yuan, H., Xu, W., Li, R., Feng, Y., & Hao, Y. (2018). Spatial distribution characteristics of rainfall for two-jet collisions in air. *Water, 10*(11), 1600.

Chapter 7
Mesoscale Analysis of Flash Flood and Sediment Disasters

7.1 Background

Mountains cover 30% of the global land area. Floods and droughts account for 70% of all natural disasters, while flash floods alone make up 50% of all natural disasters. The losses caused by flash floods are among the two most significant types of loss caused by natural disasters in 105 countries in the world. Evidently, flash floods are the primary type of natural disaster across the globe. China is a mountainous country, with 70% of its land covered by mountains, far exceeding the global average level. Flash-flood prevention and control zones alone account for 48% of China's total land area. Deaths from flash floods make up more than 70% of all the deaths caused by flooding and waterlogging. Manifestly, flash-flood prevention and control has proven to be a relatively formidable task (Wang et al. 2019).

In contrast to normal floods, flash floods are more difficult to identify, predict, and control (Borga et al. 2007), owing to their prominent characteristic that notably differentiates them from normal floods—they involve the combined action of flow and sediment. This action can result in a sharp rise of the riverbed and an abrupt increase in the water level and, thereby, can increase the risk of a disaster or even enable a small flood to cause a large disaster.

For example, due to the discharge of floodwater from the Tangjiashan landslide lake as well as the action of flash floods and debris flows after the Wenchuan earthquake that occurred on May 12, 2008, large amounts of sediment entered the river downstream of the Tangjiashan lake. As a result, the riverbed of the reach in the old Beichuan county (i.e., the Beichuan National Earthquake Ruins) continually silted up and rose. Specifically, due to sedimentation, the riverbed rose cumulatively by 5–10 m on average and over 20 m in some areas. After a flash flood that occurred on July 9, 2013, the elevation of the riverbed of this reach resulting from sedimentation reached the top of the flood banks. Consequently, the floodwater spilled over the flood banks and ran to the Beichuan National Earthquake Ruins. As another example, the Boluo Hydropower Station at the confluence of the Wahei River and Xianjiapu River in Mabian County, Sichuan province was completed and put into operation in

W. Xu, *Mesoscale Analysis of Hydraulics*,
https://doi.org/10.1007/978-981-15-9785-5_7

February 1999. Two consecutive years of flash floods from June 6, 2000 to July 28, 2001 resulted in extensive sedimentation in the confluence region, which silted up the rivers. The sedimentation layer reached approximately 5.0–7.5 m in thickness. As a result, the water level was 6.5 m higher than the elevation (822.0 m) of the top of the flood walls. Consequently, the power plant was submerged. The accumulated sediment within the power plant reached 826.5 m. This caused disastrous damage to the power station. Another more typical example took place in a village at the foot of a hill. Small rivers ran on each side of this village. After a heavy rainstorm, one of the rivers severely silted up, and its water level rose considerably. As a result, the half of the village on this side suffered a severe flash flood and sediment disaster (FFSD), which left 24 people dead. No siltation occurred in the river on the other side, and consequently, the half of the village on the other side remained unscathed.

Similar to the analysis in previous chapters, FFSDs are also macroscopic assemblies of mesoscale processes. The key to an FFSD lies in the transition of sediment particles, a type of mesoscale matter, from a moving state to a stationary state, which results in macroscopic sedimentation in a large area, ultimately evolving into a severe flood and sediment disaster (Dietrich et al. 1989; Diplas et al. 2008; Madej et al. 2009). Therefore, thoroughly determining the moving pattern of sediment particles from a mesoscale perspective is imperative for the theoretical investigation, identification, prediction, and engineering control of FFSDs.

Mesoscale analysis of FFSDs entails not only the analysis of the mechanism by which the movement of sediment particles causes disasters but also the analysis of coupled flood and sediment disaster conditions, accurate identification of disasters, simulations of flood and sediment movement and, ultimately, development of techniques to guide the control of FFSDs.

7.2 Sudden Stop and Accumulation of Sediment Particles After a Hydraulic Jump

A hydraulic jump is a classical sudden change in a flow. A heuristic understanding can be derived from an analysis of the changes in the movement of sediment particles after a hydraulic jump.

Figure 7.1 shows the sudden stop of sediment particles after a hydraulic jump (images were taken at intervals of approximately 2 s). The sediment particles moving at a relatively high velocity with the flow prior to the hydraulic jump suddenly stopped moving and remained on the bed immediately after the hydraulic jump.

Under certain hydraulic jump conditions, single particles of varying sizes stopped suddenly to varying degrees when passing through the hydraulic-jump zone. As shown in Fig. 7.2, relatively large particles were mostly able to stop suddenly at locations close to the hydraulic-jump zone. These particles stopped suddenly within a relatively small area. As the particle size (i.e., median particle diameter d_{50}) increased, there was a gradual decrease in the number of particles capable of

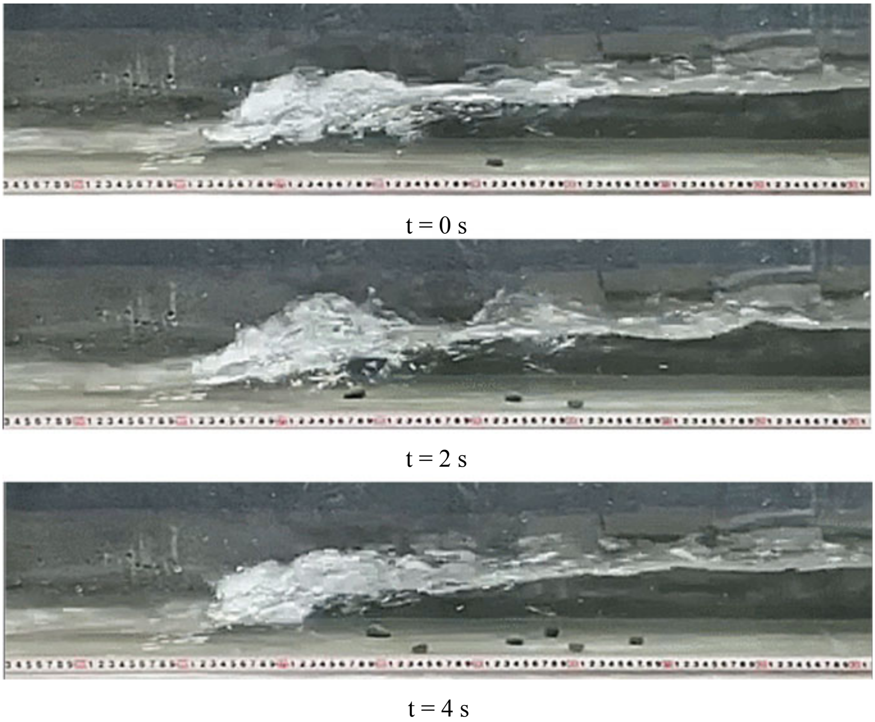


Fig. 7.1 Sudden stop of sediment particles after a hydraulic jump

basically remaining at the bottom of the flow, and many particles continued to move downstream, albeit much more slowly than before the hydraulic jump. In addition, as the particle size increased, the area where the particles stopped suddenly gradually moved downstream and increased in size. When the carrying capacity of the flow exceeded the particle size, the particles no longer stopped suddenly.

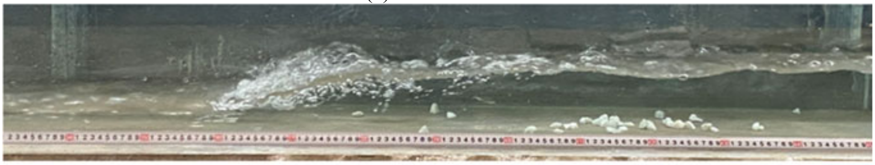
When there was a relatively large upstream sediment supply, the abovementioned sudden stop of single particles transformed into rapid, extensive sedimentation (Fig. 7.3).

Further observation found that when extensive sedimentation occurred rapidly, the sediment particles were obstructed by the accumulation body upon reaching the toe of its slope and, as a result, climbed upwards along the accumulation body and were eventually deposited on top of it. This further increased the volume of the accumulation body (Fig. 7.4).

Thus, with continuous rapid sedimentation, the local riverbed rose rapidly, and a relatively large adverse slope was formed at the front of the raised section. Subsequent sediment particles were more prone to accumulation upon reaching this adverse slope. This resulted in further upstream development of the raised section of the riverbed, which in turn moved the location of the hydraulic jump upstream. Ultimately, this led to a continuous increase in the area where the riverbed and water level rose (Fig. 7.5).



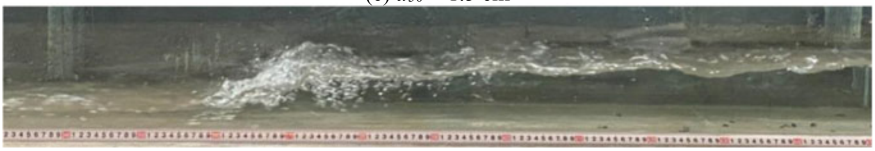
(a) d_{50} = 2.5 cm



(b) d_{50} = 1.8 cm



(c) d_{50} = 1.5 cm



(d) d_{50} = 1.0 cm

Fig. 7.2 Sudden stop of particles of varying sizes after a hydraulic jump

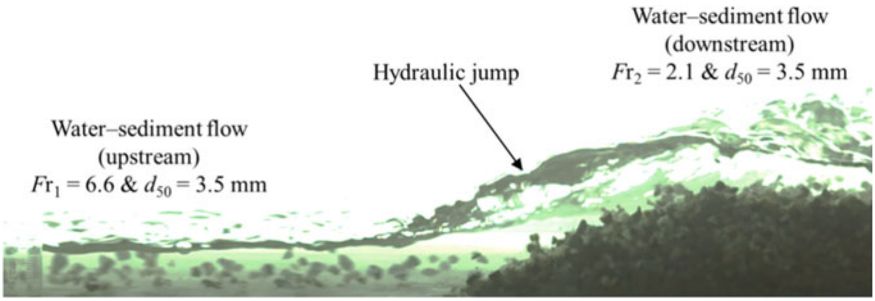


Fig. 7.3 Rapid sedimentation after a hydraulic jump

In a natural river, this process will eventually cause a flood and sediment disaster in a large area.

An accumulation body formed from extensive sedimentation was found to exhibit an undulating morphology with alternating peaks and troughs. Overall, the upstream peaks were higher than the downstream peaks. As the sediment accumulation body gradually developed upstream, its morphology continued to change with time. The flow regime in the whole accumulation zone exhibited notable variability (Fig. 7.6).

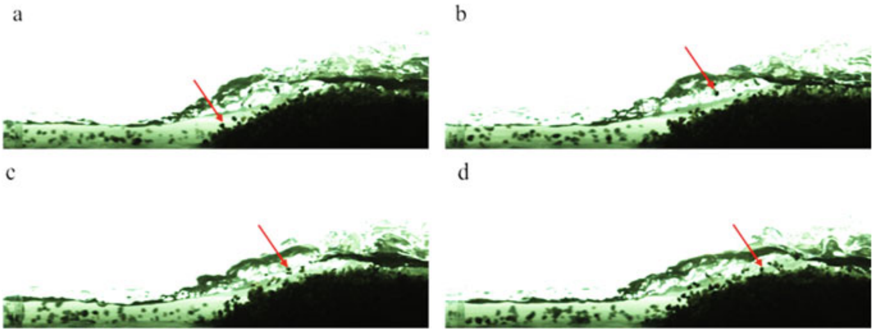


Fig. 7.4 Mesoscale deposition of sediment particles on an accumulation body

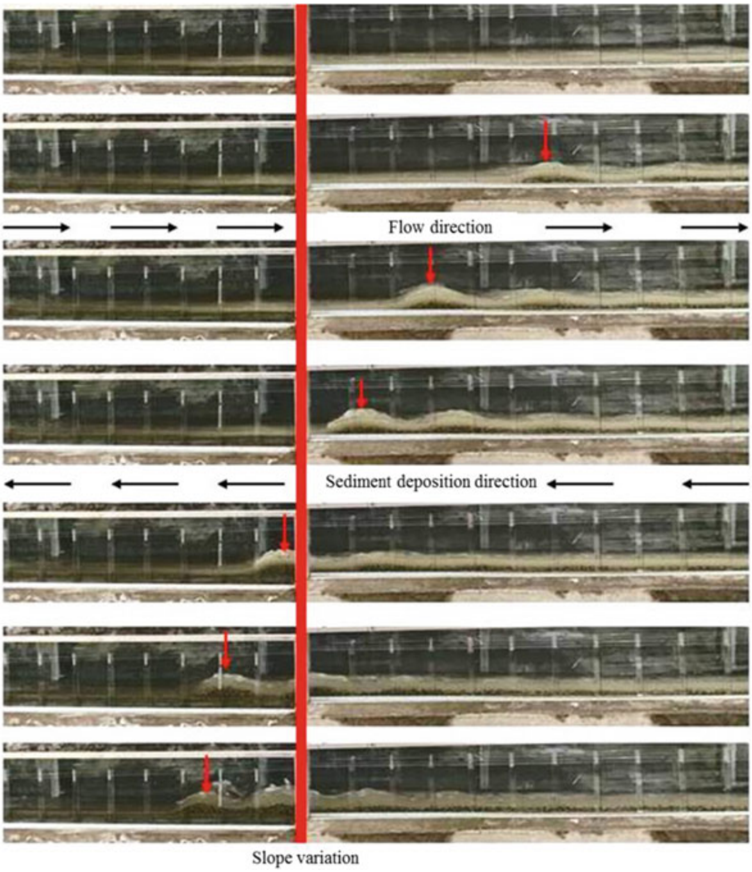


Fig. 7.5 Reverse development characteristics of a mound formed from sedimentation

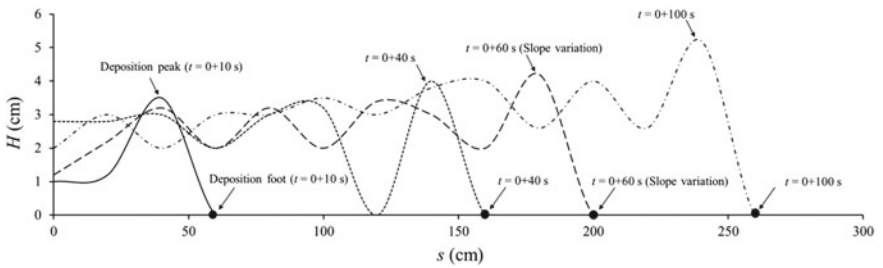


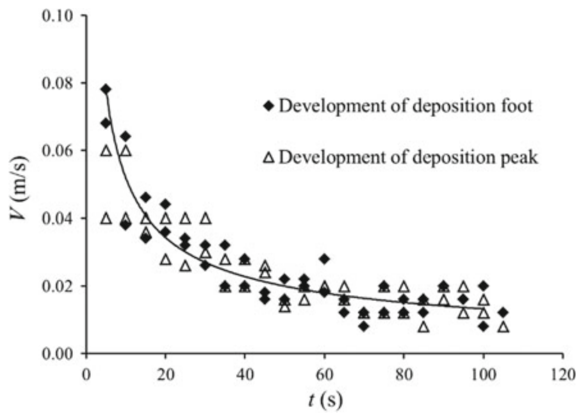
Fig. 7.6 Variation in the height of the sediment accumulation body, *H*, along the course

The variations in the rates of the reverse development (V_p and V_{fe}) of the peak and front edge, respectively, of the accumulation body formed from sedimentation with time fit a power function. At the initial stage of the formation of the accumulation body from sedimentation, V_p and V_{fe} were relatively high, and the accumulation body relatively rapidly developed upstream. As the accumulation body continuously developed upstream, V_p and V_{fe} gradually decreased and tended to level off. Throughout the process, V_p and V_{fe} were basically consistent with one another (Fig. 7.7).

Figure 7.8 shows the variation in the height of the sediment accumulation body, *H*, with time. As demonstrated in Fig. 7.8, at the initial stage, there was a relatively rapid increase in *H*. As time passed and the amount of accumulated sediment particles gradually increased, there was a gradual increase in *H*, but the rate of change in *H* with time tended to level off.

Figure 7.9 shows a schematic diagram depicting the water level–discharge relationship during a large disaster caused by a small flood. In Fig. 7.9, the original once-in-two-year flood discharge corresponds to a relatively low water level. However, sedimentation on the riverbed raises the elevation of the riverbed and, thereby, raises water level. Under severe sedimentation conditions, there is a sharp rise in the water level that corresponds to a once-in-50-year flood discharge.

Fig. 7.7 Variations in the rates of reverse development (V_p and V_{fe}) of a sediment accumulation body



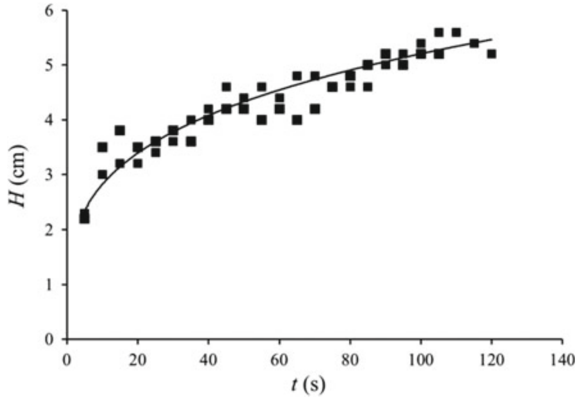


Fig. 7.8 Variation in the height of the sediment accumulation body, *H*, along the course

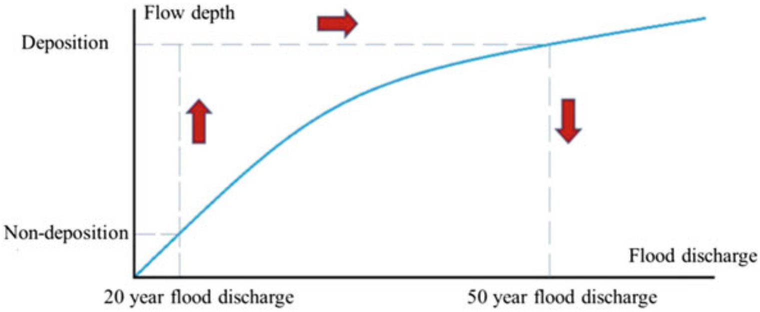
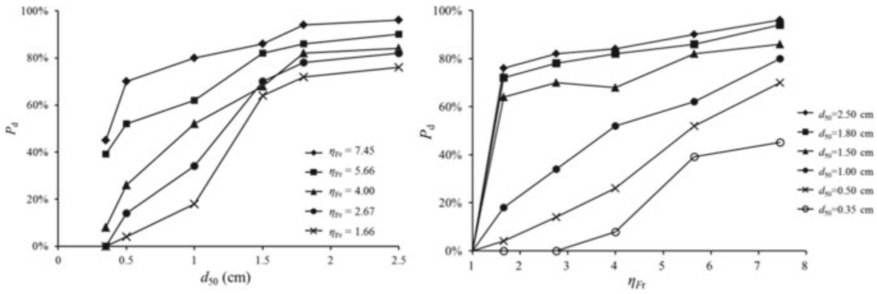


Fig. 7.9 Schematic diagram of a disaster caused by a small flood

7.3 Threshold Conditions for Combined Flash Flood and Sediment Disasters

The ratio of the number of particles that stopped suddenly and remained stationary after the hydraulic jump to the total number of particles that passed the hydraulic-jump zone in the abovementioned experiment is defined as the dwelling ratio of the particles, P_{d}. Statistical analysis has found that the median particle diameter d_{50} and the ratio of the Froude number *Fr* of the flow upstream of a hydraulic jump to that of the flow downstream of the hydraulic jump, η_{Fr}, are the main factors that affect P_{d}. η_{Fr} is calculated as follows:

$$\eta_{Fr} = \frac{Fr_1}{Fr_2} = \frac{U_1/\sqrt{gh_1}}{U_2/\sqrt{gh_2}} \tag{7.1}$$



(a) (b)

Fig. 7.10 Effects of the particle size and flow conditions on the dwelling ratio of particles, P_d

where U_1 and U_2 are the flow velocities upstream and downstream of the hydraulic jump, respectively, and h_1 and h_2 are the water depths upstream and downstream of the hydraulic jump, respectively.

Figure 7.10 shows the experimental results for the P_d–d_{50} relationships corresponding to various η_{Fr} values as well as the P_d–η_{Fr} relationships corresponding to various d_{50} values. As demonstrated in Fig. 7.10, at a relatively low η_{Fr} and a relatively small d_{50}, all the particles were able to continuously move downstream, and none of the particles stopped and remained stationary. As d_{50} and η_{Fr} increased, there was an increase in the number of particles that stopped and remained stationary as well as a gradual increase in P_d.

In the presence of an adequate sediment supply, sediment particles will begin to accumulate at a certain d_{50} and η_{Fr}. The η_{Fr} when particles begin to accumulate is referred to as the threshold η_{Fr}, which is denoted by η_{Fr0}. Thus, the threshold condition for particle accumulation at a certain d_{50} is as follows:

$$\eta_{Fr} > \eta_{Fr0} \tag{7.2}$$

As η_{Fr0} is related to d_{50}, η_{Fr0} varies significantly with d_{50}. During the accumulation of particles, the water level is not a direct factor independent of the flow velocity U. This suggests that when a threshold condition is established for FFSDs, the use of d_{50} instead of the water level to establish a threshold index can comprehensively reflect the effects of U and d_{50}. In fact, according to the bed-load motion theory, the sediment transport intensity of a bed load is directly proportional to the cube of the dimensionless parameter $U/(gd_{50})^{1/2}$. In view of this, the flash-flood research team of the State Key Laboratory of Hydraulics and Mountain River Engineering of Sichuan University has defined $U/(gd_{50})^{1/2}$ as the Fr of sediment (denoted Fr_d), i.e.,

$$Fr_d = \frac{U}{\sqrt{gd_{50}}} \tag{7.3}$$

Thus, the threshold condition for rapid particle accumulation after a hydraulic jump can be represented by the following equation:

$$\eta_{Frd} = \frac{Fr_{d,1}}{Fr_{d,2}} = \frac{U_1/\sqrt{gd_{50,1}}}{U_2/\sqrt{gd_{50,2}}} > \eta_{Frd0} \tag{7.4}$$

where η_{Frd} is the ratio of the Fr_{d} of the upstream sediment to that of the downstream sediment, the subscripts 1 and 2 signify upstream and downstream of the hydraulic jump, respectively, and the subscript 0 signifies the threshold value.

In natural rivers, sudden changes in Fr_{d} can occur not only in variable-slope hydraulic-jump zones but also in mainstream–tributary confluence regions and widening regions. While the above threshold is derived from an analysis of the hydraulic jumps over variable slopes, it is also applicable to scenarios involving other types of morphological changes in rivers, as long a possible difference in η_{Frd0} is considered. Thus, the motion evolution of the water and sediment in reaches in mainstream–tributary confluence regions as well as widening regions is analyzed briefly in the following section.

Figure 7.11 shows the experimental results for the sediment accumulation in a reach in a mainstream–tributary confluence region (Lei et al. 2019). As demonstrated in Fig. 7.11, regardless of whether the confluence angle of the mainstream and the tributary was 30°, 60°, or close to 90°, the transport of sediment stopped suddenly at the confluence when the η_{Frd} for the water and sediment supplied by the tributary reached the threshold due to the backwater effect of the mainstream, leading to extensive sedimentation.

Figure 7.12 shows the numerical simulation results for sedimentation in a widening reach of a river (Zheng et al. 2016). Similarly, as demonstrated in Fig. 7.12, after the river widened suddenly, the emergence of flood land resulted in a sudden increase in the resistance of the riverbed and a significant decrease in U, which in turn resulted in a decrease in Fr_{d}. As a consequence, the ratio of the Fr_{d} of upstream sediment to the Fr_{d} of sediment at the location where the river widened exceeded the disaster threshold. This led to sedimentation.

To derive a more general expression of η_{Frd}, it is necessary to collect and analyze a wide range of flash-flood data for various regions of natural rivers. On this basis, a threshold condition with general applicability for FFSDs can be established.

The State Key Laboratory of Hydraulics and Mountain River Engineering of Sichuan University collected and analyzed data for several hundreds of flash floods and eventually derived a threshold condition η_{Frd0} for combined flash flood and sediment disasters, as shown in Fig. 7.13.

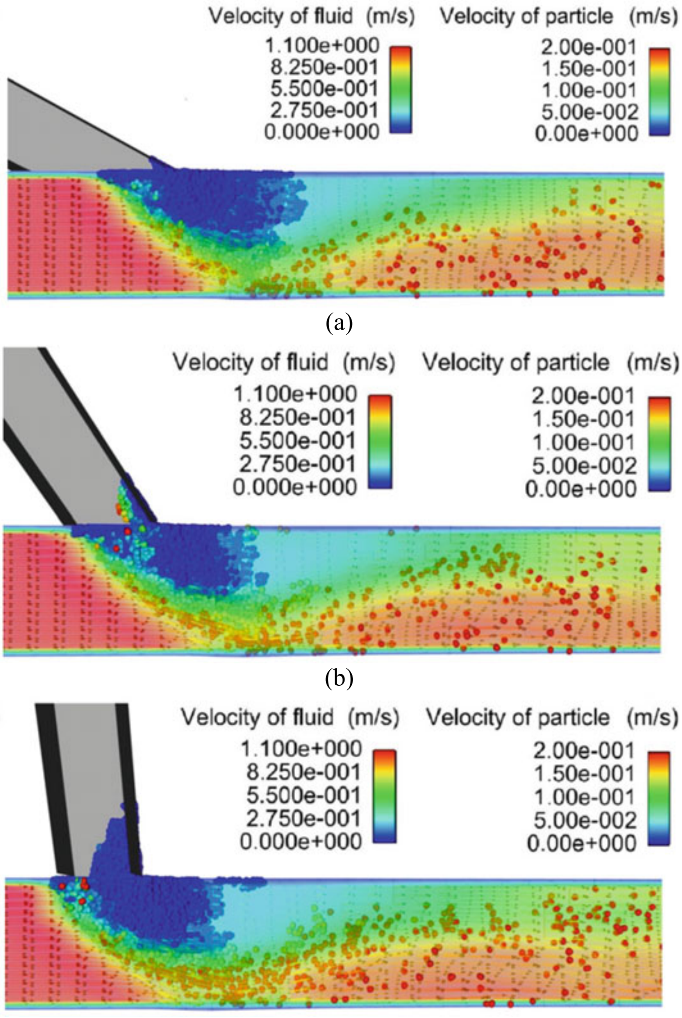


Fig. 7.11 Sedimentation in a reach in a mainstream–tributary confluence region

7.4 Identification of Disaster-Prone Regions Based on the Threshold Conditions for Combined Flash Flood and Sediment Disasters

This section briefly introduces a system developed by the State Key Laboratory of Hydraulics and Mountain River Engineering of Sichuan University based on η_{Frd0} to identify FFSD-prone regions.

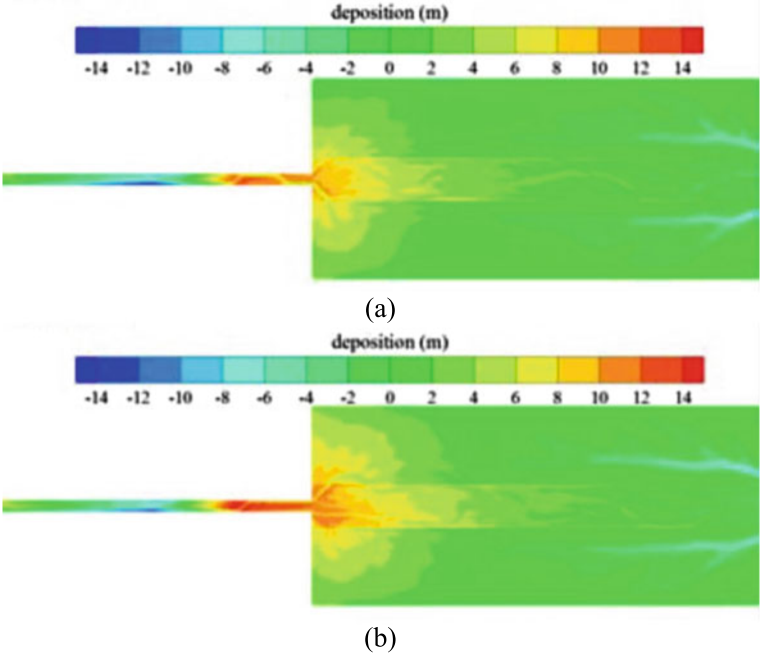
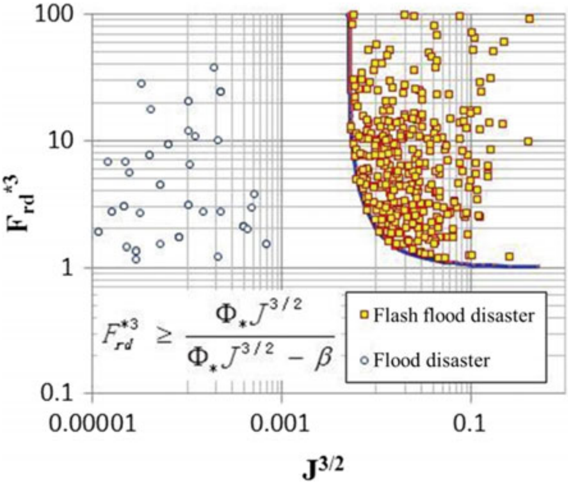


Fig. 7.12 Sedimentation in a widening reach of a river

Fig. 7.13 Threshold condition for combined flash flood and sediment disasters



Conventionally, the risk of flash floods is primarily classified using the following method: The areas affected by floods of various frequencies are first determined based on their water level values. Then, the risk levels are determined based on the flood frequencies. This risk classification method is completely reasonable and feasible for normal floods. However, for FFSDs involving large amounts of sediment, this method is problematic because it underestimates the risk and is inaccurate in predicting the locations at risk.

On the basis of the threshold condition η_{Frd0} for combined flash flood and sediment disasters and an FFSD simulation model, a more accurate risk identification system for FFSD-prone regions can be established to accurately identify real-world FFSDs.

First, for the FFSD-prone region whose risk is to be determined, as detailed of terrain data as possible and the possible upstream sediment supply conditions must be obtained. These data provide the fundamental conditions for identifying the risk of the FFSD-prone region.

Second, the sites prone to disasters under combined flood and sediment conditions are determined by hydraulic calculations based on η_{Frd0} (Fig. 7.14). η_{Frd0} is primarily controlled by Fr_{d}, which changes suddenly mainly in regions where the base slope of the riverbed levels off sharply, mainstream–tributary confluence regions, and sharply widening river reaches. Thus, particular attention should be paid to these regions.

Finally, simulations are performed using the FFSD model, with the FFSD-prone sites identified based on η_{Frd0} to further identify the specific areas at risk. The results can be used to guide the formulation of emergency plans and the provision of disaster warnings (Fig. 7.15).



Fig. 7.14 Identification of the FFSD-prone sites

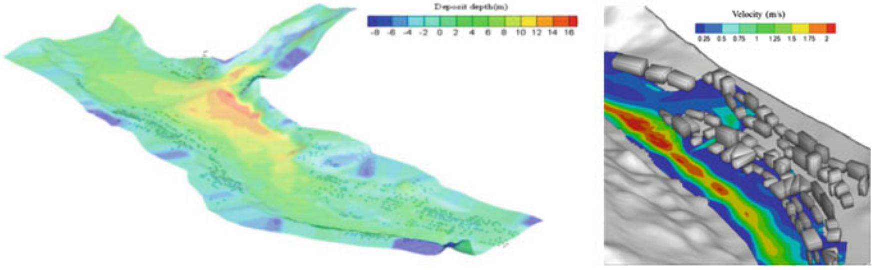


Fig. 7.15 Simulations of a region prone to disasters under combined flash flood and sediment conditions

Most prominently, the above risk identification method for disaster-prone regions has relatively high accuracy regarding the identification of the location and area of each disaster-prone site. Compared to water level analysis methods that do not consider the disaster effect of sedimentation, this method improves the accuracy by identifying the risk in FFSD-prone regions from an "area" level to a "point" level. As demonstrated in Fig. 7.16, the locations of the disaster-prone sites identified by

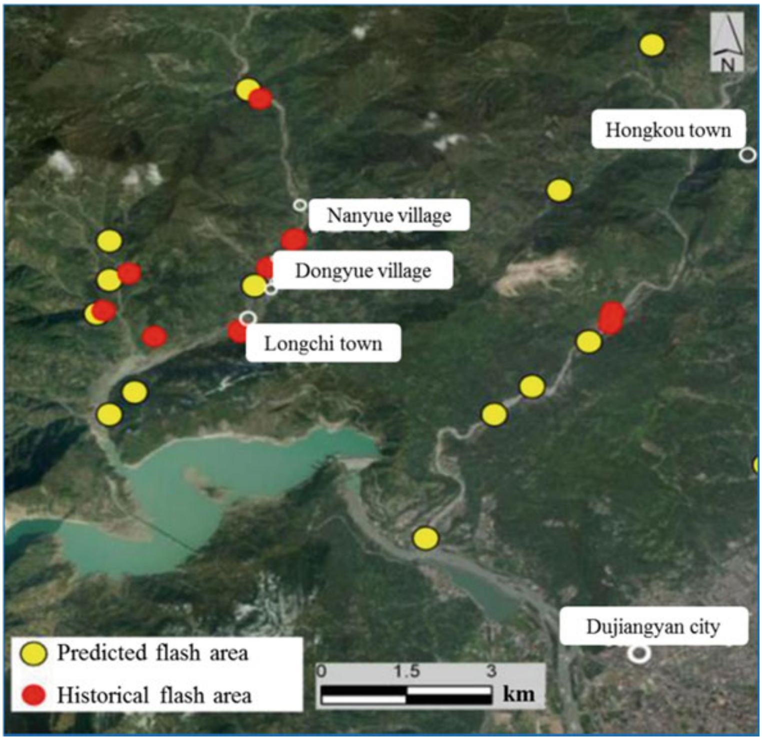


Fig. 7.16 Identification of FFSD-prone sites with an accuracy of 1–2 km

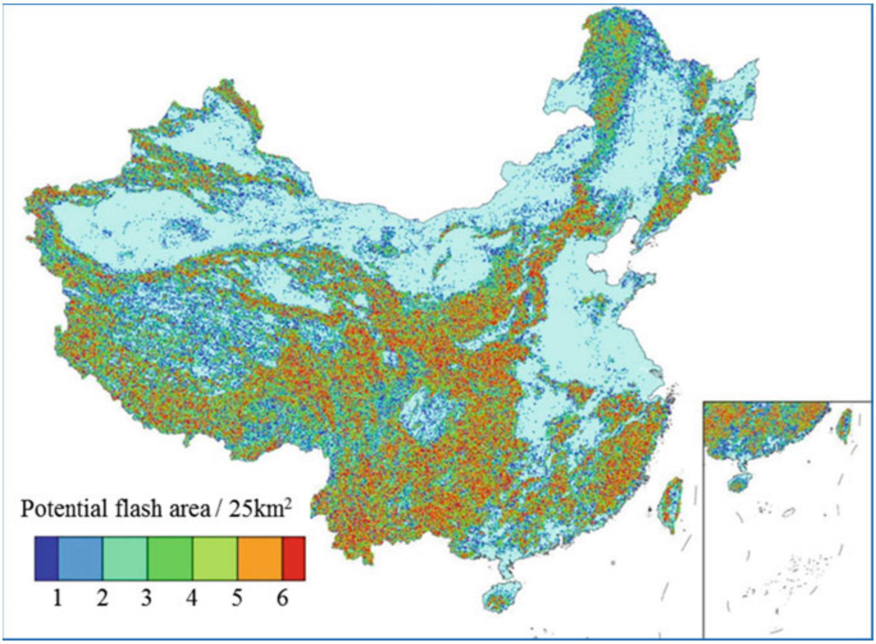


Fig. 7.17 Identification results produced by a risk identification system for FFSD-prone regions

this method are very close to those of the real-world sites where FFSDs occurred. This suggests that this identification method is effective.

The above identification method can be employed to establish a new risk identification system for FFSD-prone regions that covers all of China or even the entire globe (Fig. 7.17). This system can be first established based on open terrain data. Subsequently, users can supplement the system with new, higher-accuracy local terrain data according to their needs to improve its identification accuracy while using it. This will lead to continuous improvement in the identification accuracy of the system on the global scale. Ultimately, FFSD-prone regions can be accurately identified using this system.

Two issues are worthy of discussion, namely, the randomness and uncertainty of FFSDs and the acquisition of terrain data.

FFSDs depend primarily on three factors, namely, local river conditions, regional rainfall conditions, and upstream sediment supply. Of these three factors, the local river conditions are certain, and the regional rainfall conditions can now be determined based on 3–24 h rainfall forecasts, whereas the upstream sediment supply is notably uncertain. The above system is referred to as a risk identification system for disaster-prone regions because its core aim is to identify disaster-prone regions rather than to directly predict disasters. In other words, this system first determines whether local rivers are prone to disasters based on whether their Fr_d values reach the disaster threshold as well as the sizes of the disaster-prone regions corresponding to various

inflow conditions. Then, based on rainfall forecasts, this system determines whether it is possible for the rainfall to induce FFSDs in the presence of a sufficient sediment supply. If possible, the system will give a warning regardless of whether there is a sufficient sediment supply. In essence, this method addresses the uncertainty of upstream sediment supply conditions by increasing the number of warnings.

Terrain data are basic data for a risk identification system for FFSD-prone regions. The accuracy of terrain data, to a large extent, dictates the identification accuracy. Generally, terrain data can be obtained from digital elevation models (DEMs). However, when DEM data are unable to meet the identification accuracy requirements, it is necessary to obtain terrain data by specific field measurements, e.g., unmanned aerial vehicle surveys.

7.5 Analysis of Control Techniques Based on the Threshold Conditions for Combined Flash Flood and Sediment Disasters

The occurrence of an FFSD is dependent on the river regime, heavy rainfall, an excessive sediment supply, and human activity (Montgomery et al. 1996; Chatanantavet and Parker 2008). The key to FFSD control is to control Fr_d below the threshold by adjusting the river regime. Based on the definition of Fr_d, FFSD control techniques can be developed from the perspectives of adjusting the U values upstream and downstream of a disaster-prone river reach and the d_{50} of sediment particles. Specifically, η_Frd can be maintained below η_Frd0 by reducing the upstream U or increasing the downstream U as well as by increasing the d_{50} of the upstream sediment or reducing the d_{50} of the downstream sediment.

Some typical available FFSD control techniques conform to the above principle. Naturally, when a specific control scheme is designed, it is necessary to determine its parameters based on η_Frd0.

Wang et al. propounded a training levee line control technique for mainstream–tributary confluence regions (Wang et al. 2015; Gao et al. 2020), which is referred to as "control by diverting water" (Fig. 7.18). In this technique, the outline of the point bar formed by scouring is first determined, and the threshold U for the point-bar sediment particle movement is calculated. Then, a mathematical model is used to calculate the U distribution at the design standard flood discharge. Subsequently, the contour line of the U threshold for point-bar sediment particle movement at the outer outline of the point bar in the U distribution is used as a point-bar control line. If conditions permit, the confluence angle between the mainstream and the tributary should be minimized in each confluence region. From the perspective of controlling Fr_d, this technique, in essence, reduces η_Frd and controls it within the safe range by reducing the width of the downstream river as well as increasing the downstream U and downstream Fr_d.

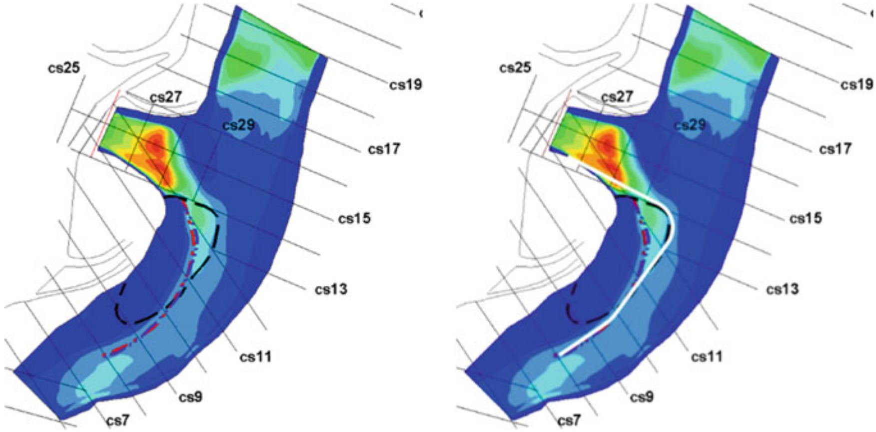


Fig. 7.18 Control by diverting water

Placing sediment-trap dams in rivers or streams is another typical FFSD control technique, which is referred to as "control by trapping sediment". A bottom current flow connection downstream of a relatively high sediment-trap dam can easily scour and damage the downstream riverbed. To address this problem, energy dissipation structures can be placed downstream of the dam in locations at various elevations. After passing the dam, a flow first enters the body of water where the first-level energy dissipation structure is located, and its energy is partially consumed. Subsequently, the flow enters the body of water where the second-level energy dissipation structure is located, and its energy is further consumed. Thus, through energy dissipation in a cascading manner, the flow enters the river downstream of a sediment-trap dam at a relatively low U after passing the dam. This approach not only fully realizes the role of a sediment-trap dam in trapping sediment but also effectively prevents the riverbed downstream of the dam from being scoured and damaged. Figure 7.19 shows a sediment-trap dam technique capable of dissipating energy and preventing scouring. From the perspective of controlling Fr_{d}, sediment trapping alters η_{Frd} by increasing the d_{50} of the upstream sediment and decreasing that of the downstream sediment. As sediment traps often have a damming effect to varying degrees, sediment trapping also generally reduces the upstream U. These effects reduce η_{Frd} to below η_{Frd0}.

Ma et al. proposed a technique that involves the placement of structures that separate water and sediment in spillways (Zhong et al. 2019), which is referred to as "control by separating sediment" (Fig. 7.20). The core of this technique is described as follows: A sediment accumulation pool is placed at the upstream end. A flow passageway and a sediment discharge passageway are established in parallel downstream of the sediment accumulation pool. The entrance of the sediment discharge passageway is connected smoothly with the sediment accumulation pool. An overflow weir is placed upstream of the flow passageway. The upstream side of the overflow weir doubles as a sediment diversion wall and can divert large sediment particles into the sediment discharge passageway and prevent them from entering the

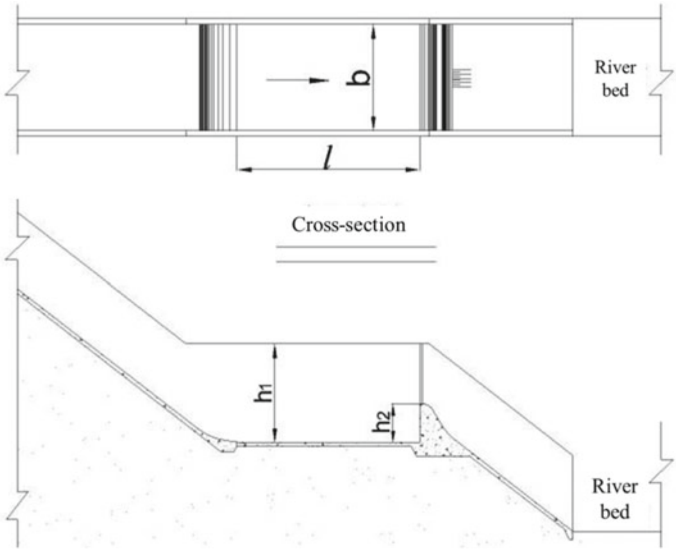


Fig. 7.19 Control by trapping sediment

downstream river and, thereby, reduce the d_{50} of the downstream sediment. From the perspective of controlling Fr_{d}, sediment separation reduces η_{Frd} by reducing the d_{50} of the downstream sediment.

Wang et al. (2014) and Lei et al. (2019) formulated a peak-staggering sediment-arresting pier technique capable of mitigating siltation in mountainous rivers, which is referred to as "control by staggering the peaks" (Fig. 7.21). According to this technique, at least three peak-staggering sediment-arresting piers in two rows are required based on the locations of the concentrated flow paths of the median-water and flood periods and the maximum thickness of the accumulated sediment after the recession of floods. Each sediment-arresting pier is placed outside the concentrated flow paths of the median-water period but within the concentrated flow paths of the flood period. Thus, the sediment-arresting piers do not affect the flow movement during the median-water and dry periods. During the sediment disaster-prone flood period, these piers arrest sediment and, thereby, cause the sediment peak to occur after the flood peak and decouple the flood and sediment processes. From the perspective of controlling Fr_{d}, peak staggering, which is the temporal and spatial separation of the flood and sediment peaks, reduces η_{Frd} by increasing the d_{50} of the upstream sediment as well as decreasing the d_{50} of the downstream sediment and the upstream U.

Figure 7.22 shows a real-world example of the engineering control of a mainstream–tributary confluence region. This region suffered severe siltation because of a flash flood. As a result, the village, schools, and enterprises sustained enormous losses. After the disaster, multiple mainstream–tributary confluence regions were

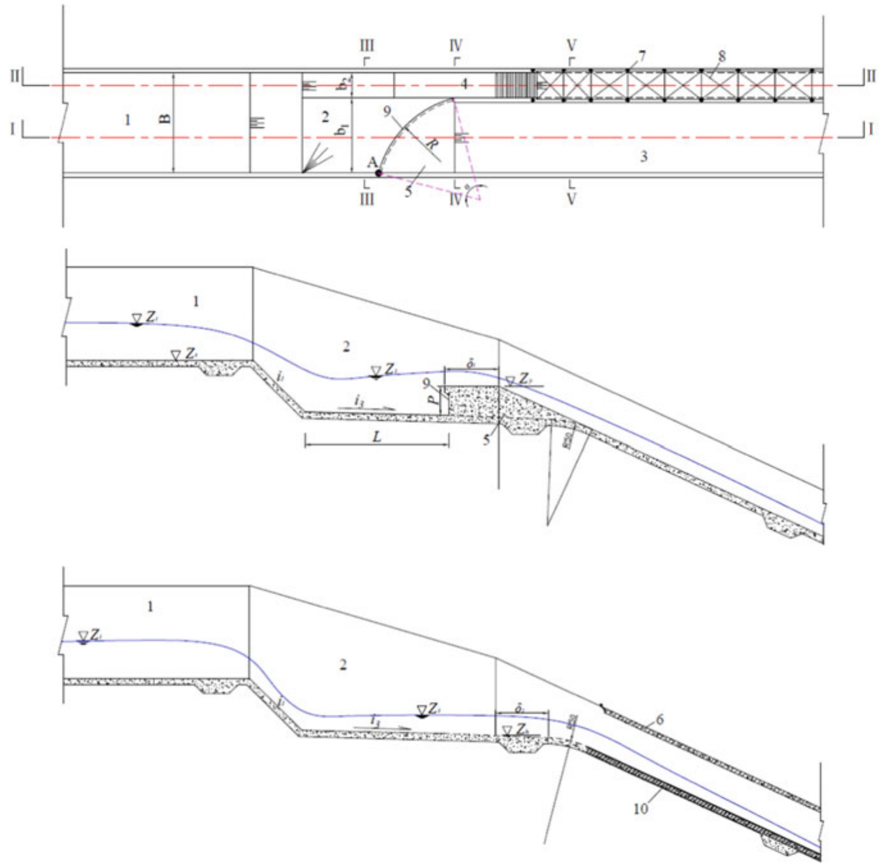


Fig. 7.20 Control by separating sediment

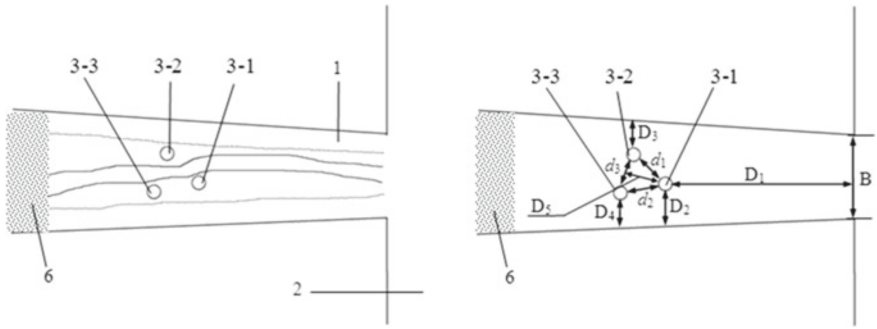


Fig. 7.21 Control by staggering the peaks



Fig. 7.22 Real-world example of the engineering control of a mainstream–tributary confluence region

controlled along the mainstream. The reaches controlled using conventional techniques were again extensively damaged during subsequent flash floods. In contrast, the reach shown in Fig. 7.22 was controlled based on the threshold Fr_{d}. Specifically, the downstream side of the end of the tributary was straightened. In addition, the angle at which the tributary flew into the mainstream was reduced. This approach prevented a sudden decrease in the Fr_{d} of the downstream sediment due to the expansion and thrust of the flow and ensured that η_{Frd} was below the threshold. After the implementation of the control measures, the confluence region remained safe during the flood season and withstood a subsequent catastrophic FFSD.

7.6 Conclusions

The following main conclusions can be derived from the analysis in this chapter:

1. The mesoscale investigation of the hydraulic jump of a sediment-laden flow shows that sediment particles suddenly stop moving after entering the slow-flow section from the rapid-flow section and, subsequently, accumulate in large amounts. In addition, the front edge of the accumulation body continuously develops upstream as a result of the interactions between the flow and sediment particles. This in turn causes the front of the hydraulic jump to move upstream and, thereby, results in chain-type sedimentation and a rise in the water level.

2. The threshold condition for combined flash flood and sediment disasters can be represented by η_{Frd}, which is the ratio of the Froude number of the upstream sediment to that of downstream sediment. When η_{Frd} reaches the threshold, rapid sedimentation occurs, the riverbed rises sharply, and water level rises suddenly. This leads to an increase in the risk of a disaster and can even allow a small flood to cause a large disaster.
3. The principle of controlling the sediment Froude number Fr_{d} can be used to design engineering control schemes for FFSDs. It is necessary to ensure that η_{Frd} is below the disaster threshold in design.

References

Borga, M., Boscolo, P., Zanon, F., & Sangati, M. (2007). Hydrometeorological analysis of the 29 August 2003 flash flood in the Eastern Italian Alps. *Journal of Hydrometeorology, 8*(5), 1049–1067.

Chatanantavet, P., & Parker, G. (2008). Experimental study of bedrock channel alluviation under varied sediment supply and hydraulic conditions. *Water Resources Research, 44*(12).

Dietrich, W. E., Kirchner, J. W., Ikeda, H., & Iseya, F. (1989). Sediment supply and the development of the coarse surface layer in gravel-bedded rivers. *Nature, 340*(6230), 215–217.

Diplas, P., Dancey, C. L., Celik, A. O., Valyrakis, M., Greer, K., & Akar, T. (2008). The role of impulse on the initiation of particle movement under turbulent flow conditions. *Science, 322*(5902), 717–720.

Gao, Y., Ye, L., Wang, Y., Xu, Z., & Wang, X. (2020). 3D numerical simulation of flow characteristics at confluence zone between Shenxigou Stream and Baisha River. *Advanced Engineering Sciences, 52*(2), 78–85.

Lei, M., Xu, Z.-X., Zhao, T., & Wang, X.-K. (2019a). Dynamics of loose granular flow and its subsequent deposition in a narrow mountainous river. *Journal of Mountain Science, 16*(6), 1367–1380.

Lei, M., Yu, H., Xu, Z., & Wang, X. (2019b). Numerical simulation of retrogressive pebble deposition in the changing slope zone of a mountainous river. *Advanced Engineering Sciences, 51*(1), 45–51.

Madej, M. A., Sutherland, D. G., Lisle, T. E., & Pryor, B. (2009). Channel responses to varying sediment input: A flume experiment modeled after Redwood Creek, California. *Geomorphology, 103*(4), 507–519.

Montgomery, D. R., Abbe, T. B., Buffington, J. M., Peterson, N. P., Schmidt, K. M., & Stock, J. D. (1996). Distribution of bedrock and alluvial channels in forested mountain drainage basins. *Nature, 381*(6583), 587–589.

Wang, X., Ye, L., Wang, Yu., & Liu, X. (2014). Experimental study on the evolution of the accumulation body in the confluence due to steep gully of the high intensity sediment transport. *Journal of Sichuan University (Engineering Science Edition), 5,* 7–13.

Wang, B., Zhou, S., Wang, H., Wang, X., & Liu, T. (2015). Regulation method in right-angled river confluence. *Journal of Sichuan University (Engineering Science Edition), S1,* 7–12.

Wang, X., Liu, X., & Zhou, J. (2019). Research framework and anticipated results of flash flood disasters under the mutation of sediment supply. *Advanced Engineering Sciences, 51*(4), 1–10.

Zheng, X.-G., Pu, J. H., Chen, R.-D., Liu, X.-N., & Shao, S. (2016). A novel explicit-implicit coupled solution method of SWE for long-term river meandering process induced by dam break.

Zhong, Y., Ma, X., Nie, R., Liu, X., & Zheng, X. (2019). Experimental study on the effect of siltation height on water level change in steep slope channel. *Advanced Engineering Sciences, 51*(6), 134–138.